frontiers | Research Topics

# Novel paradigms in cardiothoracic and abdominal disorders in veterinary practice

**Edited by**
Ahmed S. Mandour and Ryou Tanaka

**Coordinated by**
Tomohiko Yoshida

**Published in**
Frontiers in Veterinary Science

ISSN 1664-8714
ISBN 978-2-8325-4802-8
DOI 10.3389/978-2-8325-4802-8

## About Frontiers

Frontiers is more than just an open access publisher of scholarly articles: it is a pioneering approach to the world of academia, radically improving the way scholarly research is managed. The grand vision of Frontiers is a world where all people have an equal opportunity to seek, share and generate knowledge. Frontiers provides immediate and permanent online open access to all its publications, but this alone is not enough to realize our grand goals.

## Frontiers journal series

The Frontiers journal series is a multi-tier and interdisciplinary set of open-access, online journals, promising a paradigm shift from the current review, selection and dissemination processes in academic publishing. All Frontiers journals are driven by researchers for researchers; therefore, they constitute a service to the scholarly community. At the same time, the *Frontiers journal series* operates on a revolutionary invention, the tiered publishing system, initially addressing specific communities of scholars, and gradually climbing up to broader public understanding, thus serving the interests of the lay society, too.

## Dedication to quality

Each Frontiers article is a landmark of the highest quality, thanks to genuinely collaborative interactions between authors and review editors, who include some of the world's best academicians. Research must be certified by peers before entering a stream of knowledge that may eventually reach the public - and shape society; therefore, Frontiers only applies the most rigorous and unbiased reviews. Frontiers revolutionizes research publishing by freely delivering the most outstanding research, evaluated with no bias from both the academic and social point of view. By applying the most advanced information technologies, Frontiers is catapulting scholarly publishing into a new generation.

## What are Frontiers Research Topics?

Frontiers Research Topics are very popular trademarks of the *Frontiers journals series*: they are collections of at least ten articles, all centered on a particular subject. With their unique mix of varied contributions from Original Research to Review Articles, Frontiers Research Topics unify the most influential researchers, the latest key findings and historical advances in a hot research area.

Find out more on how to host your own Frontiers Research Topic or contribute to one as an author by contacting the Frontiers editorial office: frontiersin.org/about/contact

# Novel paradigms in cardiothoracic and abdominal disorders in veterinary practice

**Topic editors**
Ahmed S. Mandour — Suez Canal University, Egypt
Ryou Tanaka — Tokyo University of Agriculture and Technology, Japan

**Topic coordinator**
Tomohiko Yoshida — Obihiro University of Agriculture and Veterinary Medicine, Japan

**Citation**
Mandour, A. S., Tanaka, R., Yoshida, T., eds. (2024). *Novel paradigms in cardiothoracic and abdominal disorders in veterinary practice*. Lausanne: Frontiers Media SA.
doi: 10.3389/978-2-8325-4802-8

# Table of contents

frontiers | Frontiers in Veterinary Science

TYPE Editorial
PUBLISHED 08 April 2024
DOI 10.3389/fvets.2024.1369276



OPEN ACCESS

EDITED AND REVIEWED BY
Ali Mobasheri,
University of Oulu, Finland

*CORRESPONDENCE
Ahmed S. Mandour
✉ dr_mandour@vet.suez.edu.eg

RECEIVED 11 January 2024
ACCEPTED 04 March 2024
PUBLISHED 08 April 2024

CITATION
Mandour AS, Farag A, Yoshida T and Tanaka R (2024) Editorial: Novel paradigms in cardiothoracic and abdominal disorders in veterinary practice.
*Front. Vet. Sci.* 11:1369276.
doi: 10.3389/fvets.2024.1369276



# Editorial: Novel paradigms in cardiothoracic and abdominal disorders in veterinary practice

Ahmed S. Mandour[1,2]*, Ahmed Farag[2,3], Tomohiko Yoshida[4] and Ryou Tanaka[2]

[1]Department of Animal Medicine (Internal Medicine), Faculty of Veterinary Medicine, Suez Canal University, Ismailia, Egypt, [2]Veterinary Surgery, Tokyo University of Agriculture and Technology, Tokyo, Japan, [3]Department of Surgery, Anesthesiology, and Radiology, Faculty of Veterinary Medicine, Zagazig University, Zagazig, Egypt, [4]Department of Veterinary Surgery, Division of Veterinary Research, Obihiro University of Agriculture and Veterinary Medicine, Obihiro, Hokkaido, Japan

KEYWORDS

**cardiothoracic, ultrasound, echocardiography, biomarkers, diagnosis**

Editorial on the Research Topic
Novel paradigms in cardiothoracic and abdominal disorders in veterinary practice

Cardiothoracic and abdominal disorders constitute a large proportion of animal diseases and are the leading causes of considerable deaths in the field of veterinary medicine. There are continuous research trials to find out simple diagnostic methods to monitor internal organ functions effectively and easily with time-saving procedures, high accuracy, and minimum invasiveness. Moreover, recent treatment strategies including new therapeutic agents and/or surgical techniques as well as diagnostic biomarkers are currently highly developed. Recent research studies are focusing on new diagnostic imaging techniques such as novel ultrasonographic approaches, echocardiography-derived techniques, blood flow dynamics, etc., in addition to new surgical procedures and laboratory biomarkers. These trendy methods showed enormous potential to improve the outcome of cardiothoracic and abdominal disorders in animal models and clinical practice. In this Research Topic, nine articles were published covering the recent approaches in the aforementioned objectives which may serve as a guidance to researchers and veterinarians in the field.

The exploration of new treatments for heart failure involves evaluating potential therapeutic approaches in suitable animal models designed to mimic heart failure conditions. Over the recent decades, murine models of cardiovascular diseases have provided efficient strategies for preventing and managing cardiac dysfunctions. Establishing these models begins with precise surgical techniques and well-designed anesthetic protocols. Nevertheless, each protocol may exhibit limitations that can impact the results of the study. In this Research Topic, Farag, Mandour, Hendawy et al. wrote a systematic review covering the heart failure in murine models, considering the most common and recent surgical models of heart failure and the anesthetic protocols. Moreover, they listed the surgical procedures of each model, the proper anesthesia, and the limitations in each single model, which can guide the researcher during selection of the model.

In veterinary cardiology, novel anesthetic protocols that may save time, money, or overcome restriction on medicinal agents in certain countries are crucial. Numerous validated anesthetic agents used to create myocardial infarction (MI) model are currently controversial with certain restrictions due to ethical concerns. The combination of medetomidine, midazolam, and butorphanol (MMB) is frequently employed in various surgical operations in animals. However, there hasn't been an exploration of the use of the MMB combination to create the MI in rats. This is challenging due to the pronounced respiratory depression and prolonged recovery observed post-surgery, leading to substantial mortality rates. Farag, Mandour, Hamabe et al. established a new protocol of anesthesia to create MI in rat models using a combination of MMB (0.3/5.0/5.0 mg/kg) and atipamezole (1.0 mg/kg SC). Conclusively, subcutaneous administration of atipamezole effectively mitigates the cardiopulmonary side effects of the MMB mixture, facilitating rapid recovery and consequently enhancing the survival rate during the establishment of the MI model in rats.

Increasing evidence indicates that dental disorders contribute to the onset of cardiovascular disease. Several epidemiological studies have proposed a potential connection between periodontitis and cardiovascular diseases. In the current paper Research Topic, Elhaieg et al. used various comprehensive methods including conventional echocardiography, intraventricular pressure gradient analysis, Speckle Tracking Echocardiography, and invasive hemodynamic analysis to evaluate the heart function in rat model with periodontitis. This study suggests that periodontitis may compromise systolic function and myocardial relaxation.

Elevated pulmonary artery pressure is known as pulmonary hypertension (PH). Canine PH is commonly occurring secondary to myxomatous mitral valve disease (MMVD). Certain echocardiographic calculation as well as laboratory markers have been investigated in canine PH, however, they are still not accurate. Certain blood indices have previously been found to be indicators for prediction and prognosis of PH in human. Tangmahakul et al. examined the applicability of the blood indices in canine patients affected by MMVD with and without PH. The results confirmed a reduction in MCH and MCHC in dog patient suffering from MMVD, precapillary PH, and postcapillary PH, while PDW are associated with MMVD severity but not with the presence of PH.

In recent years, there has been a notable rise in the occurrence of hypertrophic cardiomyopathy (HCM) in feline patients within clinical practice, primarily attributed to advancements in diagnostic methods and equipment capabilities. Saito et al. evaluated myocardial function in cats affected by HCM with and without outflow obstruction (HOCM) using 2D speckle-tracking echocardiography. Their findings indicated that all HCM-affected cats exhibited a notable decrease in left ventricular (LV) longitudinal strain across the endocardial, epicardial, and overall layers, as well as in LV circumferential strain within the epicardium, in comparison to healthy cats. Cats with HOCM showed a significant reduction in both the endocardial and overall layers of LV circumferential strain when compared to healthy cats. Consequently, the diminished LV endocardial strain had a cascading effect on the values of LV strain across the entire myocardial layer, leading to the conclusion that LV myocardial function may be more compromised in HCM-affected cats with concurrent outflow obstruction.

Chronic idiopathic intestinal inflammation is a growing global health concern affecting both companion animals, especially dogs, and human patients leading to significant fluid and electrolyte losses. Interestingly, the differences observed in the handling of intestinal electrolytes in human and canine patients imply the existence of species-specific regulatory or counterregulatory mechanisms. In the context of preserving fluid and electrolyte balance, the renin-angiotensin-aldosterone system (RAAS) assumes a pivotal role. It is well-known that RAAS plays a systemic role in regulating blood pressure and cardiovascular pathology, however, it has unveiledcomplex roles in the realm of inflammatory processes. In the perspective article authored by Heilmann et al., they offered an overview of our current understanding of electrolyte transport in the context of human IBD and canine chronic inflammatory enteropathy. Additionally, they explore the role of RAAS in these conditions and propose innovative therapeutic strategies.

In the same line, Dengler et al. conducted a study to explore the gene expression of intestinal electrolyte transporters that may be implicated in either mitigating or exacerbating electrolyte losses in dogs with chronic idiopathic enteropathy. They also investigated the potential activation of the RAAS system in these dogs and explored the potential associations between the expression of intestinal electrolyte transporters and established RAAS components. Serum RAAS fingerprint analysis, mRNA levels of intestinal electrolyte transporters, and local RAAS pathway components in tissue biopsies were analyzed. The results indicated increased levels of components from both the traditional and alternative RAAS pathways in dogs with chronic idiopathic enteropathy. The study illustrated an upregulation of both traditional and alternative components of RAAS in the serum of dogs with chronic idiopathic enteropathy.

Park et al. documented an intriguing case involving 9-month-old female Pomeranian dog suffering from cyst-like lesions caused by generalized lymphatic anomaly (GLA) which involve several abdominal organs. The histopathological analysis and immunohistochemistry (IHC) confirmed that the cells lining these cyst-like lesions strongly expressed lymphatic vessel endothelial hyaluronan receptor 1. Notably, GLA should be considered in young dog when presenting with multiple cysts in various abdominal organs.

Congenital lobar emphysema (CLE) is an infrequent lower respiratory tract disorder that predominantly manifests in young dogs and cats. Edwards et al. detailed the evaluation and treatment of an 11-week-old, sexually intact female Catahoula Leopard dog presented with exercise intolerance and respiratory distress. There was hyperinflated right middle lung field, resulting in the compression of surrounding lung lobes. Following lung lobectomy, histopathology revealed the presence of bronchial cartilage hypoplasia, marked emphysema, and pleural fibrosis.

The investigations in this Research Topic have demonstrated the state of knowledge regarding the diagnosis and management of cardiothoracic disorders in cats and dogs. We anticipate that these articles will stimulate and motivate additional research into the development of cutting-edge diagnostic imaging novel echocardiography methods and the biofluid analysis of cardiac biomarkers.

## Author contributions

AM: Writing—review & editing, Writing—original draft, Validation, Supervision, Methodology, Investigation, Data curation, Conceptualization. AF: Writing—review & editing. TY: Writing—review & editing. RT: Writing—review & editing.

## Funding

The author(s) declare that no financial support was received for the research, authorship, and/or publication of this article.

## Acknowledgments

The Topic Editors appreciate the contributions of all authors to this Research Topic. Also, we greatly thank the reviewers for their valuable comments.

## Conflict of interest

The authors declare that the research was conducted in the absence of any commercial or financial relationships that could be construed as a potential conflict of interest.

## Publisher's note

frontiers | Frontiers in Veterinary Science

TYPE Original Research
PUBLISHED 05 December 2022
DOI 10.3389/fvets.2022.1064836



OPEN ACCESS

EDITED BY
Muhammad Saqib,
University of Agriculture,
Faisalabad, Pakistan

REVIEWED BY
Muhammad Athar,
Banfield Pet Hospital, United States
Jean-Claude Desfontis,
Ecole Nationale Vétérinaire
Agroalimentaire et de
l'Alimentation, France

*CORRESPONDENCE
Ahmed Farag
ahmedfarag9331@gmail.com
Ahmed S. Mandour
dr_mandour@vet.suez.edu.eg
Ryou Tanaka
ryo@vet.ne.jp

SPECIALTY SECTION
This article was submitted to
Comparative and Clinical Medicine,
a section of the journal
Frontiers in Veterinary Science

RECEIVED 08 October 2022
ACCEPTED 14 November 2022
PUBLISHED 05 December 2022

CITATION
Farag A, Mandour AS, Hamabe L,
Yoshida T, Shimada K and Tanaka R
(2022) Novel protocol to establish the
myocardial infarction model in rats
using a combination of
medetomidine-midazolam-
butorphanol (MMB) and atipamezole.
*Front. Vet. Sci.* 9:1064836.
doi: 10.3389/fvets.2022.1064836



# Novel protocol to establish the myocardial infarction model in rats using a combination of medetomidine-midazolam-butorphanol (MMB) and atipamezole

Ahmed Farag[1,2]*, Ahmed S. Mandour[1,3]*, Lina Hamabe[1], Tomohiko Yoshida[1], Kazumi Shimada[1] and Ryou Tanaka[1]*

[1]Department of Veterinary Surgery, Faculty of Veterinary Medicine, Tokyo University of Agriculture and Technology, Fuchu, Japan, [2]Department of Surgery, Anesthesiology, and Radiology, Faculty of Veterinary Medicine, Zagazig University, Zagazig, Egypt, [3]Department of Animal Medicine (Internal Medicine), Faculty of Veterinary Medicine, Suez Canal University, Ismailia, Egypt

**Background:** Myocardial infarction (MI) is one of the most common cardiac problems causing deaths in humans. Previously validated anesthetic agents used in MI model establishment are currently controversial with severe restrictions because of ethical concerns. The combination between medetomidine, midazolam, and butorphanol (MMB) is commonly used in different animal models. The possibility of MMB combination to establish the MI model in rats did not study yet which is difficult because of severe respiratory depression and delayed recovery post-surgery, resulting in significant deaths. Atipamezole is used to counter the cardiopulmonary suppressive effect of MMB.

**Objectives:** The aim of the present study is to establish MI model in rats using a novel anesthetic combination between MMB and Atipamezole.

**Materials and methods:** Twenty-five Sprague Dawley (SD) rats were included. Rats were prepared for induction of the Myocardial infarction (MI) model through thoracotomy. Anesthesia was initially induced with a mixture of MMB (0.3/5.0/5.0 mg/kg/SC), respectively. After endotracheal intubation, rats were maintained with isoflurane 1% which gradually reduced after chest closing. MI was induced through the left anterior descending (LAD) artery ligation technique. Atipamezole was administered after finishing all surgical procedures at a dose rate of 1.0 mg/kg/SC. Cardiac function parameters were evaluated using ECG (before and after atipamezole administration) and transthoracic echocardiography (before and 1 month after MI induction) to confirm the successful model. The induction time, operation time, and recovery time were calculated. The success rate of the MI model was also calculated.

**Results:** MI was successfully established with the mentioned anesthetic protocol through the LAD ligation technique and confirmed through changes in ECG and echocardiographic parameters after MI. ECG data was improved after atipamezole administration through a significant increase in

heart rate (HR), PR Interval, QRS Interval, and QT correction (QTc) and a significant reduction in RR Interval. Atipamezole enables rats to recover voluntary respiratory movement (VRM), wakefulness, movement, and posture within a very short time after administration. Echocardiographic ally, MI rats showed a significant decrease in the left ventricular wall thickness, EF, FS, and increased left ventricular diastolic and systolic internal diameter. In addition, induction time (3.440 ± 1.044), operation time (29.40 ± 3.663), partial recovery time (10.84 ± 3.313), and complete recovery time (12.36 ± 4.847) were relatively short. Moreover, the success rate of the anesthetic protocol was 100%, and all rats were maintained for 1 month after surgery with a survival rate of 88%.

**Conclusion:** Our protocol produced a more easy anesthetic effect and time-saving procedures with a highly successful rate in MI rats. Subcutaneous injection of Atipamezole efficiently counters the cardiopulmonary side effect of MMB which is necessary for rapid recovery and subsequently enhancing the survival rate during the creation of the MI model in rats.

KEYWORDS

**myocardial infarction, rat, MMB, atipamezole, anesthesia, ECG, echocardiography**

## Introduction

Myocardial infarction (MI) is the main form of ischemic heart disease which occurs due to the blockage of one or more coronary vessels leading to myocardial ischemia and necrosis (1). Acute MI remains the most severe form of coronary artery disease in humans, accounting for almost 4 million deaths each year in Europe and Northern Asia (2). The development of a simple, effective, and time-saving MI animal model is crucial to enrich our knowledge about its pathophysiology and finding better therapeutic options. Various methods have been established in laboratory animal models (3), either by using chemicals that interrupt the coronary circulation (4), coronary artery ligation *via* open thoracic cage surgery (5), or through non-invasive catheter method (6).

Owing to an increasing concern for laboratory animal welfare and third-party certification of experimental facilities, advances in rodent anesthesia are currently a topic of interest. In MI models, achieving an appropriate anesthetic effect is not only essential from the welfare viewpoint but also constitutes a great challenge that controls the success rate of the model. Generally, achieving an appropriate anesthetic effect in rodent MI models requires sufficient anesthetic depth and fewer cardiorespiratory depression. It has reported that cardiorespiratory depression affecting recovery and survival rate post-MI, subsequently affecting experimental data and the statistical power (7). As a result, an anesthetic protocol that mediates appropriate anesthetic depth while minimizing cardiorespiratory impact is worth investigating, suitable for real-time control of anesthetic depth, and might be used for both short or long durations (8).

In veterinary studies, various anesthetic combinations have been previously proven to be effective to induce MI models in rodents such as ketamine and xylazine (9, 10), a mixture of ketamine, xylazine and acepromazine (11), sodium pentobarbital (12), chloral hydrate 10% (13, 14) and inhalational anesthesia as isoflurane (induction: 5%, maintenance: 2.5%) with buprenorphine was subcutaneously administered for analgesia (15, 16).

For instance, Isoflurane has the advantages of rapid induction of anesthesia, rapid recovery, and minimal influence on hepatic metabolism; however, isoflurane may produce some unfavorable respiratory depression (7), and is not sufficient to provide adequate analgesic effect when highly invasive surgical procedures are needed (17, 18). Although ketamine is widely used in MI model induction (19), ketamine is currently classified as a narcotic drug and many countries have strengthened restrictions on its purchase, storage, and associated record-keeping procedures (20). Moreover, pentobarbital sodium is inappropriate as a general anesthetic due to its minimal analgesic effect and narrow safety margin with the undesirable cardiodepressive effects of reducing heart rate, stroke index, and cardiac index in rodents (19, 20). Consequently, the ethical restrictions and limitations of some medicines which are crucial in MI model induction increase the challenges for successful MI model establishment.

The combination between medetomidine, midazolam, and butorphanol (MMB) anesthetic is recently used in experimental animal studies as a substitute for ketamine or pentobarbital sodium (21). The anesthetic duration of MMB is longer than those of ketamine or pentobarbital sodium and is often

associated with depression of respiration and circulation, and reduction of general motor activity and neuronal activity (21). These side effects may limit the usability of MMB in MI model induction. More specifically, medetomidine causes significant cardio-respiratory depression (22). Atipamezole, a synthetic α2-adrenergic antagonist, can antagonize medetomidine-induced respiratory depression and results in rapid recovery from MMB anesthesia (21). Atipamezole is also effective for reducing the maintenance concentration of isoflurane which leads to the amelioration of cardio-respiratory depression induced by isoflurane (17).

To our knowledge combination between MMB and atipamezole has never been studied in MI models. The objective of the study is to provide an easy and successful protocol to induce the MI model using MMB, and atipamezole. Our result will be helpful for an easily induced model using ethically approved medications with a higher success rate for research purposes.

# Materials and methods

## Animals and ethical approval

The study was conducted on 25 male Sprague Dawley (SD) rats, 12 to 15 weeks of age, and weighing between 350 and 400 gm. All procedures followed the Guide for the Care and Use of Laboratory Animals and were approved by the Institutional Animal Care and Use Committee of the Tokyo University of Agriculture and Technology (Approval No R04-185). The rats had free access to food and water and were housed at 25°C with a 12 h light/dark cycle.

## Anesthetic agents

The following anesthetics were used: Medetomidine hydrochloride (Domitor®, Orion Pharma Animal Health, Helsinki, Finland), Midazolam (Dormicum®, Astellas Pharma Inc., Tokyo, Japan), Butorphanol (Vetorphale, Meiji Seika Pharma Co., Ltd.), Isoflurane Inhalation Solution (Isoflurane, Pfizer Inc., New York, USA) and Atipamezole (ATI) (Antisedan, Orion Pharma Animal Health).

## Anesthesia protocol

Firstly, a mixture was prepared by mixing medetomidine hydrochloride, midazolam, and butorphanol (MMB) at a dose rate of 0.3, 5.0, and 5.0 mg/kg BW (23, 24). The anesthetic mixture was freshly prepared and diluted with sterile saline as stock solution as described in Table 1. Rats were subcutaneously injected at a dose rate of 0.5 ml of mixture/100 gm BW. Following the loss of front paw reflex, hind paw reflex, tail reflex, corneal reflex, and body righting reflex, rats were rapidly transferred to endotracheal intubation and maintained with isoflurane 1.0 % using a rodent inhalant anesthesia apparatus.

## Induction of MI model

Following the above-mentioned anesthetic protocol, the animals were intratracheally intubated using a 16-gauge intravenous catheter before being placed in a supine position on a temperature-controlled pad at a core temperature of 35.5°C. A small incision between the third and fourth intercostal spaces was made to perform a left-sided thoracotomy. A blunt-ended retractor was used to expand the incision away from the lung to avoid its collapse. To access the heart, the pericardial sac was cut open and the site of coronary artery ligation was determined. The site of ligation of the left anterior descending (LAD) coronary artery was determined 8 mm away from the origin, then a 6-0 prolene ligature was passed underneath the LAD and secured with three knots using a tapered atraumatic needle (9). Successful ligation was confirmed by visible blanching and cyanosis of the anterior wall of the left ventricle, as well as swelling of the left atrium (25). Ribs and muscles were closed using 3-0 vicryl absorbable sutures leaving a small gap to aspirate air left in the thoracic cavity. The air was aspirated through a tube (2 mm in diameter) without touching the lungs. Nonabsorbable suture materials, such as silk 3-0, were used to suture the skin. The surgical site was dressed daily to prevent infection and to monitor for suture site dehiscence.

## Administration of atipamezole

After LAD ligation and closing of the chest, the maintenance with isoflurane was reduced to 0.5% till suturing the skin and finishing the surgical procedures. At this point, atipamezole was injected subcutaneously at a dose rate of 1.0 mg/kg (Table 1). Then, isoflurane was stopped, and rats were maintained with oxygen insufflation (2 l of oxygen per minute). After observing the initial movement of rats, the endotracheal tube was removed slowly, and rats were changed to a nose cone mask (additional oxygen insufflation) till complete recovery (Figure 1).

## Post-operative care

Standard postoperative procedures were followed to control pain and infection. After recovery, all animals were treated with gentamicin (Nacalai Tesque Co., Ltd., Tokyo, Japan) which was injected intraperitoneally ($2.4 \times 10^4$/kg/day) for 3 days (14) while carprofen (Rimadyl®, Zoetis Japan K.K., Tokyo, Japan)

TABLE 1 Concentrations and doses of the used anesthetic agents.

| Agent | Concentration (mg/ml) | Dose (mg/kg) | Volume in saline (10 ml) | Administered volume (ml/kg) |
|---|---|---|---|---|
| Medetomidine | 1.0 | 0.3 | 0.3 | 0.3 |
| Midazolam | 5.0 | 5.0 | 1.0 | 1.0 |
| Butorphanol | 5.0 | 5.0 | 1.0 | 1.0 |
| Atipamezole | 5.0 | 1.0 | 2.0 | 1.0 |

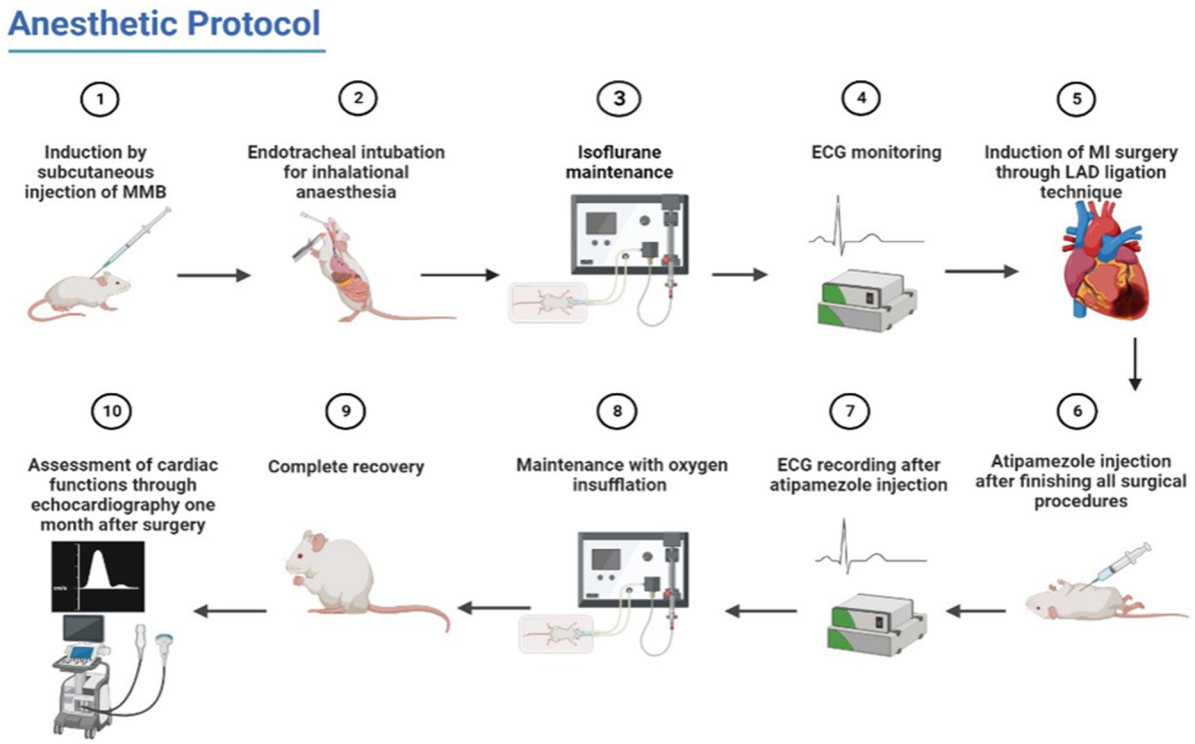


FIGURE 1
Schematic illustration of the used procedures of anesthetic protocol from induction to recovery and post-MI confirmation.

was used with a pre-surgical dose of 5.0 mg/kg/SC, followed by two post-surgery injections (26).

## Measurement of time intervals during operation

Induction time was defined as the duration from injection of anesthetic mixture to the start of the loss of a body-righting reflex. Operation time was defined as the duration from the start of MI surgery till the end of all surgical procedures. Partial recovery time was defined as the duration from the end of the operation period (atipamezole injection) till trials of animals to remove the endotracheal tube (initial movement). Meanwhile, complete recovery time was defined as the duration from the removal of the endotracheal tube and the change to a nose cone mask to restore all vital reflexes. All these durations were recorded and expressed as mean ± SD.

## ECG monitoring

The ECG signals were recorded with needle electrodes connected with PowerLab hardware (ML880 PowerLab 16/30, AD Instruments) and LabChart Pro software (LabChart v8, AD Instruments) using a previously published protocol (27). The setting of PowerLab for ECG measurements followed the instructions provided by the producer. The ECG recording started 10 min after the animal was anesthetized with (MMB; i.e., before atipamezole injection) and then was conducted

for 10 min and repeated after atipamezole administration for another 10 min. For each record, the most stable continuous segment was chosen for ECG analysis.

The ECG was recorded in an anesthetized state before and after atipamezole administration ECG parameters included RR Interval (s), heart rate (HR), atrial complex (PR interval, P wave duration, and P wave amplitude), ventricular complexes (QRS complex, QT and QTc interval duration) were recorded and analyzed.

## Confirmation of MI model

Cardiac functions were evaluated directly before and 1 month after MI. The echocardiographic machine (Hitachi-Aloka Medical Ltd., Tokyo, Japan, ProSound F75 ultrasonographic system) with a 12-MHz transducer and simultaneous ECG was used. The echocardiography was performed in accordance with the guidelines of the American Society of Echocardiography (ASE) (28, 29). All animals were anesthetized with MMB subcutaneously administered for easy and feasible examination and at the level of the papillary muscles, a two-dimensional right parasternal short-axis view of the LV was achieved using M-mode. LV was measured manually by the same observer using the ASE's leading-edge method (30), which has been validated for the rat MI model (31).

The LV internal diameter during diastole (LVIDd), LV internal diameter during systole (LVIDs), LV posterior wall diameter during diastole (LVPWd) systole (LVPWs) and (IVSd) and (IVSs) interventricular septal thickness in end-diastole and systole, respectively. Ejection fraction (EF%), and fractional shortening (FS%) were obtained from that view. From each rat, each echocardiographic parameter was measured five times and the data were averaged (32).

## Statistical analysis

Data analysis was performed using GraphPad Prism8 version 7.01 (GraphPad Software, Inc, San Diego, California). The normality of the data was tested by the Shapiro–Wilk test. To compare the cardiac function parameters before and after MI model induction, the student $T$-test was used and a $P < 0.05$ was considered statistically significant.

# Results

## Operation intervals and success of the MI model

Initially, rats were subcutaneously administered MMB at a dose rate of 0.5 ml/100 gm BW. Anesthetic induction was generally quick and easy, and most rats were orotracheally intubated in the range of 2–5 min as Mean ± SD (3.440 ± 1.044) after MMB administration. Muscle relaxation and analgesia were sufficient to begin thoracotomy immediately after anesthetic administration and the recovery time was divided into two stages: partial as Mean ± SD (10.84 ± 3.313 min) and complete as Mean ± SD (12.36 ± 4.847 min). The total operation time was 29.40 ± 3.663 min as Mean ± SD (Table 2). The success rate of the anesthetic protocol was 100%. In addition, all animals used in the current study were maintained for 1 month after surgery with a survival rate of 88% (22/25), and three rats died within 24 h after MI induction.

TABLE 2 Measurements of the anesthetic protocol durations.

| Measurement | Mean ± SD |
|---|---|
| Induction time | 3.440 ± 1.044 |
| Operation time | 29.40 ± 3.663 |
| Partial recovery time | 10.84 ± 3.313 |
| Complete recovery time | 12.36 ± 4.847 |

## Assessment of ECG

The ECG analysis before and after atipamezole injection in the operated rats is illustrated in Figures 2, 3. There were no significant differences in P duration, P amplitude, and QT interval. However, the RR interval was significantly decreased after atipamezole administration ($P = 0.0001$). In contrast, other ECG parameters such as HR, PR Interval, QRS Interval, and QTc were significantly increased ($P = 0.0001$, 0.002, 0.043, and 0.018, respectively) when compared with their values before atipamezole injection.

## Confirmation of MI model

The myocardial infarction model was successfully created with the aforementioned anesthetic protocol *via* LAD ligation approach, as evidenced by apparent blanching and cyanosis of the anterior wall of the left ventricle and swelling of the left atrium immediately following artery ligation. No clinical abnormalities were observed during the observation period. Three rats died within 24 h post-MI induction and showed rapid respiration and off food (Figure 4).

The echocardiographic parameters measured before and 1 month after MI induction are summarized in Figure 5. Changes in echocardiographic parameters can be seen after MI, as a significant decrease was observed in IVSd, IVSs, LVPWs, EF% and FS% ($P = 0.047$, 0.007, 0.007, 0.007, and 0.007, respectively). In addition, a significant increase was recorded in LVIDd

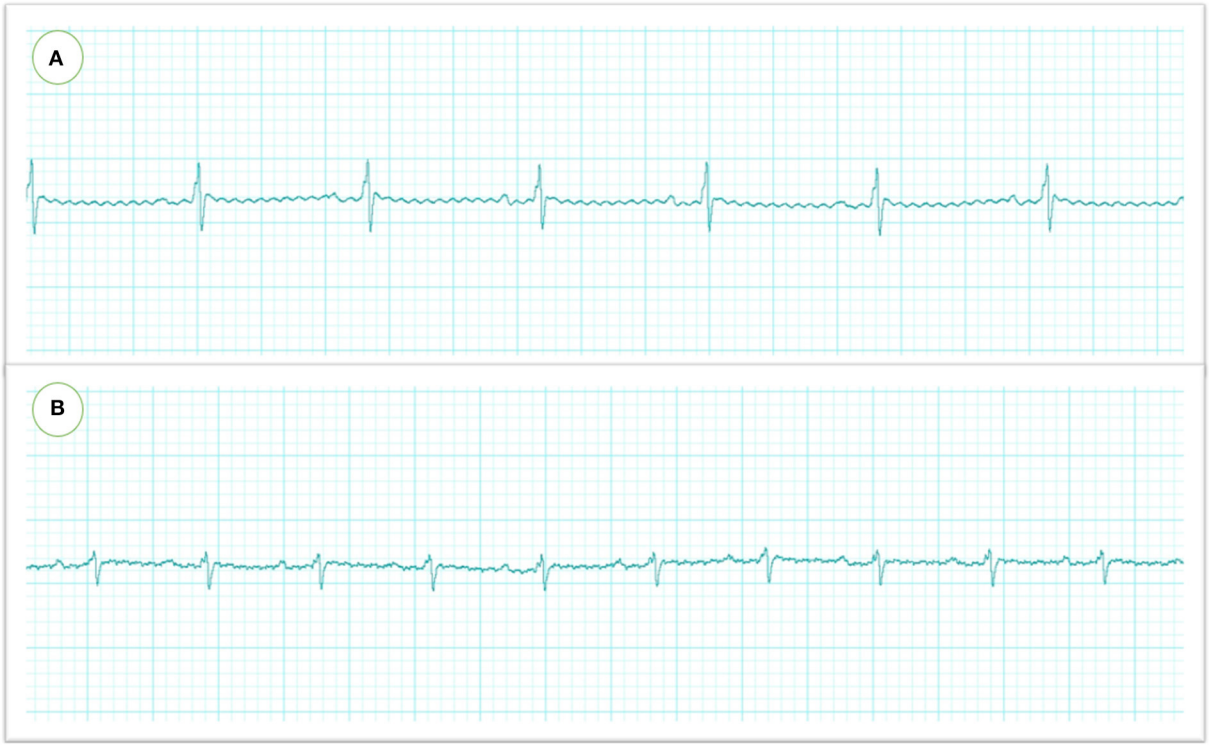


FIGURE 2
Electrocardiographic recordings in rats were measured by needle electrodes with Lab chart. The heart rate and RR intervals were significantly reduced after MMB injection (before atipamezole administration) **(A)** which were restored to the normal level after atipamezole administration **(B)**.

and LVIDs after LAD ligation ($P = 0.039$; 0.007, respectively) (Figure 6).

## Discussion

The rat model is the most commonly used to study the pathophysiology of cardiovascular diseases including ischemic heart diseases as well as other models (33, 34). Limitations regarding the anesthetic protocols because of animal welfare, ethical concerns, and public health circumstances limit the usability of well-known medications in MI models, making the establishment of MI models more difficult. In addition, scientific publications still cannot be relied upon to present a detailed description of analgesia and anesthesia protocols. Most recently, an assessment of anesthetic and analgesic regimens in publications involving non-human primates revealed the absence of critical details reporting (35). In the present study, we have developed a successful MI induction in all rats with a survival rate of 88% using the novel protocol of anesthesia (combination of MMB + Isoflurane and countered with atipamezole). The success rate of the anesthetic protocol was 100% which provides quick and easy induction of general anesthesia with facilitating orotracheally intubated, muscle relaxation and analgesia were sufficient to perform the surgery recording a very short recovery time with minimal side effects in comparison to other previous studies. Our protocol may be introduced as an alternative to ketamine, xylazine, and pentobarbital with sufficient anesthetic and time-saving effects in rats.

Regarding the anesthetic combination, the used MMB mixture has been created based on previous reports in rats and mice (23, 24, 36–39).

Midazolam is a benzodiazepine that is water soluble. In rodents, pigs, and primates, benzodiazepines can cause significant sedation; however, they are not analgesic and do not create a true general anesthetic state (40). Midazolam is used in conjunction with other drugs to induce anesthesia (41). Medetomidine is a more potent imidazole derivative than xylazine, with higher alpha2-adrenoceptor selectivity (41). Butorphanol, a synthetic opioid agonist-antagonist, is used in veterinary medicine as an analgesic agent (42). The combination of medetomidine, midazolam, and butorphanol has been reported as a reliable and safe anesthetic agent in the dog (43), sea lions (44), and red fox (45). In our study, we administered MMB in rats by subcutaneous injection as it is considered a more effective, and induced rapid,

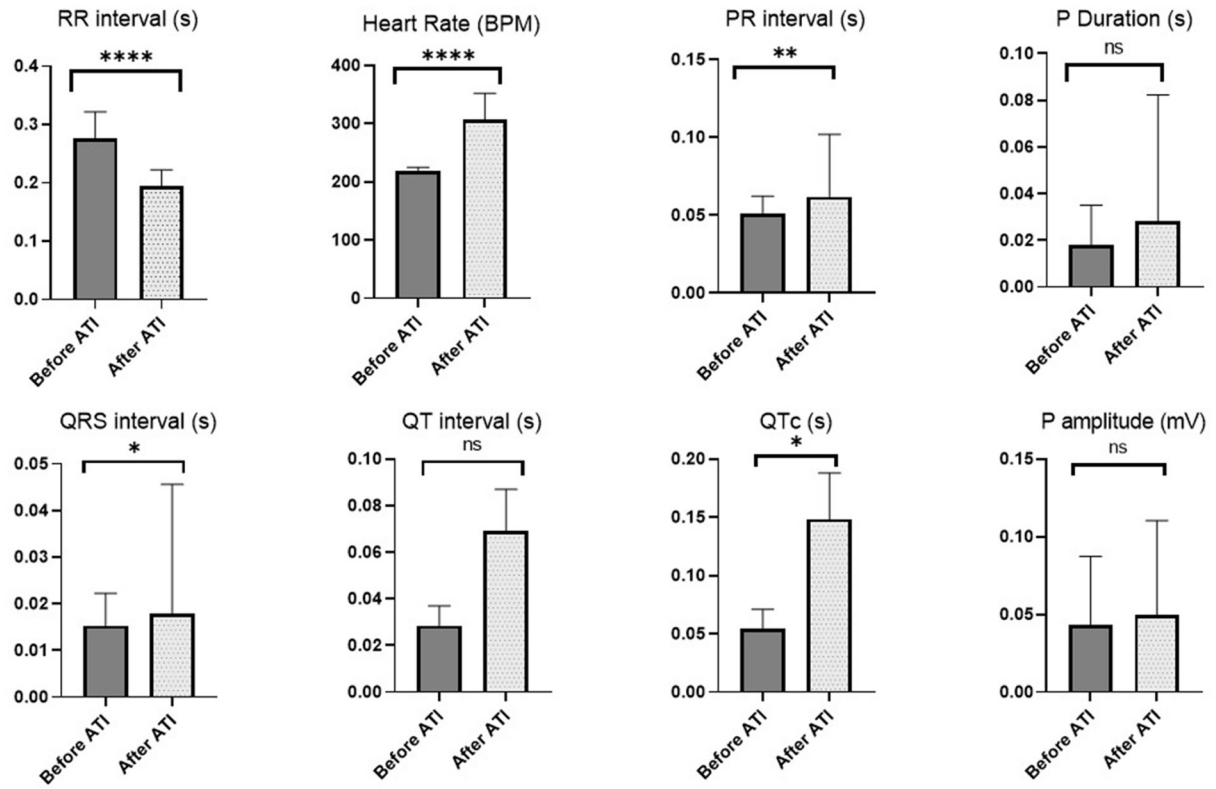


FIGURE 3
Changes in ECG parameters before atipamezole (i.e., directly after MMB) and after atipamezole administration. Asterisk used to indicate the significance, Ns $P > 0.05$ , *$P \leq 0.05$, **$P \leq 0.01$, ****$P \leq 0.0001$.


FIGURE 4
**(A)** During operation, myocardial infarction was confirmed in rats directly after LAD ligation through apparent blanching and cyanosis of the anterior wall of the left ventricle and swelling of the left atrium. **(B)** Color change of the left ventricular wall in survived rats which were maintained for 1 month with a small infarction size. **(C)** Large infarction size was observed in rats within 24 h following MI induction. red arrow; the site of infarction.

complete, and stable anesthetic effect than intraperitoneal injection (23). The intraperitoneal delivery route is the most commonly used for MMB administration in rats (37), but according to Sorrenti et al. (39), the induction time for a single dose of MMB combination administered subcutaneously in Sprague-Dawley rats was approximately

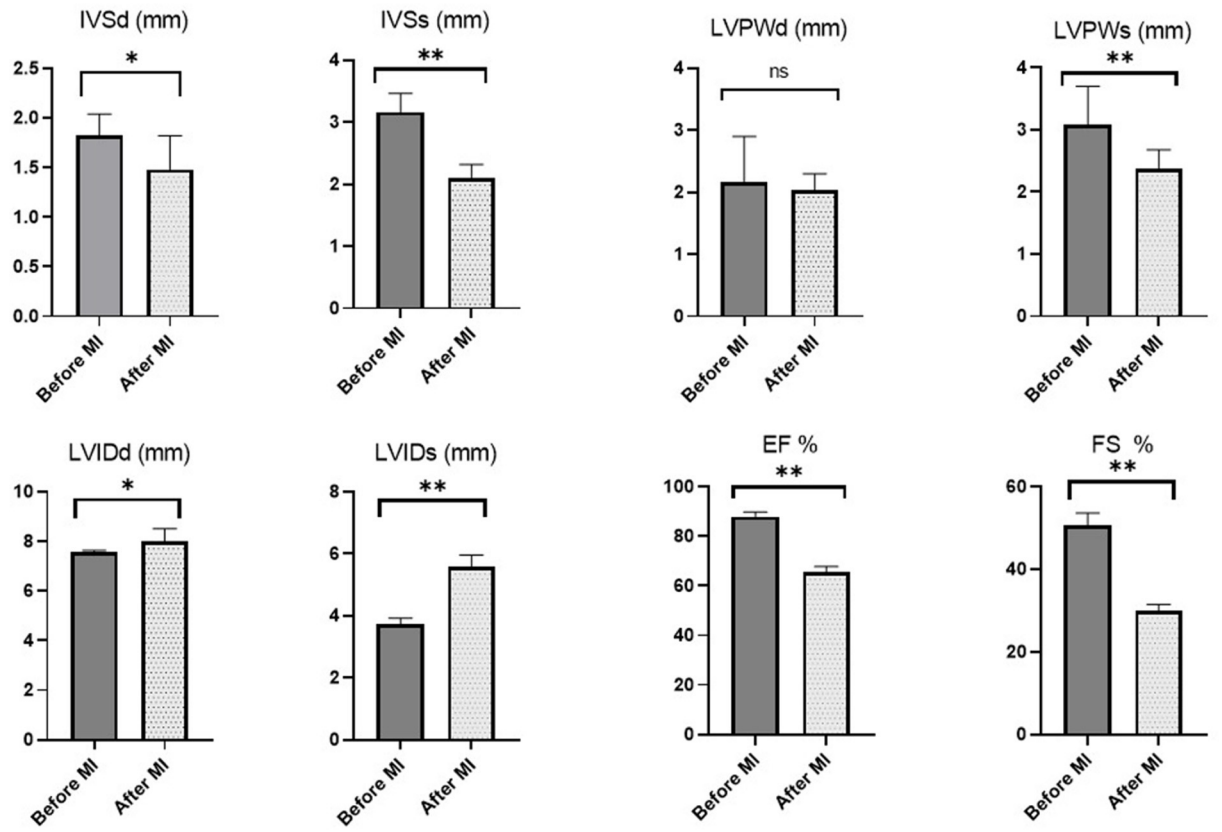


FIGURE 5
Echocardiographic measurements in rats before MI induction and 1 month later. Asterisk used to indicate the significance, Ns $P > 0.05$ , $*p < 0.05$, $**p < 0.01$.

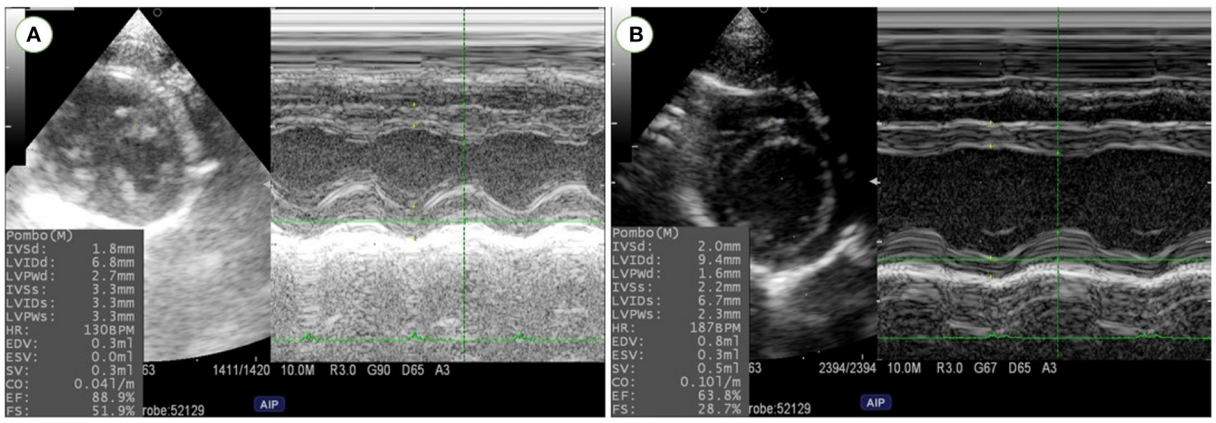


FIGURE 6
Left ventricular dimensions and function were evaluated using M-Mode echocardiography at right parasternal short axis in rats before MI induction **(A)** and one-month post-MI **(B)**. Reduction in left ventricular wall thickness and cardiac function and increase in left ventricular diameters were confirmed in MI model rats.

10 min; however, with intraperitoneal injection, this duration increased to 25 min and required one or two additional doses (39).

Isoflurane is known to have a relatively strong respiratory depression in various species (17, 46). Therefore, the main purpose of the current novel anesthetic protocol was to

attenuate cardio-respiratory depression by reduction of isoflurane concentration and minimizing MMB side effects, producing more safe and time-saving protocol for induction of MI in rats.

Atipamezole is a highly selective 2-adrenergic antagonist that is known to counteract the anesthetic effect of MMB. We administrated atipamezole with the prescribed dosage as the recovery from the anesthetic effect and hypothermia was dosage-dependent, and even after a low dose of atipamezole, the same as medetomidine, the sedation continued, even after all reflexes had been restored. As a result, giving atipamezole at the same dose as medetomidine is insufficient to promote recovery from MMB anesthesia. In addition, atipamezole's ability to counteract MMB-induced anesthesia is partially attributable to the fact that MMB primarily exerts its anesthetic effect *via* the 2-adrenoceptor (47). Furthermore, it has been reported that atipamezole can also counteract the anesthetic effect of the combination of medetomidine, butorphanol, alfaxalone, and neurosteroid anesthetic, as well as can counter the anesthetic effect of MMB (48).

Generally, medetomidine is helpful in central analgesia while butorphanol is necessary for visceral analgesia (49, 50). Administration of atipamezole during early surgical procedures will abolish the analgesic effect of medetomidine and exposes the rat to pain. To avoid such situation in the current study, atipamezole was administrated after finishing all surgical procedures. In other words, during the operation, anesthesia was achieved through the effect of the used combination with isoflurane, and postoperative analgesia was achieved successfully through pain killer.

Rats were kept under oxygen insufflation (2 l of oxygen per minute) when isoflurane maintenance was stopped to prevent problems like hypoxia. This is in agreement with Mechelinck et al., who claimed that rats under ketamine-xylazine anesthesia are susceptible to hypoxia. This could result in an increase in delayed mortality from hypoxia-related lung failure. So they recommend using additional oxygen insufflation with the prescribed dose (51). Moreover, Ballard and Spadafora (52) stated that respiratory depression caused by ketamine-xylazine narcosis seems to be the key factor in lung damage. In principle, rats' lungs can be damaged by hypoxemia. This damage begins 8 h after the hypoxic incident with pulmonary edema, most likely due to sympathetic activation, increased vascular permeability, and hypoxic pulmonary vasoconstriction, and is followed by inflammation, pulmonary fibrosis, and vascular hypertrophy (52).

In our study, we reported that the induction time of our anesthetic protocol was <5 min, these results were resemble that recorded with the ketamine/xylazine protocol (20), but with a short recovery time in total when compared to other protocols including ketamine/xylazine (20), MMB alone (23) and Pentobarbital (35). In other studies, The mean recovery time without atipamezole injection was 44.5 min and 50.0 min in males and females respectively (53).

All the operated rats in the present study were maintained for 1 month with a survival rate of 88%, and three rats died within 24 h post-surgery due to surgical errors, Lindsey et al. (54) stated that perioperative death within 24 h post-MI is usually due to surgical errors (or very large infarct sizes), and in the permanent occlusion MI model in mice, postoperative death may be due to rupture, acute heart failure, or arrhythmias (54).

The normal heart rate of rats has been reported 330–480 beats per minute (55). Kirihara et al. (56) stated that MMB had decreased heart rate and blood oxygen saturation in rats (56). The recorded heart rate in our study was in the range of 187 to 226 beats per minute, confirming the bradycardia expected with the use of an α2-agonist (57). After the administration of atipamezole, heart rate began to increase within 2 min and was fully restored after 4 min to reach 270–352 beats per minute. According to ECG data from our study, the main advantage of administering atipamezole is that it allows rats to recover voluntary respiratory movement, wakefulness, movement, and posture within a relatively short time after injection, this allows for faster extubating of operated rats, minimizing the post-anesthesia recovery period and, as a result, lowering the risk of side effects and residual effects of the anesthetics (58).

In operated rats, we found typical ischemic changes on transthoracic echocardiography, particularly significant increase in left ventricular diameters and a significant decrease in wall dimensions, EF%, and FS% following post-infarction LV remodeling in adult rats. Our findings are comparable to those of earlier studies on rats indicating a successful procedure (59, 60). Changes in cardiac function parameters with no clinical symptoms in the remaining rats suggest subclinical heart failure.

At 1-month post-infarction, morphological alterations such as an increase in LVESD and LVEDD, as well as functional changes such as a decrease in FS and EF, were clearly identified. Our data are similar to those of other reports (61–64). LAD-ligation significantly reduced regional contractility not just in the anterior, anteroseptal, and septal segments. Even adjacent regions like the lateral and posterior segments were affected. This can be explained by the distinctions between the geometries of the coronary arteries in rats and humans as there is no true circumflex artery and the LAD predominates in rats (65). As a result, the posterior and lateral regions of the left ventricle have a significant perfusion deficiency as a consequence of LAD ligation (64, 66). Differences in age, weight and echocardiographic transducers or procedures appear to provide slightly variable results in different laboratories. Based on our findings, we may conclude that we were successful in creating a novel anesthetic protocol for producing a MI model in adult rats and confirmed the efficacy of LAD ligation surgery under the used protocol.

Various animal models such as rats, rabbits, pigs and non-human primates, where sparse collateral coronary circulation

is excisting, have been introduced to study MI; however, considerable mortalities due to delayed recovery is still controversial (67–69). Until now, our protocol did not utilized in any animal model. Therefore, the current protocol worth studying in other MI or ischemic dysfunction models.

### Limitations

In our study, we did not compare our protocol to others such as ketamine and pentobarbital sodium. These drugs are no longer available in Japan and their import or use is not ethical due to being classified as narcotic drugs (20). In the current study, the effect of the used protocol on pulmonary function and blood pressure was not investigated. However, other studies have examined the detailed hemodynamic and respiratory impact of MMB alone or after antaonizing with atipamezole in rats and rabitts (23, 70) with no surgical approaches.

## Conclusion

To our knowledge, this is the first study to use anesthetic combination of MMB and a light concentration of isoflurane with atipamezole in MI rats. Subcutaneous injection of atipamezole efficiently counters the cardiopulmonary side effect of MMB which is necessary for rapid recovery and subsequently enhancing the survival rate during the establishment of the MI model. Our approach produced a more easily anesthetic effect and time-saving procedures with a highly successful rate in MI rats which may be effective in the research field of cardiothoracic disorders using rat models. Our protocol worth studying in other animal models as well.

## Data availability statement

The raw data supporting the conclusions of this article will be made available by the authors, without undue reservation.

## Ethics statement

The animal study was reviewed and approved by the experimental procedures were approved by the local Ethical Committee of the Tokyo University of Agriculture and Technology, Japan (Approval No R04-185).

## Author contributions

Experiment design: AF, AM, and RT. Induction of model: AF. Echocardiography and electrocardiography, data collection, and statistical analysis: AF and AM. Investigation: AF, AM, and KS. Writing and drafting: AF, TY, LH, and AM. Critical editing: AM. Supervision: RT. All authors reviewed and edited the final version.

## Acknowledgments

The research was supported by a full scholarship provided by the Egypt-Japan Education Partnership (EJEP) from the Ministry of Higher Education, Egypt.

## Conflict of interest

The authors declare that the research was conducted in the absence of any commercial or financial relationships that could be construed as a potential conflict of interest.

## Publisher's note

All claims expressed in this article are solely those of the authors and do not necessarily represent those of their affiliated organizations, or those of the publisher, the editors and the reviewers. Any product that may be evaluated in this article, or claim that may be made by its manufacturer, is not guaranteed or endorsed by the publisher.

## References

1. Eltzschig HK, Eckle T. Ischemia and reperfusion—from mechanism to translation. *Nat Med.* (2011) 17:1391–401. doi: 10.1038/nm.2507

2. Nichols M, Townsend N, Scarborough P, Rayner M. Cardiovascular disease in Europe 2014: epidemiological update. *Eur Heart J.* (2014) 35:2950–9. doi: 10.1093/eurheartj/ehu299

3. Katsanos K, Mitsos S, Koletsis E, Bravou V, Karnabatidis D, Kolonitsiou F, et al. Transauricular embolization of the rabbit coronary artery for experimental myocardial infarction: comparison of a minimally invasive closed-chest model with open-chest surgery. *J Cardiothorac Surg.* (2012) 7:1–9. doi: 10.1186/1749-8090-7-16

4. Zhang J, Knapton A, Lipshultz SE, Weaver JL, Herman EH. Isoproterenol-induced cardiotoxicity in sprague-dawley rats: correlation of reversible and irreversible myocardial injury with release of cardiac troponin T and roles of iNOS in myocardial injury. *Toxicol Pathol.* (2008) 36:277–8. doi: 10.1177/0192623307313010

5. Xu Z, Alloush J, Beck E, Weisleder N. A murine model of myocardial ischemia-reperfusion injury through ligation of the left anterior descending artery. *JoVE.* (2014) 3:e51329. doi: 10.3791/51329

6. Isorni M-A, Casanova A, Piquet J, Bellamy V, Pignon C, Puymirat E, Menasche P. Comparative analysis of methods to induce myocardial infarction in a closed-chest rabbit model. *Biomed Res Int.* (2015) 2015:3051. doi: 10.1155/2015/893051

7. Tsukamoto A, Uchida K, Maesato S, Sato R, Kanai E, Inomata T. Combining isoflurane anesthesia with midazolam and butorphanol in rats. *Exp Anim.* (2016) 65:223–30. doi: 10.1538/expanim.15-0113

8. Gargiulo S, Greco A, Gramanzini M, Esposito S, Affuso A, Brunetti A, et al. Mice anesthesia, analgesia, and care, Part I: anesthetic considerations in preclinical research. *ILAR J.* (2012) 53:E55–69. doi: 10.1093/ilar.53.1.55

9. Srikanth G, Prakash P, Tripathy N, Dikshit M, Nityanand S. Establishment of a rat model of myocardial infarction with a high survival rate: a suitable model for evaluation of efficacy of stem cell therapy. *J Stem Cells Regen Med.* (2009) 5:30. doi: 10.46582/jsrm.0501006

10. Azar AD, Tavakoli F, Moladoust H, Zare A, Sadeghpour A. Echocardiographic evaluation of cardiac function in ischemic rats: value of m-mode echocardiography. *Res Cardiovasc Med.* (2014) 3:22941. doi: 10.5812/cardiovascmed.22941

11. Samsamshariat SA, Samsamshariat ZA, Movahed MR. A novel method for safe and accurate left anterior descending coronary artery ligation for research in rats. *Cardiovasc Revascul Med.* (2005) 6:121–3. doi: 10.1016/j.carrev.2005.07.001

12. Dai Y, Chen Y, Wei G, Zha L, Li X. Ivabradine protects rats against myocardial infarction through reinforcing autophagy via inhibiting PI3K/AKT/mTOR/p70S6K pathway. *Bioengineered.* (2021) 12:1826–37. doi: 10.1080/21655979.2021.1925008

13. Jiang J, Gu X, Wang H, Ding S. Resveratrol improves cardiac function and left ventricular fibrosis after myocardial infarction in rats by inhibiting NLRP3 inflammasome activity and the TGF-β1/SMAD2 signaling pathway. *PeerJ.* (2021) 9:e11501. doi: 10.7717/peerj.11501

14. Fu Y, Wang S, Cui Q. Mechanism of Atorvastatin in Improving Cardiac Function in a Rat Model of Myocardial Infarction. *Indian J Pharm Sci.* (2020) 42:38–44. doi: 10.36468/pharmaceutical-sciences.spl.121

15. Sugiyama A, Ito R, Okada M, Yamawaki H. Long-term administration of recombinant canstatin prevents adverse cardiac remodeling after myocardial infarction. *Sci Rep.* (2020) 10:1–11. doi: 10.1038/s41598-020-69736-y

16. Gao G, Chen W, Yan M, Liu J, Luo H, Wang C, et al. Rapamycin regulates the balance between cardiomyocyte apoptosis and autophagy in chronic heart failure by inhibiting mTOR signaling. *Int J Mol Med.* (2020) 45:195–209. doi: 10.3892/ijmm.2019.4407

17. Tsukamoto A, Serizawa K, Sato R, Yamazaki J, Inomata T. Vital signs monitoring during injectable and inhalant anesthesia in mice. *Exp Anim.* (2015) 64:57–64. doi: 10.1538/expanim.14-0050

18. Eilers H. Anesthetic activation of nociceptors: adding insult to injury? *Mol Interv.* (2008) 8:226. doi: 10.1124/mi.8.5.6

19. Shekarforoush S, Fatahi Z, Safari F. The effects of pentobarbital, ketamine–pentobarbital and ketamine–xylazine anesthesia in a rat myocardial ischemic reperfusion injury model. *Lab Anim.* (2016) 50:179–84. doi: 10.1177/0023677215597136

20. Kawai S, Takagi Y, Kaneko S, Kurosawa T. Effect of three types of mixed anesthetic agents alternate to ketamine in mice. *Exp Anim.* (2011) 60:481–7. doi: 10.1538/expanim.60.481

21. Kamio K, Morita J, Nakanishi Y, Sasaki M, Wakamatsu M. Corneal lesions related to an anesthetic mixture of medetomidine, midazolam, and butorphanol treatment in rats. *J Toxicol Sci.* (2021) 46:561–8. doi: 10.2131/jts.46.561

22. Hedenqvist P, Roughan JV, Flecknell PA. Sufentanil and medetomidine anaesthesia in the rat and its reversal with atipamezole and butorphanol. *Lab Anim.* (2000) 34:244–51. doi: 10.1258/002367700780384762

23. Shibuta H, Yamana R, Kashimoto J, Kamio K, Suda A. Comparison of the anesthetic effect by the injection route of mixed anesthesia (medetomidine, midazolam and butorphanol) and the effect of this anesthetic agent on the respiratory function. *J Vet Med Sci.* (2020) 82:35–42. doi: 10.1292/jvms.19-0438

24. Fujiki M, Kuga K, Ozaki H, Kawasaki Y, Fudaba H. Blockade of motor cortical long-term potentiation induction by glutamatergic dysfunction causes abnormal neurobehavior in an experimental subarachnoid hemorrhage model. *Front Neural Circuits.* (2021) 15:670189. doi: 10.3389/fncir.2021.670189

25. Iborra-Egea O, Santiago-Vacas E, Yurista SR, Lupón J, Packer M, Heymans S, et al. Unraveling the molecular mechanism of action of empagliflozin in heart failure with reduced ejection fraction with or without diabetes. *JACC Basic Transl Sci.* (2019) 4:831–40. doi: 10.1016/j.jacbts.2019.07.010

26. Onohara D, Corporan DM, Kono T, Kumar S, Guyton RA, Padala M. Ventricular reshaping with a beating heart implant improves pump function in experimental heart failure. *J Thorac Cardiovasc Surg.* (2020) 163:e343–5. doi: 10.1016/j.jtcvs.2020.08.097

27. Doggett TM, Tur JJ, Alves NG, Yuan SY, Tipparaju SM, Breslin JW. Assessment of cardiovascular function and microvascular permeability in a conscious rat model of alcohol intoxication combined with hemorrhagic shock and resuscitation. *Traum Isch Injury.* (2018) 54:61–81. doi: 10.1007/978-1-4939-7526-6_6

28. Rychik J, Ayres N, Cuneo B, Gotteiner N, Hornberger L, Spevak PJ, et al. American Society of Echocardiography guidelines and standards for performance of the fetal echocardiogram. *J Am Soc Echocardiography.* (2004) 17:803–10. doi: 10.1016/j.echo.2004.04.011

29. Zacchigna S, Paldino A, Falcão-Pires I, Daskalopoulos EP, Dal Ferro M, Vodret S, et al. Towards standardization of echocardiography for the evaluation of left ventricular function in adult rodents: a position paper of the ESC working group on myocardial function. *Cardiovasc Res.* (2021) 117:43–59. doi: 10.1093/cvr/cvaa110

30. Lang RM, Bierig M, Devereux RB, Flachskampf FA, Foster E, Pellikka PA, et al. Recommendations for chamber quantification: a report from the American Society of echocardiography's guidelines and standards committee and the chamber quantification writing group, developed in conjunction with the European association of echocardiography, a branch of the European society of cardiology. *J Am Soc Echocardiography.* (2005) 18:1440–63. doi: 10.1016/j.echo.2005.10.005

31. Solomon SD, Greaves SC, Rayan M, Finn P, Pfeffer MA, Pfeffer JM. Temporal dissociation of left ventricular function and remodeling following experimental myocardial infarction in rats. *J Card Fail.* (1999) 5:213–23. doi: 10.1016/S1071-9164(99)90006-4

32. Yairo A, Mandour AS, Matsuura K, Yoshida T, Ma D, Kitpipatkun P, et al. Effect of loading changes on the intraventricular pressure measured by color M-mode echocardiography in rats. *Diagnostics.* (2021) 11:1403. doi: 10.3390/diagnostics11081403

33. Liu Chung Ming C, Sesperez K, Ben-Sefer E, Arpon D, McGrath K, McClements L, et al. Considerations to model heart disease in women with preeclampsia and cardiovascular disease. *Cells.* (2021) 10:899. doi: 10.3390/cells10040899

34. Ma D, Mandour AS, Elfadadny A, Hendawy H, Yoshida T, El-Husseiny HM, Nishifuji K, Takahashi K, Zhou Z, Zhao Y. Changes in cardiac function during the development of uremic cardiomyopathy and the effect of salvianolic acid B administration in a rat model. *Front Vet Sci.* (2022) 9:5759. doi: 10.3389/fvets.2022.905759

35. Herrmann K, Flecknell P. Retrospective review of anesthetic and analgesic regimens used in animal research proposals. *ALTEX.* (2019) 36:65–80. doi: 10.14573/altex.1804011

36. Hasegawa T, Takagi R, Tanaka Y, Ohta T, Shinohara M, Kageyama Y, et al. Differences in the Effects of pentobarbital anesthetic and combination of medetomidine hydrochloride, midazolam, and butorphanol tartrate anesthetic on electroretinogram in spontaneously diabetic torii fatty rats. *Biomed Hub.* (2022) 7:106–14. doi: 10.1159/000526189

37. Ochiai Y, Baba A, Hiramatsu M, Toyota N, Watanabe T, Yamashita K, et al. Blood biochemistry and hematological changes in rats after administration of a mixture of three anesthetic agents. *J Vet Med Sci.* (2018) 80:387–94. doi: 10.1292/jvms.17-0497

38. Doi M, Oka Y, Taniguchi M, Sato M. Transient expansion of the expression region of Hsd11b1, encoding 11β-hydroxysteroid dehydrogenase type 1, in the developing mouse neocortex. *J Neurochem.* (2021) 159:778–88. doi: 10.1111/jnc.15505

39. Sorrenti V, Cecchetto C, Maschietto M, Fortinguerra S, Buriani A, Vassanelli S. Understanding the effects of anesthesia on cortical electrophysiological recordings: a scoping review. *Int J Mol Sci.* (2021) 22:1286. doi: 10.3390/ijms22031286

40. Wolfe JW, Ehrenfeld JM. "Pharmacology of Intravenous Anesthetic Agents.," *Anesthesia Student Survival Guide*. Springer (2022). p. 57–75 doi: 10.1007/978-3-030-98675-9_4

41. Meyer RE, Fish R. Pharmacology of injectable anesthetics, sedatives, and tranquilizers. (2008) doi: 10.1016/B978-012373898-1.50006-1

42. Heavner J, Cooper DM. Pharmacology of Analgesics, p 97–123. *Anesthesia and analgesia in laboratory animals*, 2nd ed. San Diego (CA): Academic Press[Google Scholar] (2008) doi: 10.1016/B978-012373898-1.50008-5

43. Itamoto K, Hikasa Y, Sakonjyu I, Itoh H, Kakuta T, Takase K. Anaesthetic and cardiopulmonary effects of balanced anaesthesia with medetomidine–midazolam and butorphanol in dogs. *J Vet Med Series A.* (2000) 47:411–20. doi: 10.1046/j.1439-0442.2000.00302.x

44. Spelman LH. Reversible anesthesia of captive California sea lions (Zalophus californianus) with medetomidine, midazolam, butorphanol, and isoflurane. *J Zoo Wildlife Med.* (2004) 35:65–9. doi: 10.1638/01-102

45. Bertelsen MF, Villadsen L, A. comparison of the efficacy and cardiorespiratory effects of four medetomidine-based anaesthetic protocols in the red fox (*Vulpes vulpes*). *Vet Anaesth Analg.* (2009) 36:328–33. doi: 10.1111/j.1467-2995.2009.00464.x

46. Mutoh T, Kojima K, Takao K, Nishimura R, Sasaki N. Comparison of Sevoflurane with Isoflurane for Rapid Mask Induction in Midazolam and Butorphanol-sedated Dogs. *J Vet Med Series A*. (2001) 48:223–30. doi: 10.1046/j.1439-0442.2001.00350.x

47. Salonen M, Reid K, Maze M. Synergistic interaction between alpha 2-adrenergic agonists and benzodiazepines in rats. *Anesthesiology*. (1992) 76:1004–11. doi: 10.1097/00000542-199206000-00022

48. Higuchi S, Yamada R, Hashimoto A, Miyoshi K, Yamashita K, Ohsugi T. Evaluation of a combination of alfaxalone with medetomidine and butorphanol for inducing surgical anesthesia in laboratory mice. *Japanese J Vet Res*. (2016) 64:131–9. doi: 10.14943/jjvr.64.2.131

49. Alves HC, Valentim AM, Olsson IAS, Antunes LM. Intraperitoneal anaesthesia with propofol, medetomidine, and fentanyl in mice. *Lab Anim*. (2009) 43:27–33. doi: 10.1258/la.2008.007036

50. Wenger S. Anesthesia and analgesia in rabbits and rodents. *J Exot Pet Med*. (2012) 21:7–16. doi: 10.1053/j.jepm.2011.11.010

51. Mechelinck M, Kupp C, Krüger JC, Habigt MA, Helmedag MJ, Tolba RH, et al. Oxygen inhalation improves postoperative survival in ketamine-xylazine anaesthetised rats: an observational study. *PLoS ONE*. (2019) 14:e0226430. doi: 10.1371/journal.pone.0226430

52. Ballard ST, Spadafora D. Fluid secretion by submucosal glands of the tracheobronchial airways. *Respir Physiol Neurobiol*. (2007) 159:271–7. doi: 10.1016/j.resp.2007.06.017

53. Nakamura T, Ichii O, Irie T, Hosotani M, Dantsuka A, Nakamura S, et al. Usefulness of an anesthetic mixture of medetomidine, midazolam, and butorphanol in cotton rats (*Sigmodon hispidus*). *Japanese J Vet Res*. (2016) 64:273–6. doi: 10.14943/jjvr.64.4.273

54. Lindsey ML, Bolli R, Canty Jr JM, Du X-J, Frangogiannis NG, Frantz S, et al. Guidelines for experimental models of myocardial ischemia and infarction. *Am J Physiol Heart Circ Physiol*. (2018) 314:H812–38. doi: 10.1152/ajpheart.00335.2017

55. Yardley CP, Hilton SM. The hypothalamic and brainstem areas from which the cardiovascular and behavioural components of the defence reaction are elicited in the rat. *J Auton Nerv Syst*. (1986) 15:227–44. doi: 10.1016/0165-1838(86)90066-4

56. Kirihara Y, Takechi M, Kurosaki K, Kobayashi Y, Saito Y, Takeuchi T. Effects of an anesthetic mixture of medetomidine, midazolam, and butorphanol in rats—strain difference and antagonism by atipamezole. *Exp Anim*. (2016) 65:27–36. doi: 10.1538/expanim.15-0036

57. Blaudszun G, Lysakowski C, Elia N, Tramer MR. Effect of perioperative systemic α2 agonists on postoperative morphine consumption and pain intensity: systematic review and meta-analysis of randomized controlled trials. *J Am Soc Anesthesiol*. (2012) 116:1312–22. doi: 10.1097/ALN.0b013e31825681cb

58. Barrasa JLM, Rodriguez NS, Rodríguez-Pérez JC, Hidalgo AC, Garcia AT, Camarillo JAI, et al. Electrocardiographic changes in rats undergoing thoracic surgery under combined parenteral anesthesia. *Lab Anim (NY)*. (2008) 37:469–74. doi: 10.1038/laban1008-469

59. Scheer P, Sverakova V, Doubek J, Janeckova K, Uhrikova I, Svoboda P. Basic values of M-mode echocardiographic parameters of the left ventricle in outbreed Wistar rats. *Vet Med*. (2012) 57:42–52. doi: 10.17221/4971-VETMED

60. Wasmeier GH, Melnychenko I, Voigt J-U, Zimmermann WH, Eschenhagen T, Schineis N, et al. Reproducibility of transthoracic echocardiography in small animals using clinical equipment. *Coron Artery Dis*. (2007) 18:283–91. doi: 10.1097/MCA.0b013e3280d5a7e3

61. Slama M, Susic D, Varagic J, Ahn J, Frohlich ED. Echocardiographic measurement of cardiac output in rats. *Am J Physiol Heart Circ Physiol*. (2003) 284:H691–7. doi: 10.1152/ajpheart.00653.2002

62. Miranda A. Costa-e-Sousa RH, Werneck-de-Castro JPS, Mattos EC, Olivares EL, Ribeiro VP, Silva MG, Goldenberg R, Campos-de-Carvalho AC. Time course of echocardiographic and electrocardiographic parameters in myocardial infarct in rats. *An Acad Bras Cienc*. (2007) 79:639–48. doi: 10.1590/S0001-37652007000400006

63. Chen Y-F, Weltman NY Li X, Youmans S, Krause D, Gerdes AM. Improvement of left ventricular remodeling after myocardial infarction with eight weeks L-thyroxine treatment in rats. *J Transl Med*. (2013) 11:1–10. doi: 10.1186/1479-5876-11-40

64. Holinski S, Knebel F, Heinze G, Konertz W, Baumann G, Borges AC. Noninvasive monitoring of cardiac function in a chronic ischemic heart failure model in the rat: assessment with tissue Doppler and non-Doppler 2D strain echocardiography. *Cardiovasc Ultrasound*. (2011) 9:1–6. doi: 10.1186/1476-7120-9-15

65. Johns TNP, Olson BJ. Experimental myocardial infarction: I. A method of coronary occlusion in small animals. *Ann Surg*. (1954) 140:675. doi: 10.1097/00000658-195411000-00006

66. Thomas D, Ferrari VA, Janik M, Kim DH, Pickup S, Glickson JD, et al. Quantitative assessment of regional myocardial function in a rat model of myocardial infarction using tagged MRI. *Mag Res Mat Physics Biol Med*. (2004) 17:179–87. doi: 10.1007/s10334-004-0051-y

67. MIURA T, DOWNEY JM OOIWA H, OGAWA S, ADACHI T, NOTO T, SHIZUKUDA Y, et al. Progression of myocardial infarction in a collateral flow deficient species. *Jpn Heart J*. (1989) 30:695–708. doi: 10.1536/ihj.30.695

68. Pich S, Klein HH, Lindert S, Nebendahl K, Kreuzer H. Cell death in ischemic, re-perfused porcine hearts: a histochemical and functional study. *Basic Res Cardiol*. (1988) 83:550–9. doi: 10.1007/BF01906684

69. Hedström E, Engblom H, Frogner F, Åström-Olsson K, Öhlin H, Jovinge S, et al. Infarct evolution in man studied in patients with first-time coronary occlusion in comparison to different species-implications for assessment of myocardial salvage. *J Cardiovasc Mag Res*. (2009) 11:1–10. doi: 10.1186/1532-429X-11-38

70. Kirihara Y, Takechi M, Kurosaki K, Matsuo H, Kajitani N, Saito Y. Effects of an anesthetic mixture of medetomidine, midazolam, and butorphanol and antagonism by atipamezole in rabbits. *Exp Anim*. (2019) 3:18–183. doi: 10.1538/expanim.18-0183

frontiers | Frontiers in Veterinary Science

TYPE Review
PUBLISHED 27 March 2023
DOI 10.3389/fvets.2023.1103229



OPEN ACCESS

EDITED BY
Muhammad Saqib,
University of Agriculture, Pakistan

REVIEWED BY
Nirmal Parajuli,
Henry Ford Health System, United States
Misbah Ijaz,
University of Agriculture, Pakistan

*CORRESPONDENCE
Ahmed Farag
✉ ahmedfarag9331@gmail.com
Ahmed S. Mandour
✉ dr_mandour@vet.suez.edu.eg
Ryou Tanaka
✉ ryo@vet.ne.jp

SPECIALTY SECTION
This article was submitted to Comparative and Clinical Medicine, a section of the journal Frontiers in Veterinary Science

RECEIVED 20 November 2022
ACCEPTED 13 March 2023
PUBLISHED 27 March 2023

CITATION
Farag A, Mandour AS, Hendawy H, Elhaieg A, Elfadadny A and Tanaka R (2023) A review on experimental surgical models and anesthetic protocols of heart failure in rats. *Front. Vet. Sci.* 10:1103229. doi: 10.3389/fvets.2023.1103229



# A review on experimental surgical models and anesthetic protocols of heart failure in rats

Ahmed Farag[1,2]*, Ahmed S. Mandour[3]*, Hanan Hendawy[1], Asmaa Elhaieg[1], Ahmed Elfadadny[4] and Ryou Tanaka[1]*

[1]Department of Veterinary Surgery, Faculty of Veterinary Medicine, Tokyo University of Agriculture and Technology, Fuchu, Japan, [2]Department of Surgery, Anesthesiology, and Radiology, Faculty of Veterinary Medicine, Zagazig University, Zagazig, Egypt, [3]Department of Animal Medicine (Internal Medicine), Faculty of Veterinary Medicine, Suez Canal University, Ismailia, Egypt, [4]Department of Animal Internal Medicine, Faculty of Veterinary Medicine, Damanhur University, Damanhur El-Beheira, Egypt

Heart failure (HF) is a serious health and economic burden worldwide, and its prevalence is continuously increasing. Current medications effectively moderate the progression of symptoms, and there is a need for novel preventative and reparative treatments. The development of novel HF treatments requires the testing of potential therapeutic procedures in appropriate animal models of HF. During the past decades, murine models have been extensively used in fundamental and translational research studies to better understand the pathophysiological mechanisms of HF and develop more effective methods to prevent and control congestive HF. Proper surgical approaches and anesthetic protocols are the first steps in creating these models, and each successful approach requires a proper anesthetic protocol that maintains good recovery and high survival rates after surgery. However, each protocol may have shortcomings that limit the study's outcomes. In addition, the ethical regulations of animal welfare in certain countries prohibit the use of specific anesthetic agents, which are widely used to establish animal models. This review summarizes the most common and recent surgical models of HF and the anesthetic protocols used in rat models. We will highlight the surgical approach of each model, the use of anesthesia, and the limitations of the model in the study of the pathophysiology and therapeutic basis of common cardiovascular diseases.

KEYWORDS

**heart failure, rats, surgical models, anesthesia, myocardial infarction**

## 1. Introduction

Heart failure (HF) is a leading cause of death worldwide. The mortality rate of HF is very high, with ~50% of patients dying within 5 years of their initial diagnosis, which is higher than the fatality rate of most cancers. The most recent World Health Organization estimates that cardiovascular disorders kill 17.9 million people each year, accounting for ~31% of all global deaths (1), and there is a significant economic burden due to the rising prevalence of HF in industrialized countries. The enhancement in treatment for acute myocardial infarction (MI), which has reduced the mortality rate but not morbidity and is based on the rate of survivors, is at least partly responsible for this increase. Additional factors include an increased prevalence of comorbidities, which accelerate the progression of HF. Therefore, it is essential to modify these risk factors and develop new treatment strategies for HF patients (2).

The study of HF requires dependable animal models to evaluate severe changes and pharmacodynamic interactions in the structure and function of the injured myocardium and to pursue its progression to HF. In recent decades, researchers have used small animal models to better understand the pathophysiology of HF and develop more effective strategies for managing patients with congestive HF (3). Therefore, this review aims to describe the different surgical rat models commonly used for the induction of HF and to identify the most reliable anesthetic regimes required for these procedures.

## 1.1. Circulatory system in rats

Rats are mammals belonging to the Muroidea rodent superfamily. The cardiac, pulmonary, and systemic circulatory systems, as well as their valves, are similar to those of humans. The rat heart has four chambers. On the right side of the aortic arch, the brachiocephalic trunk branches into the right common carotid artery and the right subclavian artery. The left common carotid artery is located in the anterior part of the aortic arch, while the left subclavian artery is located to its left (4, 5). Furthermore, the internal mammary arteries supply coronary blood to the right and left atria (5). The rat also has no true equivalent of a circumflex artery besides a small artery such as a ramus intermediate (6); the arterial and venous systems in rats are illustrated in detail in Figure 1.

## 1.2. Anesthesia in rats

Anesthesia is an essential aspect of laboratory animal research to minimize pain and stress during experimental procedures and is also essential to ensure the reproducibility of experimental results. Appropriate anesthesia administration is crucial in achieving success in surgical experiments (7, 8). Here is a general overview of anesthesia in rats, and the various detailed protocols are explained in Table 1.

### 1.2.1. Inhalant anesthesia

Isoflurane and sevoflurane are commonly used inhalant anesthetics in rats. They are administered through a mask or nose cone to induce and maintain anesthesia. The dose and concentration of anesthetic gas can vary based on the species, weight, and age of the rat, as well as the procedure being performed (61, 62).

### 1.2.2. Intraperitoneal injection

A combination of ketamine (50–100 mg/kg) and xylazine (5–10 mg/kg) is a commonly used anesthetic protocol for intraperitoneal injections in rats. This method provides a rapid onset of anesthesia and is often used in short procedures (63, 64).

### 1.2.3. Intramuscular injection

A combination of ketamine (50–100 mg/kg) and xylazine (5–10 mg/kg) is a commonly used anesthetic protocol for intramuscular injections in rats. This method also provides a rapid onset of anesthesia and is often used as a backup when inhalant anesthesia is impossible (65).

### 1.2.4. Intravenous injection

Propofol (2–4 mg/kg) is a commonly used anesthetic for intravenous injections in rats. This method provides rapid and controlled induction of anesthesia and is often used for more invasive procedures (66).

Unfortunately, some countries have prohibited some anesthetic drugs and classified them as narcotics; for instance, Ketamine is currently classified as a narcotic medication in Japan, and numerous other countries have reinforced limitations on its purchase, possession, and related record-keeping methods (67). These decisions represent a big obstacle to their researchers and thus increase the challenges of finding alternative anesthetic protocols. Therefore, we have recently published a paper describing a novel protocol for induction of general anesthesia in rats for cardiac surgery using a mixture of injectable and inhalation anesthesia along with antagonists (60).

It is important to note that the correct protocol can vary greatly depending on the individual animal and the procedure being performed. Additionally, close monitoring of an animal's vital signs, such as heart rate, respiratory rate, and body temperature, is crucial during anesthetic procedures to ensure the safety and wellbeing of the animal.

# 2. Surgical models

## 2.1. Myocardial infarction

Coronary circulation is the main supply of blood to the cardiac tissues, and effective coronary circulation is crucial for the health of the myocardium. Constriction or blockage of one or more branches of the coronary artery is life-threatening and may cause irreversible heart damage and MI; therefore, MI is the main type of ischemic heart disease, characterized by unbalanced ischemia and myocardial necrosis (68, 69).

Despite significant improvements in prognosis, acute myocardial infarction remains the most severe manifestation of coronary artery disease, affecting over seven million people worldwide and contributing to over four million fatalities annually in Northern Asia and Europe (70, 71). MI is described as necrosis of the cardiac muscle cells caused by a prolonged lack of oxygen supply. Because of the decrease in blood circulation, there is insufficient oxygen and nutrition supply to fulfill tissue demand. As a result, cardiomyocyte death occurs (72). Furthermore, in chronic situations, MI may worsen hemodynamics, resulting in patient death. When an acute MI occurs, the patient typically has extensive pain in the chest, upper abdomen, and other regions for at least 20 mins, accompanied by symptoms such as dyspnea (73). Following MI, myocardial cells undergo acute necrosis, and fibrotic scars form during the repair phase. The formation and build-up of

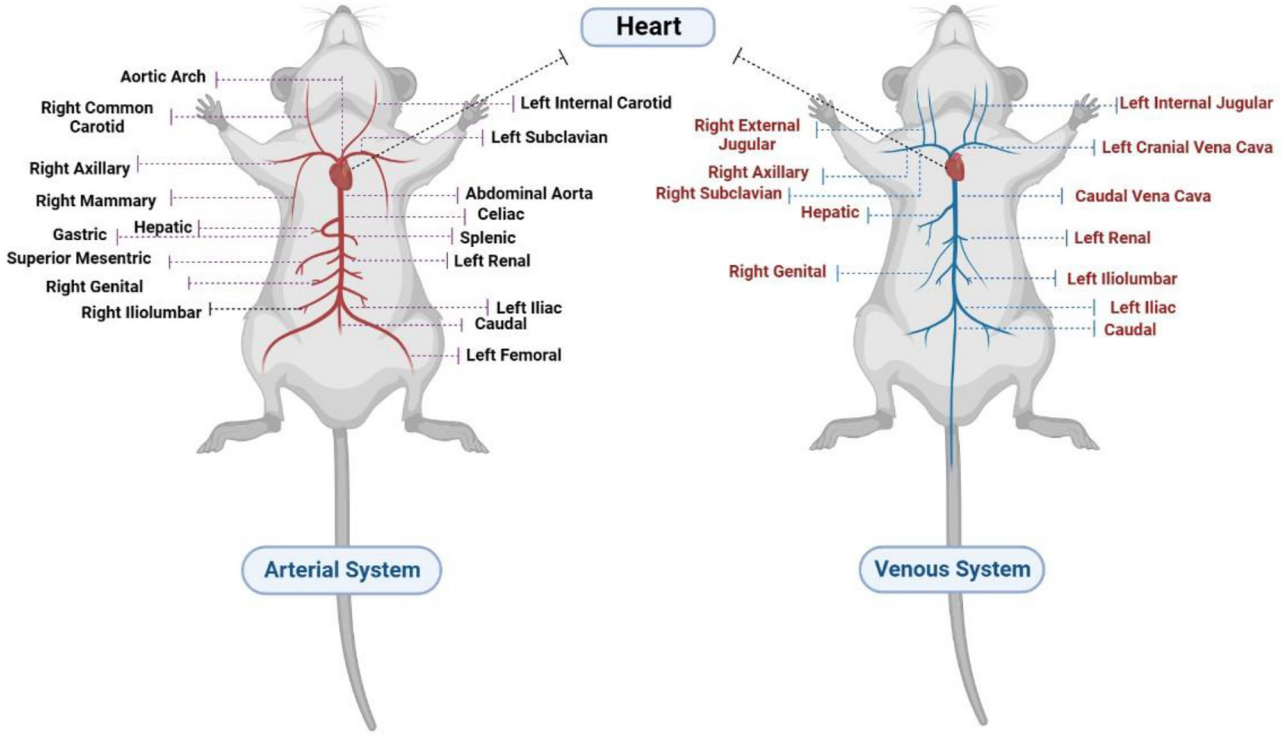


FIGURE 1
Circulatory system in rats.

fibrotic scars over time may damage the structure and function of the heart (74).

## 2.2. Surgical methods of MI

### 2.2.1. Coronary artery ligation

CAL in a rat model is a research technique commonly used to induce MI (heart attack) in rats to study the pathophysiology of the disease, test potential therapeutic interventions (75, 76), evaluate the efficacy of stem cell therapy (9), investigate changes in BM-MSCs *in vivo* and their ability to differentiate into contractile myocytes (77), and explore the effect of autophagy on acute MI and its mechanism in rats (78).

Permanent CAL results in total blood flow blockage and irreversible hypoxia, leaving most of the area at risk of infarction and a massive and permanent scar in the myocardium. This damaged area is susceptible to pathological remodeling, which leads to the progression of HF. Furthermore, the site of the artery blockage influences the size of myocardial ischemia, with ligation closer to the heart's base causing more severe damage. The use of a well-proven procedure performed by a qualified surgeon lowered the variation in infarct size based on the ligation site (79).

#### 2.2.1.1. Surgical technique

The procedure began with the injection of an anesthetic drug into the animal, followed by the use of a mechanical ventilator to secure the airway. A left thoracotomy was performed, the heart was rapidly exposed, and the initial ligation site was determined (80).

Once the site of ligation of the left anterior descending coronary artery (LAD) was identified, a cotton earbud was gently pressed onto the artery slightly below the site of ligation, immobilizing the heart, while simultaneously making the artery noticeable and easy to recognize. A non-absorbable ligature passes below the LAD and is secured with three knots using a tapered atraumatic needle. Blanching and cyanosis of the anterior wall of the left ventricle, as well as enlargement of the left atrium, are signs of successful ligation. Due to direct vision and observation of the process and targeted area of infarction, CAL provides accurate time, location, and extent of the coronary event. The ribs and muscles were closed with dissolvable sutures, with a small gap left to aspirate any remaining air in the thorax, and air was aspirated to keep the lungs from collapsing. At the time of closure, the muscle and skin stitch sites were treated with neomycin powder and betadine, respectively. Before extubation, the lungs were deflated by submerging the exit tube connected to the endotracheal tube in an underwater seal with adequate postoperative care (Figure 2) (9).

Extubation was conducted before the rats were fully awake, and a 1 mL syringe was used to carefully suction the endotracheal catheter to prevent bronchial occlusion due to heavy mucus. The rats were then placed in a recovery cage with an oxygen source for around 30 min. Analgesia (0.025 mg/kg body weight subcutaneously every 12 h) was planned for up to 72 h (81).

TABLE 1 Different anesthetic protocols used for the induction of experimental surgical models of heart failure in rats.

| Anesthetic protocols | Surgical models | References |
|---|---|---|
| A mixture of ketamine hydrochloride and xylazine hydrochloride (intraperitoneal injection) | Myocardial infarction (MI) model (80 mg/kg ketamine and 10 mg/kg xylazine) | (9, 10) |
| | Cryoinjury-induced MI model (100 mg/kg ketamine and 10 mg/kg xylazine) | (11) |
| | Ischemia-reperfusion (IR) model (40 mg/kg ketamine and 10 mg/kg xylazine) | (12) |
| | Arteriovenous shunt (AVS) model (90 mg/kg ketamine and 10 mg/kg xylazine) | (13, 14) |
| | Aortic regurgitation (AR) model (50 mg/kg ketamine and 10 mg/kg xylazine) | (15, 16) |
| Sodium pentobarbital (intraperitoneal injection) | MI model (50 mg/ kg sodium pentobarbital) | (17–19) |
| | Cryoinjury-induced MI model (50 mg/ kg sodium pentobarbital) | (20) |
| | IR model (50–60 mg/kg sodium pentobarbital) | (21–23) |
| | Aortic constriction (AC) model (40 mg/kg sodium pentobarbital) | (24, 25) |
| | AR model (50 mg/ kg sodium pentobarbital) | (26, 27) |
| | PAB model (50–60 mg/ kg sodium pentobarbital) | (28–31) |
| | AVS model (50 mg/ kg sodium pentobarbital) | (32, 33) |
| | Two kidneys, one clip (2K1C) model (40 mg/kg sodium pentobarbital) | (34–36) |
| Chloral hydrate 10 % (intraperitoneal injection) | MI model | (37, 38) |
| | IR model (350 mg/kg chloral hydrate 10 %) | (39, 40) |
| | AC model (300 mg/kg chloral hydrate 10 %) | (41, 42) |
| | 2K1C model (0.3 ml/100 g 10% chloral hydrate) | (43) |
| Isoflurane (inhalational anesthesia) | MI model (induction: 5%, maintenance: 2.5%) | (44) |
| | AC model (induction: 4%, maintenance: 2.5%) | (45) |
| | AVS model (induction: 4%, maintenance: 1.5%) | (32, 46) |
| | AR model (maintenance: 1.5%) | (47) |
| | PAB model (induction: 4% isoflurane in a mixture of 50% $O_2$ and 50% $N_2O$) | (48) |
| A mixture of ketamine, xylazine, and acepromazine. | MI model (50 mg/kg ketamine, 4 mg/kg xylazine, and 1 mg/kg acepromazine). | (49) |
| Intraperitoneal injection of sodium pentobarbital followed by an Intramuscular administration of ketamine hydrochloride. | Cryoinjury-induced MI model (30 mg/kg sodium pentobarbital and 22 mg/kg ketamine hydrochloride) | (50) |
| Intramuscular ketamine injection followed by an intraperitoneal injection of pentobarbital. | Cryoinjury-induced MI model (22 mg/kg ketamine and 30 mg/kg pentobarbital). | (51) |
| Diethyl ether (inhalational anesthesia) | Cryoinjury-induced MI model | (52) |
| A mixture of ketamine and medetomidine intramuscular injection | 2K1C model (60 mg/k ketamine and 250 μg/kg medetomidine) | (53) |
| Ketamine intraperitoneal injection | 2K1C model (90 mg/kg ketamine) | (54, 55) |
| A mixture of injectable and inhalational anesthesia ketamine hydrochloride and isoflurane | AVS model (10 mg per rat ketamine hydrochloride and subsequently anesthetized using 5% isoflurane for the first minute followed by 2–3% during the remainder of the surgery). | (56) |
| A mixture of ketamine and midazolam | AVS model | (57) |
| Methohexital sodium intraperitoneal injection | AVS model (50 mg/kg methohexital sodium). | (58) |
| A mixture of pentobarbital and xylazine intraperitoneal injection | PAB model (50 mg/kg pentobarbital and 5 mg/kg xylazine) | (59) |
| A mixture of medetomidine-midazolam-butorphanol (MMB) and isoflurane followed by atipamezole | MI model MMB (0.3/5.0/5.0 mg/kg/SC) with isoflurane 1% encountered by atipamezole 1.0 mg/kg/SC | (60) |

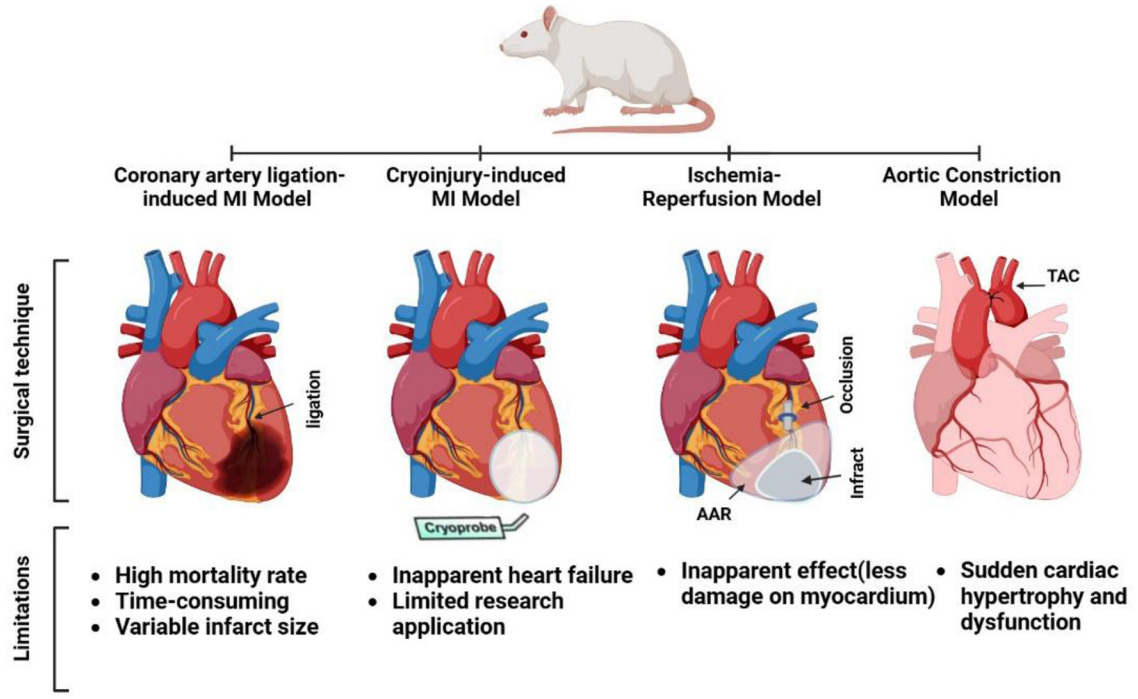


FIGURE 2
Surgical techniques and limitations for some experimental rat models of heart failure (coronary artery ligation myocardial infarction [MI], cryoinjury MI, ischemia-reperfusion, and aortic constriction models).

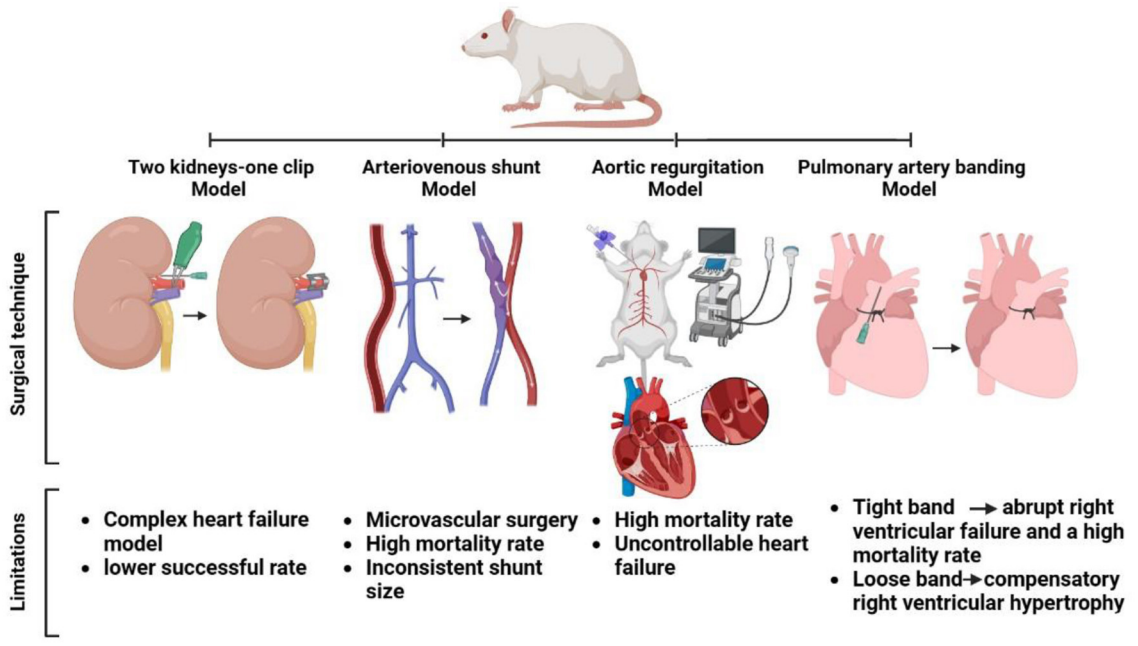


FIGURE 3
Surgical approach and shortcomings in some heart failure models in rats (two kidneys-one clip, arteriovenous shunt, aortic regurgitation, and pulmonary artery banding models).

### 2.2.1.2. Limitations

These procedures are reported to have a mortality rate of more than 50% due to malignant ventricular tachycardia in the acute phase. Furthermore, infarctions are usually mild (averaging 21% of the left ventricle), which may be due to the large amount of subpericardial collateral circulation in this species. Consequently, only

minor hemodynamic changes were observed (82). Furthermore, creating the model is time-consuming and has been increasingly criticized in terms of animal protection (83). Reichert et al. (84) mentioned that the main limitation of this technique is the risk of postoperative mortality, mostly caused by the occurrence of cardiac arrhythmias, hemorrhage, and pneumothorax.

However, the MI model using the ligation technique produces a wide variation in infarct size (85, 86). According to Pfeffer et al. (87), the extent of the infarct ranges from 8 to 65%. Widely varying results have minimal statistical significance and limited utility, and infarct size is a significant predictor of left ventricular remodeling and death. Survival, cardiac remodeling, and hemodynamic dysfunction are frequently proportional to the infarct size (88). The site of the occluding suture influences the size of the infarct and the outcomes of coronary occlusion, and it is difficult to identify the path of the LAD and the optimal ligation site in small-sized rats (49, 88).

### 2.2.2. Cryoinjury-induced MI

Cryoinjury is another technique used to create an MI rat model. It involves applying a cold probe to the surface of the heart, typically the left ventricle, to freeze and damage a small area of heart tissue. The resulting injury leads to a local inflammatory response and scar formation, mimicking the pathophysiological changes observed in human MI. This technique is commonly used to study the effects of different therapeutic interventions on cardiac repair and regeneration (89), as well as the underlying molecular and cellular mechanisms involved in cardiac remodeling after injury (90), evaluate the therapeutic effectiveness of biomaterials for cardiac repair in the MI model (91), and examine the effect of embryonic cardiomyocyte transplantation on HF progression (92).

According to Van Den Bos et al. (93), this is an ideal model for studying therapeutic interventions to restore heart function or cardiac regeneration following MI. They compared the results of myocardial injury created by cryoinjury with the CAL method and concluded that both resulted in a comparable loss of contractility and diastolic dysfunction, but the cryoinjury model demonstrated milder LV remodeling with no obvious heart failure. No obvious cardiac failure due to a minor necrotic disc-shaped lesion caused by the cryoprobe was observed. The generated lesion has cellular characteristics, such as coagulation necrosis of myocardium. Thus, it is an appropriate model for demonstrating myocardial repair (93, 94).

The pathophysiology of MI in the cryoinjury approach differs from that in other methods, such as LAD ligation, in that acute cell death occurs without accompanying ischemia. It is caused by mechanical stresses generated by the development of ice crystals in the intracellular and extracellular spaces, as well as in the vasculature (93). This technique has been employed in studies involving intracardiac cell transplantation for myocardial repair (89). Transplanted cells are easily injected at predetermined sites, and the presence of vascular reperfusion is favorable for cellular repair (93, 94).

#### 2.2.2.1. Surgical technique

Three consecutive exposures to a liquid nitrogen-cooled cryoprobe, a 6 mm stainless steel cylinder, resulted in acute LV MI. Blanching of the wall followed by hyperemia indicated the onset of MI in the heart. In addition, the cryoinjury region of an MI heart is distinguished by its pale appearance compared with the surrounding tissue (Figure 2) (89).

#### 2.2.2.2. Limitations

This method does not result in apparent HF following cryoinjury, which is most likely due to the smaller infarct size compared with coronary ligation. As a result, when an observable HF model is required, the cryo-infarction model is not a choice; in other words, cryo-infarction cannot replace the currently available HF models. Instead, it can be used as a model for evaluating medical treatments aimed at reducing cardiac remodeling and improving heart function after myocardial infarction, such as drugs that promote cardiac regeneration through progenitor cells or growth factors (93), and invasive surgical procedures involving thoracotomy, as in the LAD ligation technique (72).

### 2.2.3. Ischemia-reperfusion model

The IR rat model is a widely in used research to study the pathophysiology of ischemic injury and test potential therapeutic interventions. Its creation involves interrupting blood flow to a specific organ or tissue (ischemia) for a period of time and then restoring blood flow (reperfusion). In the case of the heart, a common approach is to temporarily occlude the coronary artery, induce myocardial ischemia, and then re-perfuse the tissue by removing the occlusion (95). This process results in a series of pathophysiological events, including oxidative stress, inflammation, and cell death, which can be studied to better understand the mechanisms of ischemic injury and identify potential therapeutic targets. The IR rat model is used to simulate ischemia-reperfusion injury that occurs in many clinical conditions, such as MI, stroke, and organ transplantation (96), and to evaluate the efficacy of human amniotic membrane mesenchymal stem cell-derived conditioned medium against IR injury (97).

Inducing MI in rodents with IR was originally tested in experimental *in vivo* organs before being used in dogs in 1988 (98). Initial apoptosis following hypoxia, as well as a smaller second wave of necrosis, causes an infarct after IR, which is, therefore, regarded as damage caused by reactive oxygen species and the opening of the mitochondrial permeability transition pores (95).

The implementation of early reperfusion in the clinical management of acute MI results in lower mortality and enhanced cardiac function (99). The period between occlusion and reperfusion ranged from 15 min to 2 h, with 30 min being the most common (100). However, there is insufficient information to support this conclusion. Some of the variances, as with the permanent CAL procedure, can be explained by factors such as operator experience and animal strain; however, the time of reperfusion adds another major level of variance and unpredictability to the outcome. As a result, 30 min after IR, the model may show infarct sizes of as low as 4%, indicating modest damage with no influence on heart function or eventual pathology, or as high as 30%, indicating minimal infarct size to significantly impair function (100, 101).

In all cases, the infarct size produced by IR was significantly smaller than that produced by the permanent CAL method because blood flow restoration rescues a portion of the affected area. One significant distinction between IR and permanent ligation (PL) is the secondary onset of reperfusion damage. This occurs as a direct result of the rapid return of blood flow to the damaged region, and is a secondary cause of cell damage and death after ischemia. In general, IR is more technically challenging than PL, resulting in smaller and more variable infarcts that frequently do not advance to other cardiovascular pathologies. However, it allows researchers to study the second wave of injury associated with blood reperfusion, which applies to clinical interventions in human acute MI patients but is not currently a therapeutic target (95).

#### 2.2.3.1. Surgical technique

The same applies to the MI model, with a difference in the ligation technique. After the heart was already visible, the LAD was temporarily ligated using a piece of tubing. The suture was cut, and the tubing was removed for reperfusion once the appropriate period of ischemia had passed (Figure 2) (39).

#### 2.2.3.2. Limitations

The most significant limitation of the IR model is that the majority of damage is still caused by ischemia, with reperfusion injury accounting for a considerably smaller second wave of post-MI injury. Therefore, reperfusion injury may have no apparent effect on the overall severity of MI (12). In addition, significant variations in the results and outcomes were mainly dependent on the IR time-course (102).

### 2.2.4. Aortic constriction model (pressure overload)

The AC model is a commonly used experimental model of left ventricular hypertrophy that involves partial constriction of the aorta to increase the pressure in the left ventricle. This model is used to study the mechanisms underlying cardiac hypertrophy and HF, to test potential therapeutic interventions (103), and to characterize the immunomodulatory response in a pressure overload model of HF (104).

Initially, banding had little or no effect on aortic flow, but as the animal grew, the relative severity of the constriction increased, resulting in heart hypertrophy, which has been utilized to mechanically replicate the cardiac consequences of aortic stenosis, systemic hypertension, and aortic coarctation in a variety of sites (3, 105).

The constriction may be thoracic, near the aortic origin (ascending AC [AAC]), or in the aortic arch between the first and second trunks (transverse AC [TAC]). The constriction can also be used in the abdominal aorta, either below or above the renal arteries, with the latter inducing hypertension due to renal hypoperfusion and concurrent LV hypertrophy. The main distinction among these models is the anatomic position of the constriction (106).

TAC and suprarenal AC cause a more gradual increase in pressure, hypertrophy, and HF, whereas AAC is frequently used to assess the effects of an early insult caused by pressure overload (107). The severity of the disease varies according to the species, age, and sex of the animal (108–110).

TAC surgery that reduces aortic diameter by 50%, causes a systolic pressure gradient of 50–60 mmHg between the aorta and the LV, resulting in clear echocardiographic evidence of LV hypertrophy and an increase in left atrial pressure around the eighth week (111). According to Weinberg et al. (109), after 18–20 weeks of compensatory LV hypertrophy, a subgroup of rats eventually showed reduced LV systolic pressure, higher LV volume, decreased ejection fraction, and clinical symptoms of overt congestive HF.

#### 2.2.4.1. Surgical technique

The anesthetized rats were placed in the supine position for TAC. Following the skin incision, the upper half of the sternum was separated in the midline using scissors, and the thymus was removed. The aortic arch was carefully dissected from surrounding tissues. A stylet (bent and blunted) 16G intravenous catheter was tied securely to the aorta between the brachiocephalic trunk and left common carotid artery using a 4.0 silk and then removed, creating partial AC. Sutures were used to close the sternotomy and skin incisions. Rats were extubated and placed in an incubator at 28–30°C for recovery (Figure 2) (45).

Rats were intraperitoneally injected with buprenorphine (0.1 mg/kg) for postoperative analgesia. In addition, the rats were administered oxytetracycline (500 mg/L of water) *via* drinking water for 7 days (112).

#### 2.2.4.2. Limitations

In the TAC model, although the onset of HF development differs significantly from that of patients with hypertension or aortic stenosis, the initiation of hypertension in this model is sudden and results in a 50% increase in LV mass within 2 weeks; thus, this is an ideal model to investigate intervention strategies that affect the development of cardiac hypertrophy (113).

AC (abdominal AC in the infrarenal and suprarenal positions) can also produce chronic LV pressure overload, which eventually leads to cardiac hypertrophy and dysfunction. The progression of this model to HF is more gradual, making it more appropriate for hypertension-related HF. Because it does not require chest opening or artificial breathing, it is more routinely utilized in rats than TAC (114, 115).

### 2.2.5. Two kidneys-one clip (2K1C) model (renal failure-induced hypertension, renovascular hypertension)

The 2K1C model is an experimental model of renovascular hypertension that involves placing a clip on one of the renal arteries to reduce blood flow to one of the kidneys. This reduction in blood flow stimulates the renin-angiotensin-aldosterone system, leading to increased blood pressure. This model was used to study the mechanisms of hypertension, test the efficacy of antihypertensive therapies (116), and study the significance of stem cell therapy in the remodeling of fibrotic kidney parenchyma (117).

The physiological function of the kidney includes maintaining electrolyte and fluid balance as well as secretion of renin, a key component of the renin-angiotensin system. Thus, its role in blood

pressure regulation and the development of hypertension is widely acknowledged. Since Goldblatt et al. (118) created an elevation in blood pressure by partially closing the renal artery in dogs in 1934, many renal-generated hypertension models have been successfully established in rats, rabbits, sheep, and cats.

According to Weber et al. (119), within 2–4 weeks of clipping the kidney, the model is characterized by significant elevations in plasma renin activity, as well as elevated circulating angiotensin II concentrations and blood pressure. After 4 weeks, plasma renin activity and angiotensin II levels returned to near-normal levels, regardless of the presence of interstitial fibrosis in the heart, particularly around the intramural coronary arteries. Within a few months, a chronic phase developed, marked by increased plasma renin activity and myocardial perivascular and interstitial fibrosis (119).

Junhong et al. used 2K1C to simulate a rat model of diastolic dysfunction and studied its biochemical alterations using proteomic techniques. They found that diastolic dysfunction was observed in hypertensive rats 8 weeks after the operation, as evidenced by increased wall thickness, fibrosis, impaired relaxation, and increased chamber stiffness (54). Another experiment was conducted in our laboratory to induce renovascular hypertension in rats to study novel echocardiographic techniques and herbal medicines in this model (120).

#### 2.2.5.1. Surgical technique

The anesthetized rats are subjected to a flank abdominal incision to expose the left renal hilum, and the renal artery and vein are carefully identified by blunt dissection. To prevent vessel compression during clip placement, an insulin needle tip with an outer diameter of 0.23 mm is employed in each of the rats. A titanium vascular clip is also gently placed around the left renal artery. After that, the needle tip is carefully removed, the contents of the abdomen are gently returned to their original location, the abdominal wall and skin are sutured, and the animals are allowed to recover (Figure 3) (43, 55). Non-steroidal anti-inflammatory flunixin meglumine (2.5 mg/kg, subcutaneously) and antibiotic enrofloxacin (5 mg/kg, subcutaneously) can be administered as postoperative treatment (121).

#### 2.2.5.2. Limitations

Renovascular hypertension created by this model usually produces a complex HF model, in which myocardial hypertrophy is eccentric due to overloading and concentric due to hypertension that develops in addition to renal failure. Although this model somewhat mimics complex renal failure-induced HF to some extent, there are some issues regarding the success rate and rapid change in the geometry of the heart, which limit the study of detailed hemodynamic investigations of the heart. In a study by Ma et al. the feasibility of a novel IVPG assessment did not show significant benefits in this model within 8 weeks. However, his data revealed clear evidence of rapid changes in myocardial strain and the efficiency of a new medicine (salvianolic acid B) to ameliorate the pathological consequences of the heart in this model (120).

The 2K1C approach is not always successful in rats; for example, in the Dussaule experiment, 19 rats did not acquire hypertension, 27 had malignant hypertension, and 12 died; only 47 (45%) established stable hypertension (122). In addition, Amann et al. (123) found that after 14 months of uremia, ventricular hypertrophy in operated rats was not accompanied by an increase in the capillary number. Although this model undoubtedly enables the analysis of hypertension following renal failure, it is difficult to determine how it may be used for human essential hypertension (124).

### 2.2.6. Arteriovenous shunt model (volume overload)

The AVS model is an experimental model that involves the surgical creation of a direct connection between an artery and vein, bypassing the capillary bed. This results in increased blood flow and pressure in the vein, mimicking the hemodynamic changes observed in certain pathological conditions, such as arteriovenous fistulas. The AVS model was used to study the effects of increased blood flow and pressure on vascular function and to test potential therapeutic interventions (32).

Aortocaval fistula (ACF)-induced chronic volume overload in rats is a well-studied rodent HF model (106). This model is simple and reliable, and it features several crucial aspects of human HF, including a gradual change from the asymptomatic to the decompensated phase, considerable neurohumoral activation (125), fluid retention, and changes in myocardial phenotype typical of HF (126).

An artificial shunt between the abdominal aorta and the inferior vena cava causes a significant increase in cardiac output and venous return, which causes compensatory, initially asymptomatic ventricular hypertrophy (127), prolonged hemodynamic overload, redistribution of cardiac output, and activation of the neurohumoral response, causing HF to appear 8–10 weeks after ACF induction (57).

AVS have been used to cause volume overload, dilated cardiomyopathy, and HF in rodents (128). Despite the limitation of requiring laparotomy, the more recent aortocaval shunt technique is a comparably faster and easier way to induce HF with good survival rates (3, 129).

The hemodynamic data in these models suggest a persistent increase in the LV diastolic volume. The Frank–Starling mechanism is responsible for maintaining a high output status in the early stages following the development of the AV shunt. This variable represents an abrupt increase in wall stress caused by volume overload, whereas changes in LV end-diastolic pressure indicate that the development of cardiac hypertrophy and dilation of the cardiac chamber tend to regulate wall stress (6).

#### 2.2.6.1. Surgical technique

Flaim et al. established a HF rat model of a chronic AVS between the abdominal aorta and the inferior vena cava, and surgical introduction of an arteriovenous fistula between the abdominal aorta and the inferior vena cava at a point ∼5 mm caudal to the left renal vein was used to induce a high cardiac output state. After general anesthesia, a midline incision in the abdominal wall was made to expose the peritoneal cavity, and the abdominal aorta and vena cava were exposed and isolated for ∼20 mm before all branches were occluded using bulldog clamps A 10 mm segment of the aorta and vena cava were isolated under a dissecting microscope by placing two bulldog clamps across the main vessels,

and openings of approximately comparable size (width, 1 mm) were made through the medial walls at the midpoint of the isolated segments. Three interrupted microsurgical sutures (9-O Ethilon) were used to unite the opposing sides of the two apertures; the clamps were removed, and the patency of the fistula was visually confirmed by the presence of mixed arterial blood in the vena cava. After closing the abdominal incision, the animal was allowed to recover (Figure 3) (125, 130).

On the other hand, Garcia and Diebold developed a simple, rapid, and effective method for exposing the vena cava and abdominal aorta by opening the abdominal cavity with a midline incision, placing a 18-gauge needle into the abdominal aorta and progressing through the medial wall into the vena cava, constricting the aorta is momentarily below the origin of the right renal artery, and quickly repairing the aortic puncture using a cyanoacrylate glue. To confirm the patency of the shunt, a pulsatile flow of oxygenated blood into the inferior vena cava is visually observed. A standard method is used to close the abdominal cavity using an absorbable suture (131).

#### 2.2.6.2. Limitations

In rats, an AV fistula is formed by a side-to-side anastomosis of the aorta and vena cava (125) or by end-to-side anastomosis of the left iliolumbar vein (56). Both operations necessitate microvascular surgery, and the circulatory system is occluded for 15–30 min. Furthermore, because these surgical procedures take 40 mins to complete, mortality rates range from 47 to 76% (56, 125). In addition, shunt size and hypertrophic and hemodynamic characteristics have been inconsistent (13).

### 2.2.7. Aortic regurgitation model (volume overload)

AR models are often created through surgical interventions such as aortic valve leaflet perforation or cusp removal. These procedures can lead to increased retrograde blood flow, resulting in AR. The severity of regurgitation can be assessed using various imaging techniques, such as echocardiography or MRI. These models can be used to study the pathophysiology and potential treatments of AR (132) and to study biological and tissue-engineered valvular and cardiovascular grafts *in vivo* (133).

AR is another volume overload model of HF that is induced by ventricular volume regurgitation and is thus directly related to the severity of aortic insufficiency. Mild AR causes only minor volume overload, whereas severe AR causes considerable LV volume overload and increasing chamber dilatation. AR can be classified as compensated or decompensated. In compensated AR, the LV first responds to volume overload by eccentric hypertrophy, preserving LV diastolic compliance and allowing LV filling pressures to stay normal or mildly elevated despite a substantial regurgitation volume. Decompensated AR is defined as LV systolic dysfunction and poor LV diastolic compliance as a result of hypertrophy and fibrosis, resulting in excessive filling pressures and HF (6, 134).

Although not the most frequently encountered valvular disease, it has been estimated based on the findings of the Framingham study that 13% of the population suffers from some degree of AR (135). While mild AR normally does not cause any significant problems, the disorder can grow silently for decades and worsen. This stealthy progression results in increased LV dilatation, hypertrophy, and, finally, HF (136, 137).

#### 2.2.7.1. Surgical technique

AR is established in anesthetized animals by exposing the right carotid artery through a right lateral neck incision. The distal common carotid artery is ligatured using a 4.0 nylon suture, followed by a arteriotomy to allow the insertion of a 0.9-mm guide wire. The thorax is scanned with an echocardiographic probe to obtain a clear view of the left ventricle, aortic valve, and ascending aorta, which is equal to a parasternal long-axis view in standard human echocardiography. Under continuous echocardiographic observation, an arterial leader catheter is moved retrogradely toward the aortic valve, and the position and passage of the catheter through the aortic valve leaflet and into the left ventricle are guided by the sonographer; an acute AR is caused by a tear in the leaflet (Figure 3) (138).

The following echocardiographic criteria were used to determine AR at the time of surgery: the color Doppler ratio of regurgitation jet width to left ventricular outflow tract obstruction diameter was 50–70%, and pulsed-wave Doppler proved reversed diastolic flow in the abdominal aorta (139). When the echocardiographic criteria determined that the severity of the regurgitation jet in the abdominal aorta was insufficient, leaflet perfusion was repeated. After the AR was established, the proximal carotid artery was ligated using 4.0 nylon sutures (140). In the first few hours following surgery, the animals were observed for any signs of respiratory distress that could indicate severe HF. They were weighed daily to check for excessive weight gain, which could be a sign of pending HF (138).

#### 2.2.7.2. Limitations

This rat model has various drawbacks in terms of AR. One of the most serious complications is the extremely high mortality rate associated with acute AR secondary to HF. Multiple aortic valve leaflet perforations can cause serious valve damage, uncontrollable HF, and death. Therefore, wire perforations should be performed while echocardiography is being monitored, and repeated perforations should be avoided (140).

Another challenge is the wire size of the perforations. Some researchers prefer thicker wires (0.9 mm), which can result in multiple leaflet injuries with severe AR, while others prefer thinner wires (0.3 mm), which result in relatively moderate AR (138, 141). Thus, a wire diameter of 0.6 mm may be more acceptable for creating a modest AR model (6).

### 2.2.8. Pulmonary artery banding model (right ventricle pressure overload models)

PAB is a surgical model used in rats to induce right ventricular (RV) pressure overload and study the development of RV hypertrophy and HF. In this model, a band is placed around the pulmonary artery, restricting blood flow to the lungs and causing an increased RV afterload. The severity of RV pressure overload can be adjusted by varying the tightness of the band. PAB is commonly used in cardiovascular research to investigate the molecular and cellular mechanisms involved in RV hypertrophy and HF to test potential therapies for these conditions (28) and to explore the

efficacy of stem cell therapy for RV failure in pulmonary arterial hypertension (142).

Pulmonary arterial hypertension (PAH) is a chronic and frequently fatal condition (143). Although the primary pathology originates in the pulmonary vasculature, mortality is determined by RV remodeling, dysfunction, and eventual failure (144). Several animal models of RV pressure overload and PAH have been developed to study the pathophysiology of PAH and RVs, as well as their response to prospective treatments. PAB, Sugen-5416 plus hypoxia (SuHx)-induced PAH, and monocrotaline (MCT)-induced PAH are some of the models used (145–148). Several studies have demonstrated that these models produce distinct RV responses in terms of adaptive RV hypertrophy in the PAB model, in contrast to the maladaptive failure in the SuHx and MCT models (28, 149). Several characteristics of maladaptive RV remodeling in the PAH model have been proposed, including RV dilation, reduced function, fibrosis, and capillary rarefication (29, 150). However, as of the confounding effects of potentially altered pulmonary vascular resistance, hypoxia, molecular modulation (e.g., VEGF inhibition), or toxins on RV function, the MCT and SuHx models cannot be used to investigate isolated RV effects of potential therapies, and the PAB model is relevant in this regard (29, 151, 152).

PAB involves constricting the pulmonary artery using a band or clip to increase the workload on the right ventricle and simulate the effects of pulmonary hypertension. A pre-adjusted hemostatic clip is the most widely used approach in small animal models of rats and mice (48, 153, 154), or a ligature tightened around the pulmonary artery (155–157). Both procedures are effective; however, the clipping approach may be easier to learn and more reproducible, whereas the ligature method does not use metal, making it better suited for MRI or ultrasound evaluation of pulmonary artery flow (158). The banding method has the advantage of allowing for accurate titration of afterload to produce RV hypertrophy, compensated RV failure, or decompensated RV failure owing to the precise diameter of the band/clip (159, 160), as evidenced by hypertrophy with preserved hemodynamics, altered hemodynamics without extracardiac symptoms of RV failure, and altered hemodynamics with extracardiac signs of RV failure (158).

#### 2.2.8.1. Surgical technique

The anesthetized animals are mechanically ventilated after intubation using a volume-controlled respirator and oxygen-enriched room air. After induction left thoracotomy, the pulmonary artery (PA) is gently torn free from the aorta using a silk thread that is threaded beneath the PA, then an 18-gauge needle is threaded alongside the PA, and the suture is securely tied around the needle and swiftly released, leaving a fixed, constricted aperture in the lumen equal to the needle's diameter. The combination of a fixed banding around the PA and the animal's growth results in dramatically elevation RV afterload over time (Figure 3) (28, 161, 162). In another technique using a clip applier with a stopper, a small clip is half-closed around the PA, and blood flow *via* the PA is restricted to the inner segment of the half-closed clip (59). Buprenorphine (15 g/kg sc) is used to relieve postoperative pain (28).

#### 2.2.8.2. Limitations

A challenge with the banded model is to include RV failure, rather than simply a well-adapted hypertrophic RV. The difficulty is that a tight band causes abrupt RV failure and mortality in adult animals, whereas a loose band causes compensatory RV hypertrophy. To overcome this, most models begin operations with weaning. This causes stenosis to worsen as the animal develops, allowing for catastrophic RV failure over time (158, 163).

## Author contributions

Review design: AF, AM, and RT. Investigation: AF, AM, HH, and AElh. Data collection: AF, AElf, and HH. Writing and drafting: AF, AM, AElh, and AElf. Critical editing: AM. Supervision: RT. All authors reviewed and edited the final version.

## Acknowledgments

This research was supported by a full scholarship provided by the Egypt-Japan Education Partnership (EJEP) of the Ministry of Higher Education, Egypt.

## Conflict of interest

The authors declare that the research was conducted in the absence of any commercial or financial relationships that could be construed as a potential conflict of interest.

## Publisher's note



## References

1. Crespo CJ, di Angelantonio E, Group WHOCVDRCW. World health organization cardiovascular disease risk charts: revised models to estimate risk in 21 global regions. *Lancet.* (2019) 7:e1332–45. doi: 10.1016/S2214-109X(19)30318-3

2. Riehle C, Bauersachs J. Small animal models of heart failure. *Cardiovasc Res.* (2019) 115:1838–49. doi: 10.1093/cvr/cvz161

3. Gomes AC, Falcao-Pires I, Pires AL, Brás-Silva C, Leite-Moreira AF. Rodent models of heart failure: an updated review. *Heart Fail Rev.* (2013) 18:219–49. doi: 10.1007/s10741-012-9305-3

4. Halpern MH. The azygos vein system in the rat. *Anat Rec.* (1953) 116:83–93. doi: 10.1002/ar.1091160108

5. Halpern MH. The dual blood supply of the rat heart. *Am J Anat.* (1957) 101:1–16.

6. Katz MG, Fargnoli AS, Gubara SM, Chepurko E, Bridges CR, Hajjar RJ. Surgical and physiological challenges in the development of left and right heart failure in rat models. *Heart Fail Rev.* (2019) 24:759–77. doi: 10.1007/s10741-019-09783-4

7. Fish RE, Brown MJ, Karas AZ. Anesthesia and analgesia in laboratory animals. 2nd (ed): American coll of Lab Ani. *Med Serv.* (2008) 302:305.

8. Luca C, Salvatore F, Vincenzo DP, Giovanni C, Attilio ILM. Anesthesia protocols in laboratory animals used for scientific purposes. *Acta Bio Med Atenei Parmens.* (2018) 89:337. doi: 10.23750/abm.v89i3.5824

9. Srikanth G, Prakash P, Tripathy N, Dikshit M, Nityanand S. Establishment of a rat model of myocardial infarction with a high survival rate: a suitable model for evaluation of efficacy of stem cell therapy. *J Stem Cells Regen Med.* (2009) 5:30. doi: 10.46582/jsrm.0501006

10. Gonçalves MSS, Silva EAP, Santos DM, Santana IR, Souza DS, Araujo AM, et al. Nerolidol attenuates isoproterenol-induced acute myocardial infarction in rats. *Naunyn Schmiedebergs Arch Pharmacol.* (2022) 395:353–63. doi: 10.1007/s00210-022-02202-w

11. Jin J, Jeong SI, Shin YM, Lim KS, Shin H, Lee YM, et al. Transplantation of mesenchymal stem cells within a poly (lactide-co-$\varepsilon$-caprolactone) scaffold improves cardiac function in a rat myocardial infarction model. *Eur J Heart Fail.* (2009) 11:147–53. doi: 10.1093/eurjhf/hfn017

12. Yücel A, Aydogan MS, Ucar M, Sarici KB, Karaaslan MG. Effects of apocynin on liver ischemia-reperfusion injury in rats. *Transpl Proc.* (2019) 14:1180–3. doi: 10.1016/j.transproceed.2019.01.108

13. Wang XI, Ren B, Liu S, Sentex E, Tappia PS, Dhalla NS. Characterization of cardiac hypertrophy and heart failure due to volume overload in the rat. *J Appl Physiol.* (2003) 94:752–63. doi: 10.1152/japplphysiol.00248.2002

14. Sethi R, Saini HK, Guo X, Wang X, Elimban V, Dhalla NS. Dependence of changes in β-adrenoceptor signal transduction on type and stage of cardiac hypertrophy. *J Appl Physiol.* (2007) 102:978–84. doi: 10.1152/japplphysiol.00921.2006

15. Noma T, Nishiyama A, Mizushige K, Murakami K, Tsuji T, Kohno M, et al. Possible role of uncoupling protein in regulation of myocardial energy metabolism in aortic regurgitation model rats. *FASEB J.* (2001) 15:1206–8. doi: 10.1096/fj.00-0569fje

16. Murakami K, Mizushige K, Noma T, Kimura S, Abe Y, Matsuo H. Effects of perindopril on left ventricular remodeling and aortic regurgitation in rats assessed by echocardiography. *Angiology.* (2000) 51:943–52. doi: 10.1177/000331970005101107

17. Dai Y, Chen Y, Wei G, Zha L, Li X. Ivabradine protects rats against myocardial infarction through reinforcing autophagy *via* inhibiting PI3K/AKT/mTOR/p70S6K pathway. *Bioengineered.* (2021) 12:1826–37. doi: 10.1080/21655979.2021.1925008

18. Moon C, Krawczyk M, Ahn D, Ahmet I, Paik D, Lakatta EG, et al. Erythropoietin reduces myocardial infarction and left ventricular functional decline after coronary artery ligation in rats. *Proc Natl Acad Sci.* (2003) 100:11612–7. doi: 10.1073/pnas.1930406100

19. Chen R, Chen W, Huang X, Rui Q. Tanshinone IIA attenuates heart failure *via* inhibiting oxidative stress in myocardial infarction rats. *Mol Med Rep.* (2021) 23:1–10. doi: 10.3892/mmr.2021.12043

20. Huwer H, Rissland J, Vollmar B, Nikoloudakis N, Welter C, Menger MD, et al. Angiogenesis and microvascularization after cryothermia-induced myocardial infarction: a quantitative fluorescence microscopic study in rats. *Basic Res Cardiol.* (1999) 94:85–93.

21. Najafi M. Effects of postconditioning, preconditioning and perfusion of L-carnitine during whole period of ischemia/reperfusion on cardiac hemodynamic functions and myocardial infarction size in isolated rat heart. *Iran J Basic Med Sci.* (2013) 16:648.

22. Ma N, Bai J, Zhang W, Luo H, Zhang X, Liu D, et al. Trimetazidine protects against cardiac ischemia/reperfusion injury *via* effects on cardiac miRNA-21 expression, Akt and the Bcl-2/Bax pathway. *Mol Med Rep.* (2016) 14:4216–22. doi: 10.3892/mmr.2016.5773

23. Bakhta O, Blanchard S, Guihot A-L, Tamareille S, Mirebeau-Prunier D, Jeannin P, et al. Cardioprotective role of colchicine against inflammatory injury in a rat model of acute myocardial infarction. *J Cardiovasc Pharmacol Ther.* (2018) 23:446–55. doi: 10.1177/1074248418763611

24. Liu Q, Hu H, Hu T, Han T, Wang A, Huang L, et al. STVNa attenuates right ventricle hypertrophy and pulmonary artery remodeling in rats induced by transverse aortic constriction. *Biomed Pharmacother.* (2018) 101:371–8. doi: 10.1016/j.biopha.2018.02.078

25. Ke Q, Liu F, Tang Y, Chen J, Hu H, Sun X, et al. The protective effect of isosteviol sodium on cardiac function and myocardial remodelling in transverse aortic constriction rat. *J Cell Mol Med.* (2021) 25:1166–77. doi: 10.1111/jcmm.16182

26. Droogmans S, Roosens B, Cosyns B, Hernot S, Weytjens C, Degaillier C, et al. Echocardiographic and histological assessment of age-related valvular changes in normal rats. *Ultrasound Med Biol.* (2009) 35:558–65. doi: 10.1016/j.ultrasmedbio.2008.10.006

27. Rafiq K, Noma T, Fujisawa Y, Ishihara Y, Arai Y, Nabi AHMN, et al. Renal sympathetic denervation suppresses de novo podocyte injury and albuminuria in rats with aortic regurgitation. *Circulation.* (2012) 125:1402–13. doi: 10.1161/CIRCULATIONAHA.111.064097

28. Faber MJ, Dalinghaus M, Lankhuizen IM, Steendijk P, Hop WC, Schoemaker RG, et al. Right and left ventricular function after chronic pulmonary artery banding in rats assessed with biventricular pressure-volume loops. *Am J Physiol Heart Circul Physiol.* (2006) 291:H1580–6. doi: 10.1152/ajpheart.00286.2006

29. Akazawa Y, Okumura K, Ishii R, Slorach C, Hui W, Ide H, et al. Pulmonary artery banding is a relevant model to study the right ventricular remodeling and dysfunction that occurs in pulmonary arterial hypertension. *J Appl Physiol.* (2020) 129:238–46. doi: 10.1152/japplphysiol.00148.2020

30. Song J, Shen S, Wei Y, Li W, Wang N. Hemodynamic characteristics of the right ventricle following gradient pulmonary artery banding in rats. *World Acad Sci J.* (2021) 3:1–8. doi: 10.3892/wasj.2021.125

31. Pan LC, Wilson DW, Segall HJ. Strain differences in the response of Fischer 344 and Sprague–Dawley rats to monocrotaline induced pulmonary vascular disease. *Toxicology.* (1993) 79:21–35.

32. Aimoto M, Yagi K, Ezawa A, Tsuneoka Y, Kumada K, Hasegawa T, et al. Chronic volume overload caused by abdominal aorto-venocaval shunt provides arrhythmogenic substrates in the rat atrium. *Biol Pharm Bull.* (2022) 45:635–42. doi: 10.1248/bpb.b22-00031

33. Brower GL. *Chronic Volume Overload: Contribution of Ventricular Remodeling to the Pathogenesis of Heart Failure in Rats*. Auburn: Auburn University (1998).

34. Bartosiewicz J, Kaminski T, Pawlak K, Karbowska M, Tankiewicz-Kwedlo A, Pawlak D. The activation of the kynurenine pathway in a rat model with renovascular hypertension. *Exp Biol Med.* (2017) 242:750–61. doi: 10.1177/1535370217693114

35. Zhuang Y, Sun L, Zhang Y, Liu G. Antihypertensive effect of long-term oral administration of jellyfish (*Rhopilema esculentum*) collagen peptides on renovascular hypertension. *Mar Drugs.* (2012) 10:417–26. doi: 10.3390/md10020417

36. Castoldi G, di Gioia CRT, Travaglini C, Busca G, Redaelli S, Bombardi C, et al. Angiotensin II increases tissue-specific inhibitor of metalloproteinase-2 expression in rat aortic smooth muscle cells *in vivo*: evidence of a pressure-independent effect. *Clin Exp Pharmacol Physiol.* (2007) 34:205–9. doi: 10.1111/j.1440-1681.2007.04573.x

37. Fu Y, Wang S, Cui Q. Mechanism of atorvastatin in improving cardiac function in a rat model of myocardial infarction. *Indian J Pharm Sci.* (2020) 14:38–44. doi: 10.36468/pharmaceutical-sciences.spl.121

38. Jiang J, Gu X, Wang H, Ding S. Resveratrol improves cardiac function and left ventricular fibrosis after myocardial infarction in rats by inhibiting NLRP3 inflammasome activity and the TGF-β1/SMAD2 signaling pathway. *PeerJ.* (2021) 9:e11501. doi: 10.7717/peerj.11501

39. Zhao T, Chen S, Wang B, Cai D. L-Carnitine reduces myocardial oxidative stress and alleviates myocardial ischemia-reperfusion injury by activating nuclear transcription-related factor 2 (Nrf2)/Heme Oxygenase-1 (HO-1) signaling pathway. *Med Sci Monit.* (2020) 26:e923251–1. doi: 10.12659/MSM.923251

40. Chen C, Hu L-X, Dong T, Wang G-Q, Wang L-H, Zhou X-P, et al. Apoptosis and autophagy contribute to gender difference in cardiac ischemia–reperfusion induced injury in rats. *Life Sci.* (2013) 93:265–70. doi: 10.1016/j.lfs.2013.06.019

41. Zhang Y-J, Zhang X-L, Li M-H, Iqbal J, Bourantas C, Li J-J, et al. The ginsenoside Rg1 prevents transverse aortic constriction–induced left ventricular hypertrophy and cardiac dysfunction by inhibiting fibrosis and enhancing angiogenesis. *J Cardiovasc Pharmacol.* (2013) 62:50–7. doi: 10.1097/FJC.0b013e31828f8d45

42. Chen Y, Li Y, Guo L, Chen W, Zhao M, Gao Y, et al. Effects of wenxin keli on the action potential and L-type calcium current in rats with transverse aortic constriction-induced heart failure. *Evid Based Compl Alternat Med.* (2013) 2013:1447. doi: 10.1155/2013/572078

43. Li L, Zhang J, Wang R, Li J, Gu Y. Establishment and evaluation of a reversible two-kidney, one-clip renovascular hypertensive rat model. *Exp Ther Med.* (2017) 13:3291–6. doi: 10.3892/etm.2017.4386

44. Sugiyama A, Ito R, Okada M, Yamawaki H. Long-term administration of recombinant canstatin prevents adverse cardiac remodeling after myocardial infarction. *Sci Rep.* (2020) 10:1–11. doi: 10.1038/s41598-020-69736-y

45. Songstad NT, Johansen D, How O-J, Kaaresen PI, Ytrehus K, Acharya G. Effect of transverse aortic constriction on cardiac structure, function and gene expression in pregnant rats. *PLoS ONE.* (2014) 9:e89559. doi: 10.1371/journal.pone.0089559

46. Cao X, Aimoto M, Nagasawa Y, Zhang H-X, Zhang C-S, Takahara A. Electrophysiological response to acehytisine was modulated by aldosterone in rats with aorto-venocaval shunts. *Biol Pharm Bull.* (2021) 14:b20–00974. doi: 10.1248/bpb.b20-00974

47. El Oumeiri B, van de Borne P, Hubesch G, Herpain A, Annoni F, Jespers P, et al. The myosin activator omecamtiv mecarbil improves wall stress in a rat model of chronic aortic regurgitation. *Physiol Rep.* (2021) 9:e14988. doi: 10.14814/phy2.14988

48. Schou UK, Peters CD, Kim SW, Frøkiær J, Nielsen S. Characterization of a rat model of right-sided heart failure induced by pulmonary trunk banding. *J Exp Anim Sci.* (2007) 43:237–54. doi: 10.1016/j.jeas.2006.10.004

49. Samsamshariat SA, Samsamshariat ZA, Movahed M-R. A novel method for safe and accurate left anterior descending coronary artery ligation for research in rats. *Cardiovasc Revascul Med.* (2005) 6:121–3. doi: 10.1016/j.carrev.2005.07.001

50. Sakai T, Li R-K, Weisel RD, Mickle DAG, Kim E-J, Tomita S, et al. Autologous heart cell transplantation improves cardiac function after myocardial injury. *Ann Thorac Surg.* (1999) 68:2074–80.

51. Li R-K, Mickle DAG, Weisel RD, Rao V, Jia Z-Q. Optimal time for cardiomyocyte transplantation to maximize myocardial function after left ventricular injury. *Ann Thorac Surg.* (2001) 72:1957–63. doi: 10.1016/S0003-4975(01)03216-7

52. Ciulla MM, Paliotti R, Ferrero S, Braidotti P, Esposito A, Gianelli U, et al. Left ventricular remodeling after experimental myocardial cryoinjury in rats. *J Surg Res.* (2004) 116:91–7. doi: 10.1016/j.jss.2003.08.238

53. Oliveira-Sales EB, Colombari DSA, Davisson RL, Kasparov S, Hirata AE, Campos RR, et al. Kidney-induced hypertension depends on superoxide signaling in the rostral ventrolateral medulla. *Hypertension.* (2010) 56:290–6. doi: 10.1161/HYPERTENSIONAHA.110.150425

54. Junhong W, Jing Y, Jizheng M, Shushu Z, Xiangjian C, Hengfang W, et al. Proteomic analysis of left ventricular diastolic dysfunction hearts in renovascular hypertensive rats. *Int J Cardiol.* (2008) 127:198–207. doi: 10.1016/j.ijcard.2007.07.003

55. Lee T-M, Lin M-S, Tsai C-H, Chang N-C. Effect of pravastatin on left ventricular mass in the two-kidney, one-clip hypertensive rats. *Am J Physiol Heart Circul Physiol.* (2006) 291:H2705–13. doi: 10.1152/ajpheart.00224.2006

56. Liu Z, Hilbelink DR, Crockett WB, Gerdes AM. Regional changes in hemodynamics and cardiac myocyte size in rats with aortocaval fistulas. 1 Developing and established hypertrophy. *Circ Res.* (1991) 69:52–8.

57. Melenovsky V, Skaroupkova P, Benes J, Torresova V, Kopkan L, Cervenka L. The course of heart failure development and mortality in rats with volume overload due to aorto-caval fistula. *Kidney Blood Press Res.* (2012) 35:167–73. doi: 10.1159/000331562

58. Nath KA, Kanakiriya SKR, Grande JP, Croatt AJ, Katusic ZS. Increased venous proinflammatory gene expression and intimal hyperplasia in an aorto-caval fistula model in the rat. *Am J Pathol.* (2003) 162:2079–90. doi: 10.1016/S0002-9440(10)64339-8

59. Hirata M, Ousaka D, Arai S, Okuyama M, Tarui S, Kobayashi J, et al. Novel model of pulmonary artery banding leading to right heart failure in rats. *Biomed Res Int.* (2015) 2015:1552. doi: 10.1155/2015/753210

60. Farag A, Mandour AS, Yoshida T, Hamabe L, Shimada K, Tanaka R. Novel protocol to establish the myocardial infarction model in rats using a combination of medetomidine-midazolam-butorphanol (MMB) and atipamezole. *Front Vet Sci.* (1880) 9:4836. doi: 10.3389/fvets.2022.1064836

61. Conzen PF, Vollmar B, Habazettl H, Frink EJ, Peter K, Messmer K. Systemic and regional hemodynamics of isoflurane and sevoflurane in rats. *Anesth Analg.* (1992) 74:79–88.

62. Ruxanda F, Gal AF, Ratiu C, Miclăuş V, Rus V, Oana LI. Comparative immunohistochemical assessment of the effect of repetitive anesthesia with isoflurane and sevoflurane on rat liver. *Rev Bras Anestesiol.* (2016) 66:465–9. doi: 10.1016/j.bjane.2015.02.003

63. Hajighahramani S, Vesal N. Evaluation of several drug combinations for intraperitoneal anaesthesia in adult male rats. *Iran J Vet Res.* (2007) 8:106–15.

64. Eisvand F, Imenshahidi M, Ghasemzadeh Rahbardar M, Tabatabaei Yazdi SA, Rameshrad M, Razavi BM, et al. Cardioprotective effects of alpha-mangostin on doxorubicin-induced cardiotoxicity in rats. *Phytother Res.* (2022) 36:506–24. doi: 10.1002/ptr.7356

65. Garcia Montero A, Burda H, Begall S. Chemical restraint of African mole-rats (*Fukomys* sp.) with a combination of ketamine and xylazine. *Vet Anaesth Analg.* (2015) 42:187–91. doi: 10.1111/vaa.12180

66. Chen H, Xu D, Zhang Y, Yan Y, Liu J, Liu C, et al. Neurons in the locus coeruleus modulate the hedonic effects of sub-anesthetic dose of propofol. *Front Neurosci.* (2021) 15:636901. doi: 10.3389/fnins.2021.636901

67. Kawai S, Takagi Y, Kaneko S, Kurosawa T. Effect of three types of mixed anesthetic agents alternate to ketamine in mice. *Exp Anim.* (2011) 60:481–7. doi: 10.1538/expanim.60.481

68. Eltzschig HK, Eckle T. Ischemia and reperfusion—from mechanism to translation. *Nat Med.* (2011) 17:1391–401. doi: 10.1038/nm.2507

69. Whellan DJ. Heart failure disease management: implementation and outcomes. *Cardiol Rev.* (2005) 13:231–9. doi: 10.1097/01.crd.0000135765.60824.2f

70. Nichols M, Townsend N, Scarborough P, Rayner M. Cardiovascular disease in Europe 2014: epidemiological update. *Eur Heart J.* (2014) 35:2950–9. doi: 10.1093/eurheartj/ehu299

71. Reed GW, Rossi JE, Cannon CP. Acute myocardial infarction. *Lancet.* (2017) 389:197–210. doi: 10.1016/S0140-6736(16)30677-8

72. Abd Halim SAS, Ghafar N, Jubri Z, Das S. Induction of myocardial infarction in experimental animals: a review. *J Clin Diagn Res.* (2018) 12:1–15. doi: 10.7860/JCDR/2018/36997.12221

73. Thygesen K, Alpert JS, White HD, Jaffe AS, Galvani M, Katus HA, et al. Universal definition of myocardial infarction. *Circulation.* (2007) 116:2634–53. doi: 10.1161/CIRCULATIONAHA.107.187397

74. Tallquist MD, Molkentin JD. Redefining the identity of cardiac fibroblasts. *Nat Rev Cardiol.* (2017) 14:484–91. doi: 10.1038/nrcardio.2017.57

75. Azizi Y, Faghihi M, Imani A, Roghani M, Nazari A. Post-infarct treatment with [Pyr1]-apelin-13 reduces myocardial damage through reduction of oxidative injury and nitric oxide enhancement in the rat model of myocardial infarction. *Peptides.* (2013) 46:76–82. doi: 10.1016/j.peptides.2013.05.006

76. Song XJ, Yang CY, Liu B, Wei Q, Korkor MT, Liu JY, et al. Atorvastatin inhibits myocardial cell apoptosis in a rat model with post-myocardial infarction heart failure by downregulating ER stress response. *Int J Med Sci.* (2011) 8:564. doi: 10.7150/ijms.8.564

77. Wang T, Sun S, Wan Z, Weil MH, Tang W. Effects of bone marrow mesenchymal stem cells in a rat model of myocardial infarction. *Resuscitation.* (2012) 83:1391–6. doi: 10.1016/j.resuscitation.2012.02.033

78. Aisa Z, Liao GC, Shen XL, Chen J, Li L, Jiang SB. Effect of autophagy on myocardial infarction and its mechanism. *Eur Rev Med Pharmacol Sci.* (2017) 21:3705–13.

79. Salimova E, Nowak KJ, Estrada AC, Furtado MB, McNamara E, Nguyen Q, et al. Variable outcomes of human heart attack recapitulated in genetically diverse mice. *NPJ Regen Med.* (2019) 4:1–15. doi: 10.1038/s41536-019-0067-6

80. Wang J, Bo H, Meng X, Wu Y, Bao Y, Li Y, et al. simple and fast experimental model of myocardial infarction in the mouse. *Tex Heart Inst J.* (2006) 33:290.

81. Ye J, Yang L, Sethi R, Copps J, Ramjiawan B, Summers R, et al. new technique of coronary artery ligation: experimental myocardial infarction in rats *in vivo* with reduced mortality. *Mol Cell Biochem.* (1997) 176:227–33.

82. Hood WB, McCarthy B, Lown B. Myocardial infarction following coronary ligation in dogs: hemodynamic effects of isoproterenol and acetylstrophanthidin. *Circ Res.* (1967) 21:191–200.

83. Klocke R, Tian W, Kuhlmann MT, Nikol S. Surgical animal models of heart failure related to coronary heart disease. *Cardiovasc Res.* (2007) 74:29–38. doi: 10.1016/j.cardiores.2006.11.026

84. Reichert K, Colantuono B, McCormack I, Rodrigues F, Pavlov V, Abid MR. Murine left anterior descending (LAD) coronary artery ligation: an improved and simplified model for myocardial infarction. *JoVE.* (2017) 122:e55353. doi: 10.3791/55353-v

85. Gao X-M, Dart AM, Dewar E, Jennings G, Du X-J. Serial echocardiographic assessment of left ventricular dimensions and function after myocardial infarction in mice. *Cardiovasc Res.* (2000) 45:330–8. doi: 10.1016/S0008-6363(99)00274-6

86. Degabriele NM, Griesenbach U, Sato K, Post MJ, Zhu J, Williams J, et al. Critical appraisal of the mouse model of myocardial infarction. *Exp Physiol.* (2004) 89:497–505. doi: 10.1113/expphysiol.2004.027276

87. Pfeffer MA, Braunwald E. Ventricular remodeling after myocardial infarction. Experimental observations and clinical implications. *Circulation.* (1990) 81:1161–72.

88. Fishbein MC, Maclean D, Maroko PR. Experimental myocardial infarction in the rat: qualitative and quantitative changes during pathologic evolution. *Am J Pathol.* (1978) 90:57.

89. Chi N-H, Yang M-C, Chung T-W, Chen J-Y, Chou N-K, Wang S-S. Cardiac repair achieved by bone marrow mesenchymal stem cells/silk fibroin/hyaluronic acid patches in a rat of myocardial infarction model. *Biomaterials.* (2012) 33:5541–51. doi: 10.1016/j.biomaterials.2012.04.030

90. Lee EJ, Kim DE, Azeloglu EU, Costa KD. Engineered cardiac organoid chambers: toward a functional biological model ventricle. *Tissue Eng A.* (2008) 14:215–25. doi: 10.1089/tea.2007.0351

91. Chi N-H, Yang M-C, Chung T-W, Chou N-K, Wang S-S. Cardiac repair using chitosan-hyaluronan/silk fibroin patches in a rat heart model with myocardial infarction. *Carbohydr Polym.* (2013) 92:591–7. doi: 10.1016/j.carbpol.2012.09.012

92. Etzion S, Battler A, Barbash IM, Cagnano E, Zarin P, Granot Y, et al. Influence of embryonic cardiomyocyte transplantation on the progression of heart failure in a rat model of extensive myocardial infarction. *J Mol Cell Cardiol.* (2001) 33:1321–30. doi: 10.1006/jmcc.2000.1391

93. van den Bos EJ, Mees BME, de Waard MC, de Crom R, Duncker DJ. A novel model of cryoinjury-induced myocardial infarction in the mouse: a comparison with coronary artery ligation. *Am J Physiol Heart Circul Physiol.* (2005) 289:H1291–300. doi: 10.1152/ajpheart.00111.2005

94. Murry CE, Wiseman RW, Schwartz SM, Hauschka SD. Skeletal myoblast transplantation for repair of myocardial necrosis. *J Clin Invest.* (1996) 98:2512–23.

95. de Villiers C, Riley PR. Mouse models of myocardial infarction: comparing permanent ligation and ischaemia-reperfusion. *Dis Model Mech.* (2020) 13:dmm046565. doi: 10.1242/dmm.046565

96. Matboli M, Hasanin AH, Hamady S, Khairy E, Mohamed RH, Aboul-Ela YM, et al. Anti-inflammatory effect of trans-anethol in a rat model of myocardial ischemia-reperfusion injury. *Biomed Pharmacother.* (2022) 150:113070. doi: 10.1016/j.biopha.2022.113070

97. Mokhtari B, Badalzadeh R, Aboutaleb N. Modulation of autophagy as the target of mesenchymal stem cells-derived conditioned medium in rat model of myocardial ischemia/reperfusion injury. *Mol Biol Rep.* (2021) 48:3337–48. doi: 10.1007/s11033-021-06359-0

98. Bolli R, Patel BS, Jeroudi MO, Lai EK, McCay PB. Demonstration of free radical generation in. *J Clin Invest.* (1988) 82:476–85.

99. Kawaguchi M, Takahashi M, Hata T, Kashima Y, Usui F, Morimoto H, et al. Inflammasome activation of cardiac fibroblasts is essential for myocardial ischemia/reperfusion injury. *Circulation.* (2011) 123:594–604. doi: 10.1161/CIRCULATIONAHA.110.982777

100. Gao E, Lei YH, Shang X, Huang ZM, Zuo L, Boucher M, et al. A novel and efficient model of coronary artery ligation and myocardial infarction in the mouse. *Circ Res.* (2010) 107:1445–53. doi: 10.1161/CIRCRESAHA.110.223925

101. de Celle T, Cleutjens JP, Blankesteijn WM, Debets JJ, Smits JF, Janssen BJ. Long-term structural and functional consequences of cardiac ischaemia–reperfusion injury *in vivo* in mice. *Exp Physiol.* (2004) 89:605–15. doi: 10.1113/expphysiol.2004.027649

102. Sodha NR, Clements RT, Feng J, Liu Y, Bianchi C, Horvath EM, et al. Hydrogen sulfide therapy attenuates the inflammatory response in a porcine model of myocardial ischemia/reperfusion injury. *J Thorac Cardiovasc Surg.* (2009) 138:977–84. doi: 10.1016/j.jtcvs.2008.08.074

103. Chen A, Li W, Chen X, Shen Y, Dai W, Dong Q, et al. Trimetazidine attenuates pressure overload-induced early cardiac energy dysfunction *via* regulation of neuropeptide Y system in a rat model of abdominal aortic constriction. *BMC Cardiovasc Disord.* (2016) 16:1–10. doi: 10.1186/s12872-016-0399-8

104. Bleske BE, Hwang HS, Zineh I, Ghannam MG, Boluyt MO. Evaluation of immunomodulatory biomarkers in a pressure overload model of heart failure. *Pharmacother J Hum Pharmacol Drug Therapy.* (2007) 27:504–9. doi: 10.1592/phco.27.4.504

105. Monnet E, Chachques JC. Animal models of heart failure: what is new? *Ann Thorac Surg.* (2005) 79:1445–53. doi: 10.1016/j.athoracsur.2004.04.002

106. Cantor EJF, Babick AP, Vasanji Z, Dhalla NS, Netticadan T. A comparative serial echocardiographic analysis of cardiac structure and function in rats subjected to pressure or volume overload. *J Mol Cell Cardiol.* (2005) 38:777–86. doi: 10.1016/j.yjmcc.2005.02.012

107. Bramlage P, Pittrow D, Wittchen H-U, Kirch W, Boehler S, Lehnert H, et al. Hypertension in overweight and obese primary care patients is highly prevalent and poorly controlled. *Am J Hypertens.* (2004) 17:904–10. doi: 10.1016/j.amjhyper.2004.05.017

108. Feldman AM, Weinberg EO, Ray PE, Lorell BH. Selective changes in cardiac gene expression during compensated hypertrophy and the transition to cardiac decompensation in rats with chronic aortic banding. *Circ Res.* (1993) 73:184–92.

109. Weinberg EO, Schoen FJ, George D, Kagaya Y, Douglas PS, Litwin SE, et al. Angiotensin-converting enzyme inhibition prolongs survival and modifies the transition to heart failure in rats with pressure overload hypertrophy due to ascending aortic stenosis. *Circulation.* (1994) 90:1410–22.

110. Xiao C-Y, Chen M, Zsengellér Z, Li H, Kiss L, Kollai M, et al. Poly (ADP-Ribose) polymerase promotes cardiac remodeling, contractile failure, and translocation of apoptosis-inducing factor in a murine experimental model of aortic banding and heart failure. *J Pharmacol Exp Therap.* (2005) 312:891–8. doi: 10.1124/jpet.104.077164

111. Litwin SE, Katz SE, Weinberg EO, Lorell BH, Aurigemma GP, Douglas PS. Serial echocardiographic-Doppler assessment of left ventricular geometry and function in rats with pressure-overload hypertrophy: chronic angiotensin-converting enzyme inhibition attenuates the transition to heart failure. *Circulation.* (1995) 91:2642–54.

112. Sankaran SK. Two different rat models for cardiac hypertrophy by constriction of ascending and abdominal aorta. *J Lab Anim Sci.* (2014) 54:20–4.

113. Breckenridge R. Heart failure and mouse models. *Dis Model Mech.* (2010) 3:138–43. doi: 10.1242/dmm.005017

114. Ku H-C, Lee S-Y, Wu Y-KA, Yang K-C, Su M-J. A model of cardiac remodeling through constriction of the abdominal aorta in rats. *JoVE.* (2016) 118:e54818. doi: 10.3791/54818-v

115. Pfeiffer J, Lorenz K. Murine models for heart failure: their creation and applicability to human still require critical and careful considerations. *Int J Cardiol Heart Vasc.* (2021) 34:868. doi: 10.1016/j.ijcha.2021.100781

116. Choopani S, Nematbakhsh M. Renal vascular response to angiotensin II administration in two kidneys-one clip hypertensive rats treated with high dose of estradiol: the role of Mas receptor. *Int J Vasc Med.* (2021) 2021:3485. doi: 10.1155/2021/6643485

117. Almeida A, Lira R, Oliveira M, Martins M, Azevedo Y, Silva KR, et al. Bone marrow-derived mesenchymal stem cells transplantation ameliorates renal injury through anti-fibrotic and anti-inflammatory effects in chronic experimental renovascular disease. *Biomed J.* (2022) 45:629–41. doi: 10.1016/j.bj.2021.07.009

118. Sun Z, Zhang Z. Historic perspectives and recent advances in major animal models of hypertension. *Acta Pharmacol Sin.* (2005) 26:295–301. doi: 10.1111/j.1745-7254.2005.00054.x

119. Weber KT, Janicki JS, Pick R, Capasso J, Anversa P. Myocardial fibrosis and pathologic hypertrophy in the rat with renovascular hypertension. *Am J Cardiol.* (1990) 65:1–7.

120. Ma D, Mandour AS, Elfadadny A, Hendawy H, Yoshida T, El-Husseiny HM, et al. Changes in cardiac function during the development of uremic cardiomyopathy and the effect of salvianolic acid B administration in a rat model. *Front Vet Sci.* (2022) 9:4798. doi: 10.3389/fvets.2022.905759

121. Neto-Neves EM, Pinheiro LC, Nogueira RC, Portella RL, Batista RI, Tanus-Santos JE. Sodium nitrite improves hypertension-induced myocardial dysfunction by mechanisms involving cardiac S-nitrosylation. *J Mol Cell Cardiol.* (2019) 134:40–50. doi: 10.1016/j.yjmcc.2019.06.012

122. Dussaule JC, Michel JB, Auzan C, Schwartz K, Corvol P, Menard J. Effect of antihypertensive treatment on the left ventricular isomyosin profile in one-clip, two kidney hypertensive rats. *J Pharmacol Exp Therap.* (1986) 236:512–8.

123. Amann K, Wiest G, Zimmer G, Gretz N, Ritz E, Mall G. Reduced capillary density in the myocardium of uremic rats—a stereological study. *Kidney Int.* (1992) 42:1079–85.

124. Doggrell SA, Brown L. Rat models of hypertension, cardiac hypertrophy and failure. *Cardiovasc Res.* (1998) 39:89–105.

125. Flaim SF, Minteer WJ, Nellis SH, Clark DP. Chronic arteriovenous shunt: evaluation of a model for heart failure in rat. *Am J Physiol Heart Circul Physiol.* (1979) 236:H698–704.

126. Toischer K, Rokita AG, Unsöld B, Zhu W, Kararigas G, Sossalla S, et al. Differential cardiac remodeling in preload vs. afterload. *Circulation.* (2010) 122:993–1003. doi: 10.1161/CIRCULATIONAHA.110.943431

127. Ruzicka M, Yuan B, Leenen FH. Effects of enalapril vs. losartan on regression of volume overload-induced cardiac hypertrophy in rats. *Circulation.* (1994) 90:484–91.

128. Ozek C, Zhang F, Lineaweaver WC, Chin BT, Eiman T, Newlin L, et al. new heart failure model in rat by an end-to-side femoral vessel anastomosis. *Cardiovasc Res.* (1998) 37:236–8.

129. Brower GL, Levick SP, Janicki JS. Inhibition of matrix metalloproteinase activity by ACE inhibitors prevents left ventricular remodeling in a rat model of heart failure. *Am J Physiol Heart Circul Physiol.* (2007) 292:H3057–64. doi: 10.1152/ajpheart.00447.2006

130. Abassi Z, Goltsman I, Karram T, Winaver J, Hoffman A. Aortocaval fistula in rat: a unique model of volume-overload congestive heart failure and cardiac hypertrophy. *J Biomed Biotechnol.* (2011) 2011:9497. doi: 10.1155/2011/729497

131. Garcia R, Diebold S. Simple, rapid, and effective method of producing aortocaval shunts in the rat. *Cardiovasc Res.* (1990) 24:430–2.

132. Maslov MY, Foianini S, Mayer D, Orlov M, Lovich MA. Interaction between sacubitril and valsartan in preventing heart failure induced by aortic valve insufficiency in rats. *J Card Fail.* (2019) 25:921–31. doi: 10.1016/j.cardfail.2019.09.008

133. Sugimura Y, Schmidt AK, Lichtenberg A, Assmann A, Akhyari P. A rat model for the *in vivo* assessment of biological and tissue-engineered valvular and vascular grafts. *Tissue Eng C Methods.* (2017) 23:982–94. doi: 10.1089/ten.tec.2017.0215

134. Mann DL, Barger PM, Burkhoff D. Myocardial recovery and the failing heart: myth, magic, or molecular target? *J Am Coll Cardiol.* (2012) 60:2465–72. doi: 10.1016/j.jacc.2012.06.062

135. Singh JP, Evans JC, Levy D, Larson MG, Freed LA, Fuller DL, et al. Prevalence and clinical determinants of mitral, tricuspid, and aortic regurgitation (the Framingham Heart Study). *Am J Cardiol.* (1999) 83:897–902.

136. Bonow RO. Aortic regurgitation. *Curr Treat Options Cardiovasc Med.* (2000) 2:125–32. doi: 10.1007/s11936-000-0005-2

137. Borer JS, Bonow RO. Contemporary approach to aortic and mitral regurgitation. *Circulation.* (2003) 108:2432–8. doi: 10.1161/01.CIR.0000096400.00562.A3

138. Plante E, Couet J, Gaudreau M, Dumas MP, Drolet MC, Arsenault M. Left ventricular response to sustained volume overload from chronic aortic valve regurgitation in rats. *J Card Fail.* (2003) 9:128–40. doi: 10.1054/jcaf.2003.17

139. Tani LY, Minich LL, Day RW, Orsmond GS, Shaddy RE. Doppler evaluation of aortic regurgitation in children. *Am J Cardiol.* (1997) 80:927–31.

140. Munakata H, Assmann A, Poudel-Bochmann B, Horstkötter K, Kamiya H, Okita Y, et al. Aortic conduit valve model with controlled moderate aortic regurgitation in rats: a technical modification to improve short-and long-term outcome and to increase the functional results. *Circul J.* (2013) 77:2295–302. doi: 10.1253/circj.CJ-12-1439

141. Toshihiko U, Tamahito Y, Hiroyuki M, Yujiro H, Mitsuyoshi N. A simple method for producing graded aortic insufficiencies in rats and subsequent development of cardiac hypertrophy. *J Pharmacol Methods.* (1989) 22:249–57.

142. Loisel F, Provost B, Haddad F, Guihaire J, Amsallem M, Vrtovec B, et al. Stem cell therapy targeting the right ventricle in pulmonary arterial hypertension: is it a potential avenue of therapy? *Pulm Circ.* (2018) 8:2045893218755979. doi: 10.1177/2045893218755979

143. Benza RL, Miller DP, Barst RJ, Badesch DB, Frost AE, McGoon MD. An evaluation of long-term survival from time of diagnosis in pulmonary arterial hypertension from the REVEAL registry. *Chest.* (2012) 142:448–56. doi: 10.1378/chest.11-1460

144. Voelkel NF, Quaife RA, Leinwand LA, Barst RJ, McGoon MD, Meldrum DR, et al. Right ventricular function and failure: report of a National Heart, Lung, and Blood

Institute working group on cellular and molecular mechanisms of right heart failure. *Circulation.* (2006) 114:1883–91. doi: 10.1161/CIRCULATIONAHA.106.632208

145. Leeuwenburgh BPJ, Helbing WA, Steendijk P, Schoof PH, Baan J. Biventricular systolic function in young lambs subject to chronic systemic right ventricular pressure overload. *Am J Physiol Heart Circul Physiol.* (2001) 281:H2697–704. doi: 10.1152/ajpheart.2001.281.6.H2697

146. Breeman KTN, Dufva M, Ploegstra MJ, Kheyfets V, Willems TP, Wigger J, et al. Right ventricular-vascular coupling ratio in pediatric pulmonary arterial hypertension: a comparison between cardiac magnetic resonance and right heart catheterization measurements. *Int J Cardiol.* (2019) 293:211–7. doi: 10.1016/j.ijcard.2019.05.021

147. Borgdorff MAJ, Koop AMC, Bloks VW, Dickinson MG, Steendijk P, Sillje HHW, et al. Clinical symptoms of right ventricular failure in experimental chronic pressure load are associated with progressive diastolic dysfunction. *J Mol Cell Cardiol.* (2015) 79:244–53. doi: 10.1016/j.yjmcc.2014.11.024

148. Yoshiyuki R, Tanaka R, Fukushima R, Machida N. Preventive effect of sildenafil on right ventricular function in rats with monocrotaline-induced pulmonary arterial hypertension. *Exp Anim.* (2016) 65:215–22. doi: 10.1538/expanim.15-0070

149. Kullo IJ, Jouni H, Austin EE, Brown S-A, Kruisselbrink TM, Isseh IN, et al. Incorporating a genetic risk score into coronary heart disease risk estimates: effect on low-density lipoprotein cholesterol levels (the MI-GENES Clinical Trial). *Circulation.* (2016) 133:1181–8. doi: 10.1161/CIRCULATIONAHA.115.020109

150. Yoshiyuki R, Fukushima R, Tanaka R, Machida N. Comparison of preventive effect of sildenafil and therapeutic effect of sildenafil treatment in rats with monocrotaline-induced pulmonary arterial hypertension. *J Vet Med Sci.* (2016) 78:15–544. doi: 10.1292/jvms.15-0544

151. Yoshiyuki R, Nakata TM, Fukayama T, Hamabe L, Huai-Che H, Suzuki S, et al. Pimobendan improves right ventricular myocardial contraction and attenuates pulmonary arterial hypertension in rats with monocrotaline-induced pulmonary arterial hypertension. *J Med Ultrason.* (2014) 41:173–80. doi: 10.1007/s10396-013-0488-6

152. Shimamura S, Endo H, Kutsuna H, Kobayashi M, Hirao H, Shimizu M, et al. Effect of intermittent administration of sustained release isosorbide dinitrate (sr-ISDN) in rats with pressure-overload heart. *J Vet Med Sci.* (2006) 68:213–7. doi: 10.1292/jvms.68.213

153. Rai N, Veeroju S, Schymura Y, Janssen W, Wietelmann A, Kojonazarov B, et al. Effect of riociguat and sildenafil on right heart remodeling and function in pressure overload induced model of pulmonary arterial banding. *Biomed Res Int.* (2018) 2018:3584. doi: 10.1155/2018/3293584

154. Andersen S, Schultz JG, Holmboe S, Axelsen JB, Hansen MS, Lyhne MD, et al. A pulmonary trunk banding model of pressure overload induced right ventricular hypertrophy and failure. *JoVE.* (2018) 119:e58050. doi: 10.3791/58050-v

155. Mendes-Ferreira P, Santos-Ribeiro D, Adão R, Maia-Rocha C, Mendes-Ferreira M, Sousa-Mendes C, et al. Distinct right ventricle remodeling in response to pressure overload in the rat. *Am J Physiol Heart Circul Physiol.* (2016) 311:H85–95. doi: 10.1152/ajpheart.00089.2016

156. Wang Q, Chen K, Lin H, He M, Huang X, Zhu H, et al. Induction of right ventricular failure by pulmonary artery constriction and evaluation of right ventricular function in mice. *JoVE.* (2019) 147:e59431. doi: 10.3791/59431

157. Janssen W, Schymura Y, Novoyatleva T, Kojonazarov B, Boehm M, Wietelmann A, et al. 5-HT2B receptor antagonists inhibit fibrosis and protect from RV heart failure. *Biomed Res Int.* (2015) 2015:9487. doi: 10.1155/2015/438403

158. Andersen A, van der Feen DE, Andersen S, Schultz JG, Hansmann G, Bogaard HJ. Animal models of right heart failure. *Cardiovasc Diagn Ther.* (2020) 10:1561. doi: 10.21037/cdt-20-400

159. Andersen A, Povlsen JA, Johnsen J, Jespersen NR, Bøtker HE, Nielsen-Kudsk JE. sGC–cGMP–PKG pathway stimulation protects the healthy but not the failing right ventricle of rats against ischemia and reperfusion injury. *Int J Cardiol.* (2016) 223:674–80. doi: 10.1016/j.ijcard.2016.08.264

160. Andersen S, Schultz JG, Andersen A, Ringgaard S, Nielsen JM, Holmboe S, et al. Effects of bisoprolol and losartan treatment in the hypertrophic and failing right heart. *J Card Fail.* (2014) 20:864–73. doi: 10.1016/j.cardfail.2014.08.003

161. Hoashi T, Matsumiya G, Miyagawa S, Ichikawa H, Ueno T, Ono M, et al. Skeletal myoblast sheet transplantation improves the diastolic function of a pressure-overloaded right heart. *J Thorac Cardiovasc Surg.* (2009) 138:460–7. doi: 10.1016/j.jtcvs.2009.02.018

162. Braun MU, Szalai P, Strasser RH, Borst MM. Right ventricular hypertrophy and apoptosis after pulmonary artery banding: regulation of PKC isozymes. *Cardiovasc Res.* (2003) 59:658–67. doi: 10.1016/S0008-6363(03)00470-X

163. Bogaard HJ, Natarajan R, Henderson SC, Long CS, Kraskauskas D, Smithson L, et al. Chronic pulmonary artery pressure elevation is insufficient to explain right heart failure. *Circulation.* (2009) 120:1951–60. doi: 10.1161/CIRCULATIONAHA.109.883843

frontiers | Frontiers in Veterinary Science

TYPE Case Report
PUBLISHED 05 May 2023
DOI 10.3389/fvets.2023.1154210



OPEN ACCESS

EDITED BY
Ahmed S. Mandour,
Suez Canal University, Egypt

REVIEWED BY
Ahmed Elfadadny,
Tokyo University of Agriculture and Technology, Japan
Sang-Kwon Lee,
Kyungpook National University, Republic of Korea

*CORRESPONDENCE
Hakyoung Yoon
✉ knighttt7240@gmail.com

†These authors have contributed equally to this work

RECEIVED 30 January 2023
ACCEPTED 13 April 2023
PUBLISHED 05 May 2023

CITATION
Park S-H, Lee J-H, Salas EN, Kim M, Han J-i, Lee K and Yoon H (2023) Case report: Generalized lymphatic anomaly of multiple abdominal organs in a young dog.
*Front. Vet. Sci.* 10:1154210.
doi: 10.3389/fvets.2023.1154210



# Case report: Generalized lymphatic anomaly of multiple abdominal organs in a young dog

So-Hyeon Park[1†], Jung-Ha Lee[2†], Elisa N. Salas[3], Myeongsu Kim[4], Jae-ik Han[4], Kichang Lee[1] and Hakyoung Yoon[1*]

[1]Department of Veterinary Medical Imaging, College of Veterinary Medicine, Jeonbuk National University, Iksan-si, Republic of Korea, [2]V Animal Medical Center, Jeju-si, Jeju-do, Republic of Korea, [3]IDEXX Laboratories, Inc., Westbrook, ME, United States, [4]Laboratory of Wildlife Medicine, College of Veterinary Medicine, Jeonbuk National University, Iksan-si, Republic of Korea

A 9-month-old, female Pomeranian dog presented with vomiting and lethargy. Ultrasonography revealed multilobulated anechoic round shape structures at the ovarian and uterine locations. Through computed tomography scan, an extensive non-contrast multilobulated fluid-filled mass suspected of originating from the walls of the ovary, uterus, urinary bladder and rectum was observed. Ovariohysterectomy and urinary bladder biopsy were performed. Histopathological examination revealed numerous cystic lesions lined by plump cuboidal cells believed to be of epithelial origin. Immunohistochemical staining showed that the cyst-like lesions lining cells were strongly positive for lymphatic vessel endothelial hyaluronan receptor 1. Based on these results, lesions were identified as generalized lymphatic anomaly (GLA), in which lymphangiomas develop in multiple organs. After 6 months follow-up, the size of the cysts remaining in the region of the bladder did not undergo much change. GLA should be included in the differential diagnosis when multiple cystic lesions are interspersed in multiple organs.

KEYWORDS

**lymphangiomatosis, lymphangioma, lymphatic malformation, multi-organs, canine, cystic lesions**

## 1. Introduction

Lymphatic anomaly (lymphangioma, lymphatic malformation, lymphangiomatosis), a rare congenital disorder of the lymphatic system, is considered to arise from a failure of primitive lymphatic systems to adequately separate from or communicate with the venous system (1). These malformations cause dilation and proliferation of lymphatic vessels in animal & human.

Canine lymphatic anomalies have most commonly been reported in the skin, soft tissue, and retroperitoneum (2–7). It is seldom observed in parenchymal organs, and only two cases have been reported in the liver and spleen (8, 9).

In human, according to the International Society for the Study of Vascular Anomalies (ISSVA), Lymphatic anomlies can be divided into cystic lymphatic anomaly and complex lymphatic anomaly, depending on whether they occur in solitary lesions or multiple organs. Cystic lymphatic anomaly mainly occurs in the head, neck and extermities, and is divided into macro and micro depending on the size. Complex anomalies have been reported in <1% of humans and have not yet been reported in animals. It occurs in various organs such as various bones, liver, and spleen. There are three types of complex anomaly, GLA, Gorham-Stout disease (GSD), and Channel type lymphatic anomaly (CCLA), and there is a subtype

of GLA, Kaposiform lymphangiomatosis (KLA). KLA is characterized by being surrounded by Kaposi-form cells, and mainly causes diseases in the chest. GSD is a disease that causes bone destruction and CCLA is a disease known as lymphangiectasia, which occurs when lymphatic vessels are damaged by obstruction of lymphatic vessels. GLA can also occur in bone, but it does not cause destruction (10, 11).

The clinical symptoms and prognosis of lymphatic anomaly varies depending on the locations of the affected organ and sizes of cystic lesions. Leakage of lymph or chyle may be intraperitoneal or intrathoracic, and hypoalbuminemia, hypoproteinemia, and lymphocytopenia may occur due to lymphangiectasia (11).

Lymphatic malformation is characterized by cystic lesions on Ultrasonography (US), Computed tomography (CT), and Magnetic resonance imaging (MRI). The existence and location of the cystic structures can be determined using US, and information about the range of lesions and adhesion of the surrounding tissues can be obtained through CT. In human, when GLA is suspected, MRI is used to identify abdominal and thoracic lesions and to identify mesenteric and retroperitoneal cyst-like lesions. MRI can evaluate soft tissues with good resolution and without radiation exposure. Also, MRI is known to be good for detecting minimal lymphatic lesions, and it is known to show hyper signal intensity in fat-saturated T2-weighted MRI and intense enhancement in gadolinium contrast agent (12–14).

However, immunostaining such as lymphatic vessel endothelial hyaluronan receptor 1 (LYVE-1), podoplanin, and Vascular endothelial growth factor receptor 3 (VEGFR-3) specific to lymphatic vessels is required for diagnosis. In humans, studies on genes related to lymphatic anomaly have been conducted, but no studies have been conducted in dogs yet (15, 16).

This is the first case of a dog with lymphatic anomaly in several parenchymal organs including ovary, uterus, intestine and bladder. Imaging diagnosis and immunohistochemistry was performed, and follow-up was performed 6 months later.

## 2. Case description

A 9-month-old Pomeranian dog presenting with vomiting and lethargy, was admitted to a local animal hospital. No abnormal findings were observed in body temperature, blood pressure, respiration rate, or pulse. Also, No remarkable abnormal findings were observed in the serum biochemistry panel and complete blood count.

Abdominal radiography (1417WGC, Rayence Co., Ltd., Hwaseong-si-, South Korea) was performed. In the lateral view, a tubular structure of soft tissue opacity with a size of 11.17 × 5.92 mm was observed in the ventral aspect of the descending colon in the caudoventral aspects of abdominal cavity at L1 to pelvis level. Therefore, the small intestine was cranially displaced (Figure 1A). In the chest radiography, increased opacity of the cranial lung lobe was observed in the lateral view, but this was considered to be due to summation of the muscles of the forelimb. In the VD view, the opacity of the left cranial lung lobe was increased, but the left deviation of the heart was observed, so atelectasis was considered first.

Abdominal US (ACUSON juniper, Siemens Healthineers, Erlangen, Germany) using 3.6–12.9 MHz linear transducers identified multiloculated anechoic structures with acoustic enhancement at the ovarian and uterine locations (Figure 1B), which was similarly observed near the urinary bladder (UB). Due to the size and range of the cystic lesion, the exact location could not be determined by US. The walls of the cysts were thin (< 1 mm) and of various sizes and shapes with the largest being 2.37 × 2.27 cm. The boundary between the organs and cystic lesions was unclear due to displacement and obscuring by the structures.

CT was performed using a multislice CT scanner (TSX-031A; Toshiba Medical Systems Co., Ltd., Tochigi, Japan). The imaging parameters were as follows: 120 kVp, 200 mAs; matrix size, 512 × 512; rotation time, 0.75 s; and, slice thickness, 1 mm. For CT scans, the dog was induced with propofol (6 mg/kg, IV), and anesthesia was maintained by isoflurane. After obtaining the pre-contrast images, iohexol (750 mg iodine/kg) was manually injected into the cephalic vein. Postcontrast images were obtained after 120 s. Multilobulated structures were observed, starting from the vagina and extending to the uterine cervix and horns. The septa of the cystic structures were connected to the uterine wall, and the margin of the uterus was spiculated (Figures 1D, E). Therefore, the lesions were considered to originate from the uterine wall. In addition, they were observed to be in contact with the ventral aspect of the rectum, caudolateral aspect of the UB, both ovaries, part of the small intestine, and both sides of the anal sac, so the possibility of adhesion as the origin of the cystic structures could not be excluded. The lumens of multiple cystic lesions (up to 3.83 × 2.93 × 5.58 cm [L × H × W]) were observed with fluid attenuation (HU:13), and no significant enhancement was observed, but the walls showed significant enhancement. A multilobulated cystic structure similar to that observed in the uterus was also observed at the location presumed to be the left sublumbar lymph node, which expanded to the left gluteus medius muscle through the pelvic canal (Figure 1C). No bone lesion or ascites was observed around the mass, and no significant enlargement of the surrounding lymph nodes was observed. This mass was supplied with blood by the bilateral ovarian and vaginal arteries. No obvious abnormal findings were observed in the lung parenchyma and bronchus, and neither pleural effusion nor pneumothorax was observed.

Ovariohysterectomy and biopsy of the UB were performed to remove and diagnose the lesions. The dog was induced with propofol (6 mg/kg, IV), and anesthesia was maintained using isoflurane. Multiple cystic lesions originating from the walls of the uterine, ovary, urinary bladder, and intestine were widely observed, and cyst-like lesions and adjacent organs adhered to each other. Therefore, it was difficult to clearly demarcate and remove the lesions. After ventral median celiotomy, the ovarian pedicles and uterine body were clamped and ligated with polydioxanone. As complete resection of the cysts was impossible; debulking was

Abbreviations: GLA, generalized lymphatic anomaly; CLA, complex lymphatic anomaly; US, ultrasonography; CT, computed tomography; LYVE-1, lymphatic vessel endothelial hyaluronan receptor 1; UB, urinary bladder; FFPE, formalin-fixed and paraffin-embedded; GSD, Gorham-Stout disease; CCLA, Channel type lymphatic anomaly; KLA, Kaposiform lymphangiomatosis.

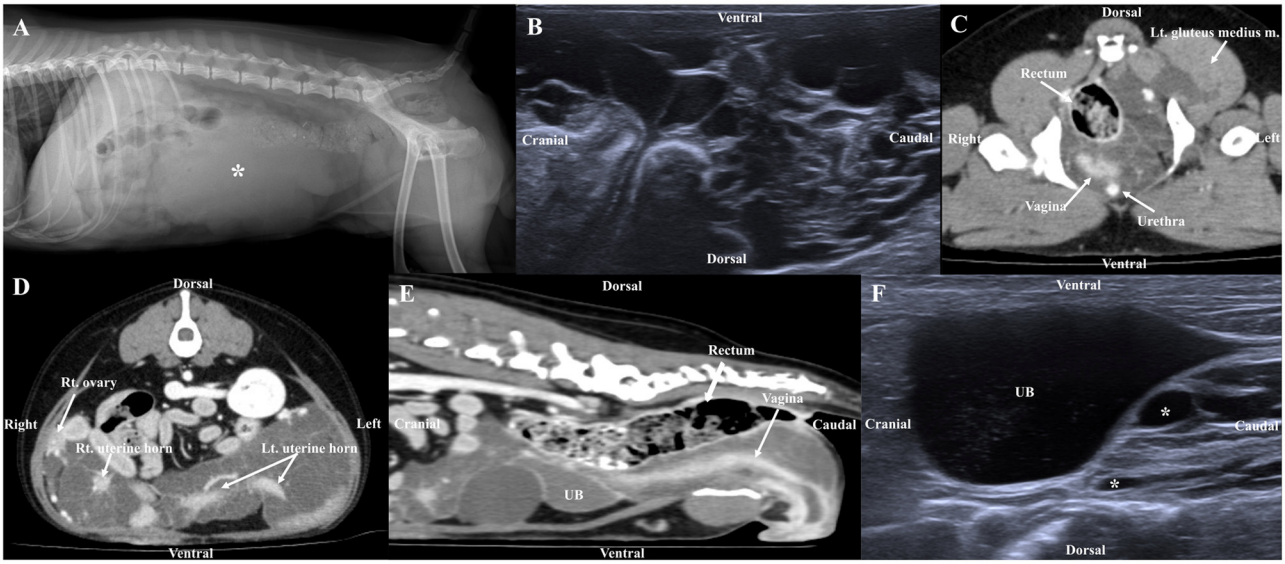


FIGURE 1
Radiographic image **(A)**, ultrasonography **(B, F)**, post-contrast CT **(C, D, E)** in a dog with lymphatic anomaly. **(A)** The tubular structure of soft tissue opacity (asterisk) in the caudoventral abdomen, **(B)** Ultrasonographic image shows multiple anechoic structures in the ovary and uterus, **(C)** Multilobulated cystic lesions originating from the left sublumbar lymph node expand through the pelvic canal to the left gluteus medius muscle, **(D, E)** Multiple cystic lesions were observed extensively in contact with the urinary bladder (UB), ovary, uterine, rectum, making it difficult to determine the origin and **(F)** Ultrasound image 6 months post-surgery, the size of cystic lesions remaining around the bladder was similar to that of 6 months prior.

performed. Tissues of the ovaries, uterine horns, and UB were fixed in 10% neutral-buffered formalin and sent for histological evaluation in a laboratory (IDEXX Laboratories Inc., Seoul, South Korea).

Grossly, multiple pale yellow, clear-to-serous cystic structures were observed in the ovary and uterus (Figure 2A). Histological examination of the three organs confirmed numerous cystic structures lined by spindle to cuboidal cells. The ovary contained cyst-like lesions within the mesovarium and the ovarian parenchyma (Figure 2B). The uterus exhibited cyst-like leisons penetrating the myometrium (Figure 2C). The UB contained cystic structures within its smooth muscle wall (Figure 2D). Immunostaining using LYVE-1 in the ovary, uterus, and bladder tissue was performed to confirm whether it was derived from the lymphatic system. The cystic structures were Pancytokeratin AE1/AE3 negative throughout all the tissue, ruling them out as classically defined cysts: expansile spaces lined by epithelium. Rather, they exhibit intermediate to strong cytoplasmic immunoreactivity for LYVE-1, supporting endothelium lined spaces supportive of GLA (Figures 3A–C). The control tissue showed strong immunoreactivity in the lymphatics, but the arterioles showed no immunoreactivity (Figure 3A). However, intermediate immunoreactivity is also noted within endothelial cells lining blood-filled vascular spaces (Figures 3B, C).

DNA was extracted from the formalin-fixed and paraffin-embedded (FFPE) samples through the MagMAX™ FFPE DNA/RNA Ultra Kit (Thermo Fisher Scientific, Waltham, MA, USA) and QIAamp DNA FFPE Tissue Kit (Qiagen, Hilden, Germany) for Neuroblastoma RAS viral oncogene homolog (NRAS) gene sequencing. The NRAS coding region was amplified twice using forward (TACAAACTG GTGGTGGTTGG) and reverse (TCCAACAGACAGGTTTCACC) primers by HotStarTaq master mix kit (Qiagen, Hilden, Germany).

As a result, the peak size of the our patient was observed to be 44 base pairs both the times, instead of 150 base pairs with NRAS gene in a normal dog.

At the 6-months follow-up, the vomiting had disappeared and no significant change in the size of the cystic lesions remaining in the region of the bladder was seen (Figure 1F).

## 3. Discussion

In human medicine, lymphangiomatosis refers to lymphatic anomaly occuring in multiple organs and is known as CLA. GLA, one of the CLAs, is distinguished from other types like GSD, CCLA in that there are no bone destruction and no leakage of lymph (10, 11). Our patient was considered GLA because lymphatic anomaly occurred in multiple organs and there were no ascites or bone lesions. Since the previously reported canine lymphangiomatosis was a case of multiple cysts in one organ rather than multiple organs (3, 9, 17, 18), the use of the term lymphangiomatosis may cause confusion as to whether it is a single organ or multiple organs. So the authors referred to our case as GLA.

Lymphatic anomalies in humans, most commonly occurs in the neck (75%) and axillary sites (20%) and have rarely been reported in the mediastinum, omentum, mesentery, retroperitoneum, colon, pelvis, and bone. Less than 1% of cases are reported in internal organs, and

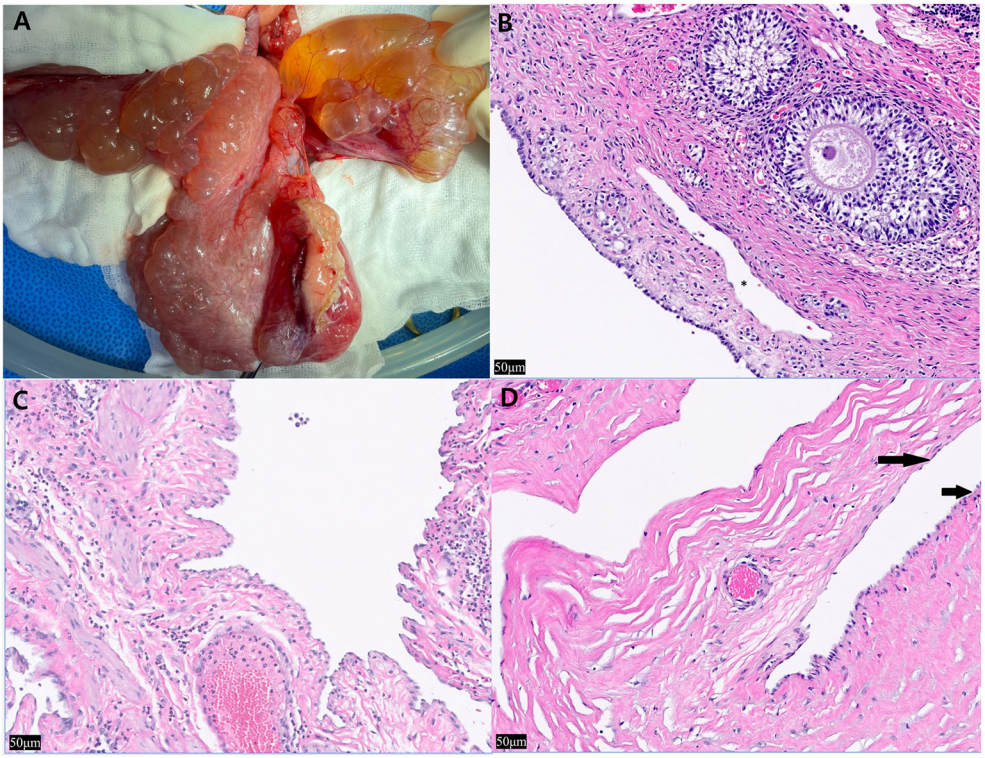


FIGURE 2
Intra-operative photographs of the ovary and uterus and histopathological findings after hematoxylin and eosin staining of the ovary, uterine horn, and urinary bladder. **(A)** The multiple thin-walled cystic structures expand the uterine smooth muscle, ovary and are see on the serosa. Cyst-like lesions and adjacent organs adhered to each other, so it was difficult to clearly demarcate and remove the lesions, **(B)** left ovary, approximately five cyst-like structures are seen peripheral to the ovum (*) (×20), **(C)** left uterine horn, the structures multifocally expand the myometrium. Most were empty and contained intraluminal pale eosinophilic proteinaceous material. Low to moderate numbers of neutrophils are noted bordering the vasculature with no associated necrosis, inflammation, or reactive vessels (×20). **(D)** Within the smooth muscle wall of the urinary bladder, the structures are lined by spindle cells (long arrow) and hypertrophied cuboidal cells (short arrow) (×20).

involvement of three or more intra-abdominal organs is extremely rare in humans (19). Canine lymphatic anomalies have most commonly been reported in the skin, soft tissue, and retroperitoneum (2–6). It is seldom observed in parenchymal organs, and only two cases have been reported in the liver and spleen (8, 9). There have been no reports of urinary bladder, ovary, uterus, or rectum, and no lymphatic anomaly has been reported in more than two parenchymal organs.

Cystic structures are observed in various orgnas on US and CT in our case. In Considering the patient's age, the possibility of neoplastic cyst was considered low. Since the lumen was intact on CT, the possibility of intraluminal lesions was considered low. Considering that the wall of the uterus is irregularly observed in connection with the septa of the cystic lesions, it was considered that the cyst originated from the wall of the organ rather than from the mesentery or peritoneal lesion. Therefore, GLA, adenomyosis and paramesonephric cyst were considered as differential diagnoses, which can't be ditinguished by imaging alone, and immunostaining tests are required. Becase GLA has been reported not only in young human patients, but also in older human patients, care should be taken not to misdiagnose GLA as metastatic cancer when cystic lesions occur in multiple organs (20, 21).

In human, the presence of chylous fluid in cysts with high triglycerides is pathognomonic for lymphangioma, and according to what has been reported so far, it has a common feature that small lymphocytes are mainly seen (22, 23). Therefore, fluid analysis can provide good information for diagnosing GLA. But depending on the location of the lymphatic anomaly, the fluid within the cyst may be clear transudate or chylous (24). Similarly, as a result of fluid analysis in a dog with lymphangioma in a previous report, it was considered as a transudate, and small lymphocytes were mainly observed (7). Fluid collections, whether chylorous or not, are mostly anechoic on ultrasound, and it is difficult to distinguish between simple fluid and chylous even on CT.

Lymphangiography can reveal leakage or obstruction of the lymphatic pathway. If a patient presents with pleural effusion or ascites, lymphangiography may be helpful to identify the lymphatic pathway for diagnosis and treatment planning (25). However, this is a major feature seen in CCLA, and in GLA, lymphangiography may not show any special findings.

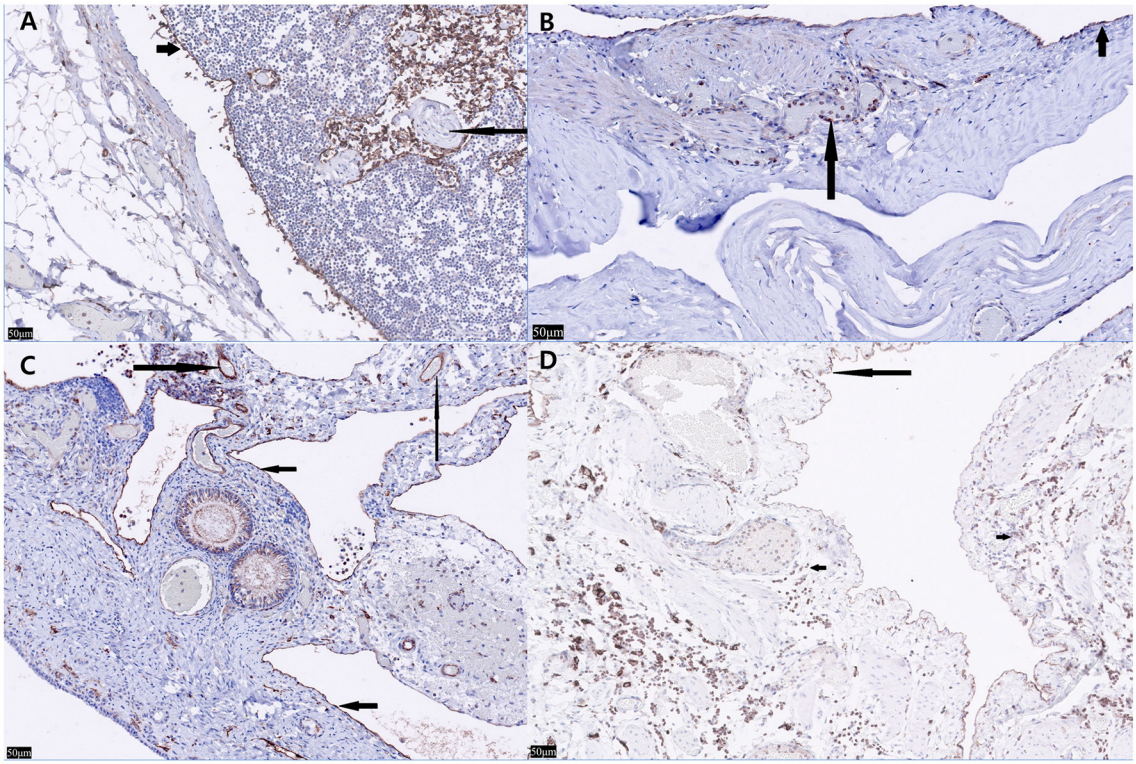


FIGURE 3
Lyve-1 immunostaining of the ovary, uterine horn, urinary bladder, and normal canine lymph node. **(A)** In the normal canine lymph node (control tissue), strong immunoreactivity is seen within lymphatics with nonspecific staining of leukocytes within the lymphatics (short arrow). Neither the arterioles nor interstitial leukocytes show immunoreactivity (long arrow) (×20). **(B)** In the urinary bladder, Lyve-1 reveals strong cytoplasmic immunoreactivity within the spindle cells both lining the cystic spaces (short arrow) and within the endothelial cells lining blood-filled vascular spaces (long arrow) (×20). **(C)** In the left ovary, Lyve-1 reveals strong cytoplasmic immunoreactivity lining the cystic spaces (short arrows). Intermediate immunoreactivity is also noted within endothelial cells lining blood-filled vascular spaces (Long arrows) (×20). **(D)** In nonspecific staining of leukocytes is seen (short arrows) in the left uterine horn, cells lining the cystic spaces show intermediate to strong immunoreactivity to Lyve-1 (long arrow) (×20).

Histopathology and immunostaining of LYVE-1, a marker associated with lymphatic vessels, must be performed to distinguish whether it is derived from lymphatic vessels vs. vascular endothelium (18). Caution is warranted while interpreting LYVE-1 and other Immunohistochemical findings. The H&E findings with the immunohistochemistry must be weighed together. LYVE-1, a CD44 homolog was thought to be restricted to lymphatics and did not stain endothelial cells, but subsequent studies showed non-lymphatic endothelial cells within hepatic sinusoids. Embryonic lymphangiogensis is under debate, but both vasculature and lymphatics are lined by endothelium. Other markers previously thought to be specific to lymphatics have been shown to lack specificity: VEGFR-3 has been seen in a subset of angiogenic vessels associated with pathologic conditions (26). Podoplanin is seen in smaller lymphatics lacking smooth muscle and not in high endothelial venules, and is also expressed in osteoblasts, renal podocytes and type I pulmonary alveolar cells. LYVE-1 has also been identified in hepatic sinusoids in normal livers and down regulated in sinusoids in some pathologic hepatic conditions (27). In our case, LYVE-1 staining was seen in blood filled vessels with intermediate staining (Figure 3C) and in empty endothelial lined vessels with intermediate to strong staining. These findings in conjunction with multiple empty cystic spaces seen in Figure 2 support a lymphatic origin.

In humans, the PIK3CA gene and NRAS gene are known to be associated with generalized lymphatic anomaly, but there is no study on the related genes in animals (15, 16). Therefore, in the present case, DNA was extracted and PCR was performed using FFPE tissue for NRAS gene sequencing, but the peak size was observed to be 44bp instead of 150, which was the base pairs of the target gene. This is considered as an amplification occurring by attaching primer dimers to each other, given that the same result was obtained both times and target gene was not detected. This may be because of deterioration due to oxidation of nucleic acid as the surface of the paraffin sections was exposed to the air, since PCR was performed more than 6 months after the paraffin-embedded sample was made. In addition, factors like formalin, tissue processing, sectioning and staining procedures, incubation at high temperature during the paraffin embedding process are also thought to have influenced DNA damage (28).

In humans, five out of six patients with lymphatic anomaly of the UB showed clinical signs of hematuria (29). To reduce the possibility of recurrence in most cases, partial cystectomy with complete resection rather than transurethral resection or laser

ablation was performed as a treatment method. A patient with lymphatic anomaly in the uterine corpus showed clinical symptoms of back pain, leg edema, and abdominal distension, and was treated surgically through hysterectomy (30). In our case, there were no specific clinical symptoms, other than vomiting and lethargy. Since that there was no vomiting after debulking, it was considered to be due to an increase in abdominal pressure caused by cysts occupying most of the abdominal cavity.

The best treatment for lymphatic anomalies is surgical removal. However, since lymphangioma often includes deep tissue, complete resection may not be possible, and if only the superficial part is removed, the recurrence rate is approximately 20% in humans (29). If complete removal is not possible, medical treatment is available. In humans, sclerotherapy with OK-432, doxycycline, and bleomycin is the most commonly used alternative treatment for lymphangioma, because sclerotherapy is safe and has no serious side effects (10). Sclerotherapy destroys the vessel' endothelium, causing obstruction and fibrosis. Radiation therapy and sirolimus, which suppress the activity of the mTOR and promote lymphangiogenesis, have also been used as treatments in humans. However, there are few cases in which these treatments have been applied to dogs. Recently, there has been a case of canine lymphatic anomaly treated with sclerotherapy, electrochemotherapy, and radiation therapy (6) and a case of lymphangiosarcoma treated with toceranib, a tyrosine kinase inhibitor (15, 31).

Our study has several limitations. First, biopsy of the rectum was not performed. However, the US and CT showed the same pattern as the cysts in other organs, and since the same immunostaining results were obtained in all other five sites, the cyst observed in the rectum was also considered to be caused by GLA. Second, complete resection was not achieved in our case. Only debulking was performed because the cysts were so extensive that complete resection was impossible. In addition, sclerotherapy was not performed, because the cyst was multilobulated. Radiation therapy can be applied, but radiation hazards can occur in the heart and lungs, and since there is a case that showed a good prognosis without treatment other than debulking in humans, only debulking was performed in our case (14, 32). At 6 months follow-up, the size of the remaining cysts was maintained, and no clinical symptoms or specific findings were observed. Third, genetic testing didn't work properly. Further studies on GLA-related genes through fresh frozen tissue or blood are considered necessary. Fourth, fluid analysis of the cyst was not performed. However, It is considered that there was no significant effect on the diagnosis because the higher-level examination, such as biopsy and immunostaining, was performed. Finally, follow-up period was short. Thus, it is difficult to judge the effectiveness of the treatment and the prognosis of the GLA.

To the best of our knowledge, in veterinary medicine, this is the first case of lymphatic anomaly of the ovary, uterus, bladder, and rectum, and the first case of GLA involving more than two parenchymal organs. In the case of multiple cysts in multiple organs of the abdominal cavity in young dogs, GLA should be included in the differential diagnosis.

## Ethics statement

Ethical approval was not required for the study because the case report is a description of a clinical case. Written informed consent was obtained from the owners for the participation of their animals in this study.

## Author contributions

S-HP and J-HL drafted the manuscript. S-HP, J-HL, and HY contributed to case management. HY confirmed the cases and revised the final submission. ES performed the pathological studies. MK and J-iH performed the gene analysis. All authors contributed to the article and approved the submitted version.

## Conflict of interest

ES was employed by IDEXX Laboratories, Inc.

The remaining authors declare that the research was conducted in the absence of any commercial or financial relationships that could be construed as a potential conflict of interest.

## Publisher's note



## References

1. Manning SC, Perkins J. Lymphatic malformations. *Curr Opin Otolaryngol Head Neck Surg.* (2013) 21:571–5. doi: 10.1097/MOO.0000000000000007

2. Berry W, Nesbit J, Pearson J. Lymphangiomatosis of the pelvic limb in a Maltese dog. *J Small Animal Pract.* (1996) 37:340–3. doi: 10.1111/j.1748-5827.1996.tb02405.x

3. Maeda S, Fujino Y, Tamamoto C, Suzuki S, Fujita A, Takahashi M, et al. Lymphangiomatosis of the systemic skin in an old dog. *J Vet Med Sci.* (2013) 75:187–90. doi: 10.1292/jvms.12-0321

4. Stambaugh JE, Harvey CE, Goldschmidt MH. Lymphangioma in four dogs. *J Am Vet Med Assoc.* (1978) 173:759–61.

5. Driessen F, Cushing T, Baines SJ. Retroperitoneal lymphatic malformation in a dog. *Acta Vet Scand.* (2020) 62:8. doi: 10.1186/s13028-020-0506-9

6. Locker SH, Maxwell EA, Vilaplana Grosso F, Bertran J, Shiomitsu K. Novel treatment of recurrent abdominal lymphatic malformations in a dog. *Vet Rec Case Rep.* (2021) 9:3. doi: 10.1002/vrc2.127

7. Belanger MC, Mikaelian I, Girard C, Daminet S. Invasive multiple lymphangiomas in a young dog. *J Am Anim Hosp Assoc.* (1999) 35:507–9. doi: 10.5326/15473317-35-6-507

8. Ramirez GA, Sanchez-Salguero X, Molin J. Primary Cystic Lymphangioma of the spleen in an adult dog. *J Comp Pathol.* (2020) 178:22–6. doi: 10.1016/j.jcpa.2020.06.006

9. Yamagami T, Takemura N, Washizu T, Komori S, Amasaki H, Washizu M. Hepatic lymphangiomatosis in a young dog. *J Vet Med Sci.* (2002) 64:743–5. doi: 10.1292/jvms.64.743

10. Liu X, Cheng C, Chen K, Wu Y, Wu Z. Recent progress in Lymphangioma. *Front Pediatr.* (2021) 9:735832. doi: 10.3389/fped.2021.735832

11. Makinen T, Boon LM, Vikkula M, Alitalo K. Lymphatic malformations: genetics, mechanisms and therapeutic strategies. *Circ Res.* (2021) 129:136–54. doi: 10.1161/CIRCRESAHA.121.318142

12. Ricci KW, Iacobas I. How we approach the diagnosis and management of complex lymphatic anomalies. *Pediatr Blood Cancer.* (2022) 69:e28985. doi: 10.1002/pbc.28985

13. Ozeki M, Nozawa A, Yasue S, Endo S, Asada R, Hashimoto H, et al. The impact of sirolimus therapy on lesion size, clinical symptoms, and quality of life of patients with lymphatic anomalies. *Orphanet J Rare Dis.* (2019) 14:1–11. doi: 10.1186/s13023-019-1118-1

14. Ozeki M, Fukao T. Generalized lymphatic anomaly and Gorham–Stout disease: overview and recent insights. *Advances in wound care.* (2019) 8:230–45. doi: 10.1089/wound.2018.0850

15. Manevitz-Mendelson E, Leichner GS, Barel O, Davidi-Avrahami I, Ziv-Strasser L, Eyal E, et al. Somatic NRAS mutation in patient with generalized lymphatic anomaly. *Angiogenesis.* (2018) 21:287–98. doi: 10.1007/s10456-018-9595-8

16. Rodriguez-Laguna L, Agra N, Ibañez K, Oliva-Molina G, Gordo G, Khurana N, et al. Somatic activating mutations in PIK3CA cause generalized lymphatic anomaly. *J Exp Med.* (2019) 216:407–18. doi: 10.1084/jem.20181353

17. Oui H, Lamm C, Stiver S, Williams B, Kwon SY, Bae Y, et al. Congenital lymphangiomatosis and an enteric duplication cyst in a young dog. *J Small Anim Pract.* (2014) 55:379–82. doi: 10.1111/jsap.12208

18. Gross TL, Ihrke PJ, Walder EJ, Affolter VK. *Skin Diseases of the Dog and Cat: Clinical and Histopathologic Diagnosis*. Hoboken, NJ: John Wiley and Sons. (2008).

19. Mohammadi A, Ghasemi-rad M, Abassi F. Asymptomatic lymphangioma involving the spleen and mediastinum in adults. *Med Ultrason.* (2013) 15:154–6. doi: 10.11152/mu.2013.2066.152.am1mgr2

20. Spencer KR, Miettinen MM, Maki RG, Mehnert JM. When benign tumors mimic malignancies: a case of lymphangiomatosis masquerading as metastatic disease. *Rare Cancers Ther.* (2013) 1:21–7. doi: 10.1007/s40487-013-0001-9

21. Qutub W, Lewis K, Gonzalez R, Quaife R, Russ P, McCarter M. Lymphangiomatosis masquerading as metastatic melanoma. *Am Surg.* (2006) 72:367–70. doi: 10.1177/000313480607200420

22. Bosch-Príncep R, Castellano-Megías VM, Alvaro-Naranjo T, Martínez-González S, Salvadó-Usach MT. Fine needle aspiration cytology of a cervical lymph node lymphangioma in an adult. A case report. *Acta cytologica.* (1999) 43:442–6. doi: 10.1159/000331097

23. François S, Martin M, Costa O, Urbain D, Mana F. *Cystic Lymphangioma: Are Triglycerides Always Measurable? Case Reports in Gastrointestinal Medicine.* (2018) 2018:9591420. doi: 10.1155/2018/9591420

24. Trenor III CC, Chaudry G. Complex lymphatic anomalies. *In: Seminars in pediatric surgery.* (2014) Amsterdam, Netherlands: Elsevier. doi: 10.1053/j.sempedsurg.2014.07.006

25. Chaudry G. Complex lymphatic anomalies and therapeutic options. *Tech Vasc Interv Radiol.* (2019) 22:100632. doi: 10.1016/j.tvir.2019.100632

26. Jussila L, Alitalo K. Vascular growth factors and lymphangiogenesis. *Physiol Rev.* (2002) 82:673–700. doi: 10.1152/physrev.00005.2002

27. Carreira CM, Nasser SM, di Tomaso E, Padera TP, Boucher Y, Tomarev SI, et al. LYVE-1 is not restricted to the lymph vessels: expression in normal liver blood sinusoids and down-regulation in human liver cancer and cirrhosis. *Cancer Res.* (2001) 61:8079–84.

28. Turashvili G, Yang W, McKinney S, Kalloger S, Gale N, Ng Y, et al. Nucleic acid quantity and quality from paraffin blocks: defining optimal fixation, processing and DNA/RNA extraction techniques. *Exp Mol Pathol.* (2012) 92:33–43. doi: 10.1016/j.yexmp.2011.09.013

29. He W, Jin L, Lin FF Qi XL, He XL, Zhang DH, et al. Cavernous lymphangioma of the urinary bladder in an adult woman: an additional case report of a rare lesion and literature review. *BMC Urol.* (2021) 21:145. doi: 10.1186/s12894-021-00907-3

30. Furui T, Imai A, Yokoyama Y, Sato E, Tamaya T. Cavernous lymphangioma arising from uterine corpus. *Gynecol Oncol.* (2003) 90:195–9. doi: 10.1016/S0090-8258(03)00197-5

31. Kim J-H, Yoon H, Yoon H-Y, Eom K, Sung H-J, Kim J-H. Successful management of lymphangiosarcoma in a puppy using a tyrosine kinase inhibitor. *The Canadian Veterinary Journal.* (2018) 59:367.

32. Kumar B, Bhatnagar A, Upadhyaya VD, Gangopadhyay AN. Small intestinal lymphangioma presenting as an acute abdomen with relevant review of literature. *J Clini Diag Res.: JCDR.* (2017) 11:PD01. doi: 10.7860/JCDR/2017/22703.9962

frontiers | Frontiers in Veterinary Science

TYPE Original Research
PUBLISHED 22 June 2023
DOI 10.3389/fvets.2023.1191211



OPEN ACCESS

EDITED BY
Ryou Tanaka,
Tokyo University of Agriculture and Technology, Japan

REVIEWED BY
Hussein M. El-Husseiny,
Tokyo University of Agriculture and Technology, Japan
Ana Patrícia Fontes-Sousa,
University of Porto, Portugal

*CORRESPONDENCE
Ryohei Suzuki
✉ ryoheisuzuki0130@gmail.com

RECEIVED 21 March 2023
ACCEPTED 25 May 2023
PUBLISHED 22 June 2023

CITATION
Saito T, Suzuki R, Yuchi Y, Fukuoka H, Satomi S, Teshima T and Matsumoto H (2023) Comparative study of myocardial function in cases of feline hypertrophic cardiomyopathy with and without dynamic left-ventricular outflow-tract obstruction.
*Front. Vet. Sci.* 10:1191211.
doi: 10.3389/fvets.2023.1191211



# Comparative study of myocardial function in cases of feline hypertrophic cardiomyopathy with and without dynamic left-ventricular outflow-tract obstruction

Takahiro Saito, Ryohei Suzuki*, Yunosuke Yuchi, Haru Fukuoka, Shuji Satomi, Takahiro Teshima and Hirotaka Matsumoto

Laboratory of Veterinary Internal Medicine, School of Veterinary Medicine, Faculty of Veterinary Science, Nippon Veterinary and Life Science University, Tokyo, Japan

In recent years, hypertrophic cardiomyopathy (HCM) in cats has become much more common in clinical practice due to improvements in diagnostic techniques and equipment performance. One phenotype is obstructive HCM with left ventricular (LV) outflow tract obstruction (DLVOTO). It has been reported that the presence or absence of DLVOTO does not affect long-term prognosis in cats with HCM. In this study, we evaluated and compared myocardial function in HCM-affected cats with and without DLVOTO using the two-dimensional speckle-tracking echocardiography. LV longitudinal strain of the endocardial, epicardial, and whole layer and LV circumferential strain of the epicardium were significantly decreased in all HCM-affected cats compared to healthy cats. However, these values were not significantly different between those with and without DLVOTO. In contrast, the endocardial and whole layers of LV circumferential strain were only significantly decreased in HCM-affected cats with DLVOTO compared to healthy cats. This could be attributed to the fact that the LV pressure load associated with DLVOTO affected the endocardial myocardium more in the LV endocardial layer, and that lower values of LV endocardial strain lowered the values of LV strain in the whole layer. In conclusion, our results suggest that LV myocardial function may have been more compromised in the HCM-affected cats with DLVOTO.

KEYWORDS

**cat, cardiomyopathy, speckle tracking echocardiography, myocardial function, strain**

## 1. Introduction

Hypertrophic cardiomyopathy (HCM) in the cat is a cardiac disease that is frequently encountered in the clinical practice. HCM is characterized by myocardial hypertrophy and its phenotype is diverse. The prognosis of cats with HCM also varies from asymptomatic cases to cats with congestive heart failure even at a young age (1–5). One phenotype, systolic anterior motion of the mitral valve leaflet, is an event in which the tip of the mitral valve septal apex is pulled toward the aortic outflow tract during systole. This event involved in mitral regurgitation, as well as dynamic left-ventricular (LV) outflow-tract obstruction (DLVOTO), which results in

pressure overload in the left ventricle (6). DLVOTO causes an increased left ventricular pressure, which leads to increased wall stress and myocardial ischemia (7). The presence of DLVOTO in humans aggravates the pathogenesis of HCM and is a poor prognostic factor (8); however, it has been reported that the presence or absence of DLVOTO in feline HCM does not affect the long-term prognosis (4).

Recently, two-dimensional speckle-track echocardiography (2D-STE) has been widely performed to evaluate HCM in cats and humans (9–14). 2D-STE studies in cats with HCM have shown that assessment of segmental radial and circumferential deformities in systole (12) and torsion (14), as well as diastolic deformities (12, 13), can be helpful in distinguishing cats with HCM from healthy cats.

Therefore, we hypothesized that myocardial function in HCM-affected cats with DLVOTO (HOCM) would be decreased compared to HCM-affected cats without DLVOTO (HNCM). This study aimed to analyze myocardial function using 2D-STE and compared the results between the HNCM and HOCM.

## 2. Materials and methods

A prospective cross-sectional design was used in this study. This study was conducted in accordance with our institution's guidelines (Guidelines for the Care and Use of Animals at Nippon Veterinary and Life Science University) and was approved by the university's ethics committee (approval number: R2-4). With prior informed consent and agreement, all cat owners participated in the study.

### 2.1. Animals

Sixty-seven client-owned cats (healthy cats: $n = 16$; HCM-affected cats: $n = 51$) were included in this study. All cats underwent a physical examination, blood pressure measurement, electrocardiogram, chest radiograph and echocardiography. The cats classified as healthy cats had no abnormal findings on these examinations. Some HCM-affected cats were already on medication. No history of medication, cardiac disease, or clinical signs were noted in the other cats. The diagnosis of HCM was made by confirming LV hypertrophy on echocardiography and excluding diseases that might cause LV hypertrophy. LV hypertrophy was defined as LV wall thickness ≥ 6 mm at end-diastole as evaluated by echocardiography. LV wall thickening was confirmed using LV short-axis images averaged over three consecutive heartbeats (15). The following previously reported criteria were used to diagnose HOCM: Peak LV outflow-tract velocity (LVOT Vmax) > 2.5 m/s and systolic anterior motion of mitral valve leaflet on B-mode (14, 16). Other cardiomyopathies were ruled out by checking for normal to near-normal LV systolic function using allometric scaling, referring to previous reports (17, 18). Cats with suspected dehydration, hypertension (Systolic blood pressure greater than 160 mmHg), or other cardiovascular or systemic disease were excluded.

### 2.2. Echocardiography

Conventional echocardiography was performed by experienced researchers using Vivid E95 echocardiography scanner and 12 MHz transducer (GE Healthcare, Tokyo, Japan). During the examination, the lead II electrocardiogram was concurrently acquired and monitored on the screen. Holding during echocardiography was performed with an assisting human hand, and all cats were not sedated. Data were obtained for at least 5 heartbeats. Analysis of the echocardiographic data was performed on a separate day from the acquisition of the images by one researcher using an offline workstation (EchoPAC PC, version 204, GE Healthcare, Tokyo, Japan). The left atrial-to-aortic diameter ratio was measured in the right parasternal short-axis view at the level of basal heart. The end-diastolic interventricular septal thickness (IVSd), LV end-diastolic posterior wall thickness (LVPWd), LV end-diastolic internal diameter (LVIDd), LV end-systolic internal diameter, and fractional shortening were measured in the right parasternal short-axis view at the level of the chordae tendineae. Relative LV wall thickness (RWT) was calculated using the following formula:

$$\mathrm{RWT} = \left(\mathrm{IVSd}\left[\mathrm{mm}\right] + \mathrm{LVPWd}\left[\mathrm{mm}\right]\right) / \left(\mathrm{LVIDd}\left[\mathrm{mm}\right]\right)$$

Trans-mitral inflow in the left apical four-chamber view was measured by pulsed-wave Doppler, and the peak velocities of the early diastolic wave (E-wave) and late diastolic wave (A-wave) were determined. The E-wave to A-wave velocity ratio (E/A) was also calculated. In the case of fusion of E- and A-waves, values for cases containing these waves were excluded.

### 2.3. Two-dimensional speckle-tracking echocardiography

An overview of the 2D-STE analysis for cats has been previously described (9, 14, 15, 19, 20). 2D-STE analysis is performed using high-quality images obtained from conventional echocardiography. For evaluation of LV myocardial deformation, images of the left ventricle at the level of the papillary muscle were acquired in the right parasternal short-axis view and the left apical four-chamber view. Left apical four-chamber view images modified for right heart measurements were also obtained to analyze right myocardial deformations (21). Longitudinal and circumferential systolic strain peaks (SL and SC, respectively) were obtained in the endocardium, the entire layer, and the epicardium of the LV (LV-SL and LV-SC, respectively) (21). SC was measured at the papillary muscle level of the LV (14, 22). The endocardial-to-epicardial strain ratio (Endo/Epi), which is believed to reflect compensatory mechanisms of cardiac function in patients with HCM, was also calculated (23, 24). Previous studies have shown observer variability in 2D-STE analysis in our laboratory (14, 19–21).

### 2.4. Statistical analysis

Variables in each table are expressed as mean ± standard deviation values. Commercially available software (R 2.8.1; https://www.r-project.org/) was used for statistical analyses. One-way analysis of variance followed by Tukey's multiple comparison test for normally distributed data or Kruskal–Wallis test followed by Steel–Dwass test for non-normally distributed data was used to compare continuous variables between groups. The significance level was set at $p < 0.05$.

# 3. Results

## 3.1. Demographic data

Data regarding demographic characteristics and physical examination results are summarized in Table 1. Nineteen of the 51 cats with HCM belonged to the HNCM, while the remaining 32 belonged to the HOCM. There were no significant differences in age, weight, heart rate, or blood pressure between the two groups. There were significant differences in LVOT Vmax between healthy cats and the HNCM, healthy cats and the HOCM, and the HNCM and HOCM.

## 3.2. Echocardiography

The echocardiographic variable data are summarized in Table 2. IVSd, LVPWd, and RWT were significantly higher in the HNCM and HOCM than in healthy cats (all $p < 0.01$). E-wave velocity of the HOCM was increased compared to healthy cats and HNCM ($p < 0.05$). E-wave and E/A analyses were partially excluded because of waveform fusion in some cases.

## 3.3. Two-dimensional speckle-tracking echocardiography

The 2D-STE results are summarized in Table 3. Representative results of the 2DSTE method in the endocardium are shown in Figure 1. In addition, box-and-whisker diagrams of the LV-SL and LV-SC are also shown in Figures 2, 3, respectively. The LV-SL of whole layer was significantly decreased in the HNCM and HOCM compared to healthy cats ($p < 0.05$). There was no significant difference in LV-SL in any layer between the HNCM and HOCM. LV-SC in the epicardium was significantly decreased in the HNCM and HOCM compared to healthy cats (both $p < 0.01$). LV-SC in the HOCM of the endocardium and whole layers were decreased compared to healthy cats ($p = 0.01$, $p < 0.01$ respectively). There was no significant difference in LV-SC in any layer between the HNCM and HOCM. The LV-SL Endo/Epi was increased in the HNCM and HOCM compared to healthy cats ($p < 0.01$, $p = 0.02$ respectively). In comparison, there was no significant difference in LV-SC Endo/Epi between the HNCM and HOCM.

TABLE 1 Clinical characteristics in healthy cats and cats with cardiomyopathy.

| Variables | Healthy cats ($n$=16) | HNCM ($n$=19) | HOCM ($n$=32) |
|---|---|---|---|
| Age (year) | 6.7 ± 4.4 | 6.2 ± 3.6 | 3.6 ± 2.7 |
| Sex (male/female) | 9/7 | 11/8 | 19/13 |
| Body weight (kg) | 4.4 ± 1.6 | 4.2 ± 0.7 | 4.0 ± 1.3 |
| Heart rate (bpm) | 200 ± 32.0 | 183.1 ± 37.3 | 182.6 ± 24.7 |
| Systolic blood pressure (mmHg) | 136.4 ± 14.3 | 133.3 ± 15.2 | 130.0 ± 16.4 |
| LVOT Vmax (m/s) | 0.9 ± 0.3 | 1.0 ± 0.3* | 4.0 ± 0.9*† |
| ACVIM (B1, B2, C) | – | 12, 4, 3 | 21, 7, 4 |
| Medication (yes/no) | 0/16 (0%) | 15/19 (79%) | 9/32 (28%) |
| ACE inhibitor | – | 5/19 (26%) | 3/32 (9%) |
| Beta Blocker | – | 11/19 (58%) | 5/32 (16%) |
| Pimobendan | – | 2/19 (11%) | 1/32 (3%) |
| Diuretic | – | 1/19 (5%) | 2/32 (6%) |

LVOT Vmax, peak velocity of left-ventricular outflow-tract; ACVIM, American College of Veterinary Internal Medicine. Continuous variables are displayed as mean ± standard deviation. *: Values that was significantly different from the healthy cats ($p < 0.05$). †: Values that was significantly different from the HNCM ($p < 0.05$).

TABLE 2 Results of conventional echocardiographic indices in cats.

| Variables | Healthy cats ($n$=16) | HNCM ($n$=19) | HOCM ($n$=32) |
|---|---|---|---|
| LA/Ao | 1.3 ± 0.2 | 1.4 ± 0.4 | 1.4 ± 0.3 |
| IVSd (mm) | 3.8 ± 0.4 | 4.8 ± 1.8* | 6.2 ± 1.5* |
| LVPWd (mm) | 4.1 ± 0.7 | 5.3 ± 1.8* | 6.2 ± 1.9* |
| LVIDd (mm) | 14.5 ± 1.5 | 11.8 ± 4.6 | 13.3 ± 1.8 |
| RWT | 0.5 ± 0.1 | 0.8 ± 0.1* | 1.0 ± 0.3* |
| FS (%) | 47.5 ± 7.6 | 42.3 ± 6.9 | 48.6 ± 11.6 |
| E-wave (m/s) | 0.6 ± 0.2 | 0.6 ± 0.1 | 0.9 ± 0.3*† |
| E/A | 0.1 ± 0.2 | 1.2 ± 0.8 | 1.2 ± 1.1 |

LA/Ao, left atrial-to-aortic diameter ratio; IVSd, end-diastolic interventricular septal thickness; LVPWd, end-diastolic LV free-wall thickness; LVIDd, end-diastolic LV internal diameter; RWT, relative left ventricular wall thickness; FS, fractional shortening; E/A, E-wave to A-wave ratio. Continuous variables are displayed as mean ± standard deviation. *: The value is significantly different from the healthy cats ($p < 0.05$). †: The value is significantly different from the HNCM ($p < 0.05$).

# 4. Discussion

In this study, the HNCM and HOCM had decreased LV-SL in whole layers and LV-SC in the epicardium, which is consistent with the results of previous studies (20). Previous 2D-STE studies in cats with HCM have reported lower longitudinal strain in asymptomatic HCM cats than in healthy cats (13, 19). This has been shown to be caused by myocardial dysfunction and histopathologic changes (10, 11, 25, 26). Along with histopathological changes such as modifications in myocardial fiber orientation, myocardial compensatory mechanisms are believed to be linked with these dysfunctions (14, 19, 27). Even in human HCM, there are cases in which LV-SL in whole layers is decreased, even if the left ventricular ejection fraction appears normal. These cases have been reported to have a poor prognosis (28) and should not be judged as having normal LV systolic function based on conventional echocardiography only. However, in this study, there was no significant difference in LV-SL between the HNCM and HOCM in whole layer, so it was unlikely that the HOCM would have a worse prognosis based on LV-SL results. Previous studies on cats reported no differences in survival between the HNCM and HOCM (4). In contrast, in humans, HOCM is reported to be associated with a shorter survival time and worse prognosis owing to DLVOTO than HNCM (7). The detailed cause of why DLVOTO has a poorer prognosis in HCM is unknown. However, the mechanism has been discussed in previous papers as follows (7); The increased left ventricular pressure due to DLVOTO is expected to result in increased wall stress. Myocardium also devotes more effort to contraction, which can lead to myocardial ischemia. These abnormalities may contribute to eventual cardiomyocyte death and scarring (29–31).

These changes are thought to result in stiffening of the myocardium, leading to diastolic dysfunction (32–34) as well as increased susceptibility to electrical instability and sudden death. DLVOTO of HCM-affected cats may reduce endocardial myocardial function through a mechanism similar to that reported in humans (7). In addition, the decreased LV-SC in the endocardial may have inevitably decreased LV-SC in the whole layer. The aforementioned human study also reported that older patients with HOCM (age ≥ 40 years) were more likely to experience deterioration than younger patients with HOCM by a similar mechanism (7). It is unclear whether it is appropriate to extrapolate this mechanism directly to cats, and the fact that the duration of obstruction is different in cats than in humans may be related to the finding that survival is not affected in the former. Nevertheless, based on this mechanism and the results of this study, we believe that careful evaluation of the long-term prognosis of cats with HOCM is warranted in the future.

TABLE 3 Strain assessed by two-dimensional speckle tracking echocardiography in healthy cats and cats with cardiomyopathy.

| Variables | Healthy cats (*n*=16) | HNCM (*n*=19) | HOCM (*n*=32) |
|---|---|---|---|
| LV-SL (%) | | | |
| Whole layer | 20.3 ± 3.5 | 14.8 ± 5.1* | 14.7 ± 4.3* |
| Endocardium | 23.3 ± 3.8 | 18.9 ± 5.5* | 18.1 ± 4.9* |
| Epicardium | 17.6 ± 3.3 | 12.7 ± 3.7* | 12.3 ± 3.7* |
| Endo/Epi | 1.3 ± 0.1 | 1.5 ± 0.1* | 1.5 ± 0.3* |
| LV-SC (%) | | | |
| Whole layer | 20.1 ± 4.3 | 16.5 ± 2.8 | 15.6 ± 4.2* |
| Endocardium | 38.7 ± 7.3 | 32.8 ± 6.2 | 30.6 ± 7.8* |
| Epicardium | 7.4 ± 3.0 | 6.3 ± 1.5* | 6.0 ± 2.4* |
| Endo/Epi | 6.4 ± 3.8 | 5.4 ± 1.8 | 5.7 ± 2.3 |

LV-SL, peak systolic strain in the longitudinal direction at left ventricles; LV-SC, peak systolic strain in the circumferential direction at left ventricles; End, endocardium; Epi, epicardium. Continuous variables are displayed as mean ± standard deviation. *: The value is significantly different from the healthy cats ($p < 0.05$).

In this study, LV-SL Endo/Epi was significantly increased in the HOCM and HNCM compared to the healthy cats, but there was no significant difference in LV-SC Endo/Epi. However, LV-SC Endo/Epi was decreased in the HOCM and HNCM compared to the healthy cats, although the difference was not significant. LV-SC Endo/Epi in asymptomatic cats-affected HCM was increased compared to healthy cats in a previous study, although there was no significant difference in LV-SL Endo/Epi (20). Increased LV-SC Endo/Epi is considered to be circumferential endocardial compensation for depressed epicardial contraction (20, 23, 24). Therefore, the HCM-affected cats included in this study were relatively severe and the compensatory mechanisms may have become dysfunctional. Although this study included cats with HCM of various American College of Veterinary Internal Medicine stages and thus the results should be interpreted with caution, a lower LV-SC Endo/Epi may be associated with worse prognosis in cats-affected HCM.

There were several limitations to the study. The sample size was small, which may have affected the results owing to case bias. In addition, some affected cats were prescribed oral medications, which may have affected the results. Furthermore, diagnosis was based on echocardiography, and not pathological findings. The study also included cats with HCM of varying severities, which may have affected the results. Specifically, it is possible that pathological severity was milder in the HNCM, resulting in a significant difference only in the HOCM compared to the healthy cats. However, no significant

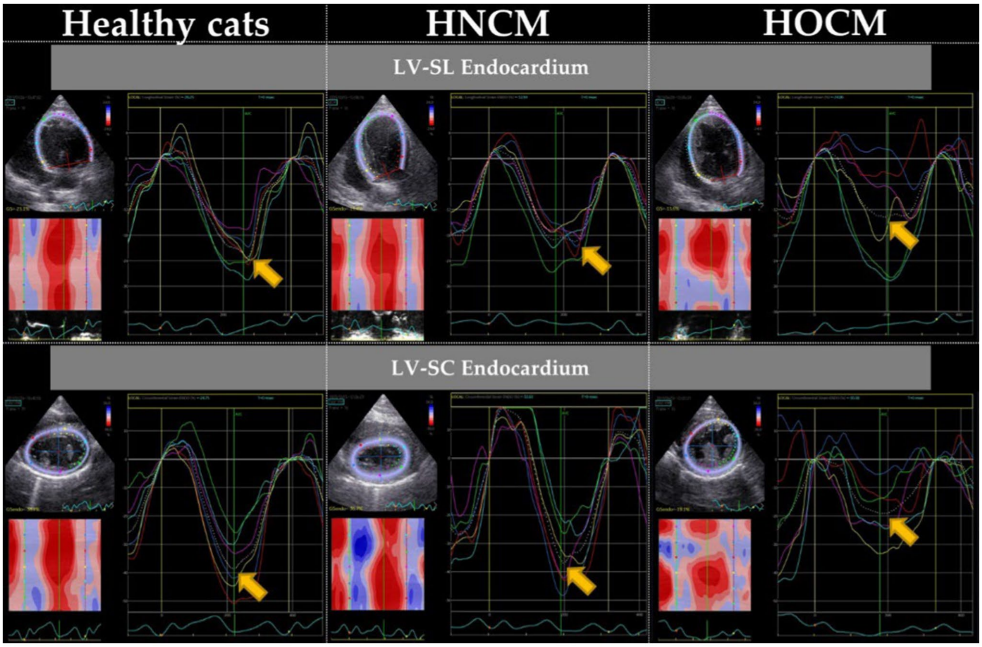


FIGURE 1
Myocardial motion analysis results of endocardium by 2D-STE method (representative data). LV-SL, peak systolic strain in the longitudinal direction at left ventricles; LV-SC, peak systolic strain in the circumferential direction at left ventricles. Arrows indicate the peak of the endocardium.

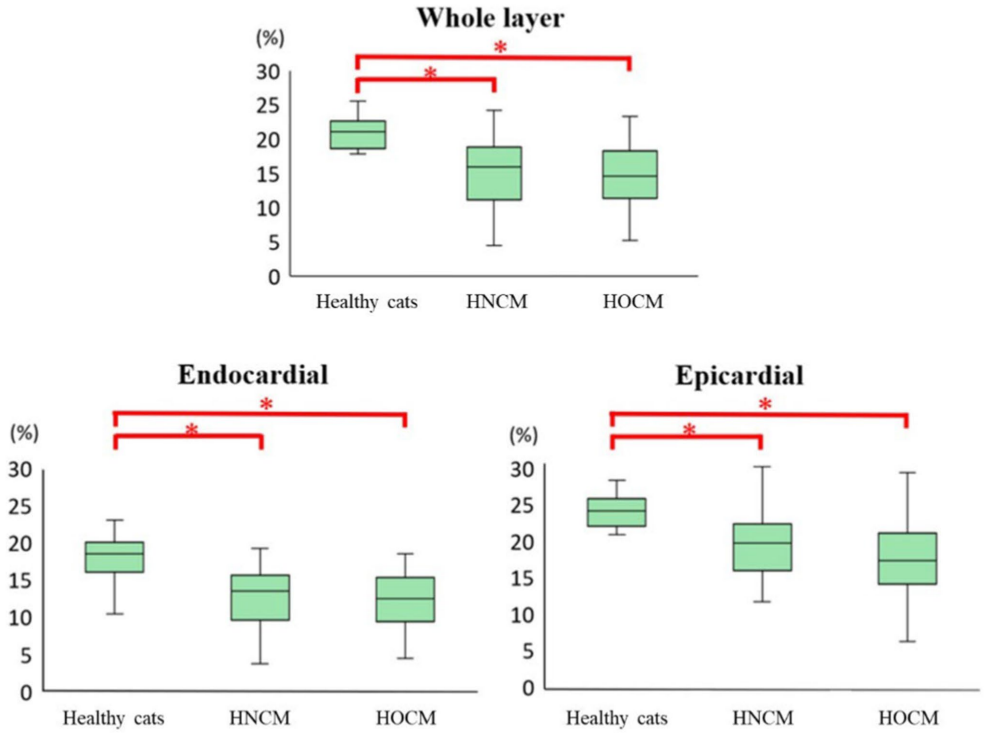


FIGURE 2
Results of longitudinal strain by 2D-STE method (box-and-whisker diagram). *The value is significantly different from the healthy cats ($p<0.05$).

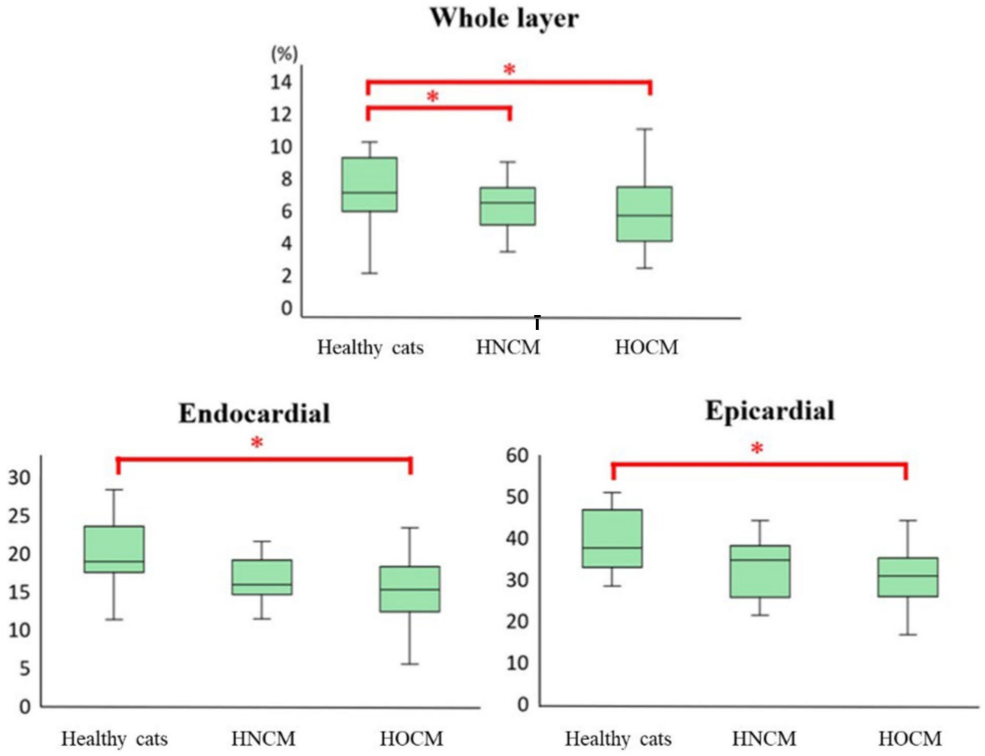


FIGURE 3
Results of circumferential strain by 2D-STE method (box-and-whisker diagram). *The value is significantly different from the healthy cats ($p<0.05$).

differences were found between the HNCM and HOCM with respect to left ventricular wall thickness or American College of Veterinary Internal Medicine stage. Therefore, it is considered that there is no extreme difference in severity of disease.

## 5. Conclusion

Our results also indicate that 2D-STE is useful for detecting HCM, as shown in previous studies, and that cats with HOCM may have worse myocardial function than those with HNCM. However, predicting prognosis requires caution, and further studies are warranted to clarify these aspects.

## Data availability statement

The original contributions presented in the study are included in the article/supplementary material, further inquiries can be directed to the corresponding author.

## Ethics statement

The animal study was reviewed and approved by Nippon Veterinary and Life Science University. Written informed consent was obtained from the owners for the participation of their animals in this study.

## Author contributions

RS and TS conceptualized and designed the study, acquired and interpreted the data, and drafted and critically revised the manuscript. YY, HF, and SS acquired, analyzed, and summarized the data and approved the article. TT and HM acquired and interpreted the data, supervised the study, and approved the article. All authors contributed to the article and approved the submitted version.

## Funding

This research was funded by the Japan Society for the Promotion of Science KAKENHI (grant number 22K05995).

## Acknowledgments

This study was conducted at the Laboratory of Veterinary Internal Medicine, School of Veterinary Science, Nippon Veterinary and Life Science University, Tokyo, Japan. We would also like to thank Editage (www.editage.com) for English language editing.

## Conflict of interest

The authors declare that the research was conducted in the absence of any commercial or financial relationships that could be construed as a potential conflict of interest.

## Publisher's note



## References

1. Rush JE, Freeman LM, Fenollosa NKBD. Population and survival characteristics of cats with hypertrophic cardiomyopathy: 260 cases (1990–1999). *J Am Vet Med Assoc*. (2002) 220:202–7. doi: 10.2460/javma.2002.220.202

2. Payne JR, Brodbelt DC, Luis FV. Cardiomyopathy prevalence in 780 apparently healthy cats in rehoming centres (the CatScan study). *J Vet Cardiol*. (2015) 17:S244–57. doi: 10.1016/j.jvc.2015.03.008

3. Paige CF, Abbott JA, Elvinger FPR. Prevalence of cardiomyopathy in apparently healthy cats. *J Am Vet Med Assoc*. (2009) 234:1398–403. doi: 10.2460/javma.234.11.1398

4. Fox PR, Keene BW, Lamb K, Schober KA, Chetboul V, Luis Fuentes V, et al. International collaborative study to assess cardiovascular risk and evaluate long-term health in cats with preclinical hypertrophic cardiomyopathy and apparently healthy cats: the REVEAL study. *J Vet Intern Med*. (2018) 32:930–43. doi: 10.1111/jvim.15122

5. Fox PR. Hypertrophic cardiomyopathy. Clinical and pathologic correlates. *J Vet Cardiol*. (2003) 5:39–45. doi: 10.1016/S1760-2734(06)70051-0

6. Fox PR, Liu SK, Maron BJ. Echocardiographic assessment of spontaneously occurring feline hypertrophic cardiomyopathy. An animal model of human disease. *Circulation*. (1995) 92:2645–51. doi: 10.1161/01.CIR.92.9.2645

7. Maron MS, Olivotto I, Betocchi S, Casey SA, Lesser JR, Losi MA, et al. Effect of left ventricular outflow tract obstruction on clinical outcome in hypertrophic cardiomyopathy. *N Engl J Med*. (2003) 348:295–303. doi: 10.1056/NEJMoa021332

8. Williams LK, Chan RH, Carasso S, Durand M, Misurka J, Crean AM, et al. Effect of left ventricular outflow tract obstruction on left atrial mechanics in hypertrophic cardiomyopathy. *Biomed Res Int*. (2015) 2015:1–10. doi: 10.1155/2015/481245

9. Suzuki R, Mochizuki Y, Yoshimatsu H, Niina A, Teshima T, Matsumoto H, et al. Early detection of myocardial dysfunction using two-dimensional speckle tracking echocardiography in a young cat with hypertrophic cardiomyopathy. *J Feline Med Surg Open Reports*. (2018) 4:205511691875621. doi: 10.1177/2055116918756219

10. Liu Y, Deng Y, Li X, et al. Assessment of left ventricular longitudinal regional myocardial systolic function by strain imaging echocardiography in patients with hypertrophic cardiomyopathy. *J Huazhong Univ Sci Technol Med Sc*. (2005) 25:703–5. doi: 10.1007/BF02896176

11. Serri K, Reant P, Lafitte M, Berhouet M, Le Bouffos V, Roudaut R, et al. Global and regional myocardial function quantification by two-dimensional strain: application in hypertrophic cardiomyopathy. *J Am Coll Cardiol*. (2006) 47:1175–81. doi: 10.1016/j.jacc.2005.10.061

12. Takano H, Isogai T, Aoki A, Wakao Y, Fujii Y. Feasibility of radial and circumferential strain analysis using 2D speckle tracking echocardiography in cats. *J Vet Med Sci*. (2015) 77:193–201. doi: 10.1292/jvms.13-0241

13. Sugimoto K, Fujii Y, Sunahara H, Aoki T. Assessment of left ventricular longitudinal function in cats with subclinical hypertrophic cardiomyopathy using tissue Doppler imaging and speckle tracking echocardiography. *J Vet Med Sci*. (2015) 77:1101–8. doi: 10.1292/jvms.14-0354

14. Suzuki R, Mochizuki Y, Yoshimatsu H, Ohkusa T, Teshima T, Matsumoto H, et al. Myocardial torsional deformations in cats with hypertrophic cardiomyopathy using two-dimensional speckle-tracking echocardiography. *J Vet Cardiol*. (2016) 18:350–7. doi: 10.1016/j.jvc.2016.06.004

15. Suzuki R, Mochizuki Y, Yuchi Y, Yasumura Y, Saito T, Teshima T, et al. Assessment of myocardial function in obstructive hypertrophic cardiomyopathy cats with and without response to medical treatment by carvedilol. *BMC Vet Res*. (2019) 15:1–8. doi: 10.1186/s12917-019-2141-0

16. Jackson BL, Adin DB, Lehmkuhl LB. Effect of atenolol on heart rate, arrhythmias, blood pressure, and dynamic left ventricular outflow tract obstruction in cats with subclinical hypertrophic cardiomyopathy. *J Vet Cardiol Off J Eur Soc Vet Cardiol*. (2015) 17:S296–305. doi: 10.1016/j.jvc.2015.03.002

17. Luis Fuentes V, Abbott J, Chetboul V, Côté E, Fox PR, Häggström J, et al. ACVIM consensus statement guidelines for the classification, diagnosis, and management of cardiomyopathies in cats. *J Vet Intern Med*. (2020) 34:1062–77. doi: 10.1111/jvim.15745

18. Visser LC, Sloan CQ, Stern JA. Echocardiographic assessment of right ventricular size and function in cats with hypertrophic cardiomyopathy. *J Vet Intern Med*. (2017) 31:668–77. doi: 10.1111/jvim.14688

19. Suzuki R, Mochizuki Y, Yoshimatsu H, Teshima T, Matsumoto H, Koyama H. Determination of multidirectional myocardial deformations in cats with hypertrophic cardiomyopathy by using two-dimensional speckle-tracking echocardiography. *J Feline Med Surg*. (2017) 19:1283–9. doi: 10.1177/1098612X17691896

20. Suzuki R, Mochizuki Y, Yoshimatsu H, Niina A, Teshima T, Matsumoto H, et al. Layer-specific myocardial function in asymptomatic cats with obstructive hypertrophic cardiomyopathy assessed using 2-dimensional speckle-tracking echocardiography. *J Vet Intern Med*. (2019) 33:37–45. doi: 10.1111/jvim.15339

21. Suzuki R, Yuchi Y, Kanno H, Teshima T, Matsumoto H, Koyama H. Left and right myocardial functionality assessed by two-dimensional speckle-tracking echocardiography in cats with restrictive cardiomyopathy. *Animals*. (2021) 11:1578. doi: 10.3390/ani11061578

22. Hutagalung A. Noninvasive clinical assessment of systolic torsional motions by two-dimensional speckle-tracking echocardiography in dogs with myxomatous mitral valve disease. *Angew Chemie Int Ed*. (1967) 6:951–2. doi: 10.1111/jvim.12024

23. Ozawa K, Funabashi N, Takaoka H, Kamata T, Kanaeda A, Saito M, et al. Characteristic myocardial strain identified in hypertrophic cardiomyopathy subjects with preserved left ventricular ejection fraction using a novel multi-layer transthoracic echocardiography technique. *Int J Cardiol*. (2015) 184:237–43. doi: 10.1016/j.ijcard.2015.01.070

24. Okada K, Yamada S, Iwano H, Nishino H, Nakabachi M, Yokoyama S, et al. Myocardial shortening in 3 orthogonal directions and its transmural variation in patients with nonobstructive hypertrophic cardiomyopathy. *Circ J*. (2015) 79:2471–9. doi: 10.1253/circj.CJ-15-0646

25. Popović ZB, Kwon DH, Mishra M, Buakhamsri A, Greenberg NL, Thamilarasan M, et al. Association between regional ventricular function and myocardial fibrosis in hypertrophic cardiomyopathy assessed by speckle tracking echocardiography and delayed hyperenhancement magnetic resonance imaging. *J Am Soc Echocardiogr Off Publ Am Soc Echocardiogr*. (2008) 21:1299–305. doi: 10.1016/j.echo.2008.09.011

26. Urbano-Moral JA, Rowin EJ, Maron MS, Crean A, Pandian NG. Investigation of global and regional myocardial mechanics with 3-dimensional speckle tracking echocardiography and relations to hypertrophy and fibrosis in hypertrophic cardiomyopathy. *Circ Cardiovasc Imaging*. (2014) 7:11–9. doi: 10.1161/CIRCIMAGING.113.000842

27. Carasso S, Yang H, Woo A, Vannan MA, Jamorski M, Wigle ED, et al. Systolic myocardial mechanics in hypertrophic cardiomyopathy: novel concepts and implications for clinical status. *J Am Soc Echocardiogr Off Publ Am Soc Echocardiogr*. (2008) 21:675–83. doi: 10.1016/j.echo.2007.10.021

28. Liu H, Pozios I, Haileselassie B, Nowbar A, Sorensen LL, Phillip S, et al. Role of global longitudinal strain in predicting outcomes in hypertrophic cardiomyopathy. *Am J Cardiol*. (2017) 120:670–5. doi: 10.1016/j.amjcard.2017.05.039

29. Maron BJ, Wolfson JK, Epstein SE, Roberts WC. Intramural ("small vessel") coronary artery disease in hypertrophic cardiomyopathy. *J Am Coll Cardiol*. (1986) 8:545–57. doi: 10.1016/S0735-1097(86)80181-4

30. Cannon RO, Rosing DR, Maron BJ, Leon MB, Bonow RO, Watson RM, et al. Myocardial ischemia in patients with hypertrophic cardiomyopathy: contribution of inadequate vasodilator reserve and elevated left ventricular filling pressures. *Circulation*. (1985) 71:234–43. doi: 10.1161/01.CIR.71.2.234

31. Factor SM, Butany J, Sole MJ, Wigle ED, Williams WC, Rojkind M. Pathologic fibrosis and matrix connective tissue in the subaortic myocardium of patients with hypertrophic cardiomyopathy. *J Am Coll Cardiol*. (1991) 17:1343–51. doi: 10.1016/S0735-1097(10)80145-7

32. Wigle ED, Sasson Z, Henderson MA, Ruddy TD, Fulop J, Rakowski H, et al. Hypertrophic cardiomyopathy. The importance of the site and the extent of hypertrophy. A review. *Prog Cardiovasc Dis*. (1985) 28:1–83. doi: 10.1016/0033-0620(85)90024-6

33. Wigle ED, Rakowski H, Kimball BP, Williams WG. Hypertrophic cardiomyopathy. *Clin Spectr Treatment Circ*. (1995) 92:1680–92. doi: 10.1161/01.CIR.92.7.1680

34. Maron BJ, Bonow RO, Cannon RO, Leon MB, Epstein SE. Hypertrophic cardiomyopathy. Interrelations of clinical manifestations, pathophysiology, and therapy (2). *N Engl J Med*. (1987) 316:844–52. doi: 10.1056/NEJM198704023161405

## Glossary

| | |
|---|---|
| 2D-STE | Two-dimensional speckle-tracking echocardiography |
| A-wave | Peak velocity of the late diastolic wave |
| DLVOTO | Dynamic left-ventricular outflow-tract obstruction |
| E-wave | Peak velocity of the early diastolic wave |
| E/A | E-wave to A-wave velocity ratio |
| FS | Fractional shortening |
| HCM | Hypertrophic cardiomyopathy |
| HNCM | Non-obstructive HCM |
| HOCM | Obstructive HCM |
| IVSd | End-diastolic interventricular septal thickness |
| LA/Ao | Left atrium to aortic diameter ratio |
| LV | Left-ventricular |
| LVIDd | End-diastolic LV internal diameter |
| LVOT Vmax | Peak velocity of left-ventricular outflow-tract |
| LVPWd | End-diastolic LV free-wall thickness |
| RWT | Relative left-ventricular wall thickness |
| SC | Circumferential strain |
| SL | Longitudinal strain |

frontiers | Frontiers in Veterinary Science

TYPE Case Report
PUBLISHED 27 June 2023
DOI 10.3389/fvets.2023.1083376



OPEN ACCESS

EDITED BY
Ahmed S. Mandour,
Suez Canal University, Egypt

REVIEWED BY
Francisco Ruben Carvallo Chaigneau,
Virginia Tech, United States
Elizabeth Anne Rozanski,
Tufts University, United States

*CORRESPONDENCE
Cassie N. Lux
✉ clux@utk.edu

†These authors have contributed equally to this work and share first authorship

RECEIVED 28 October 2022
ACCEPTED 08 June 2023
PUBLISHED 27 June 2023

CITATION
Edwards LM, Lux CN, Everett M and Hecht S (2023) Case report: Treatment of congenital lobar emphysema with lung lobectomy in a puppy. *Front. Vet. Sci.* 10:1083376. doi: 10.3389/fvets.2023.1083376



# Case report: Treatment of congenital lobar emphysema with lung lobectomy in a puppy

Lauren M. Edwards†, Cassie N. Lux*†, Matthew Everett and Silke Hecht

Department of Small Animal Clinical Sciences, University of Tennessee College of Veterinary Medicine, Knoxville, TN, United States

An 11-week-old, sexually intact female Catahoula Leopard dog was evaluated for a multiple-week history of exercise intolerance and intermittent periods of respiratory distress. Thoracic radiographs revealed a markedly hyperinflated right lung field, with compression of the surrounding lung lobes. Thoracic computed tomography further localized the hyperinflation to the right middle lung lobe, with suspicion of congenital lobar emphysema. A right intercostal thoracotomy with right middle lung lobectomy was performed successfully. Histopathology results confirmed bronchial cartilage hypoplasia with marked emphysema and pleural fibrosis. The puppy recovered from surgery uneventfully and was discharged from the hospital without any postoperative complications. At 18 months postoperatively, the dog was clinically normal with no return of respiratory distress. This case report describes successful surgical treatment of a large breed puppy with the uncommonly reported condition of congenital lobar emphysema.

KEYWORDS

**canine, lung lobectomy, lobar emphysema, congenital, computed tomography**

## Introduction

Congenital lobar emphysema (CLE) is a rare lower respiratory tract disease that most commonly presents in young dogs and cats, with age ranges in the literature from 6 weeks to 24 months of age (1–8). The literature predominately reports CLE in small or toy breed dogs, with rare reports in large breed dogs (9). Clinical signs reported in the literature include respiratory signs such as exercise intolerance, coughing, tachypnea or dyspnea, and cyanosis (1, 3–6, 8–13). Additionally, subcutaneous emphysema, pneumothorax, and pneumomediastinum have been noted on imaging and physical examination (3, 4, 7, 8, 13, 14). Congenital lobar emphysema is characterized by alveolar air accumulation resulting in hyperinflation of the affected lung lobes, most commonly due to bronchial cartilage hypoplasia, dysplasia, or aplasia leading to bronchial collapse (1–6, 8, 10, 11, 13–18). In the human literature, there are 3 recognized etiologies of lobar emphysema: bronchial cartilage dysplasia, which may range from hypoplastic and flaccid cartilage to a complete absence of tissue; external bronchial compression; and idiopathic (19, 20). Idiopathic etiologies have also been reported in veterinary patients, in which no bronchial abnormalities were identified on histopathology (7, 9, 10, 12). While many cases reported in the veterinary literature have bronchial abnormalities, ~80% of people diagnosed with CLE have an undetermined etiology, and only 20% have associated bronchial abnormalities (19). Surgical intervention with lung lobectomy of the affected lobes has been reported to result in successful treatment and recovery; however, older literature predominantly reported death or euthanasia in dogs

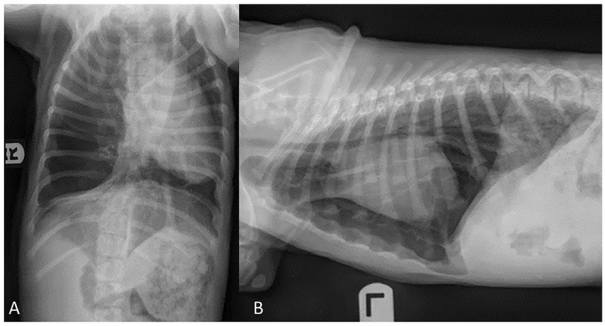


FIGURE 1
Ventrodorsal **(A)** and lateral **(B)** radiographic projections of an 11-week old, sexually intact, female Catahoula Leopard dog with congenital lobar emphysema. Noted in image **(A)**, is a left mediastinal shift, and images **(A, B)** depict a hyperlucent right lung lobe and displacement of the cardiac silhouette.

affected with CLE (10–14, 16, 21). The case report described here details diagnosis and treatment of a large-breed puppy with CLE.

## Case presentation

Informed consent was obtained from the owner for publication of this case report. An 11-week-old, sexually intact, female Catahoula Leopard dog with a weight of 6 kg was evaluated for a multiple-week history of exercise intolerance and intermittent periods of respiratory distress. At 8 weeks of age, the primary veterinarian performed thoracic radiographs to investigate for causes of exercise intolerance and respiratory distress (Figures 1A, B). The thoracic radiographs revealed a markedly hyperinflated and hyperlucent right lung lobe with compression of the surrounding lobes, displacement of the cardiac silhouette, and a leftward mediastinal shift. The dog was subsequently referred to a specialty hospital for further diagnostics and care with a differential diagnosis including congenital lobar emphysema based on the above radiographic changes.

On presentation to the soft tissue surgery service at the referral hospital, physical examination revealed absent right lung sounds and increased, harsh left lung sounds on thoracic auscultation. The dog's respiratory effort was moderately increased on presentation. Her temperature (100.4° F, 38°C), pulse (150 beats per min), and the remainder of her physical examination were within normal limits. Bloodwork abnormalities were consistent with the young age of the patient, including a mild anemia (hematocrit 35.1%; reference range 40.5–59.9%), lymphocytosis (lymphocytes 5.18 x $10^3$/μL; reference range 1.10–3.96 x $10^3$/μL), mild panhypoproteinemia (albumin 2.9 g/dL; reference range 3.2–4.3 g/dL and globulins 1.5 g/dL; reference range 1.9–3.1 g/dL), hyperphosphatemia (7.8 mg/dL; reference range, 2.5–5.9), hyperkalemia (4.9 mmol/L; reference range, 2.-4.7 mmol/L) and a mild elevation in ALP (295 U/L; reference range, 13–240 U/L). To further characterize the pulmonary pathology, a thoracic computed tomography (CT) scan was performed under general anesthesia with the intention to proceed directly to surgery pending the results of the CT scan. The patient was sedated with an intramuscular injection of butorphanol (0.4 mg/kg) and alfaxalone (2 mg/kg), after which anesthesia was induced with an intravenous injection of ketamine (5 mg/kg) and midazolam (0.25 mg/kg). General anesthesia was maintained with vaporized sevoflurane and continuous rate infusions of ketamine (10–20 mg/kg/h) and fentanyl (5–10 μg/kg/h).

A transverse multislice submillimeter helical dataset was obtained from the thoracic inlet to the cranial abdomen with a 40-slice helical CT scanner (Philips Brilliance-40, Philips International B.V., Amsterdam, Netherlands). To decrease risk of pulmonary rupture and pneumothorax, a breath hold was not utilized when acquiring the CT images. A pre- and post-contrast study was completed using iodinated contrast material (Optiray, 0.45 mL/kg of 350 mg I/mL IV).

Images revealed a severely distended right middle lung lobe with hypoattenuating parenchyma relative to the remaining lung lobes. Furthermore, the pulmonary vessels throughout the right middle lung lobe were decreased in size and the primary bronchus was mildly dilated, with abrupt narrowing in the distal bronchus.

Distension of the right middle lung lobe resulted in a marked leftward displacement of the heart and other mediastinal structures as well as the right cranial, right caudal and accessory lung lobes (Figure 2). Consequential compression of the left caudal and left cranial lung lobes also occurred. Multifocal regions of increased pulmonary attenuation and ground glass patterns throughout the displaced and compressed lung lobes were noted and attributed to atelectasis. A diagnosis of CLE was suspected based on hyperinflation of the right middle lung lobe and abrupt narrowing of the bronchus within the right middle lung most likely related to bronchial hypoplasia and less likely bronchial compression. The remaining changes of the thoracic cavity were deemed likely to be secondary to compression and displacement from the right middle lung lobe.

With careful consideration for the age of the patient and prognosis without treatment, it was elected to continue with surgical intervention. The dog proceeded to surgery immediately following the CT scan under the same anesthetic event. A fentanyl loading dose of 5 μg/kg was administered intravenously, and Normosol-R intravenous fluids were administered at a rate of 3 ml/kg/h. In addition to the vaporized sevoflurane, continuous rate infusions of ketamine (10–20 mg/kg/h) and fentanyl (5–10 μg/kg/h) were utilized to maintain a surgical plane of anesthesia.

Following aseptic preparation of the right lateral thoracic wall, the patient was positioned for surgery in left lateral recumbency. Mechanical ventilation was started prior to incision of the thoracic wall. A right lateral intercostal thoracotomy was performed with a 12 cm incision made in a dorsoventral direction along the 5$^{th}$ intercostal space. A standard intercostal thoracotomy approach with sharp and blunt dissection of the subcutaneous tissues and thoracic wall musculature was performed, and finochietto retractors were used for retraction of the ribs to aid in visualization.

The markedly inflated right middle lung lobe was manipulated to access the hilus, resulting in a majority of the lobe being

Abbreviations: CLE, congenital lobar emphysema; CT, computed tomography.

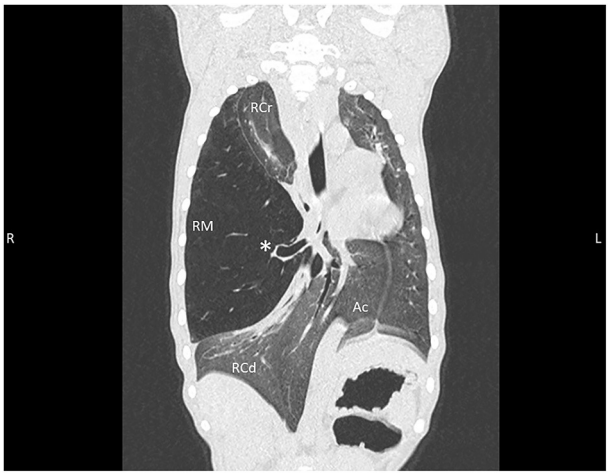


FIGURE 2
Thoracic CT dorsal reconstruction images from an 11-week old, sexually intact, female Catahoula Leopard dog with congenital lobar emphysema. Note the hyperinflated right middle lung lobe (RM) with an abrupt narrowing of the main stem bronchus (asterisk); leftward deviation of the heart, mediastinal structures, and accessory lung lobe (Ac); and diffuse increased attenuation/ground glass pattern within remaining right cranial (RCr) and right caudal (RCd) lung lobes as well as left lung.

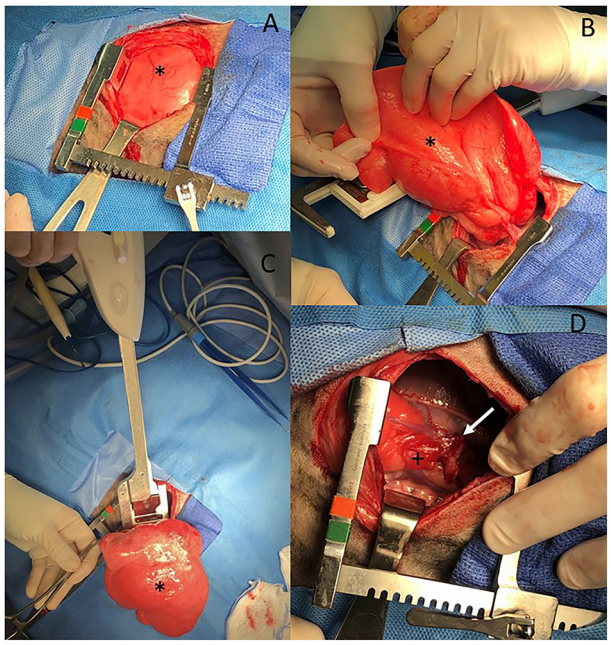


FIGURE 3
**(A–D)** Intraoperative images from an 11-week old, sexually intact, female Catahoula Leopard dog with CLE. The head is to the right and dorsal is on the bottom of all images. The right middle lung lobe (asterisk in all images) is occupying a majority of the right thoracic cavity **(A)** and is hyperinflated **(A, B)**. A lung lobectomy was performed with a DST Series TA Stapler using a 30 mm V3 vascular stapler **(C)**. The right middle lung hilus can be seen with the staple line (white arrow) following lobectomy, and the right caudal lung lobe has an area of atelectasis (+) **(D)**.

externalized from the thoracic cavity (Figure 3). A DST Series$^{TM}$ TA$^{TM}$ Stapler (Medtronic, Minneapolis, MN) with a 30 mm V3 Vascular (Medtronic, Minneapolis, MN) cartridge was used to seal the bronchus, artery and vein at the hilus of the right middle lung lobe. A scalpel was then used to excise the lung lobe distal to the staples. An exploratory exam of the right hemithorax was performed and was within normal limits except for notation of an atelectatic right caudal lung lobe.

A local block of bupivacaine (6 mg; 1 mg/kg) and lidocaine (6 mg; 1 mg/kg) was placed into the intercostal muscles cranial to, at the level of, and caudal to the incision. A red rubber catheter connected to a 3-way stopcock and 20 mL syringe was passed through the incision prior to closure for evacuation of air from the thorax. The ribs were apposed using simple interrupted sutures of 3-0 PDS, and the musculature of the thoracic wall was apposed with 3-0 Monocryl in a simple continuous pattern. Prior to closure of the skin, the anesthetist was consulted as to whether substantial resistance was noted during hand-ventilation. Air was suctioned from the thoracic cavity until anesthesia noted minimal resistance to ventilation. Negative pressure was not re-established within the thoracic cavity due to concern of re-expansion injury to the remaining lung lobes. The thoracic catheter used for air evacuation was removed prior to closure of the skin, and the skin was apposed in an intradermal pattern using 4-0 Monocryl.

Histopathology was performed including hematoxylin and eosin (H&E) stain, Masson's trichrome stain to identify collagen, and immunohistochemistry antibodies for AE1/AE3 cytokeratin to identify epithelial cells and α-smooth muscle actin (α-SMA) to evaluate bronchial smooth muscle of the resected right middle lung lobe (Figures 4–7). Results revealed bronchial cartilage hypoplasia characterized by variable quality cartilage to the absence of

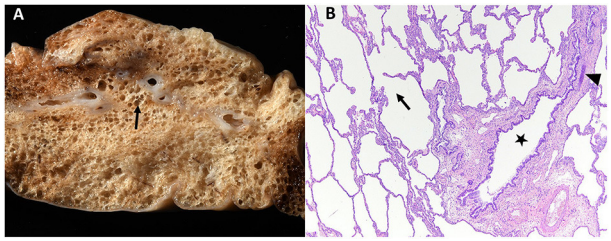


FIGURE 4
Gross **(A)** and histopathologic **(B)** images of the right middle lung lobe affected by CLE are depicted. Ruptured alveoli are present in the lung lobe: grossly this is visible as air pockets within the lung tissue (surrounding the arrow, **A**) and microscopically as discontinuity of the alveolus wall (arrow within alveolus, **B**). In image **(B)**, bronchial cartilage is present as a small discontinuous basophilic band (arrow head), which should fully surround a normal bronchus. This represents bronchial cartilage hypoplasia and is the cause of the bronchus in image **(B)** (star) being partially collapsed instead of rounded.

cartilage, dilated and coalescing alveoli consistent with marked emphysema, abnormal bronchial smooth muscle architecture, and expanded connective tissues and collagen with pleural fibrosis (Figures 4–7). The microscopic findings were consistent with the suspected clinical diagnosis of congenital lobar emphysema.

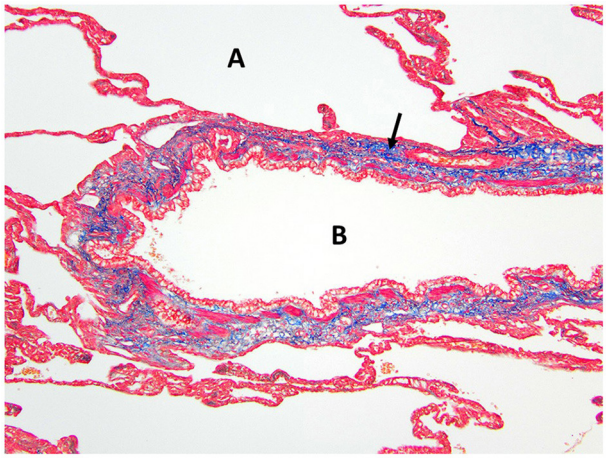


FIGURE 5
Masson's trichrome staining of the right middle lung lobe highlights the abundant collagen/connective tissues (arrow) surrounding the bronchus B with no cartilage present. A, alveolus.

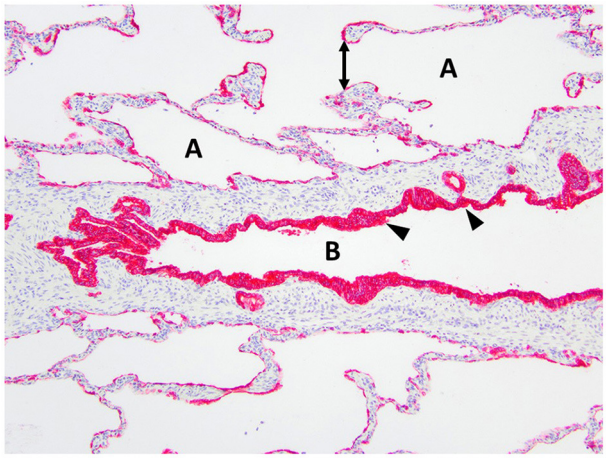


FIGURE 6
Immunohistochemistry AE1/AE3 cytokeratin of the right middle lung lobe highlights the bronchial epithelium with multilayered columnar to cuboidal epithelium and invaginations (arrowheads). The bronchus is identified as B. The alveoli are identified as A and contain ruptured septa with clubbed ends (double arrow).

The dog recovered uneventfully from anesthesia and was maintained on a fentanyl constant rate infusion (2–5 μg/kg/h IV, titrated to effect), gabapentin (10 mg/kg PO every 8 h), and carprofen (2 mg/kg PO every 12 h). Oxygen supplementation at an $FiO_2$ of 30–40% was provided for 8 h via an oxygen cage, and the dog had a normal respiratory rate and effort the following day out of oxygen supplementation. The dog was discharged 24 h postoperatively with no apparent complications. The owners reported the dog continued to recover well from surgery. As of 18 months postoperatively, the dog was doing clinically well, with no dyspnea or exercise intolerance per owner communication.

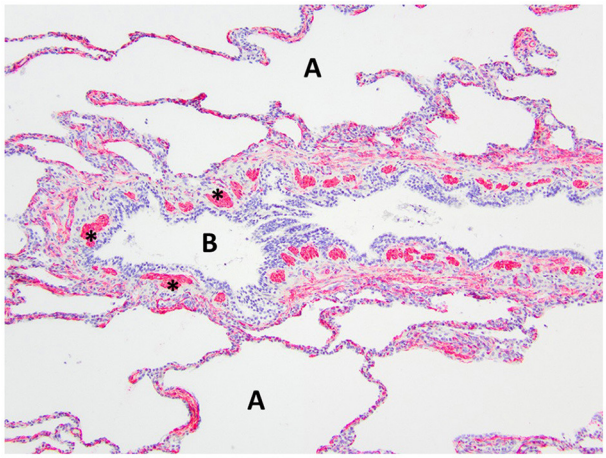


FIGURE 7
Immunohistochemistry α-SMA for smooth muscle of the right middle lung lobe highlights the abnormal bronchial smooth muscle architecture as the discontinuous smooth muscle bundles (asterisks) surrounding the bronchus B. A, alveoli.

## Discussion

This case report details the clinical treatment of a young dog diagnosed with CLE and undergoing successful surgical management of this condition. The diagnostic imaging, surgical, and histopathologic findings were all considered characteristic of CLE. Congenital lobar emphysema is a rare lower respiratory tract disease that is characterized by alveolar air accumulation with resulting hyperinflation of the affected lung lobes. Air accumulation is believed to be due to dynamic airway collapse, in which entry of air on inspiration occurs normally, however, abnormal bronchial collapse during expiration does not allow air to escape (1, 2, 9, 13, 19). It is this overdistension due to hyperinflation that causes the lung to be generally non-functional. Abnormal bronchial collapse and obstruction on expiration has been reported to be associated with bronchial cartilage hypoplasia, dysplasia, and aplasia; external bronchial compression; and idiopathic etiologies (1–7, 10–12, 14, 17, 18).

Histopathology of the lung lobe removed from the dog reported here revealed bronchial cartilage hypoplasia with marked emphysema and pleural fibrosis. The microscopic findings of this lung lobe including the abundant collagen with no cartilage around the bronchus on the Masson's trichrome stain, the abnormal bronchial smooth muscle architecture on the α-SMA immunostaining, the cuboidal and invaginated epithelium lining the bronchus on the AE1/AE3 immunostaining, and the many areas of discontinuous ruptured alveolar septa were consistent with a diagnosis of CLE and previously reported (7, 8, 14). The pathologist commented that the deficient bronchial cartilage and bronchial atresia resulting in defects in the bronchial walls caused greater volumes of air to enter the affected lobe on inspiration than exited on expiration, resulting in air trapping and the clinical presentation of a hyperinflated lung lobe. The bronchial hypoplasia diagnosed here has been previously documented as associated with

CLE in 10 reported cases in the literature (4–6, 14–17). Pleural fibrosis has been noted in other dogs with histopathologic analysis of the affected lung lobes, however the clinical significance of pleural fibrosis, as it pertains to CLE in dogs, is not described (7, 8, 14). Although some reported cases in dogs have determined CLE to be idiopathic in nature, it appears the dog in this report developed CLE due to the aforementioned bronchial abnormalities (7, 9, 10, 12).

The dog in this report was 11 weeks old at the time of surgery with clinical signs starting as early as 8 weeks old. Although CLE is often diagnosed in young animals, the dog in this report is one of the youngest dogs to have been clinically affected by CLE and successfully treated with surgical excision of the affected lung lobe. The 10 previous CLE patients with descriptions of successful surgical treatment consisted of nine dogs, ranging from 6 weeks to 10 years of age, and one 5-month-old kitten (1–9, 18). On evaluation of the previously reported cases, the median age at the time of successful treatment of CLE in the nine dogs was 20 weeks and was also 20 weeks in the only reported cat (1–9, 18). Importantly, this case report highlights a successful anesthetic and invasive surgical event for a pediatric puppy (<12 weeks old), which comes with additional risks due to the immature age including reduced ability to respond to cardiovascular changes; immature renal, hepatic, and thermoregulatory functions; and reduced pulmonary reserve with high oxygen consumption (22, 23).

Of the 10 case reports with successful surgical treatment described previously, lobectomy has been performed on the following affected lung lobes in dogs and cats with CLE: 7/10 for the right middle lung lobe, 2/10 for the left caudal subsegment of the left cranial lung lobe, and 1/10 for the left caudal subsegment of the left cranial lung lobe and accessory lobe simultaneously (1–9, 18). A recent retrospective study of 14 dogs and 3 cats with lobar emphysema suspected a congenital etiology in 14/17 animals (17). In the same report, 8/17 animals underwent lung lobectomy with confirmed CLE diagnosis of the right middle lung lobe in all 8 cases, though one dog and one cat also had the right cranial and right caudal lobes affected, respectively (17). The dog in the case reported here, similar to other cases, was affected with CLE in the right middle lung lobe.

Although a variety of large-breed dogs with CLE have been reported (9, 11, 12, 17), descriptions of successful surgical intervention in the literature for large breed dogs are limited to a single case report of an Old English Sheepdog (9). Therefore, the description of successful surgical intervention for the dog in this report supplements the literature for surgical intervention in large-breed dogs. Although it is possible that other large-breed dogs were treated surgically, breed descriptions for dogs undergoing surgery were not available for one report (17). The majority of reports with successful surgical treatment are in small breed dogs (1, 3–8, 18).

Hyperinflation of the affected lung lobe on the thoracic radiographs resulted in pursuit of a CT scan to further define pulmonary pathology in the dog described here. Evidence of hyperinflation and hyperlucency of the affected lung lobes, mediastinal shift, pulmonary atelectasis, and elevation of the cardiac silhouette from the sternum were common findings in 15 previous cases that utilized radiography in their diagnosis of CLE (1–13, 16, 18). Of the 15 cases diagnosed by thoracic radiography and supporting clinical signs, only five went on to utilize CT for surgical planning (2, 3, 5, 6, 8). The CT scan in this dog revealed severely expanded pulmonary parenchyma with hypoattenuation compared to the surrounding lung lobes consistent with hyperinflation, which was also seen in all previously reported cases undergoing CT (2, 3, 5, 6, 8). The value of CT lies in the ability to diagnose other concurrent conditions in the pulmonary parenchyma and thoracic cavity such as pneumothorax, pneumomediastinum, bullae or blebs, bronchial abnormalities, and concurrent abnormalities in other lung lobes, which are all variably reported in the literature (2, 3, 5, 6, 8). It is important to note that multiple cases have been reported involving more than one lung lobe based on CT diagnosis (5, 17). Therefore, if a CT scan is not performed prior to surgical intervention, consideration should be made to approach the thoracic cavity via a median sternotomy instead of an intercostal thoracotomy if there is any concern that additional lung lobes on opposite sides of the thoracic cavity may be affected. This will allow for effective exploration of both hemithoraces. The additional findings in the dog of this case report due to use of the CT scan included abrupt narrowing of the bronchus in the affected lung lobe, compression with atelectasis of local lung lobes, and displaced thoracic structures.

It should be noted that not all patients are immature at the time of CLE diagnosis, and some patients may be asymptomatic for CLE (4, 8, 16–18). However, most patients do exhibit clinical signs related to CLE and at an immature age, similar to the dog of this report. Out of the total 18 cases with surgical intervention for CLE reported in the literature (1–9, 18), only one case of perioperative death has been reported (1–9, 17, 18). In addition, 7/18 reported cases also detail long-term follow-up revealing clinically normal dogs (1–6, 8). Given the reported good short- and long-term outcomes, the literature supports surgical removal of affected lung lobes as treatment of choice for CLE, particularly for clinically affected dogs. Prognosis for the dog of this case report is excellent given the lack of dyspnea or exercise intolerance at 18 months postoperatively, as well as confirmation on preoperative imaging that the remaining lung lobes were within normal limits.

## Data availability statement

The original contributions presented in the study are included in the article/supplementary material, further inquiries can be directed to the corresponding author.

## Ethics statement

Ethical review and approval was not required for the animal study because this is a case report of a clinical case and underwent no changes to clinical care as a result of this case report. Written informed consent was obtained from the owners for the participation of their animals in this study. Written informed consent was obtained from the individual(s) for the publication of any potentially identifiable images or data included in this article.

## Author contributions

CL, SH, and ME were involved in the clinical management of this case. CL, SH, and LE discussed the case. LE was responsible for drafting the manuscript. All authors read and approved the final version of the manuscript.

## Acknowledgments

The authors would like to acknowledge the hospital staff at the University of Tennessee Veterinary Medical Center for the care provided to this patient.

## Conflict of interest

The authors declare that the research was conducted in the absence of any commercial or financial relationships that could be construed as a potential conflict of interest.

## Publisher's note



## References

1. Billet JPHG, Sharpe A. Surgical treatment of congenital lobar emphysema in a puppy. *J Small Anim Pract.* (2002) 43:84–7. doi: 10.1111/j.1748-5827.2002.tb00035.x

2. Blonk M, van de Maele I, Combes A, Stablay B, De Cock H, Polis I, et al. Congenital lobar emphysema in a kitten. *J Small Anim Pract.* (2017) 58:659–63. doi: 10.1111/jsap.12668

3. Han JH, Kim JH. Concurrent pulmonary hypoplasia and congenital lobar emphysema in a young dog with tension pneumothorax: a rare congenital pulmonary anomaly. *Acta Vet Scand.* (2019) 61:1–6. doi: 10.1186/s13028-019-0472-2

4. Matsumoto H, Kakehata T, Hyodo T, Hanada K, Tsuji Y, Hoshino S, et al. Surgical correction of congenital lobar emphysema in a dog. *J Vet Med Sci.* (2004) 66:217–9. doi: 10.1292/jvms.66.217

5. Regier PJ, Gallastegui A, Craft WF. Successful treatment of congenital lobar emphysema in multiple lung lobes in an English Bulldog puppy. *J Am Anim Hosp Assoc.* (2021) 57:96–100. doi: 10.5326/JAAHA-MS-7088

6. Ruth J, Rademacher N, Ogden D, Rodriguez D, Gaschen L. Imaging diagnosis: congenital lobar emphysema in a dog. *Vet Radiol Ultrasound.* (2011) 52:79–81. doi: 10.1111/j.1740-8261.2010.01732.x

7. Stephens JA, Parnell NK, Clarke K, Blevins WE, DeNicola D. Subcutaneous emphysema, pneumomediastinum, and pulmonary emphysema in a young schipperke. *J Am Anim Hosp Assoc.* (2002) 38:121–4. doi: 10.5326/0380121

8. Yun S, Lee H, Lim J, Lee K, Jang K, Shiwa N, et al. Congenital lobar emphysema concurrent with pneumothorax and pneumomediastinum in a dog. *J Vet Med Sci.* (2016) 28:909–12. doi: 10.1292/jvms.15-0362

9. Mitchell C, Nykamp S. Imaging diagnosis: congenital lobar emphysema in an old English sheepdog puppy. *Vet Radiol Ultrasound.* (2006) 47:465–7. doi: 10.1111/j.1740-8261.2006.00178.x

10. Herrtage ME, Clarke DD. Congenital lobar emphysema in two dogs. *J Small Anim Pract.* (1985) 26:453–64. doi: 10.1111/j.1748-5827.1985.tb02225.x

11. Hoover JP, Henry GA, Panciera RJ. Bronchial cartilage dysplasia with multifocal lobar bullous emphysema and lung torsions in a pup. *J Am Vet Med Assoc.* (1992) 201:599–602.

12. Tennant BJ, Haywood S. Congenital bullous emphysema in a dog: a case report. *J Small Anim Pract.* (1987) 28:109–16. doi: 10.1111/j.1748-5827.1987.tb05975.x

13. Voorhout G, Goedegebuure SA, Nap RC. Congenital lobar emphysema caused by aplasia of bronchial cartilage in a Pekingese puppy. *Vet Pathol.* (1986) 23:83–4. doi: 10.1177/030098588602300116

14. Gopalakrishnan G, Stevenson GW. Congenital lobar emphysema and tension pneumothorax in a dog. *J Vet Diagn Invest.* (2007) 19:322–5. doi: 10.1177/104063870701900319

15. Amis TC, Hager D, Dungworth DL, Hornof W. Congenital bronchial cartilage hypoplasia with lobar hyperinflation (congenital lobar emphysema) in an adult Pekingese. *J Am Anim Hosp Assoc.* (1987) 23:321–9.

16. Moon HS, Lee MH, Han JH, Kim SK, Lee SG. Asymptomatic congenital lobar emphysema in a Pekingese dog. *J Anim Vet Adv.* (2007) 6:556–8.

17. Warwick H, Guillem J, Batchelor D, Schwarz T, Liuti T, Griffin S, et al. Imaging findings in 14 dogs and 3 cats with lobar emphysema. *J Vet Intern Med.* (2021) 35:1935–42. doi: 10.1111/jvim.16183

18. Orima H, Fujita M, Aoki S, Washizu M, Yamagami T, Umeda M, et al. A case of lobar emphysema in a dog. *J Vet Med Sci.* (1992) 54:797–8. doi: 10.1292/jvms.54.797

19. Karnak I, Senocak ME, Ciftci AO, Buyukamukcu N. Congenital lobar emphysema: diagnostic and therapeutic considerations. *J Pediatr Surg.* (1999) 34:1347–51. doi: 10.1016/S0022-3468(99)90009-X

20. Stovin P. Congenital lobar emphysema. *Thorax.* (1959) 3:254–62. doi: 10.1136/thx.14.3.254

21. Coutu MP, Rousset N, Cosford K. Dynamic cervical lung herniation causing dysphagia in a puppy. *Vet Rec Case Rep.* (2015) 3:1–5. doi: 10.1136/vetreccr-2015-000193

22. Kustritiz MV. Early spay-neuter: clinical considerations. *Clin Tech Small Anim Pract.* (2002) 17:124–8. doi: 10.1053/svms.2002.34328

23. Grubb TL, Jimenez TE, Pettifer GR. Ch 53: neonatal and pediatric patients. In: Grimm KA, Lamont LA, Tranquilli WJ, Green SA, Robertson SA, editors. *Veterinary Anesthesia and Analgesia: Fifth Edition of Lumb and Jones.* Ames, Iowa: John Wiley & Sons, Inc. (2015). p. 983–7. doi: 10.1002/9781119421375.ch53

frontiers | Frontiers in Veterinary Science

TYPE Perspective
PUBLISHED 29 June 2023
DOI 10.3389/fvets.2023.1180125



OPEN ACCESS

EDITED BY
Ahmed S. Mandour,
Suez Canal University, Egypt

REVIEWED BY
Walaa Mohamadein,
Suez Canal University, Egypt

*CORRESPONDENCE
Romy M. Heilmann
✉ romy.heilmann@kleintierklinik.uni-leipzig.de

RECEIVED 05 March 2023
ACCEPTED 16 June 2023
PUBLISHED 29 June 2023

CITATION
Heilmann RM, Csukovich G, Burgener IA and Dengler F (2023) Time to eRAASe chronic inflammation: current advances and future perspectives on renin-angiotensin-aldosterone-system and chronic intestinal inflammation in dogs and humans.
*Front. Vet. Sci.* 10:1180125.
doi: 10.3389/fvets.2023.1180125



# Time to eRAASe chronic inflammation: current advances and future perspectives on renin-angiotensin-aldosterone-system and chronic intestinal inflammation in dogs and humans

Romy M. Heilmann[1]*, Georg Csukovich[2], Iwan A. Burgener[2] and Franziska Dengler[3]

[1]Department for Small Animals, College of Veterinary Medicine, University of Leipzig, Leipzig, Germany, [2]Small Animal Internal Medicine, University of Veterinary Medicine Vienna, Vienna, Austria, [3]Institute of Physiology, Pathophysiology and Biophysics, University of Veterinary Medicine Vienna, Vienna, Austria

Chronic idiopathic intestinal inflammation is an increasing worldwide problem that affects companion animals, especially dogs, and human patients. Although these disease entities have been intensely investigated recently, many questions remain, and alternative therapeutic options are needed. Diarrhea caused by dysregulation of intestinal electrolyte transport and subsequent fluid and electrolyte losses often leads to secondary consequences for the patient. Currently, it is not exactly clear which mechanisms are involved in the dysregulation of intestinal fluid absorption, but differences in intestinal electrolyte shifts between human and canine patients suggest species-specific regulatory or counterregulatory mechanisms. Several intestinal electrolyte transporters are differentially expressed in human patients with inflammatory bowel disease (IBD), whereas there are virtually no studies on electrolyte transporters and their endocrine regulation in canine chronic inflammatory enteropathy. An important mechanism involved in regulating fluid and electrolyte homeostasis is the renin-angiotensin-aldosterone-system (RAAS), which may affect intestinal $Na^+$ transport. While RAAS has previously been considered a systemic regulator of blood pressure, additional complex roles of RAAS in inflammatory processes have been unraveled. These alternative RAAS pathways may pose attractive therapeutic targets to address diarrhea and, thus, electrolyte shifts in human IBD and canine chronic inflammatory enteropathy. This article comparatively summarizes the current knowledge about electrolyte transport in human IBD and canine chronic inflammatory enteropathy and the role of RAAS and offers perspectives for novel therapeutic avenues.

KEYWORDS

**alternative RAAS, chronic inflammatory enteropathy, inflammatory bowel disease, electrolyte transport, enteroids, tight junctions**

## 1. Chronic intestinal inflammation—a one-health perspective

Human IBD—comprising mainly Crohn's disease (CD) and ulcerative colitis (UC)—has a high prevalence in industrialized countries, and patients often experience severe distress and significantly reduced quality of life. Healthcare costs to treat IBD in humans are immense, amounting to 15–30 billion US dollars annually in the United States and about 5 billion Euros in Europe (1). The exact prevalence of chronic inflammatory enteropathy (CIE) in dogs is currently unknown, but it is estimated at 1%–2% in referral settings (2). CIE in dogs can range in severity and is subcategorized based on the response to treatment (2). In contrast to canine CIE, different compartments of the intestines are predominantly affected in patients with CD and UC, likely reflecting differences in the disease pathogenesis. Overt inflammatory responses are a common characteristic, resulting from environmental factors (dietary and microbial antigens) combined with a genetic predisposition (3). Dogs have accompanied humans and shared the human lifestyle for over 1,000 years, and it is thus not surprising that they develop similar civilization diseases. The prevalence of idiopathic IBD—either responsive (immunosuppressant-responsive enteropathy, IRE) or not responsive (non-responsive enteropathy, NRE) to immunosuppressive treatment—as a form of chronic inflammatory enteropathies (CIE) in dogs increased simultaneously with the rise of IBD in humans and both diseases share many characteristics, including pathogenesis and clinical signs (4–7). In dogs, CIE is characterized by chronic gastrointestinal signs, exclusion of other underlying diseases, and confirmation of gastrointestinal inflammation together with a response to treatment with either an elimination diet alone (food-responsive enteropathy, FRE) or in combination with immunosuppressant medication (IRE or NRE) (2, 6, 7). The resulting diarrhea and accompanying shifts in plasma electrolytes can severely compromise the dogs' and their owners' quality of life.

A hallmark of IBD is diarrhea due to intestinal hypersecretion and hampered reabsorption of electrolytes and fluid, often accompanied by serum electrolyte changes. Although the clinical signs are similar and largely overlapping, reports suggest different compensatory mechanisms to be activated both in the intestinal epithelium and on the systemic level in affected humans and dogs (8–10), which might also call for different therapeutic approaches. While hyponatremia is the most common electrolyte change in human IBD (11), hypokalemia appears more prevalent in canine CIE (9), suggesting species-specific compensatory mechanisms. A better understanding of the pathophysiologic mechanisms in dogs with CIE is expected to help identify novel therapeutic targets that could ameliorate diarrhea in affected dogs and be valuable for treating human IBD patients. While IBD in people has been under investigation for decades, significantly less is currently known about the pathophysiology of chronic idiopathic intestinal inflammation (CIE) in dogs.

## 2. Pathophysiology of diarrhea—gastrointestinal electrolyte transport and barrier formation

Central functions of the intestinal epithelium are the formation of a tight barrier to shield the host from luminal microbiota and other noxae and the vectorial transport of nutrients, electrolytes, and water. Uptake and secretion of nutrients and electrolytes are the major driving force for the (mostly paracellular) absorption and secretion of water. The gastrointestinal tract faces large fluid and electrolyte shifts, and the healthy intestinal mucosa absorbs about 98% of that fluid (12, 13). The (passive) movement of water is driven by the (active) uptake or secretion of electrolytes, primarily $Cl^-$ and $Na^+$. Due to its high absorptive capacity, the colonic epithelium can compensate for an increased secretion and/or defective absorptive capacity in the small intestine (14). Diarrhea develops if the compensatory capacity of the colon is exceeded and is often accompanied by serum electrolyte changes. The highest fecal water output is thus seen with disease involving the colon (12). Not surprisingly, diarrhea is invariably seen in humans with IBD, particularly in UC (15). In dogs, the lesions are typically more heterogeneously distributed in the gastrointestinal tract, and about 80% of affected animals show diarrhea (9). This lower prevalence of diarrhea [80% in dogs vs. 100% in people (9, 15)] might indicate a slightly more efficient compensation of intestinal malabsorption in dogs than in people.

Both increased secretion and reduced absorption of electrolytes cause diarrhea in human IBD patients (16). However, colonic absorption could still compensate for this if the colonic absorptive and re-absorptive transport mechanisms remain intact (17, 18). The main mechanisms for the uptake of luminal electrolytes—and thus the absorption of water—in the mammalian intestine is $Na^+$-coupled cotransporters, particularly the $Na^+/H^+$-exchanger family (NHE) and the epithelial $Na^+$ channel (ENaC). Both are downregulated in human IBD (19, 20) and rodent models of dextran-sulfate-sodium-induced colitis, along with the $Na^+/K^+$-ATPase that generates the gradient for the effective uptake of $Na^+$ from the intestinal lumen (11, 20, 21), causing a decreased (re-)absorption of water. A knockout of NHE3, but not of NHE2, leads to diarrhea in a mouse model (22), and NHE3 was demonstrated to be the major isoform for $Na^+$ absorption across the canine ileum epithelium (23).

This finding is especially interesting in conjunction with reports of increased serum aldosterone levels in human IBD patients (11, 24), suggesting a systemic attempt at a counter-regulation mediated by the renin-angiotensin-aldosterone system (RAAS) as ENaC, NHE3 and $Na^+/K^+$-ATPase are upregulated by aldosterone (25–27). Other transport proteins might also be involved in the dysregulation of intestinal fluid absorption, such as the anion exchangers putative anion transporter 1 (PAT1), down-regulated in adenoma (DRA), the $Cl^-$ channel cystic fibrosis transmembrane conductance regulator (CFTR) (16, 28), monocarboxylate transporter 1 (MCT1) (11, 21), and anion exchanger 2 (AE2). The $Na^+/K^+/2Cl^-$ cotransporter (NKCC) on the basolateral side of the epithelium might have a pivotal role in regulating the driving force for intestinal secretion [e.g., by CFTR and chloride channel 2 (CLC2)]. Similarly, basolateral $K^+$ channels might be important in driving colonic secretion. The $K^+$ channel KCNN4 is specifically upregulated in human IBD patients (29), and additional $K^+$ channels or pumps may be located in the intestinal epithelial brush border membrane (16), but their role in human IBD (and canine CIE) is poorly understood. The effect of CIE on intestinal electrolyte transport in dogs has not been investigated to date.

Following established electrolyte gradients, the secretion and reabsorption of water mainly take the paracellular route. Therefore, the epithelial barrier formed by tight junction proteins is an important factor in the pathogenesis of diarrhea. Tight junctions and

other cell–cell contacts are essential components located between adjacent epithelial and endothelial cells throughout the mammalian organism. In human IBD, the barrier-forming claudins 3, 4, 5, 7, and 8 are downregulated and disoriented from the plasma membrane, as are occludin and ZO-1, whereas the pore-forming claudin 2 is upregulated (30) along with increased paracellular permeability (20). In dogs with CIE, the expression of claudins or occludin is not altered in the duodenum, but colonic occludin mRNA levels are decreased (31). Apart from these findings, the regulation of tight junction proteins has yet to be investigated in dogs with CIE (32), but a thorough understanding of their role would be a major premise for further studying the pathomechanisms of CIE-related diarrhea in dogs. The colonic expression of occludin and claudin 8 is regulated (along with ENaC) by aldosterone (33), which may imply an additional therapeutic potential for RAAS in IBD and potentially also CIE in dogs.

## 3. Classical and alternative RAAS pathways—great complexity and far-reaching effects

RAAS has been extensively studied in cardiovascular and renal pathophysiology, and it appears to have much greater non-linear complexity than previously known (34). It acts on intestinal transport and barrier function, as described above. In addition, RAAS is involved in other intestinal functions, including the absorption of glucose and peptides, gastrointestinal motility, and the regulation of mesenteric blood flow (35, 36). Given the differences in electrolyte imbalances between canine CIE and human IBD patients, RAAS pathways might be differentially activated in these conditions.

Classically, renin cleaves angiotensinogen to angiotensin I (Ang I), which is then processed by angiotensin-converting enzyme (ACE) to the vasoconstrictor Ang II that activates aldosterone. This "traditional RAAS" has been well characterized as a circulatory blood pressure regulator (Figure 1A) and has presented a pharmacotherapeutic target for decades. In contrast, the existence of additional peptides derived from Ang I and II that constitute the "alternative RAAS" and their role in cardiovascular physiology and disease pathogenesis has long been neglected. The involvement of these recently discovered factors (Figure 1B) challenges the former simple concept of RAAS but also lends itself to potential novel therapeutic avenues beyond managing cardiovascular pathologies. Recent evidence also supports the coexistence of localized "tissue RAAS" mediating local (paracrine) effects.

Renin, a peptidase, represents the rate-limiting step in the RAAS cascade. After release from epithelioid cells of the renal juxtaglomerular apparatus into the circulation, renin cleaves an N-terminal decapeptide from angiotensinogen, a glycoprotein of the globulin superfamily synthesized in the liver and (though controversial) adipose tissue (37, 38), resulting in Ang I. The biologically active octapeptide Ang II results from the cleavage of Ang I by ACE, which is expressed primarily by pulmonary and renal endothelial cells and has also been detected in other tissues, including the myocardium and intestines (39). ACE is most active when bound to cell membranes. Together with the short half-life of Ang I and II, this indicates localized actions of RAAS (40). Similarly, an effect of renin and/or Ang II at the tissue level, rather than in the circulation, is supported by detecting (pro-)renin receptors in several tissues, such as the heart, brain, placenta, kidney, and liver (41).

The main effect of Ang II is an increase in systemic blood pressure by regulating vasoconstriction and cardiac output (42). As an intermediate effect, increased $Na^+$ reabsorption in the proximal renal tubules (via NHE3) and induction of thirst and salt appetite, subsequently increasing extracellular volume and, thus, blood pressure, are induced (43–45). As a longer-term effect, Ang II stimulates (a) the expression and secretion of aldosterone, thus increasing the reabsorption of $Na^+$ in the renal collecting ducts via ENaC on the gene expression level and (b) hypothalamic antidiuretic hormone (ADH, vasopressin) secretion leading to the insertion of aquaporins in the renal collecting ducts (25). Together, these mechanisms increase water reabsorption and thus blood volume and systemic blood pressure (Figure 1). It is important to recognize, however, that the enhanced reabsorption of $Na^+$ in the collecting ducts causes a concurrent loss of $K^+$ due to the extrusion of $K^+$ via apical channels into the lumen of the renal collecting ducts, which is driven by the electrochemical gradient that increases with the reabsorption of $Na^+$ (46).

Beyond these direct and indirect effects on systemic blood pressure, Ang II also elicits immunomodulatory effects by inducing proinflammatory cytokines and chemokines (e.g., TNFα, IL-6, and TGF-β1) in renal tubular cells and cells of the immune system (47–49). Ang II is also involved in hypertrophic remodeling (e.g., of the myocardium) by inducing cell proliferation and growth, but a direct effect of Ang II on extracellular matrix synthesis has also been observed (24, 47, 50). Thus, Ang II is presumed to be involved in the pathologic process of fibrogenesis (e.g., cardiac, renal, and hepatic fibrosis) (51, 52), which is also a major factor in the pathogenesis of human IBD (53). The binding of prorenin to its tissue receptor further contributes to myocardial fibrosis via the activation of intracellular signaling pathways (54, 55).

Four angiotensin-receptor (ATR) isoforms have been described, AT1R–AT4R. The ATRs are G-protein coupled transmembrane receptors (40) that might dictate the effects of Ang II by spatial differences in tissue abundance. AT1R is the primary receptor mediating the effects of Ang II and is expressed in most tissues, particularly the liver, adipose tissue, and placenta (39, 56). While AT1R is well characterized, the exact functions of the remaining three isoforms of ATR remain currently unknown. AT2R is found primarily during fetal development but may be upregulated under pathological conditions in adulthood (43), especially those affecting the lungs or smooth muscle (56). A vasodilatory effect of AT2R (i.e., opposing AT1R-mediated effects) has also been reported (40, 57, 58) and may provide a "safety net" preventing exaggerated and counterproductive effects of Ang II via AT1R.

Besides these traditional RAAS components, additional enzymes are described to act on Ang I and Ang II, representing the "alternative RAAS" (Figure 1B). To date, the best characterized is ACE2, which can cleave a nonapeptide, Ang (1–9), from Ang I or a heptapeptide, Ang (1–7), from Ang II (59, 60). Interestingly, one of the first observations of an alternative route of Ang I breakdown to Ang (1–7), independent from ACE, was in dogs (61). Ang (1–9) can also be converted to Ang (1–7) by ACE. Ang (1–7) responses can counteract those of Ang II [i.e., vasorelaxant, anti-proliferative, anti-inflammatory, anti-fibrotic,

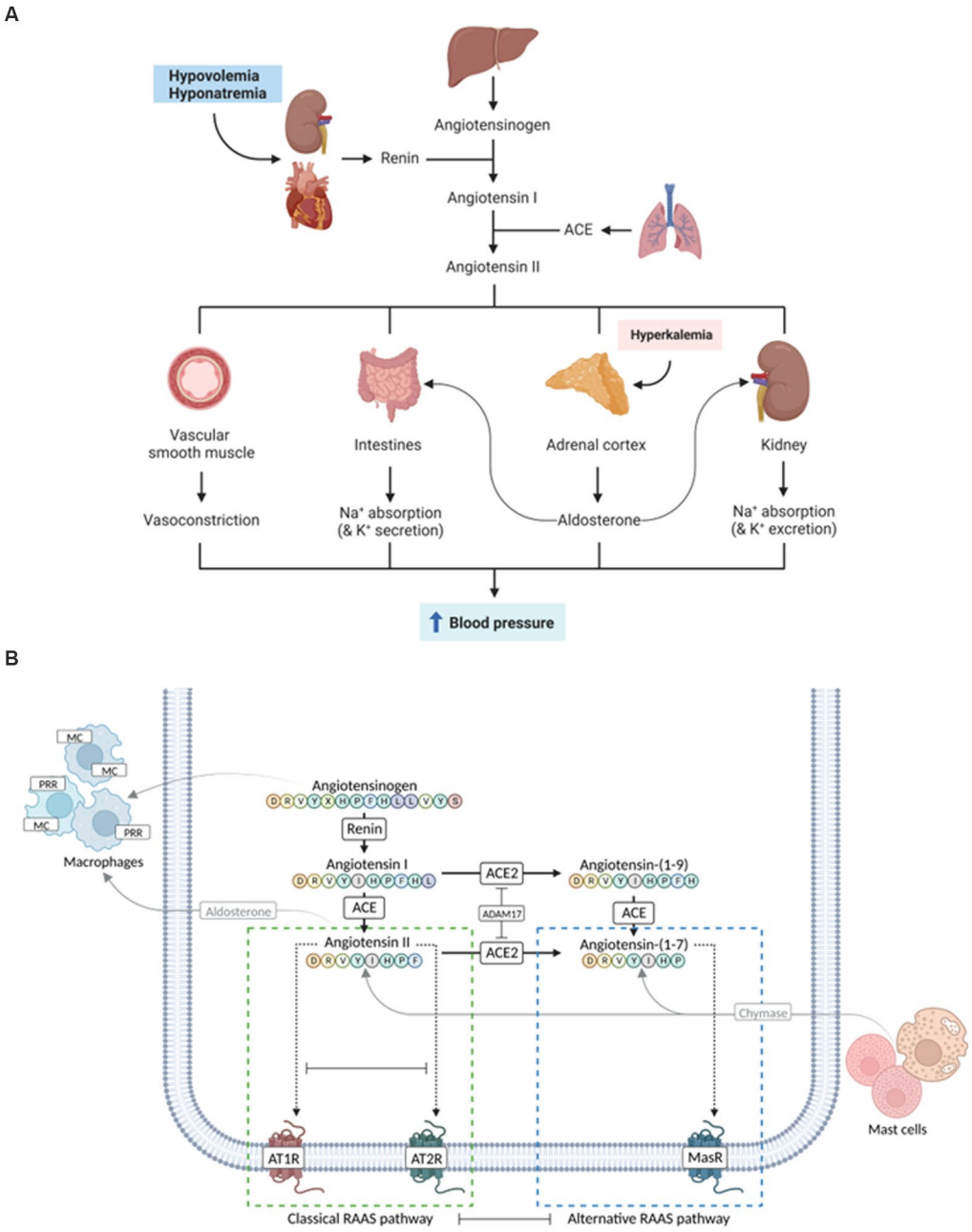


FIGURE 1
Evolution of the complexity of the renin-angiotensin-aldosterone system (RAAS). **(A)** Traditional simple view of the RAAS involving mostly cardiovascular and renal effects. **(B)** More recent complex view on classical and alternative RAAS pathways that might play a role in human inflammatory bowel disease (IBD) and/or canine chronic inflammatory enteropathy (CIE). Whereas the activation of the classical arm leads to vasoconstrictive, proinflammatory, profibrotic, and prothrombotic effects (green dashed box), components of the alternative RAAS pathways result in vasodilatory, anti-inflammatory, antifibrotic, and antithrombotic responses (blue dashed box). ACE, angiotensin-converting enzyme; ATR, angiotensin receptor; MR, mineralocorticoid receptor; PRR, prorenin receptor. Images created with BioRender.com.

and thus likely (cardio-)protective] (59, 62, 63), presumably via binding to AT2R (54, 59). In hypertensive rats, Ang (1–7) reduced the heart rate but not systemic blood pressure (63). Simultaneously, the formation of Ang (1–7) from Ang II is inherent in decreased Ang II concentrations. With the discovery of Mas, an additional RAAS receptor was identified that might act as the main receptor for Ang (1–7) and thus the "alternative arm" of RAAS (59, 62, 64). The pathophysiologic role and effects of Ang (1–7) have raised hopes for a therapeutic application to address the adverse effects of Ang II in various pathologies. However, the pathways and effects of Ang II are currently still controversial and remain first to be clarified (63). Formation of Ang (2–8) (also referred to as Ang III) and Ang (3–8) (also known as Ang IV) has also been described (40). These peptides bind to AT1R and elicit similar effects as Ang II (54).

## 4. RAAS crossroads between adaptation, disease, and novel therapeutic targets

Components of the RAAS have paracrine and/or autocrine cytokine-like effects and regulate inflammation, tissue repair, and fibrosis (21, 65, 66), all important factors in the pathogenesis of canine CIE and human IBD. In addition to upregulating adhesion molecules, Ang II is chemotactic for inflammatory cells, particularly of the mononuclear lineage. These cells produce RAAS components following activation (mediated by IL-1, TNF-α, NF-κB, and/or PPARγ), resulting in a positive-feedback loop with the potential to perpetuate chronic inflammatory responses (66–68). Ang II also has profibrotic effects via TGF-β, connective tissue growth factor stimulation, and inhibition of matrix metalloproteinase (MMP)-mediated extracellular matrix degradation (69). While conflicting data exist on TGF-β expression in canine CIE depending on the gastrointestinal segment affected (4, 70–73), and unlike in humans stricturing behavior is not observed in affected dogs, intestinal mucosal MMP-2 and -9 activities are increased in canine CIE (74). Toll-like receptor (TLR) and RAGE (receptor for advanced glycation end products) expression are dysregulated in canine CIE (5, 75, 76), and RAAS blockade has anti-inflammatory effects by suppression of TLR2 and TLR4 in humans (77).

Inhibition of RAAS pathways [e.g., Ang II production by ACE inhibitors (ACEIs) or its effects by ATR blockers (ARBs)] could downregulate inflammatory mediators and the innate immune receptors TLR2, TLR4, and RAGE. This concept presents a novel therapeutic strategy that targets the inflammatory response in canine CIE and warrants further study. Classical and alternative RAAS pathways (Figure 1B) are complementary systems with the potential to oppose or compensate for the actions of the contralateral arm (60, 77, 78), and their balance (or imbalance) might play an important role in the pathogenesis of intestinal inflammation. Thus, a (receptor) specific approach is most promising for therapeutically targeting the RAAS. The alternative RAAS has anti-inflammatory properties (59, 60). Ang (1–7) is a promising therapeutic target that attenuated intestinal inflammation in a rodent model of IBD (78). Components of classical and alternative RAAS are expressed in the intestinal mucosa in humans (34, 78, 79), with disparate ACE2 imbalances in the small intestine (downregulation) and colon (upregulation) in IBD patients (59, 62, 79). ACE2, as the main enzyme for cleavage of Ang II to Ang (1–7) which neutralizes the pro-inflammatory and pro-fibrotic effects of Ang II, might be critical for mounting pro- vs. anti-inflammatory responses (80). It is expressed in the gastrointestinal tract in cats (81) but has not been investigated in dogs. Circulating ACE and ACE2 act as decoy receptors, and the plasma ACE2/ACE ratio is increased in people with IBD. Cleavage of ACE2 is controlled by the metalloprotease ADAM17 (34), and ACE2 induction by cardiovascular pathology—shifting the balance between Ang peptides in plasma—is more pronounced in dogs than people (82). MasR is expressed in the canine ileum (83) but remains to be investigated in canine CIE. Likewise, tissue prorenin receptor (PRR) and mineralocorticoid receptor (MR) expression (e.g., by macrophages), as well as chymase activation (e.g., by mast cells), can modulate local RAAS effects (Figure 1B) and inflammatory responses (43) but remain to be studied in canine CIE. ACEIs (decreasing the production of Ang II), Ang II blockade (antagonizing AT1R signaling), MR or PRR antagonists, and/or chymase inhibitors could be useful and inexpensive alternative or adjunct therapeutic options for chronic intestinal inflammation (39, 84, 85) and potentially other autoinflammatory diseases (e.g., autoimmune hepatitis) in dogs.

## 5. Discussion and conclusions

Humans and dogs are close companions and share several civilization diseases, including idiopathic IBD and CIE. Although the shared Western lifestyle is proposed as a common denominator in the etiology of both conditions, there appear to be some species-specific differences in the disease characteristics, including the primary disease localization and distribution, resulting electrolyte changes, and potentially corresponding (counter-)regulatory mechanisms. While the current body of knowledge and research is more extensive for human IBD than canine CIE, a complete understanding of the underlying pathophysiology and possible mechanistic approach to therapy needs to be improved in both species. Exploration of alternative treatment options for dogs with CIE is needed as currently available drugs—particularly corticosteroids—carry significant side effects and biologicals (e.g., monoclonal antibodies against receptors or inflammatory cytokines) are not currently available (and very unlikely available soon) as a treatment option for canine CIE (86). Understanding commonalities and species-specific differences can be expected to result in the development of improved treatment strategies, and targeting RAAS might be one of these options. A thorough understanding of the role of RAAS pathways in the pathophysiology of canine CIE is needed to assess the therapeutic potential and potential side effects. Novel research methods, particularly canine intestinal organoids (Figure 2) that provide a reproducible and stable *in vitro* system for disease modeling and drug development (87–90), will be vital to further evaluate the effects of RAAS modifiers on epithelial ion transport, inflammatory responses, and intestinal barrier function comparatively. Organoids will allow to implement the 3R principles (6) and pave the way for urgently needed novel disease-specific treatment strategies in canine CIE and human IBD.

## Data availability statement

The original contributions presented in the study are included in the article/supplementary material, further inquiries can be directed to the corresponding author.

## Author contributions

RH, IB, and FD: conceptualization. RH and FD: manuscript draft. RH and GC: figures. All authors contributed to the article and approved the submitted version.

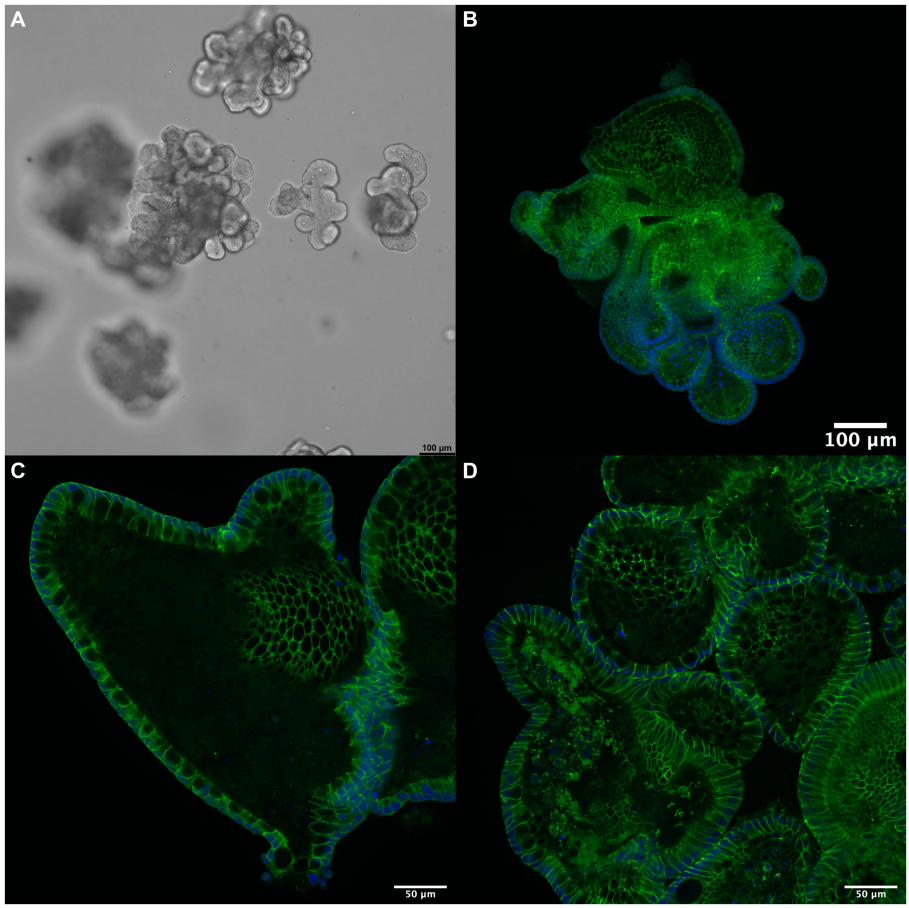


FIGURE 2
3D intestinal organoids for drug discovery. **(A)** Canine enteroids (shown in culture, phase contrast microscopy) pose an advanced *in vitro* model to investigate the pathophysiology of canine CIE further. These organoids allow the study of epithelial transport, inflammation, and barrier function: immunofluorescent staining (green) for **(B)** occludin, **(C)** claudin-1, and **(D)** claudin-7 indicates the formation of a functional polarized epithelium expressing tight junction proteins. Cell nuclei are counterstained with DAPI (blue). Scale bars: 100µm **(A,B)** and 50µm **(C,D)**.

## Funding

This work was funded by a grant from the Leipzig veterinary junior scientist support program financed by the "Freundeskreis Tiermedizin," the Faculty of Veterinary Medicine, and by Ceva Santé Animale. GC was funded by the Austrian Academy of Sciences (ÖAW), DOC fellowship grant number 26349.

## Acknowledgments

The immunofluorescent imaging was performed using resources of the VetCore Facility (VetImaging) at Vetmeduni, Austria. The authors also acknowledge support from the German Research Foundation (DFG) and the University of Leipzig within the program of Open Access Publishing.

## Conflict of interest

The authors declare that the research was conducted in the absence of any commercial or financial relationships that could be construed as a potential conflict of interest.

## Publisher's note

All claims expressed in this article are solely those of the authors and do not necessarily represent those of their affiliated organizations, or those of the publisher, the editors and the reviewers. Any product that may be evaluated in this article, or claim that may be made by its manufacturer, is not guaranteed or endorsed by the publisher.

## References

1. Yu Q, Zhu C, Feng S, Xu L, Hu S, Chen H, et al. Economic burden and health care access for patients with inflammatory bowel diseases in China: web-based survey study. *J Med Internet Res*. (2021) 23:e20629. doi: 10.2196/20629

2. Heilmann RM, Jergens AE. Canine chronic enteropathy – current state-of-the-art and emerging concepts. *Front Vet Sci*. (2022) 9:923013. doi: 10.3389/fvets.2022.923013

3. Sartor RB. Mechanisms of disease: pathogenesis of Crohn's disease and ulcerative colitis. *Nat Clin Pract Gastroenterol Hepatol*. (2006) 3:390–407. doi: 10.1038/ncpgasthep0528

4. Heilmann RM, Suchodolski JS. Is inflammatory bowel disease in dogs and cats associated with a Th1 or Th2 polarization? *Vet Immunol Immunopathol*. (2015) 168:131–4. doi: 10.1016/j.vetimm.2015.10.008

5. Heilmann RM, Allenspach K. Pattern-recognition receptors: signaling pathways and dysregulation in canine chronic enteropathies-brief review. *J Vet Diagn Invest*. (2017) 29:781–7. doi: 10.1177/1040638717728545

6. Jergens AE, Simpson KW. Inflammatory bowel disease in veterinary medicine. *Front Biosci (Elite Ed)*. (2012) E4:1404–19. doi: 10.2741/470

7. Washabau RJ, Day MJ, Willard MD, Hall EJ, Jergens AE, Mansell J, et al. Endoscopic, biopsy, and histopathologic guidelines for the evaluation of gastrointestinal inflammation in companion animals. *J Vet Intern Med*. (2010) 24:10–26. doi: 10.1111/j.1939-1676.2009.0443.x

8. Allenspach K, Wieland B, Gröne A, Gaschen F. Chronic enteropathies in dogs: evaluation of risk factors for negative outcome. *J Vet Intern Med*. (2007) 21:700–8. doi: 10.1892/0891-6640(2007)21

9. Heilmann RM, Becher A, Dengler F. Electrolyte imbalances in dogs with chronic inflammatory enteropathies. *Top Companion Anim Med*. (2021) 46:100597. doi: 10.1016/j.tcam.2021.100597

10. Atreya R, Siegmund B. Location is important: differentiation between ileal and colonic Crohn's disease. *Nat Rev Gastroenterol Hepatol*. (2021) 18:544–58. doi: 10.1038/s41575-021-00424-6

11. Magalhães D, Cabral JM, Soares-da-Silva P, Magro F. Role of epithelial ion transports in inflammatory bowel disease. *Am J Physiol Gastrointest Liver Physiol*. (2016) 310:G460–76. doi: 10.1152/ajpgi.00369.2015

12. Johnson LR. *Physiology of the gastrointestinal tract*. Amsterdam, Boston: Elsevier Academic Press (2006). 2000 p.

13. Kiela PR, Ghishan FK. Physiology of intestinal absorption and secretion. *Best Pract Res Clin Gastroenterol*. (2016) 30:145–59. doi: 10.1016/j.bpg.2016.02.007

14. Priyamvada S, Gomes R, Gill RK, Saksena S, Alrefai WA, Dudeja PK. Mechanisms underlying dysregulation of electrolyte absorption in inflammatory bowel disease-associated diarrhea. *Inflamm Bowel Dis*. (2015) 21:2926–35. doi: 10.1097/MIB.0000000000000504

15. Perler BK, Ungaro R, Baird G, Mallette M, Bright R, Shah S, et al. Presenting symptoms in inflammatory bowel disease: descriptive analysis of a community-based inception cohort. *BMC Gastroenterol*. (2019) 19:47. doi: 10.1186/s12876-019-0963-7

16. Kunzelmann K, Mall M. Electrolyte transport in the mammalian colon: mechanisms and implications for disease. *Physiol Rev*. (2002) 82:245–89. doi: 10.1152/physrev.00026.2001

17. Code CF, Bass P, McClary GB, Newnum RL, Orvis AL. Absorption of water, sodium and potassium in small intestine of dogs. *Am J Physiol*. (1960) 199:281–8. doi: 10.1152/ajplegacy.1960.199.2.281

18. Clarke AM, Miller M, Shields R. Intestinal transport of sodium, potassium, and water in the dog during sodium depletion. *Gastroenterology*. (1967) 52:846–58. doi: 10.1016/S0016-5085(67)80072-6

19. Amasheh S, Barmeyer C, Koch CS, Tavalali S, Mankertz J, Epple H-J, et al. Cytokine-dependent transcriptional down-regulation of epithelial sodium channel in ulcerative colitis. *Gastroenterology*. (2004) 126:1711–20. doi: 10.1053/j.gastro.2004.03.010

20. Ghishan FK, Kiela PR. Epithelial transport in inflammatory bowel diseases. *Inflamm Bowel Dis*. (2014) 20:1099–109. doi: 10.1097/MIB.0000000000000029

21. Anbazhagan AN, Priyamvada S, Alrefai WA, Dudeja PK. Pathophysiology of IBD associated diarrhea. *Tissue Barriers*. (2018) 6:e1463897. doi: 10.1080/21688370.2018.1463897

22. Schultheis PJ, Clarke LL, Meneton P, Miller ML, Soleimani M, Gawenis LR, et al. Renal and intestinal absorptive defects in mice lacking the NHE3 $Na^+/H^+$ exchanger. *Nat Genet*. (1998) 19:282–5. doi: 10.1038/969

23. Maher MM, Gontarek JD, Bess RS, Donowitz M, Yeo CJ. The $Na^+/H^+$ exchange isoform NHE3 regulates basal canine ileal $Na^+$ absorption in vivo. *Gastroenterology*. (1997) 112:174–83. doi: 10.1016/S0016-5085(97)70232-4

24. Hume GE, Radford-Smith GL. ACE inhibitors and angiotensin II receptor antagonists in Crohn's disease management. *Expert Rev Gastroenterol Hepatol*. (2008) 2:645–51. doi: 10.1586/17474124.2.5.645

25. Rossier BC, Baker ME, Studer RA. Epithelial sodium transport and its control by aldosterone: the story of our internal environment revisited. *Physiol Rev*. (2015) 95:297–340. doi: 10.1152/physrev.00011.2014

26. Cho JH, Musch MW, Bookstein CM, McSwine RL, Rabenau K, Chang EB. Aldosterone stimulates intestinal $Na^+$ absorption in rats by increasing NHE3 expression of the proximal colon. *Am J Phys*. (1998) 274:C586–94. doi: 10.1152/ajpcell.1998.274.3.C586

27. Zaika O, Mamenko M, Staruschenko A, Pochynyuk O. Direct activation of ENaC by angiotensin II: recent advances and new insights. *Curr Hypertens Rep*. (2013) 15:17–24. doi: 10.1007/s11906-012-0316-1

28. Donowitz M, Li X. Regulatory binding partners and complexes of NHE3. *Physiol Rev*. (2007) 87:825–72. doi: 10.1152/physrev.00030.2006

29. Süss C, Broncy L, Pollinger K, Kunst C, Gülow K, Müller M, et al. KCNN4 expression is elevated in inflammatory bowel disease: this might be a novel marker and therapeutic option targeting potassium channels. *J Gastrointestin Liver Dis*. (2020) 29:539–47. doi: 10.15403/jgld-903

30. Rosenthal R, Günzel D, Theune D, Czichos C, Schulzke J-D, Fromm M. Water channels and barriers formed by claudins. *Ann N Y Acad Sci*. (2017) 1397:100–9. doi: 10.1111/nyas.13383

31. Ogawa M, Osada H, Hasegawa A, Ohno H, Yanuma N, Sasaki K, et al. Effect of interleukin-1β on occludin mRNA expression in the duodenal and colonic mucosa of dogs with inflammatory bowel disease. *J Vet Intern Med*. (2018) 32:1019–25. doi: 10.1111/jvim.15117

32. Wilke VL, Nettleton D, Wymore MJ, Gallup JM, Demirkale CY, Ackermann MR, et al. Gene expression in intestinal mucosal biopsy specimens obtained from dogs with chronic enteropathy. *Am J Vet Res*. (2012) 73:1219–29. doi: 10.2460/ajvr.73.8.1219

33. Amasheh S, Milatz S, Krug SM, Markov AG, Günzel D, Amasheh M, et al. Tight junction proteins as channel formers and barrier builders. *Ann N Y Acad Sci*. (2009) 1165:211–9. doi: 10.1111/j.1749-6632.2009.04439.x

34. Garg M, Burrell LM, Velkoska E, Griggs K, Angus PW, Gibson PR, et al. Upregulation of circulating components of the alternative renin-angiotensin system in inflammatory bowel disease: a pilot study. *J Renin-Angiotensin-Aldosterone Syst*. (2015) 16:559–69. doi: 10.1177/1470320314521086

35. Garg M, Angus PW, Burrell LM, Herath C, Gibson PR, Lubel JS. Review article: the pathophysiological roles of the renin-angiotensin system in the gastrointestinal tract. *Aliment Pharmacol Ther*. (2012) 35:414–28. doi: 10.1111/j.1365-2036.2011.04971.x

36. Neurath MF. Host-microbiota interactions in inflammatory bowel disease. *Nat Rev Gastroenterol Hepatol*. (2020) 17:76–7. doi: 10.1038/s41575-019-0248-1

37. Matsusaka T, Niimura F, Shimizu A, Pastan I, Saito A, Kobori H, et al. Liver angiotensinogen is the primary source of renal angiotensin II. *JASN*. (2012) 23:1181–9. doi: 10.1681/ASN.2011121159

38. Pahlavani M, Kalupahana NS, Ramalingam L, Moustaid-Moussa N. Regulation and functions of the renin-angiotensin system in white and brown adipose tissue. *Compr Physiol*. (2017) 7:1137–50. doi: 10.1002/cphy.c160031

39. Spencer AU, Yang H, Haxhija EQ, Wildhaber BE, Greenson JK, Teitelbaum DH. Reduced severity of a mouse colitis model with angiotensin converting enzyme inhibition. *Dig Dis Sci*. (2007) 52:1060–70. doi: 10.1007/s10620-006-9124-2

40. Atlas SA. The renin-angiotensin aldosterone system: pathophysiological role and pharmacologic inhibition. *J Manag Care Pharm*. (2007) 13:9–20. doi: 10.18553/jmcp.2007.13.s8-b.9

41. Nguyen G, Delarue F, Burcklé C, Bouzhir L, Giller T, Sraer J-D. Pivotal role of the renin/prorenin receptor in angiotensin II production and cellular responses to renin. *J Clin Invest*. (2002) 109:1417–27. doi: 10.1172/JCI14276

42. Peach MJ. Renin-angiotensin system: biochemistry and mechanisms of action. *Physiol Rev*. (1977) 57:313–70. doi: 10.1152/physrev.1977.57.2.313

43. Ames MK, Atkins CE, Pitt B. The renin-angiotensin-aldosterone system and its suppression. *J Vet Intern Med*. (2019) 33:363–82. doi: 10.1111/jvim.15454

44. Li XC, Zheng X, Chen X, Zhao C, Zhu D, Zhang J, et al. Genetic and genomic evidence for an important role of the $Na^+/H^+$ exchanger 3 in blood pressure regulation and angiotensin II-induced hypertension. *Physiol Genomics*. (2019) 51:97–108. doi: 10.1152/physiolgenomics.00122.2018

45. Li XC, Wang C-H, Leite AP, Zhuo JL. Intratubular, intracellular, and mitochondrial angiotensin II/AT1 (AT1a) receptor/NHE3 signaling plays a critical role in angiotensin II-induced hypertension and kidney injury. *Front Physiol*. (2021) 12:702797. doi: 10.3389/fphys.2021.702797

46. Poulsen SB, Fenton RA. $K^+$ and the renin-angiotensin-aldosterone system: new insights into their role in blood pressure control and hypertension treatment. *J Physiol*. (2019) 597:4451–64. doi: 10.1113/JP276844

47. Kagami S, Border WA, Miller DE, Noble NA. Angiotensin II stimulates extracellular matrix protein synthesis through induction of transforming growth factor-beta expression in rat glomerular mesangial cells. *J Clin Invest*. (1994) 93:2431–7. doi: 10.1172/JCI117251

48. Ruiz-Ortega M, Ruperez M, Lorenzo O, Esteban V, Blanco J, Mezzano S, et al. Angiotensin II regulates the synthesis of proinflammatory cytokines and chemokines in the kidney. *Kidney Int Suppl*. (2002) 62:S12–22. doi: 10.1046/j.1523-1755.62.s82.4.x

49. Ruiz-Ortega M, Bustos C, Hernández-Presa MA, Lorenzo O, Plaza JJ, Egido J. Angiotensin II participates in mononuclear cell recruitment in experimental immune complex nephritis through nuclear factor-kappa B activation and monocyte chemoattractant protein-1 synthesis. *J Immunol*. (1998) 161:430–9. doi: 10.4049/jimmunol.161.1.430

50. Rupérez M, Ruiz-Ortega M, Esteban V, Lorenzo O, Mezzano S, Plaza JJ, et al. Angiotensin II increases connective tissue growth factor in the kidney. *Am J Pathol*. (2003) 163:1937–47. doi: 10.1016/S0002-9440(10)63552-3

51. Saber S. Angiotensin II: a key mediator in the development of liver fibrosis and cancer. *Bull Natl Res Cent*. (2018) 42:42. doi: 10.1186/s42269-018-0020-7

52. Li A, Zhang J, Zhang X, Wang J, Wang S, Xiao X, et al. Angiotensin II induces connective tissue growth factor expression in human hepatic stellate cells by a transforming growth factor β-independent mechanism. *Sci Rep*. (2017) 7:7841. doi: 10.1038/s41598-017-08334-x

53. Park JM, Kim J, Lee YJ, Bae SU, Lee HW. Inflammatory bowel disease-associated intestinal fibrosis. *J Pathol Transl Med*. (2023) 57:60–6. doi: 10.4132/jptm.2022.11.02

54. Brown MJ. Renin: friend or foe? *Heart*. (2007) 93:1026–33. doi: 10.1136/hrt.2006.107706

55. Ichihara A, Kaneshiro Y, Takemitsu T, Sakoda M, Suzuki F, Nakagawa T, et al. Nonproteolytic activation of prorenin contributes to development of cardiac fibrosis in genetic hypertension. *Hypertension*. (2006) 47:894–900. doi: 10.1161/01.HYP.0000215838.48170.0b

56. Uhlén M, Fagerberg L, Hallström BM, Lindskog C, Oksvold P, Mardinoglu A, et al. Proteomics. Tissue-based map of the human proteome. *Science*. (2015) 347:1260419. doi: 10.1126/science.1260419

57. Bader M. Tissue renin-angiotensin-aldosterone systems: targets for pharmacological therapy. *Annu Rev Pharmacol Toxicol*. (2010) 50:439–65. doi: 10.1146/annurev.pharmtox.010909.105610

58. Mederos Y, Schnitzler M, Storch U, Gudermann T. Mechanosensitive Gq/11 protein-coupled receptors mediate myogenic vasoconstriction. *Microcirculation*. (2016) 23:621–5. doi: 10.1111/micc.12293

59. Bader M. ACE2, angiotensin-(1–7), and mas: the other side of the coin. *Pflugers Arch*. (2013) 465:79–85. doi: 10.1007/s00424-012-1120-0

60. Donoghue M, Hsieh F, Baronas E, Godbout K, Gosselin M, Stagliano N, et al. A novel angiotensin-converting enzyme-related carboxypeptidase (ACE2) converts angiotensin I to angiotensin 1-9. *Circ Res*. (2000) 87:E1–9. doi: 10.1161/01.res.87.5.e1

61. Santos RA, Brosnihan KB, Chappell MC, Pesquero J, Chernicky CL, Greene LJ, et al. Converting enzyme activity and angiotensin metabolism in the dog brainstem. *Hypertension*. (1988) 11:I153–7. doi: 10.1161/01.hyp.11.2_pt_2.i153

62. Santos RA, Sampaio WO, Alzamora AC, Motta-Santos D, Alenina N, Bader M, et al. The ACE2/angiotensin-(1-7)/MAS axis of the renin-angiotensin system: focus on angiotensin-(1-7). *Physiol Rev*. (2018) 98:505–53. doi: 10.1152/physrev.00023.2016

63. Stoyell-Conti FF, Chabbra A, Puthentharayil J, Rigatto K, Speth RC. Chronic administration of pharmacological doses of angiotensin 1-7 and iodoangiotensin 1-7 has minimal effects on blood pressure, heart rate, and cognitive function of spontaneously hypertensive rats. *Physiol Rep*. (2021) 9:e14812. doi: 10.14814/phy2.14812

64. Bader M, Ganten D. Update on tissue renin-angiotensin systems. *J Mol Med (Berl)*. (2008) 86:615–21. doi: 10.1007/s00109-008-0336-0

65. Pacurari M, Kafoury R, Tchounwou PB, Ndebele K. The renin-angiotensin-aldosterone system in vascular inflammation and remodeling. *Int J Inflam*. (2014) 2014:689360. doi: 10.1155/2014/689360

66. Triantafillidis JK, Malgarinos G, Rentis A, Vagianos K. Primary aldosteronism during long-term ulcerative colitis: a diagnostic challenge. *Ann Gastroenterol*. (2014) 27:432–3.

67. Dandona P, Kumar V, Aljada A, Ghanim H, Syed T, Hofmayer D, et al. Angiotensin II receptor blocker valsartan suppresses reactive oxygen species generation in leukocytes, nuclear factor-kappa B, in mononuclear cells of normal subjects: evidence of an antiinflammatory action. *J Clin Endocrinol Metab*. (2003) 88:4496–501. doi: 10.1210/jc.2002-021836

68. Ferrario CM, Strawn WB. Role of the renin-angiotensin-aldosterone system and proinflammatory mediators in cardiovascular disease. *Am J Cardiol*. (2006) 98:121–8. doi: 10.1016/j.amjcard.2006.01.059

69. Ogata H, Noguchi H, Ohtsubo T, Liao J, Kohara H, Yamada K, et al. Angiotensin II type I receptor blocker, losartan, inhibits fibrosis in liver by suppressing TGF-beta1 production. *Integr Mol Med*. (2016) 3:3. doi: 10.15761/IMM.1000199

70. German AJ, Helps CR, Hall EJ, Day MJ. Cytokine mRNA expression in mucosal biopsies from German shepherd dogs with small intestinal enteropathies. *Dig Dis Sci*. (2000) 45:7–17. doi: 10.1023/A:1005436721798

71. Jergens AE, Sonea IM, O'Connor AM, Kauffman LK, Grozdanic SD, Ackermann MR, et al. Intestinal cytokine mRNA expression in canine inflammatory bowel disease: a meta-analysis with critical appraisal. *Comp Med*. (2009) 59:153–62.

72. Kołodziejska-Sawerska A, Rychlik A, Depta A, Wdowiak M, Nowicki M, Kander M. Cytokines in canine inflammatory bowel disease. *Pol J Vet Sci*. (2013) 16:165–71. doi: 10.2478/pjvs-2013-0025

73. Dumusc SD, Ontsouka EC, Schnyder M, Hartnack S, Albrecht C, Bruckmaier RM, et al. Cyclooxygenase-2 and 5-lipoxygenase in dogs with chronic enteropathies. *J Vet Intern Med*. (2014) 28:1684–91. doi: 10.1111/jvim.12463

74. Hanifeh M, Rajamäki MM, Syrjä P, Mäkitalo L, Kilpinen S, Spillmann T. Identification of matrix metalloproteinase-2 and -9 activities within the intestinal mucosa of dogs with chronic enteropathies. *Acta Vet Scand*. (2018) 60:16. doi: 10.1186/s13028-018-0371-y

75. Burgener IA, König A, Allenspach K, Sauter SN, Boisclair J, Doherr MG, et al. Upregulation of toll-like receptors in chronic enteropathies in dogs. *J Vet Intern Med*. (2008) 22:553–60. doi: 10.1111/j.1939-1676.2008.0093.x

76. Cabrera-García AI, Protschka M, Alber G, Kather S, Dengler F, Müller U, et al. Dysregulation of gastrointestinal RAGE (receptor for advanced glycation end products) expression in dogs with chronic inflammatory enteropathy. *Vet Immunol Immunopathol*. (2021) 234:110216. doi: 10.1016/j.vetimm.2021.110216

77. Dasu MR, Riosvelasco AC, Jialal I. Candesartan inhibits toll-like receptor expression and activity both in vitro and in vivo. *Atherosclerosis*. (2009) 202:76–83. doi: 10.1016/j.atherosclerosis.2008.04.010

78. Khajah MA, Fateel MM, Ananthalakshmi KV, Luqmani YA. Anti-inflammatory action of angiotensin 1-7 in experimental colitis. *PLoS One*. (2016) 11:e0150861. doi: 10.1371/journal.pone.0150861

79. Santos RA, Ferreira AJ, Verano-Braga T, Bader M. Angiotensin-converting enzyme 2, angiotensin-(1-7) and Mas: new players of the renin-angiotensin system. *J Endocrinol*. (2013) 216:R1–R17. doi: 10.1530/JOE-12-0341

80. Potdar AA, Dube S, Naito T, Li K, Botwin G, Haritunians T, et al. Altered intestinal ACE2 levels are associated with inflammation, severe disease, and response to anti-cytokine therapy in inflammatory bowel disease. *Gastroenterology*. (2021) 160:809–822.e7. doi: 10.1053/j.gastro.2020.10.041

81. Chiocchetti R, Galiazzo G, Fracassi F, Giancola F, Pietra M. ACE2 expression in the cat and tiger gastrointestinal tracts. *Front Vet Sci*. (2020) 7:514. doi: 10.3389/fvets.2020.00514

82. Larouche-Lebel É, Loughran KA, Huh T, Oyama MA. Effect of angiotensin receptor blockers and angiotensin converting enzyme 2 on plasma equilibrium angiotensin peptide concentrations in dogs with heart disease. *J Vet Intern Med*. (2021) 35:22–32. doi: 10.1111/jvim.16025

83. Hamamura-Yasuno E, Iguchi T, Kumagai K, Tsuchiya Y, Mori K. Identification of the dog orthologue of human MAS-related G protein coupled receptor X2 (MRGPRX2) essential for drug-induced pseudo-allergic reactions. *Sci Rep*. (2020) 10:16146. doi: 10.1038/s41598-020-72819-5

84. Inokuchi Y, Morohashi T, Kawana I, Nagashima Y, Kihara M, Umemura S. Amelioration of 2,4,6-trinitrobenzene sulphonic acid induced colitis in angiotensinogen gene knockout mice. *Gut*. (2005) 54:349–56. doi: 10.1136/gut.2003.036343

85. Salmenkari H, Korpela R, Vapaatalo H. Renin–angiotensin system in intestinal inflammation—angiotensin inhibitors to treat inflammatory bowel diseases? *Basic Clin Pharmacol Toxicol*. (2021) 129:161–72. doi: 10.1111/bcpt.13624

86. Makielski K, Cullen J, O'Connor A, Jergens AE. Narrative review of therapies for chronic enteropathies in dogs and cats. *J Vet Intern Med*. (2019) 33:11–22. doi: 10.1111/jvim.15345

87. Kramer N, Pratscher B, Meneses AM, Tschulenk W, Walter I, Swoboda A, et al. Generation of differentiating and long-living intestinal organoids reflecting the cellular diversity of canine intestine. *Cells*. (2020) 9:9. doi: 10.3390/cells9040822

88. Ambrosini YM, Park Y, Jergens AE, Shin W, Min S, Atherly T, et al. Recapitulation of the accessible interface of biopsy-derived canine intestinal organoids to study epithelial-luminal interactions. *PLoS One*. (2020) 15:e0231423. doi: 10.1371/journal.pone.0231423

89. Chandra L, Borcherding DC, Kingsbury D, Atherly T, Ambrosini YM, Bourgois-Mochel A, et al. Derivation of adult canine intestinal organoids for translational research in gastroenterology. *BMC Biol*. (2019) 17:33. doi: 10.1186/s12915-019-0652-6

90. Weng X-H, Beyenbach KW, Quaroni A. Cultured monolayers of the dog jejunum with the structural and functional properties resembling the normal epithelium. *Am J Physiol Gastrointest Liver Physiol*. (2005) 288:G705–17. doi: 10.1152/ajpgi.00518.2003

frontiers | Frontiers in Veterinary Science

TYPE Brief Research Report
PUBLISHED 31 August 2023
DOI 10.3389/fvets.2023.1217839



OPEN ACCESS

EDITED BY
Ahmed S. Mandour,
Suez Canal University, Egypt

REVIEWED BY
Elsayed Metwally,
Suez Canal University, Egypt
Walaa Mohamadein,
Seuz Canal University, Egypt

*CORRESPONDENCE
Romy M. Heilmann
✉ romy.heilmann@kleintierklinik.uni-leipzig.de
Franziska Dengler
✉ franziska.dengler@vetmeduni.ac.at

RECEIVED 05 May 2023
ACCEPTED 18 August 2023
PUBLISHED 31 August 2023

CITATION
Dengler F, Domenig O, Kather S, Burgener IA, Steiner JM and Heilmann RM (2023) Dysregulation of intestinal epithelial electrolyte transport in canine chronic inflammatory enteropathy and the role of the renin-angiotensin-aldosterone-system. *Front. Vet. Sci.* 10:1217839. doi: 10.3389/fvets.2023.1217839



# Dysregulation of intestinal epithelial electrolyte transport in canine chronic inflammatory enteropathy and the role of the renin-angiotensin-aldosterone-system

Franziska Dengler[1]*, Oliver Domenig[2], Stefanie Kather[3], Iwan A. Burgener[4], Joerg M. Steiner[5] and Romy M. Heilmann[3]*

[1]Institute of Physiology, Pathophysiology and Biophysics, University of Veterinary Medicine Vienna, Vienna, Austria, [2]Attoquant Diagnostics, Vienna, Austria, [3]Department for Small Animals, College of Veterinary Medicine, University of Leipzig, Leipzig, SN, Germany, [4]Small Animal Internal Medicine, University of Veterinary Medicine Vienna, Vienna, Austria, [5]Gastrointestinal Laboratory, School of Veterinary Medicine and Biomedical Sciences, Texas A&M University, College Station, TX, United States

Chronic diarrhea is a hallmark sign of canine chronic inflammatory enteropathy (CIE), leading to fluid and electrolyte losses. Electrolyte homeostasis is regulated by the renin-angiotensin-aldosterone-system (RAAS), which might be involved in (counter-)regulating electrolyte losses in canine CIE. Whether and which electrolyte transporters are affected or if RAAS is activated in canine CIE is unknown. Thus, intestinal electrolyte transporters and components of the RAAS were investigated in dogs with CIE. Serum RAAS fingerprint analysis by mass spectrometry was performed in 5 CIE dogs and 5 healthy controls, and mRNA levels of intestinal electrolyte transporters and local RAAS pathway components were quantified by RT-qPCR in tissue biopsies from the ileum (7 CIE, 10 controls) and colon (6 CIE, 12 controls). Concentrations of RAAS components and mRNA expression of electrolyte transporters were compared between both groups of dogs and were tested for associations among each other. In dogs with CIE, associations with clinical variables were also tested. Components of traditional and alternative RAAS pathways were higher in dogs with CIE than in healthy controls, with statistical significance for Ang I, Ang II, and Ang 1–7 (all $p < 0.05$). Expression of ileal, but not colonic electrolyte transporters, such as $Na^+/K^+$-ATPase, $Na^+/H^+$-exchanger 3, $Cl^-$ channel 2, down-regulated in adenoma, and $Na^+$-glucose-cotransporter (all $p < 0.05$) was increased in CIE. Our results suggest that the dys- or counter-regulation of intestinal electrolyte transporters in canine CIE might be associated with a local influence of RAAS. Activating colonic absorptive reserve capacities may be a promising therapeutic target in canine CIE.

KEYWORDS

**diarrhea, dog, inflammatory bowel disease, intestinal epithelial transport, mRNA expression, mass spectrometry, RAAS, SGLT1**

# 1. Introduction

Both inflammatory bowel disease (IBD) in humans and chronic inflammatory enteropathy (CIE) in dogs show an increasing incidence that poses an immense burden on the healthcare system (1). A frequent clinical sign that significantly negatively impacts the patient's quality of life is chronic diarrhea, the discharge of loose to watery feces causing electrolyte losses, plasma electrolyte shifts, and secondary systemic consequences (2, 3). Because the intestinal absorption of electrolytes is extensively regulated, it would be expected that counterregulatory mechanisms to balance fluid and electrolyte deficiencies caused by the disease are activated. A major regulator of electrolyte and fluid homeostasis is the renin-angiotensin-aldosterone system (RAAS), which controls systemic blood pressure and volume by regulating vascular tone and the reabsorption of $Na^+$ and water. Beyond this traditional systemic role, RAAS has recently gained increasing attention as a local autocrine and paracrine mediator. Within that scope, RAAS effects beyond the classical modulation of (primarily renal and intestinal) electrolyte transport may include developing and perpetuating inflammation and fibrotic tissue remodeling (4, 5). An upregulation of individual components of RAAS has been observed in human IBD patients (6). Altered expression patterns and dysfunction of several ion transporters, especially $Na^+/H^+$-exchanger (NHE) 3, epithelial $Na^+$-channel (ENaC), $Na^+/K^+$-ATPase, down-regulated in adenoma (DRA), and putative anion transporter 1 (PAT1), appear to occur in human patients with IBD (7–9). This might be a consequence of inflammatory signaling or be regulated directly or indirectly by the multimodal effects of RAAS and contribute to the plasma electrolyte shifts observed in IBD patients. While hyponatremia is the most important electrolyte shift in human IBD patients, dogs with CIE more commonly show hypokalemia (3), suggesting differences in the pathophysiology and compensatory mechanisms between species. This difference may also be associated with a difference in the primary localization of the inflammatory lesions along the gastrointestinal tract between human IBD and canine CIE patients. However, neither the possible activation of RAAS nor lack thereof or the intestinal expression of electrolyte transporters has been investigated in canine CIE thus far.

As a prelude to further functional analyses, our study aimed to investigate (i) the gene expression of intestinal electrolyte transporters with a putative role in salvaging or contributing to electrolyte losses in dogs with CIE, (ii) the possibility of activation of the RAAS in dogs with CIE, and (iii) the possible association between the expression of intestinal electrolyte transporters and currently known RAAS components.

# 2. Materials and methods

## 2.1. Animals

Healthy control dogs were required to be free from having any clinical signs of gastrointestinal disease or receiving medication known to affect the gastrointestinal tract, to be regularly vaccinated and dewormed, and – for the serum controls – to have a normal complete blood cell count and serum biochemistry profile.

Dogs with CIE had clinical signs of chronic enteropathy (i.e., vomiting, diarrhea, and/or weight loss for ≥3 weeks); other possible etiologies of these clinical signs (e.g., atypical hypoadrenocorticism, exocrine pancreatic insufficiency) were excluded. Intestinal inflammation was documented histologically, and the response to treatment supported a diagnosis of CIE (10). These dogs could not have (i) received any anti-inflammatory and/or immunosuppressive medication or RAAS-acting agent (i.e., angiotensin-converting enzyme [ACE] inhibitor, angiotensin receptor blocker, aldosterone-antagonist or other diuretic, ß-blocker, calcium channel blocker, or mineralocorticoid) within 4 weeks prior to enrollment and sampling and (ii) evidence of cardiac disease or renal insufficiency. Clinical disease severity was determined using the canine chronic enteropathy clinical activity index (CCECAI), which includes the 3-point-scale evaluation of the dog's attitude/activity, appetite, frequency of vomiting, stool consistency, frequency of defecation, weight loss, serum albumin concentration, peripheral edema/ ascites, and pruritus score (11). Gastrointestinal tissue biopsies were histologically evaluated by a 3-point scale grading structural and inflammatory lesions (12).

Serum samples ($n = 5$) and endoscopic tissue biopsies from the ileum ($n = 7$) and colon ($n = 6$) of dogs with CIE were from a previous study (13) that was approved by the Regional Council of the State of Saxony, Chemnitz/Leipzig, Germany (#TVV 06–17). Control tissues were full-thickness biopsies from the ileum ($n = 10$) and colon ($n = 12$) of purpose-bred healthy dogs that were euthanized for an unrelated project at the School of Veterinary Medicine and Biomedical Sciences at Texas A&M University, United States (Animal Use Protocol #TAMU 2009–0123). Serum from age- and sex-matched healthy controls ($n = 5$) were surplus materials from the blood donor bank at the Department for Small Animals, University of Leipzig, Germany.

## 2.2. Real-time quantitative polymerase chain reaction (RT-qPCR) analyses

Biopsies were stored in RNAlater® (Qiagen, Hilden, Germany) at −80°C until RNA isolation. Total RNA was isolated from the tissue, and cDNA was prepared as described previously (14). Briefly, total RNA was extracted with the ReliaPrep™ RNA Miniprep System (Promega GmbH, Mannheim, Germany) according to the manufacturer's protocol, including treatment with DNase. RNA concentration and quality were determined spectrophotometrically (DeNovix DS-11, Wilmington, DE, United States), and 1 µg of high-quality RNA was used for cDNA synthesis using the GoScript™ Reverse Transcriptase Kit (Promega, Mannheim, Germany).

For qPCR, a ready-to-use SYBR green master mix (GoTaq®, Promega, Mannheim, Germany) with 112 nM primer mix was used. Primers were designed with the Primer BLAST tool from the National Center for Biotechnology Information (NCBI, Bethesda, MD, United States) using known sequences from the Basic Local Alignment Search Tool (BLAST) in the NCBI gene bank database (Table 1) and were synthesized by Microsynth (Balgach, SG, Switzerland). A no-template control (NTC) with DNase-free water instead of cDNA was included in each run. For each sample and gene, qPCR reactions were run in duplicates, and the amplification specificity was checked by melting curve analysis. Following denaturation at 95°C, extension and annealing were performed at 60°C, and the quantification cycle was determined using the CFX Maestro software (Biorad, Vienna, Austria). The $\Delta\Delta C_t$ method was used to analyze the data and compare the mRNA expression of the electrolyte transporters $Na^+/K^+$-ATPase (*ATP1A1*), *ENAC*, *NHE3*, renal outer medullary $K^+$ channel (*ROMK*),

TABLE 1 Primers used for qPCR.

| Gene name | Gene bank accession no. | Primer sequence (5′ – 3′) |
|---|---|---|
| *ATP1A1* | NM_001389224.1 | F: ACTCAGAACCGGATGACCGT<br>R: ATCGAACGAGACACCACTCTG |
| *AE2* | XM_003639553.5 | F: AGAGCAAGCGGGTTATGCC<br>R: AGAAAGAATCTGCGCCCGAG |
| *CFTR* | NM_001007143.1 | F: GGACAGAGAGCTGGCATCAA<br>R: CTGCTTTGGTGACTTCCCCT |
| *CLC2* | XM_038445731.1 | F: CCGGTCTTTGTTATCGGAGC<br>R: ATCCGGTAAGTGCTGCTGTC |
| *DRA* | XM_038423776.1 | F: CTGGGATTCTCTCTGCGGTC<br>R: GAGCTGCCAGGACAGACTTTT |
| *ENAC* | XM_038439216.1 | F: GGGATCAAAAATGGCCTGTCC<br>R: CATCCTGCCCATGCACCATT |
| *HPRT1* | NM_001003357.2 | F: CCCAGCGTCGTGATTAGTGA<br>R: CACTTTTTCCAAATCCTCAGCGT |
| *MCT1* | XM_038423242.1 | F: CCGCGCATAACGGTATTTGG<br>R: CCTCCATCTGGGGGAGTGTA |
| *MCT4* | XM_038675356.1 | F: ATCGTGGGCACCCAGAAGTT<br>R: CAAGAGCTTGCCTCCCGAT |
| *NHE2* | XM_038680184.1 | F: CCCTGGCGAAGATAGGCTT<br>R: CTAGCAGCAGGCCAACCATT |
| *NHE3* | XM_038462883.1 | F: GTGGTCACCTTCAAATGGCAC<br>R: GTGTGATAGGTGGAAGCCGAT |
| *PPID* | XM_038688725.1 | F: TGGAAATGTCGCATCCGTCC<br>R: CAATTCGACCAACTCGCTCC |
| *ROMK* | XM_038664232.1 | F: GCACGCACTCTCCAGATCAGA<br>R: CTTTGCCGAGAATGCCCAAA |
| *SDHA* | XM_535807.6 | F: TCCGTGTGGGAAGTGTGTTA<br>R: GTGTTCCAGACCATTCCTCG |
| *VIM* | NM_001287023.1 | F: GGATGCACTCAAAGGGACTAATG<br>R: GTCTTGGTAGTTAGCAGCTTCG |

cystic fibrosis transmembrane conductance regulator (*CFTR*), *NHE2*, *CLC-2*, *DRA*, monocarboxylate transporter 1 (*MCT1*), and $Na^+$-glucose co-transporter 1 (*SGLT1*); as well as the local RAAS components angiotensin II receptor type 1 (*AGTR1*) and a disintegrin and metalloproteinase (*ADAM*). Samples were normalized using the same amounts of RNA and cDNA for processing. Hypoxanthine guanine phosphoribosyltransferase 1 (*HPRT1*), peptidylprolyl-isomerase D (*PPID*), and succinate dehydrogenase subunit A (*SDHA*) served as reference genes after their stability was confirmed using Reffinder (15). The geometric mean of all reference genes' $C_t$ values was calculated for each sample and used for normalization. Additionally, vimentin (*VIM*) expression was used to normalize mesenchymal tissue content across intestinal biopsy specimens.

## 2.3. Mass spectrometry-based serum RAAS profiling

Serum samples stored at −20°C were submitted to a commercial laboratory (Attoquant Diagnostics, Vienna, Austria) to quantify equilibrium concentrations of RAAS components (angiotensin I [Ang I], Ang II, Ang III, Ang IV, Ang (1-7), Ang (1-5), and aldosterone) by liquid chromatography–tandem mass spectrometry (LC–MS/MS) as previously described (16, 17). Briefly, serum samples were equilibrated for 1 h at 37°C prior to stabilization, spiked with stable isotope-labeled Ang peptides and deuterated aldosterone (internal standard), subjected to C18-based solid-phase extraction and LC–MS/MS analysis using a reverse-analytical column in a triple quadrupole MS (Xevo TQ-S; Waters, Eschborn, Germany). After normalizing the recovered RAAS components against their internal standards, the concentrations of these analytes were calculated based on calibration curves using integrated chromatograms (16, 17). PRA-S (a marker for serum renin activity), ACE-S (a marker for serum ACE activity), AA2 ratio (a marker for adrenocortical responsiveness), and ALT-S (a marker for renin-independent alternative serum RAAS activity) were calculated as described (18–20).

## 2.4. Statistics

A commercial statistical software program (JMP® v.13, SAS Institute, Cary, NC, United States) was used for all statistical analyses. Data were assessed for normality using a Shapiro–Wilk test, and the summary statistics were reported as medians and ranges (continuous data) or counts and percentages (categorical data). Non-parametric two-group comparisons were performed using a Wilcoxon rank-sum test, and a Spearman correlation coefficient (ρ) was calculated to assess for possible correlations. Statistical significance was set at $p < 0.05$ and a Bonferroni correction for multiple comparisons was applied if indicated.

# 3. Results

## 3.1. mRNA expression of electrolyte transporters and local RAAS components

Significant upregulation of the ileal epithelial mRNA expression of the electrolyte transporters *ATP1A1* ($p = 0.0218$), *NHE3* ($p = 0.0491$), *CLC-2* ($p = 0.0009$), and *DRA* ($p = 0.0128$), along with the glucose transporter *SGLT1* ($p = 0.0015$), was detected in dogs with CIE compared to healthy controls (Figure 1A). No significant difference was observed for ileal *ENAC* ($p = 0.1571$), *ROMK* ($p = 0.3562$), and *CFTR* ($p = 0.6961$) expression between CIE and healthy controls. Furthermore, no differences were detected between both groups of dogs in the colonic epithelial expression of *ATP1A1* ($p = 0.8513$), *NHE3* ($p = 0.4260$), *ROMK* ($p = 1.0000$), *CFTR* ($p = 0.4824$), *DRA* ($p = 0.6734$), *MCT1* ($p = 0.6473$), *ENAC* ($p = 0.2059$), *CLC-2* ($p = 0.2229$), and *NHE2* ($p = 0.3024$) in dogs with CIE compared to the control group (Figure 1A).

Significant downregulation of the ileal epithelial *AGTR1* and *ADAM* expression (both $p = 0.0359$) was seen in dogs with CIE compared to healthy controls (Figure 1B), which was also not mirrored in the colon ($p = 0.7078$ and $p = 0.3487$).

## 3.2. Serum concentrations of RAAS components

Components of both traditional and alternative RAAS pathways were increased in serum from dogs with CIE compared

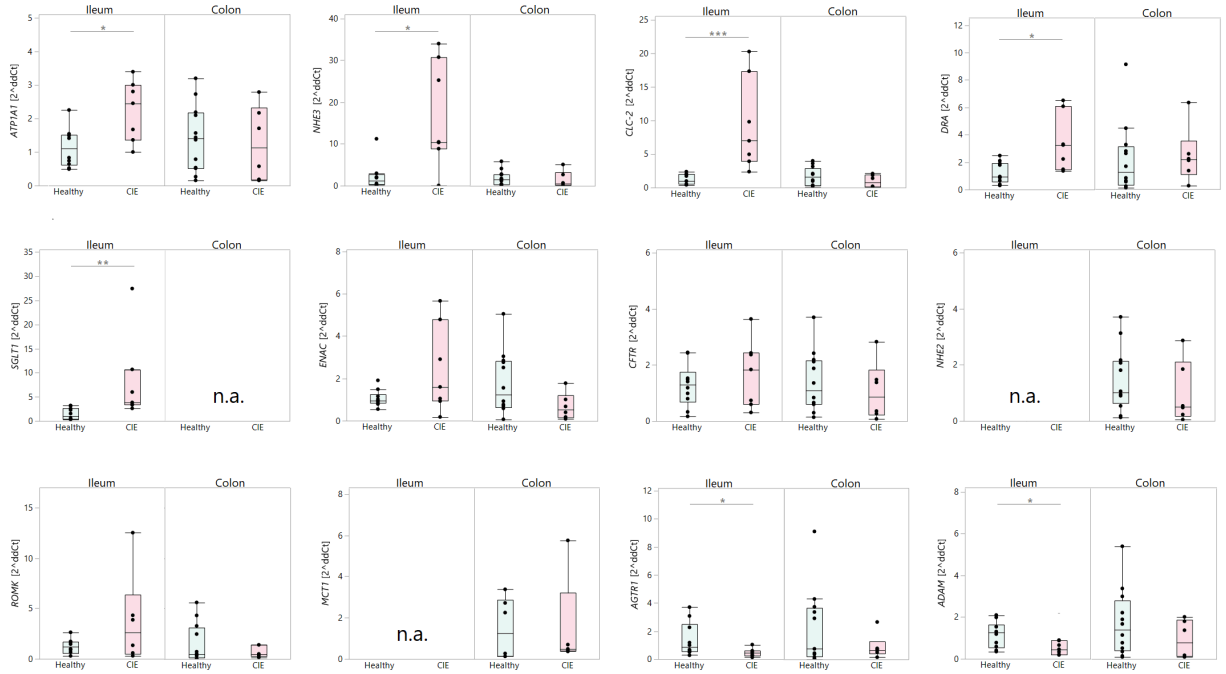


FIGURE 1
Electrolyte transporter and selected tissue RAAS component mRNA expression in the ileal and colonic mucosa from dogs with CIE compared to healthy controls. The expression of ileal *ATP1A1, NHE3, CLC-2, DRA*, and *SGLT1* mRNA was increased in dogs with CIE (all $p < 0.05$), whereas there were no differences in the expression of *ENAC, CFTR*, and *ROMK* mRNA in the ileum. No differences in the expression of any of the transporters were detected in the colonic mucosa. Local RAAS imbalance comprised a downregulated ileal (but not colonic) *AGTR1* and *ADAM* mRNA expression in dogs with CIE (* indicates significance at $p < 0.05$, ** indicates significance at $p < 0.01$, *** indicates significance at $p < 0.001$). *ADAM*: a disintegrin and metalloproteinase; *AGTR1*: angiotensin II receptor type 1; *ATP1A1*: $Na^+/K^+$-ATPase; *CFTR*: cystic fibrosis transmembrane conductance regulator; *CLC-2*: $Cl^-$ channel 2; *DRA*: down-regulated in adenoma; *ENAC*: epithelial $Na^+$ channel; *MCT1*: monocarboxylate transporter 1; *NHE2*: $Na^+/H^+$-exchanger 2; *NHE3*: $Na^+/H^+$-exchanger 3; *ROMK*: renal outer medullary $K^+$ channel; *SGLT1*: $Na^+$-glucose co-transporter 1; n.a.: not abundant.

to healthy control dogs (Figure 2A). Ang I, Ang II, Ang IV, and Ang 1–7 as well as PRA-S were significantly upregulated in CIE (all $p = 0.0367$) compared to healthy dogs, whereas statistical significance was not reached for the differences in serum Ang III and Ang 1–5 (both $p = 0.0947$) or aldosterone ($p = 0.2101$; Figure 2B). Mildly but insignificantly decreased ACE-S and AA2 ratios (both $p = 0.6761$) and ALT-S ($p = 0.2963$) were seen in dogs with CIE. Traditional and alternative RAAS components were highly correlated in dogs with CIE, with few significant correlations in healthy dogs (Figure 2C).

## 3.3. Association of serum RAAS components with patient characteristics and intestinal electrolyte transporter and local RAAS component mRNA expression

Few correlations of serum RAAS components with patient and disease characteristics were seen in the CIE group of dogs (Figure 3A). Lower serum AA2 ratios, reflecting decreased adrenal responsiveness to Ang II, were strongly correlated with higher $K^+$, lower corrected $Cl^-$, higher histologic lesion scores in the ileum, and lower serum cobalamin concentrations. Notably, *SGLT1* mRNA expression was highly correlated with several RAAS components (Ang I, Ang III, Ang IV, aldosterone, PRA-S, and AA2 ratio) and the severity of diarrhea in dogs with CIE (Figure 3B). No other significant correlations were seen between the expression of ileal electrolyte transporters, endogenous glucocorticoid (serum cortisol), and RAAS components in the serum.

# 4. Discussion

Chronic diarrhea is a hallmark of canine CIE and a major factor impairing affected dogs' and their owners' quality of life. Thus, a more detailed understanding of the mechanisms involved in the pathogenesis of diarrhea and the corresponding counterregulatory mechanisms is of urgent interest to improve the therapeutic approach in affected dogs. This preliminary study aimed to characterize possible changes in the expression of intestinal electrolyte transporters in canine CIE and to investigate the potential role of RAAS in their regulation.

The results demonstrate an upregulation of electrolyte transporter mRNA expression in the ileum, which is usually more affected than the colon in canine CIE. Particularly the $Na^+$-transporters *ATP1A1* and *NHE3* were significantly upregulated in dogs with CIE compared to healthy dogs. *ENAC* appeared numerically upregulated, but the difference between CIE and healthy controls did not reach statistical significance. This upregulation could be interpreted as a compensatory attempt to increase $Na^+$ and thus also water absorption in the diseased intestine. *DRA* was also increased in CIE and might be involved in NaCl absorption, cooperating with *NHE3* (7), and contribute to water reabsorption. These findings contrast with the reduced expression and

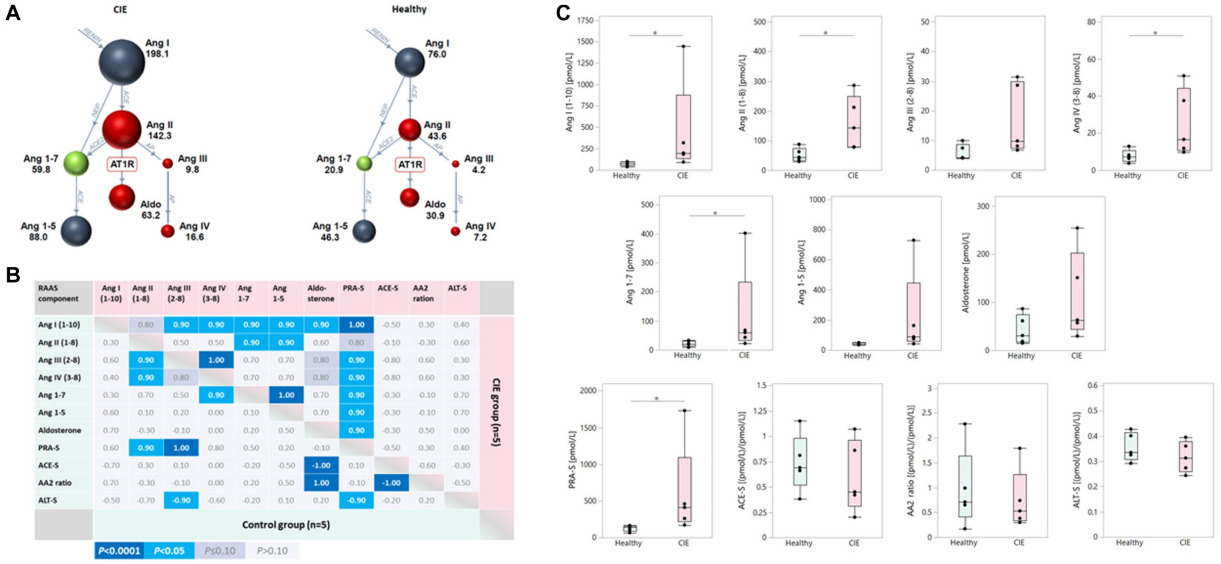


FIGURE 2
Upregulation of serum RAAS components in canine CIE. **(A)** Serum RAAS fingerprint visualizing the upregulation of both the traditional and alternative RAAS arms in dogs with CIE (*n*=5; left panel) compared to healthy controls (*n*=5; right panel). Individual colored dots (and numbers) reflect the median concentrations for each analyte. **(B)** Correlation among serum RAAS components in dogs with CIE and healthy controls. The Spearman correlation coefficients (ρ) for the individual correlations are shown, with the color scheme (indicated below the table) reflecting the respective significance levels for each correlation. **(C)** Two-group comparisons for the individual analytes in serum show traditional and alternative RAAS components to be increased in dogs with CIE compared to controls, with statistical significance reached for Ang I, Ang II, Ang IV, and Ang 1–7 as well as PRA-S (* indicates significance at $p<0.05$). Ang I (1-10): angiotensin I; Ang II (1-8): angiotensin II; Ang III (2-8): angiotensin III; Ang IV (3-8): angiotensin IV; Ang 1–7: angiotensin 1–7; Ang 1–5: angiotensin 1–5; PRA-S: marker of plasma renin activity (calculated); ACE-S: ratio of Ang II (1-8) to Ang I (1-10) = marker of angiotensin-converting enzyme (ACE) activity; AA2 ratio: ratio of aldosterone to Ang II (1-8) = marker of adrenal responsiveness to Ang II (1-8); ALT-S: ratio of [Ang 1–7+Ang 1–5] to [Ang I (1-10) + Ang II (1-8) + Ang 1–7+Ang 1–5]=marker of renin-independent alternative serum RAAS activity.

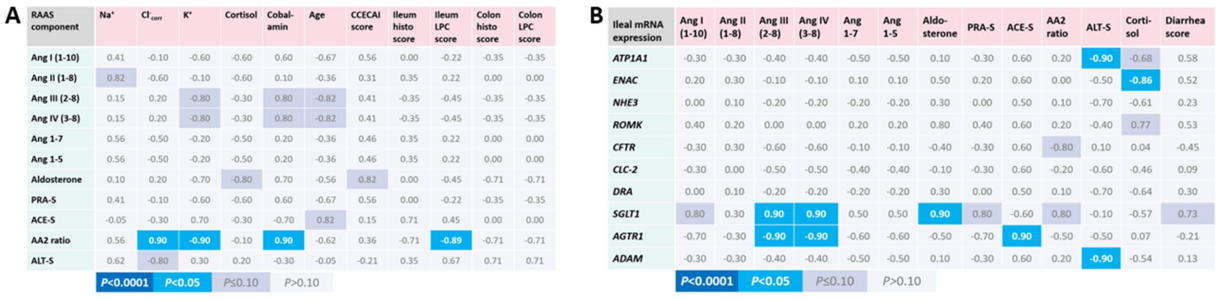


FIGURE 3
Association of serum RAAS activation with patient and disease characteristics, intestinal electrolyte transporter, and local RAAS component expression in canine CIE. **(A)** Correlations of serum RAAS components with patient and disease characteristics. Only the calculated serum AA2 ratio was significantly positively correlated with serum corrected $Cl^-$ and cobalamin concentrations and was inversely correlated with serum $K^+$ concentrations and histologic lesion scores in the ileum. **(B)** Correlations of serum RAAS components with the mRNA expression of electrolyte transporters, *ADAM*, and *AGTR1*. Shown are the Spearman correlation coefficients (ρ) for the individual correlations, with the color scheme (indicated below the table) reflecting the respective significance levels for each correlation.

function of *DRA*, *ENAC*, and *ATP1A1* in rodent colitis models and human IBD patients (7–9, 21–25), suggesting species-specific differences in the dysregulation or counter-regulation of these transporters.

Another explanation for these discrepant results among dogs, humans, and experimental rodents might be the primary location of the disease. Human IBD, including Crohn's disease (CD) and ulcerative colitis, mostly affects the colon and disease localization strictly to the ileum is seen in only approximately 30% of CD cases (26). In contrast, canine CIE has a more heterogenous distribution along the gastrointestinal tract and lesions often predominate in the small intestine, particularly in the ileum (27, 28). Along with these species-specific differences, it is reasonable to assume that the sites and mechanisms of dysregulation or counter-regulation would also differ. In human CD, the differentiation between ileal and colonic disease has been proposed to account for differences in the pathogenesis, optimal therapeutic approaches, and the corresponding treatment success rates (26, 29). Thus, the results obtained for canine CIE may generally resemble human ileal CD more closely than CD with predominantly colonic inflammatory lesions. Differential

investigation of the transepithelial electrolyte transport in human ileal and colonic CD is lacking thus far and these hypotheses warrant further study in canine CIE and human IBD.

Upregulation of the NaCl uptake mechanisms might be an attempt to compensate for electrolyte and free water losses associated with the maldigestion and malabsorption resulting from the exacerbated immune response of the intestinal mucosa. These counterregulatory mechanisms could be induced, exacerbated, or otherwise modulated by the RAAS as a regulator of systemic blood pressure activated by low plasma NaCl concentrations (30). A regulatory effect of RAAS on colonic electrolyte transport has been established, specifically an upregulation of *ENAC* and *ATP1A1* by aldosterone (31). This regulatory effect appears to be mediated both on the functional and transcriptional level (32). Also, an upregulation of NHE3 in the proximal colon, but not the ileal or renal epithelium, was demonstrated in aldosterone-treated rats (33). These transport mechanisms stimulate NaCl and free water absorption, leading to an increase in blood pressure. Stimulation of the $Na^+$ absorption by RAAS would also explain the predominance of hypokalemia in dogs with CIE (3), as $K^+$ losses usually accompany renal and intestinal $Na^+$ absorption and is in line with the strong inverse correlation of $K^+$ plasma levels with serum AA2 ratios we found in this study. Human IBD, in contrast, is mostly associated with hyponatremia (3), further supporting our hypothesis of differential regulation of electrolyte transporters in canine CIE and human IBD.

In addition to aldosterone, Ang II has been shown to affect intestinal electrolyte absorption (34), such as via activation of ENaC by AGTR1 stimulation (34). However, its effects may be dose- and receptor-dependent (34, 35): while low to moderate Ang II levels stimulate $Na^+$ and thus water absorption, presumably via the sympathetic and enteric nervous system, high levels of Ang II inhibit absorptive processes, which is proposed to be mediated by increased prostaglandin concentrations in the intestinal mucosa (35) and indicate an ambivalent effect of RAAS depending on the local mucosal microenvironment. As the primary site of intestinal RAAS-mediated regulation of electrolyte homeostasis, the colon has an enormous absorptive reserve capacity to compensate for fluid losses in the proximal gastrointestinal tract. Therefore, it is surprising that no changes in the expression of any colonic electrolyte transporters investigated – at least on the mRNA level – were seen in the dogs with CIE, given the finding of significant upregulation of the traditional and alternative RAAS arms in these dogs and their presentation with diarrhea of varying severity. We can only speculate as to the possible reasons for this finding. The extent of RAAS activation might not be sufficient to induce an upregulation of electrolyte transporter transcription in the colon, which would be consistent with the overall mild plasma electrolyte alterations reported (3). Furthermore, the sampling site of the colonic tissue biopsies might have been too far proximal, because the regulatory response was observed to vary between the proximal and distal colon in rats (36). In addition, serum concentrations of electrolytes and RAAS components might be affected by regulatory efforts of other organs (e.g., kidneys) and/or dietary $Na^+$ concentrations.

Only very few significant correlations were detected between the overexpressed electrolyte transporter genes in the intestinal mucosa and the concentrations of RAAS components in serum. While this does not exclude a RAAS-mediated upregulation of the ileal electrolyte transporters, a direct effect on their transcription levels appears less likely. Still, translational or functional effects of certain traditional and/or alternative RAAS components could be mediated by AGTRs. In contrast, the strong correlation observed between mucosal *SGLT1* mRNA levels and several serum RAAS components supports a regulatory effect of RAAS on intestinal *SGLT1* expression. A relationship between SGLT1 activity and RAAS has been reported previously, but the effects of RAAS appear to be receptor-dependent (37–39). While activation of AGTR1 inhibits the activity of SGLT1, AGTR2 activation enhances SGLT1 activity (37). To our knowledge, an effect of RAAS on *SGLT1* gene expression has not previously been reported. Similar to the upregulation of *NHE3* and *ATP1A1,* an increased expression and activity of SGLT1 would enhance the absorption of osmotically active $Na^+$ and glucose, thus ameliorating diarrhea. Whether this concept lends itself to an effective adjunct or even a sole nutritional approach requires further investigation.

The varying effects of RAAS on SGLT1 activity reported in the literature and the lack of correlations between the mucosal expression of most investigated electrolyte transporters and serum RAAS components in our study could also point to a local action of RAAS. Such a local RAAS activity could be mediated by the locally expressed AGTRs and be only partially dependent on or completely independent of systemic RAAS control. Local effects of the AGTR1-agonist losartan have been shown in the canine stomach (40), suggesting a functional local RAAS in the canine gastrointestinal tract. The downregulation of *AGTR1* in the inflamed ileal mucosa in canine CIE could be interpreted as a local counterregulatory mechanism to negate the increased availability of ligands either as a negative feedback loop or an effort to limit the effects of these ligands to specific target tissues. Compared to the results of this study on canine CIE, only some systemic RAAS components were found to be increased (ACE2, Ang 1–7, and Ang II), and aldosterone concentrations decreased in humans with IBD compared to healthy controls (6). Increasing evidence supports the existence of alternative (local) RAAS activity that counteracts the systemic effects of traditional RAAS pathways (41, 42). This alternative RAAS consists of small peptides derived from Ang I or II, such as Ang (1–9) and Ang (1–7), and additional receptors for RAAS components including Mas (4, 42, 43). While systemic RAAS effects are predominantly pro-inflammatory, these alternative pathways appear to be primarily anti-inflammatory and anti-fibrotic, promoting epithelial recovery (44). Whether these opposing effects apply to canine CIE and offer therapeutic potential, however, requires further investigation.

Similar to the ambivalent effects on local SGLT1 activity, binding of Ang II to AGTR1 elicits pro-inflammatory effects, whereas it may have anti-inflammatory effects via AGTR2 (45). Hence, differential regulation and pleiotropic effects of RAAS on intestinal mucosal electrolyte transport can be reasonably assumed.

In conclusion, our results indicate an upregulation of ileal, but not colonic, electrolyte transport mechanisms to enhance distal intestinal absorption of $Na^+$ and free water in dogs with CIE. Hence, targeting colonic electrolyte uptake mechanisms to modulate its absorptive reserve capacity might pose a novel therapeutic avenue for CIE patients. We could also demonstrate an upregulation of traditional and alternative RAAS components in serum specimens from diarrheic dogs with CIE. Although a relationship between systemic RAAS and intestinal electrolyte transporter levels would appear plausible, a direct association and regulatory effects remain to be proven in future studies. Targeting the traditional and alternative RAAS pathways may be a novel therapeutic avenue to ameliorate diarrhea in dogs with CIE.

## Data availability statement

The original contributions presented in the study are included in the article/supplementary materials, further inquiries can be directed to the corresponding authors.

## Ethics statement

The animal study was reviewed and approved. Serum samples ($n = 5$) and endoscopic tissue biopsies from the ileum ($n = 7$) and colon ($n = 6$) of dogs with CIE were surplus materials from a previous study that was approved by the Regional Council of the State of Saxony, Chemnitz/Leipzig, Germany (#TVV 06–17). Control tissues were full-thickness biopsies from the ileum ($n = 10$) and colon ($n = 12$) of purpose-bred healthy dogs that were euthanized for an unrelated project at the School of Veterinary Medicine and Biomedical Sciences at Texas A&M University, United States (Animal Use Protocol #TAMU 2009–0123). Serum from age- and sex-matched healthy controls ($n = 5$) were surplus materials from the blood donor bank at the Department for Small Animals, University of Leipzig, Germany. Written informed consent was obtained from the owners for the participation of their animals in this study.

## Author contributions

FD and RMH: conception of the work and drafting the manuscript. FD, OD, SK, IAB, JMS, and RMH: acquisition, analysis, or interpretation of data, and revising the manuscript. All authors provide approval for publication of the content and agree to be accountable for all aspects of the work.

## Funding

This work was funded by a grant from the Leipzig veterinary junior scientist support program financed by the "Freundeskreis Tiermedizin," the Faculty of Veterinary Medicine, and by Ceva Santé Animale.

## Acknowledgments

The authors appreciate the excellent technical assistance of Alexandra Petric. The qPCR was conducted using equipment at the VetCore Facility of the Vetmeduni Vienna. The author(s) acknowledge support from the German Research Foundation (DFG) and Universität Leipzig within the program of Open Access Publishing.

## Conflict of interest

OD is employed by Attoquant Diagnostics.

The remaining authors declare that the research was conducted in the absence of any commercial or financial relationships that could be construed as a potential conflict of interest.

## Publisher's note



## References

1. Yu Q, Zhu C, Feng S, Xu L, Hu S, Chen H, et al. Economic burden and health care access for patients with inflammatory bowel diseases in China: web-based survey study. *J Med Internet Res*. (2021) 23:e20629. doi: 10.2196/20629

2. Barkas F, Liberopoulos E, Kei A, Elisaf M. Electrolyte and acid-base disorders in inflammatory bowel disease. *Ann Gastroenterol*. (2013) 26:23–8.

3. Heilmann RM, Becher A, Dengler F. Electrolyte imbalances in dogs with chronic inflammatory enteropathies. *Top Companion Anim Med*. (2022) 46:100597. doi: 10.1016/j.tcam.2021.100597

4. Bader M. ACE2, angiotensin-(1–7), and mas: the other side of the coin. *Pflügers Arch*. (2013) 465:79–85. doi: 10.1007/s00424-012-1120-0

5. Ferrario CM, Strawn WB. Role of the renin-angiotensin-aldosterone system and proinflammatory mediators in cardiovascular disease. *Am J Cardiol*. (2006) 98:121–8. doi: 10.1016/j.amjcard.2006.01.059

6. Garg M, Burrell LM, Velkoska E, Griggs K, Angus PW, Gibson PR, et al. Upregulation of circulating components of the alternative renin-angiotensin system in inflammatory bowel disease: a pilot study. *J Renin-Angiotensin-Aldosterone Syst*. (2015) 16:559–69. doi: 10.1177/1470320314521086

7. Ghishan FK, Kiela PR. Epithelial transport in inflammatory bowel diseases. *Inflamm Bowel Dis*. (2014) 20:1099–109. doi: 10.1097/MIB.0000000000000029

8. Amasheh S, Barmeyer C, Koch CS, Tavalali S, Mankertz J, Epple H-J, et al. Cytokine-dependent transcriptional down-regulation of epithelial sodium channel in ulcerative colitis. *Gastroenterology*. (2004) 126:1711–20. doi: 10.1053/j.gastro.2004.03.010

9. Sullivan S, Alex P, Dassopoulos T, Zachos NC, Iacobuzio-Donahue C, Donowitz M, et al. Downregulation of sodium transporters and NHERF proteins in IBD patients and mouse colitis models: potential contributors to IBD-associated diarrhea. *Inflamm Bowel Dis*. (2009) 15:261–74. doi: 10.1002/ibd.20743

10. Heilmann RM, Jergens AE. Canine chronic enteropathy - current state-of-the-art and emerging concepts. *Front Vet Sci*. (2022) 9:923013. doi: 10.3389/fvets.2022.923013

11. Allenspach K, Wieland B, Gröne A, Gaschen F. Chronic enteropathies in dogs: evaluation of risk factors for negative outcome. *J Vet Intern Med*. (2007) 21:700–8. doi: 10.1892/0891-6640(2007)21[700:CEIDEO]2.0.CO;2

12. Washabau RJ, Day MJ, Willard MD, Hall EJ, Jergens AE, Mansell J, et al. Endoscopic, biopsy, and histopathologic guidelines for the evaluation of gastrointestinal inflammation in companion animals. *J Vet Intern Med*. (2010) 24:10–26. doi: 10.1111/j.1939-1676.2009.0443.x

13. Cabrera-García AI, Protschka M, Alber G, Kather S, Dengler F, Müller U, et al. Dysregulation of gastrointestinal RAGE (receptor for advanced glycation end products) expression in dogs with chronic inflammatory enteropathy. *Vet Immunol Immunopathol*. (2021) 234:110216. doi: 10.1016/j.vetimm.2021.110216

14. Dengler F, Sternberg F, Grages M, Kästner SB, Verhaar N. Adaptive mechanisms in no flow vs. low flow ischemia in equine jejunum epithelium: different paths to the same destination. *Front Vet Sci*. (2022) 9:947482. doi: 10.3389/fvets.2022.947482

15. Xie F, Xiao P, Chen D, Xu L, Zhang B. miRDeepFinder: a miRNA analysis tool for deep sequencing of plant small RNAs. *Plant Mol Biol*. (2012) 80:75–84. doi: 10.1007/s11103-012-9885-2

16. Domenig O, Manzel A, Grobe N, Königshausen E, Kaltenecker CC, Kovarik JJ, et al. Neprilysin is a mediator of alternative renin-angiotensin-system activation in the murine and human kidney. *Sci Rep*. (2016) 6:33678. doi: 10.1038/srep33678

17. Sotillo S, Ward JL, Guillot E, Domenig O, Yuan L, Smith JS, et al. Dose-response of benazepril on biomarkers of the classical and alternative pathways of the renin-angiotensin-aldosterone system in dogs. *Sci Rep*. (2023) 13:2684. doi: 10.1038/s41598-023-29771-x

18. Pavo N, Goliasch G, Wurm R, Novak J, Strunk G, Gyöngyösi M, et al. Low- and high-renin heart failure phenotypes with clinical implications. *Clin Chem*. (2018) 64:597–608. doi: 10.1373/clinchem.2017.278705

19. Burrello J, Buffolo F, Domenig O, Tetti M, Pecori A, Monticone S, et al. Renin-angiotensin-aldosterone system triple-a analysis for the screening of primary

Aldosteronism. *Hypertension*. (2020) 75:163–72. doi: 10.1161/HYPERTENSIONAHA.119.13772

20. Zoufaly A, Poglitsch M, Aberle JH, Hoepler W, Seitz T, Traugott M, et al. Human recombinant soluble ACE2 in severe COVID-19. *Lancet Respir Med*. (2020) 8:1154–8. doi: 10.1016/S2213-2600(20)30418-5

21. Magalhães D, Cabral JM, Soares-da-Silva P, Magro F. Role of epithelial ion transports in inflammatory bowel disease. *Am J Physiol Gastrointest Liver Physiol*. (2016) 310:G460–76. doi: 10.1152/ajpgi.00369.2015

22. Sandle GI, Higgs N, Crowe P, Marsh MN, Venkatesan S, Peters TJ. Cellular basis for defective electrolyte transport in inflamed human colon. *Gastroenterology*. (1990) 99:97–105. doi: 10.1016/0016-5085(90)91235-x

23. Malakooti J, Saksena S, Gill RK, Dudeja PK. Transcriptional regulation of the intestinal luminal $Na^+$ and $cl^-$ transporters. *Biochem J*. (2011) 435:313–25. doi: 10.1042/BJ20102062

24. Priyamvada S, Gomes R, Gill RK, Saksena S, Alrefai WA, Dudeja PK. Mechanisms underlying dysregulation of electrolyte absorption in inflammatory bowel disease-associated diarrhea. *Inflamm Bowel Dis*. (2015) 21:2926–35. doi: 10.1097/MIB.0000000000000504

25. Rahman MM, Borthakur A, Afroz S, Arthur S, Sundaram U. Unique regulation of intestinal villus epithelial cl-/HCO3- exchange by cyclooxygenase pathway metabolites of arachidonic acid in a mouse model of spontaneous ileitis. *Int J Mol Sci*. (2021) 22:22. doi: 10.3390/ijms22084171

26. Atreya R, Siegmund B. Location is important: differentiation between ileal and colonic Crohn's disease. *Nat Rev Gastroenterol Hepatol*. (2021) 18:544–58. doi: 10.1038/s41575-021-00424-6

27. Casamian-Sorrosal D, Willard MD, Murray JK, Hall EJ, Taylor SS, Day MJ. Comparison of histopathologic findings in biopsies from the duodenum and ileum of dogs with enteropathy. *J Vet Intern Med*. (2010) 24:80–3. doi: 10.1111/j.1939-1676.2009.0427.x

28. Procoli F, Mõtsküla PF, Keyte SV, Priestnall S, Allenspach K. Comparison of histopathologic findings in duodenal and ileal endoscopic biopsies in dogs with chronic small intestinal enteropathies. *J Vet Intern Med*. (2013) 27:268–74. doi: 10.1111/jvim.12041

29. Pierre N, Salée C, Vieujean S, Bequet E, Merli A-M, Siegmund B, et al. Review article: distinctions between ileal and colonic Crohn's disease: from physiology to pathology. *Aliment Pharmacol Ther*. (2021) 54:779–91. doi: 10.1111/apt.16536

30. Mirabito Colafella KM, Bovée DM, Danser AH. The renin-angiotensin-aldosterone system and its therapeutic targets. *Exp Eye Res*. (2019) 186:107680. doi: 10.1016/j.exer.2019.05.020

31. Rossier BC, Baker ME, Studer RA. Epithelial sodium transport and its control by aldosterone: the story of our internal environment revisited. *Physiol Rev*. (2015) 95:297–340. doi: 10.1152/physrev.00011.2014

32. Garty H, Palmer LG. Epithelial sodium channels: function, structure, and regulation. *Physiol Rev*. (1997) 77:359–96. doi: 10.1152/physrev.1997.77.2.359

33. Cho JH, Musch MW, Bookstein CM, McSwine RL, Rabenau K, Chang EB. Aldosterone stimulates intestinal Na+ absorption in rats by increasing NHE3 expression of the proximal colon. *Am J Phys*. (1998) 274:C586–94. doi: 10.1152/ajpcell.1998.274.3.C586

34. Zaika O, Mamenko M, Staruschenko A, Pochynyuk O. Direct activation of ENaC by angiotensin II: recent advances and new insights. *Curr Hypertens Rep*. (2013) 15:17–24. doi: 10.1007/s11906-012-0316-1

35. Levens NR. Control of intestinal absorption by the renin-angiotensin system. *Am J Physiol*. (1985) 249:G3–G15. doi: 10.1152/ajpgi.1985.249.1.G3

36. Amasheh S, Epple HJ, Mankertz J, Detjen K, Goltz M, Schulzke JD, et al. Differential regulation of ENaC by aldosterone in rat early and late distal colon. *Ann N Y Acad Sci*. (2000) 915:92–4. doi: 10.1111/j.1749-6632.2000.tb05227.x

37. Casselbrant A, Malinauskas M, Marschall H-U, Wallenius V, Fändriks L. Angiotensin II exerts dual actions on sodium-glucose transporter 1-mediated transport in the human jejunal mucosa. *Scand J Gastroenterol*. (2015) 50:1068–75. doi: 10.3109/00365521.2015.1019557

38. Wong TP, Debnam ES, Leung PS. Diabetes mellitus and expression of the enterocyte renin-angiotensin system: implications for control of glucose transport across the brush border membrane. *Am J Physiol Cell Physiol*. (2009) 297:C601–10. doi: 10.1152/ajpcell.00135.2009

39. Wong TP, Debnam ES, Leung PS. Involvement of an enterocyte renin-angiotensin system in the local control of SGLT1-dependent glucose uptake across the rat small intestinal brush border membrane. *J Physiol*. (2007) 584:613–23. doi: 10.1113/jphysiol.2007.138578

40. Truse R, Voß F, Herminghaus A, Schulz J, Weber AP, Mettler-Altmann T, et al. Local gastric RAAS inhibition improves gastric microvascular perfusion in dogs. *J Endocrinol*. (2019) 241:235–47. doi: 10.1530/JOE-19-0030

41. Heilmann RM, Csukovich G, Burgener IA, Dengler F. Time to eRAASe chronic inflammation: current advances and future perspectives on renin-angiotensin-aldosterone-system and chronic intestinal inflammation in dogs and humans. *Front Vet Sci*. (2023) 10:10. doi: 10.3389/fvets.2023.1180125

42. Santos RA, Sampaio WO, Alzamora AC, Motta-Santos D, Alenina N, Bader M, et al. The ACE2/angiotensin-(1-7)/MAS Axis of the renin-angiotensin system: focus on angiotensin-(1-7). *Physiol Rev*. (2018) 98:505–53. doi: 10.1152/physrev.00023.2016

43. Donoghue M, Hsieh F, Baronas E, Godbout K, Gosselin M, Stagliano N, et al. A novel angiotensin-converting enzyme–related carboxypeptidase (ACE2) converts angiotensin I to angiotensin 1-9. *Circ Res*. (2000):87. doi: 10.1161/01.RES.87.5.e1

44. Garg M, Angus PW, Burrell LM, Herath C, Gibson PR, Lubel JS. Review article: the pathophysiological roles of the renin-angiotensin system in the gastrointestinal tract. *Aliment Pharmacol Ther*. (2012) 35:414–28. doi: 10.1111/j.1365-2036.2011.04971.x

45. Salmenkari H, Korpela R, Vapaatalo H. Renin–angiotensin system in intestinal inflammation—angiotensin inhibitors to treat inflammatory bowel diseases? *Basic Clin Pharmacol Toxicol*. (2021) 129:161–72. doi: 10.1111/bcpt.13624

frontiers | Frontiers in Veterinary Science

TYPE Original Research
PUBLISHED 15 September 2023
DOI 10.3389/fvets.2023.1234768



OPEN ACCESS

EDITED BY
Ahmed S. Mandour,
Suez Canal University, Egypt

REVIEWED BY
Ana Patrícia Fontes-Sousa,
University of Porto, Portugal
Federico Bonsembiante,
University of Padua, Italy

*CORRESPONDENCE
Sirilak Disatian Surachetpong
✉ sirilak.d@chula.ac.th

RECEIVED 05 June 2023
ACCEPTED 23 August 2023
PUBLISHED 15 September 2023

CITATION
Tangmahakul N, Orton EC and Surachetpong SD (2023) Investigation of red blood cell and platelet indices in adult dogs suffered from myxomatous mitral valve disease with and without pulmonary hypertension. *Front. Vet. Sci.* 10:1234768. doi: 10.3389/fvets.2023.1234768



# Investigation of red blood cell and platelet indices in adult dogs suffered from myxomatous mitral valve disease with and without pulmonary hypertension

Nattawan Tangmahakul[1], E. Christopher Orton[2] and Sirilak Disatian Surachetpong[1]*

[1]Department of Veterinary Medicine, Faculty of Veterinary Science, Chulalongkorn University, Bangkok, Thailand, [2]Department of Clinical Sciences, College of Veterinary Medicine and Biomedical Science, Colorado State University, Fort Collins, CO, United States

**Background:** Pulmonary hypertension (PH) is a common complication of cardiopulmonary disease. In dogs, PH commonly occurs secondary to myxomatous mitral valve disease (MMVD). Red blood cell and platelet indices including mean corpuscular volume (MCV), mean corpuscular hemoglobin (MCH), mean corpuscular hemoglobin concentration (MCHC), red cell distribution width (RDW), mean platelet volume (MPV) and platelet distribution width (PDW), have previously been found to be indicators for predicting and prognosing PH in humans. Therefore, this study aimed to investigate whether these indices are associated with MMVD and/or PH in dogs.

**Methods:** Two hundred and forty-six dogs were retrospectively recruited for the study and classified into 4 groups: normal ($n = 49$), MMVD ($n = 102$), PH ($n = 17$), MMVD+PH ($n = 78$). A sub-analysis was performed in dogs with MMVD without evidence of PH according to stage B1 ($n = 20$), stage B2 ($n = 15$), stage C ($n = 67$). The data are expressed as median (interquartile range).

**Results and discussion:** No significant differences ($p < 0.05$) were found in MCV, RDW and MPV among all groups (normal, MMVD, PH and MMVD+PH). However, decreases in MCH and MCHC were found in MMVD [22.40 (20.90-23.50) pg and 35.25 (33.08-36.90) g/dL], MMVD+PH [22.25 (20.85-23.98) pg and 35.65 (33.30-37.33) g/dL] and PH groups [21.20 (20.60-22.20) pg and 33.80 (32.75-35.70) g/dL] compared to the normal dogs [24.29 (23.55-24.90) pg and 38.20 (37.50-39.05) g/dL] ($p < 0.001$). Decreases in PDW were found in dogs in the MMVD+PH [15.10 (14.98-15.30) %] groups compared to dogs in the normal group [15.30 (15.10-15.50) %] ($p = 0.004$). Sub-analysis of MMVD dogs without PH showed a decrease in MCH in dogs with stage B2 MMVD [21.00 (20.50-22.90) pg] and stage C MMVD [22.40 (20.90-23.20) pg] compared to normal dogs [24.29 (23.55-24.90) pg] ($p < 0.001$). MCHC of dogs with stage B1 [36.55 (33.53-37.78) g/dL] ($p = 0.004$), B2 [32.90 (32.00-35.00) g/dL] ($p < 0.001$) and C MMVD [35.30 (33.30-36.80) g/dL] ($p < 0.001$) were lower than those of normal dogs [38.20 (37.50-39.05) g/dL]. PDW in the stage C MMVD group [15.10 (15.00-15.30) %] was reduced compared to the normal group [15.30 (15.10-15.50) %] ($p = 0.042$) and the stage B1 MMVD group [15.35 (15.23-15.68) %] ($p = 0.002$). MCH, MCHC and PDW were negatively correlated with the left atrial and left ventricular size.

**Conclusion:** Decreases in MCH and MCHC are related to MMVD, precapillary PH and postcapillary PH while PDW are associated with MMVD severity but not with the presence of PH.

KEYWORDS

cardiology, myxomatous mitral valve disease, platelet distribution width, pulmonary hypertension, red cell distribution width

## Introduction

The consensus statement guideline of the American College of Veterinary Internal Medicine categorizes pulmonary hypertension (PH) into six groups: pulmonary arterial hypertension, PH due to left heart disease, PH secondary to respiratory disease/hypoxia, pulmonary emboli/thrombi/thromboembolism, parasitic disease, and PH with multifactorial or unclear mechanism (1). In older small breed dogs, PH commonly occurs secondary to myxomatous mitral valve disease (MMVD) (2). However, PH is also commonly found as a complication of respiratory and heartworm disease in dogs (3–5). Several studies in human patients have focused on the relationship between red blood cells (RBC) and platelet indices and disease progression and prognosis (6–14).

Red cell distribution width (RDW) measures size-heterogeneity of the circulating red blood cells (15). Red cell distribution width can be routinely reported as part of the complete blood count. This parameter is altered in various diseases such as anemia (16), cancer (17), and inflammatory diseases (18). Red cell distribution width has also been mentioned as a predictive and prognostic biomarker for heart failure, myocardial infarction, and PH in human patients because it positively correlates with the adverse outcomes of these cardiovascular diseases (6, 7, 9, 19, 20). The studies in human patients with heart failure showed that RDW had a positive correlation with N-terminal pro B-type natriuretic peptide, a powerful prognostic biomarker for heart failure (6). Moreover, increased RDW was related to the progression of complications and a decrease in survival time (7, 19). The study in human patients with PH revealed that an elevated RDW decreased the survival time (9). Consequently, RDW was a predictive or prognostic marker for morbidity and mortality of heart failure. An association between elevated RDW and adverse outcome has also been noted in dogs with MMVD (21). Therefore, RDW may be a candidate for detecting the progression of cardiovascular disease. RBC indices can be used to differentiate the type of anemia (22). Mean corpuscular volume (MCV) quantifies the average volume of RBC, while mean corpuscular hemoglobin (MCH) indicates the calculated hemoglobin amount per a single RBC, and mean corpuscular hemoglobin concentration (MCHC) reflects the calculated hemoglobin concentration in RBC (22, 23). Changes in RBC count, hemoglobin, hematocrit, MCH, MCHC, and RDW were reported previously in human with PH (24). Furthermore, negative correlation between RDW and MCV was found in dogs with MMVD (21).

Platelets play an important role in the inflammatory process because activated platelets secrete various inflammatory mediators (25, 26). The determination of platelet indices such as mean platelet volume (MPV) and platelet distribution width (PDW) can be routinely performed using an automated hematologic analyzer (25). The MPV reflects platelet production, activation, and function. PDW provides information on the variability of platelet size, which may also reflect platelet activation. Increased MPV and PDW have been found in several diseases associated with inflammatory conditions, including many cardiac diseases (27). Increases in MPV and PDW have been associated with increased severity of heart disease, heart failure, and adverse progressive cardiac outcome in human patients (10, 12, 28, 29). MPV was increased in human patients with mitral regurgitation (MR) from various causes and correlated with the severity of MR (13). An increased PDW was found in patients with heart failure (12). Furthermore, increased MPV and PDW were observed in patients with left-sided heart disease (28). MPV and PDW were prognostic biomarkers for cardiac diseases and heart failure. In addition, increases in these platelet indices have been noted in patients with PH (8, 11, 14). An increased MPV was revealed in various causes of PH (8). Elevated MPV and PDW were found in human patients with precapillary PH, and MPV may be a prognostic marker for PH due to positive association with the severity of PH (11, 14).

A study of RDW in dogs with PH has been published (30, 31). However, there is no study investigating both red blood cell and platelet indices that primarily focuses in MMVD dogs with PH. Therefore, this study aimed to investigate the changes in MCV, MCH, MCHC, RDW, MPV and PDW in normal dogs and dogs with PH or MMVD, or both.

## Materials and methods

### Animals

Data of dogs were retrieved retrospectively from the electronic medical records of the Small Animal Teaching Hospital, Faculty of Veterinary Science, Chulalongkorn University, Thailand. Signalment, history, physical, radiographic and echocardiographic findings, and hematologic and blood chemical profiles were noted. Since MMVD commonly occurs in senior small breed dogs, the inclusion criteria included dogs older than 6 years and weighing up to 15 kg. To assess the changes in RBC and platelet indices in dogs with PH, the dogs were divided into four groups of healthy dogs (normal group), dogs with MMVD (MMVD group), dogs with MMVD and PH (MMVD+PH group), and dogs with PH caused by other causes (PH group). The normal group consisted of healthy dogs that attended the Small Animal Teaching Hospital for a health checkup, and no abnormalities and diseases were found on physical examination, radiography, and echocardiography. Based on the criteria for PH secondary to left-sided heart disease (1), only dogs with left heart enlargement or MMVD stage B2 or greater were included in the MMVD+PH group. To clarify whether the severity of MMVD affected the change in RBC and platelet indices, a sub-analysis was performed in MMVD dogs without evidence of PH according to stage B1, stage B2 and stage C.

### Diagnosis and staging of MMVD and PH

The diagnosis and staging MMVD and PH were performed following the American College of Veterinary Internal Medicine guidelines (1, 32). Briefly, dogs were diagnosed with MMVD based on clinical presentation, radiography, and echocardiography. Dogs with stage B1 MMVD had mitral regurgitation without evidence of congestive heart failure (CHF) and structural changes in the heart. Dogs with stage B2 MMVD had left atrium to aorta ratio (LA/Ao) in the right parasternal short-axis view in early diastole >1.6, normalized left ventricular internal dimension at end-diastole (LVIDd) >1.7, and mitral

regurgitation without evidence of heart failure. Dogs with stage C MMVD had mitral regurgitation, left atrial and ventricular enlargement, and previous history of pulmonary edema. Dogs with stage C MMVD responded to standard treatment with furosemide, spironolactone, angiotensin- converting enzyme inhibitor and pimobendan. Dogs with stage D MMVD exhibited clinical signs that were unresponsive to standard treatment of stage C MMVD and required additional medications such as antiarrhythmic drug and other diuretics (32). The underlying causes of PH were evaluated and classified. The peak tricuspid regurgitation (TR) velocity and the number of different anatomic sites with echocardiographic signs of PH were used to identify PH which included from low (≤3.0 m/s peak TR velocity, and no or 1 different anatomic site with echocardiographic signs of PH) to high (≤3.0 m/s peak TR velocity with 3 different anatomic sites of echocardiographic signs, 3.0–3.4 m/s peak TR velocity with ≥2 different anatomic sites of echocardiographic signs, or > 3.4 m/s peak TR velocity with ≥1 different anatomic site of echocardiographic signs of PH) probability of PH (1). The anatomic sites of echocardiographic signs of PH were investigated in the ventricles, pulmonary artery, and right atrium and caudal vena cava (1). Dogs with pregnancy and/or other systemic and inflammatory diseases, diagnosed through history taking, physical examination, hematology, and radiography were excluded.

## Red blood cell indices, platelet indices, and echocardiographic data collection

Hematological and blood chemistry profiles, and echocardiographic data were collected. The complete blood count and blood chemistry were performed by automated analyzers (BC-5000 Vet and BS-800, Mindray, China). The recorded complete blood count included red blood cell (RBC) count, hematocrit, MCV, MCH, MCHC, RDW, platelet count, MPV, PDW, and white blood cell (WBC) count. Thin blood smears were performed for screening blood morphology. Echocardiographic examination was conducted by an investigator (SS) utilizing a 4–12 MHz phased array transducer and an ultrasound machine (M9, Mindray, China). Echocardiographic data included left atrial size (LA) size, aorta size (Ao), the ratio of the left atrial dimension to the aortic annulus dimension, interventricular septum thickness at end-diastole (IVSd), LVIDd, left ventricular posterior wall thickness at end-diastole (LVPWd), interventricular septum thickness at end-systole (IVSs), left ventricular internal dimension at end-systole (LVIDs), left ventricular posterior wall thickness at end-systole (LVPWs), fractional shortening (FS), peak TR velocity, and calculated pulmonary arterial pressure (PAP).

## Statistical analysis

The computer-based program, SPSS version 22 (IBM, United States) was used for statistical analysis. Data distribution was analyzed with the Shapiro–Wilk test. Differences in hematologic and echocardiographic data between groups were assessed with the Kruskal-Wallis and Dunn post-hoc tests. The Mann–Whitney U test was used to analyze the differences in peak TR velocity between the MMVD+PH and PH groups. The receiver operating characteristic (ROC) curves with area under curve (AUC) were performed to determine whether the significant RBC and platelet indices could predictor MMVD and PH. An AUC value indicates the discriminatory power of these indices, where an AUC ≤ 0.75 implies no clinical utility, 0.75 < AUC < 0.97 indicates a moderately discriminative value, and an AUC of 0.97 represents an extremely clinical value (33). The optimal cut-point values for these significant RBC and platelet indices were calculated using Youden's index and were used to estimate the sensitivity and specificity (34). Spearman's rank correlation and multivariable regression analysis were used to examine the relationship between the quantitative and qualitative variables, respectively. Evidence of a difference for all tests was at $p < 0.05$. All data were expressed in median (interquartile range).

# Results

## Animals

The normal group ($n = 49$) consisted of 21 males and 28 females, including 21 Shih Tzus, 12 Chihuahuas, 6 Yorkshire Terriers, 3 Pomeranians, 1 Dachshund, and 6 mixed breeds. The MMVD group ($n = 102$) was composed of 20 dogs with stage B1, 15 dogs with stage B2 and 67 dogs with stage C MMVD. This group comprised 62 males and 40 females, with 31 Chihuahuas, 19 Pomeranians, 15 Poodles, 8 Shih Tzus, 4 Yorkshire Terriers, 2 Maltese, 2 Miniature Pinschers, 1 Beagle, 1 Chinese Crested Hairless Dog, 1 Finnish Splitz, 1 Miniature Schnauzer, 1 Dachshund and 16 mixed breeds. The MMVD+PH group ($n = 78$) included 7 dogs with stage B2, 68 dogs with stage C, and 3 dogs with stage D MMVD and PH. This group had 7 dogs with low probability of PH, 51 dogs with intermediate probability of PH, and 20 dogs with high probability of PH. There were 41 males and 37 females in the MMVD+PH group including 26 Chihuahuas, 14 Pomeranians, 10 Poodles, 9 Shih Tzus, 2 Miniature Pinchers, 1 Jack Russell Terrier, 1 Maltese, 1 Shetland Sheepdog, and 14 mixed breeds. The PH group ($n = 17$) included 14 dogs with PH due to respiratory problems and 3 dogs with PH due to heartworm disease. This group had 2 dogs with low probability of PH, 13 dogs with intermediate probability of PH, and 2 dogs with high probability of PH. There were 10 males and 7 females with 7 Pomeranians, 5 Chihuahuas, 1 Miniature Pincher, 1 Shih Tzu, 1 Jack Russell Terrier, 1 French Bulldog and 1 mixed breed dog. The age of the normal dogs was lower than that of the other groups ($p < 0.05$). No significant difference in age was found between the disease groups (Tables 1, 2).

Echocardiographic results showed the greater LA/Ao and LVIDd in the MMVD and MMVD+PH groups compared with the normal and PH groups ($p < 0.001$). The peak TR velocity and calculated PAP of MMVD+PH was greater than those of PH group ($p = 0.017$) (Table 1). In sub-analysis of MMVD group, the greater LA/Ao, LVIDd and %FS were found in dogs with stage B2 and C MMVD compared with the normal dogs ($p < 0.001$). Moreover, LA/Ao and LVIDd, and %FS of dogs with stage C MMVD were greater than those of dogs with stage B1 MMVD ($p < 0.001$) (Table 3).

## Analysis of red blood cell and platelet indices

No difference in MCV and RDW was observed among groups. MCH and MCHC of dogs in MMVD, MMVD+PH, and PH groups were lower than those of normal dogs ($p < 0.001$) (Table 1 and Figure 1). Comparison of neither MCH nor MCHC between the disease groups revealed any significant difference. Analysis of

10.3389/fvets.2023.1234768

TABLE 1 Signalment, hematological profiles, and echocardiographic data of dogs in the present study.

| | Normal ($n = 49$) | MMVD ($n = 102$) | MMVD + PH ($n = 78$) | PH ($n = 17$) | $p$-value |
|---|---|---|---|---|---|
| Age (years) | 8.00 (7.00–10.00) | 12.00 (10.00–13.00)[a] | 11.50 (10.00–13.00)[a] | 11.00 (9.00–13.50)[a] | <0.001 |
| Gender (M/F) | 21/28 | 62/40 | 41/37 | 10/7 | |
| Weight (kg) | 5.50 (2.92–6.80) | 4.32 (3.40–5.50) | 4.62 (3.34–6.06) | 4.00 (2.50–5.95) | 0.215 |
| RBC ($\times 10^6$ cells/μL) | 6.57 (6.16–7.44) | 7.15 (6.39–7.62) | 6.77 (6.01–7.54) | 7.12 (6.11–7.94) | 0.120 |
| Hematocrit (%) | 42.80 (38.80–47.00) | 44.85 (40.00–48.50) | 42.60 (38.55–46.50) | 43.20 (39.10–48.45) | 0.124 |
| MCV (fL) | 63.80 (61.80–64.95) | 63.95 (60.90–65.78) | 63.80 (60.58–66.58) | 62.80 (60.30–66.25) | 0.901 |
| MCH (pg) | 24.29 (23.55–24.90) | 22.40 (20.90–23.50)[a] | 22.25 (20.85–23.98)[a] | 21.20 (20.60–22.20)[a] | <0.001 |
| MCHC (g/dL) | 38.20 (37.50–39.05) | 35.25 (33.08–36.90)[a] | 35.65 (33.30–37.33)[a] | 33.80 (32.75–35.70)[a] | <0.001 |
| RDW (%) | 14.00 (13.05–14.55) | 13.85 (13.10–14.70) | 14.10 (13.20–15.03) | 14.10 (13.45–14.45) | 0.480 |
| Platelet count ($\times 10^3$ cells/μL) | 283.00 (228.50–341.00) | 325.50 (257.25–414.00) | 395.00 (294.50–468.75)[a] | 389.00 (283.00–454.00) | 0.001 |
| MPV (fL) | 10.10 (9.05–11.35) | 10.70 (9.70–11.40) | 10.35 (9.70–11.33) | 11.00 (9.15–12.50) | 0.233 |
| PDW (%) | 15.30 (15.10–15.50) | 15.20 (15.00–15.40) | 15.10 (14.98–15.30)[a] | 15.20 (15.00–15.40) | 0.008 |
| WBC ($\times 10^3$ cells/μL) | 8.37 (6.98–10.82) | 8.63 (7.42–10.96) | 9.59 (7.79–11.65) | 8.79 (7.15–10.80) | 0.230 |
| Neutrophil ($\times 10^3$ cells/μL) | 5.87 (4.05–7.31) | 6.09 (4.95–7.69) | 6.98 (5.29–8.58) | 6.51 (5.56–8.16) | 0.064 |
| Eosinophil ($\times 10^3$ cells/μL) | 0.31 (0.20–0.30) | 0.31 (0.21–0.48) | 0.37 (0.22–0.54) | 0.28 (0.22–0.43) | 0.848 |
| Basophil ($\times 10^3$ cells/μL) | 0.02 (0.01–0.03) | 0.01 (0.00–0.02)[a] | 0.01 (0.00–0.02)[a] | 0.01 (0.00–0.02) | 0.006 |
| Lymphocyte ($\times 10^3$ cells/μL) | 1.53 (1.18–1.94) | 1.33 (1.06–1.77) | 1.44 (1.11–1.87) | 1.32 (1.00–1.79) | 0.393 |
| Monocyte ($\times 10^3$ cells/μL) | 0.57 (0.44–0.83) | 0.50 (0.25–0.76) | 0.49 (0.21–0.89) | 0.44 (0.17–0.88) | 0.071 |
| LA (cm/kg) | 0.92 (0.81–1.04) | 1.96 (1.62–2.42)[a,c] | 1.90 (1.53–2.43)[a,c] | 1.43 (1.33–1.75)[a] | <0.001 |
| Ao (cm/kg) | 0.76 (0.68–0.86) | 1.15 (0.91–1.32)[a] | 0.97 (0.79–1.15)[a,b] | 1.04 (0.96–1.18)[a] | <0.001 |
| LA/Ao | 1.20 (1.11–1.35) | 1.75 (1.47–2.15)[a,c] | 2.10 (1.77–2.40)[a,b,c] | 1.43 (1.22–1.67) | <0.001 |
| IVSd (cm/kg) | 0.47 (0.40–0.52) | 0.43 (0.38–0.49) | 0.42 (0.36–0.49) | 0.47 (0.41–0.59) | 0.053 |
| LVIDd (cm/kg) | 1.22 (1.17–1.37) | 1.77 (1.50–1.94)[a,c] | 1.83 (1.65–2.00)[a,c] | 1.30 (1.19–1.51) | <0.001 |
| LVPWd (cm/kg) | 0.38 (0.33–0.43) | 0.40 (0.36–0.46) | 0.41 (0.35–0.46) | 0.44 (0.36–0.49) | 0.181 |
| IVSs (cm/kg) | 0.61 (0.52–0.67) | 0.64 (0.56–0.72) | 0.68 (0.59–0.77)[a] | 0.60 (0.56–0.74) | 0.011 |
| LVIDs (cm/kg) | 0.74 (0.62–0.80) | 0.88 (0.74–1.01)[a,c] | 0.86 (0.69–1.04)[a] | 0.76 (0.61–0.85) | <0.001 |
| LVPWs (cm/kg) | 0.64 (0.56–0.71) | 0.67 (0.60–0.75) | 0.69 (0.59–0.79) | 0.59 (0.53–0.69) | 0.018* |
| %FS | 39.86 (34.75–45.68) | 47.49 (41.86–53.12) | 51.13 (44.50–55.47)[a] | 47.50 (38.67–50.47)[a] | <0.001 |
| TR (m/s) | – | – | 3.70 (3.29–4.32)[c] | 3.52 (2.86–3.76) | 0.017 |
| Calculated PAP (mmHg) | – | – | 54.97 (43.24–74.62)[c] | 49.51 (32.82–56.55) | 0.017 |

Values are median (interquartile).

Ao, aorta; FS, fractional shortening; IVSd, interventricular septum thickness at end-diastole; IVSs, interventricular septum thickness at end-systole; LA, left atrium; LA/Ao, the ratio of the left atrial dimension to the aortic annulus dimension; LVIDd, left ventricular internal dimension at end-diastole; LVIDs, left ventricular internal dimension at end-systole; LVPWd, left ventricular posterior wall thickness at end-diastole; LVPWs, left ventricular posterior wall thickness at end-systole; MCH, mean corpuscular hemoglobin; MCHC, mean corpuscular hemoglobin concentration; MCV, mean corpuscular volume; MPV, mean platelet volume; PAP, pulmonary arterial pressure; PDW, platelet distribution width; RBC, red blood cell; RDW, red cell distribution width; TR, tricuspid regurgitation; WBC, white blood cell.

The p values represent the significant difference among 4 groups by the Kruskal-Wallis test.

The peak TR velocity was analyzed by Mann–Whitney U test.

*No significant difference was found after analysis with Dunn's test.

[a]Indicates significant difference from the normal group.

[b]Indicates significant difference from the MMVD group.

[c]Indicates significant difference from the PH group.

platelet indices, MPV and PDW, revealed lower PDW in MMVD+PH groups compared to the normal group ($p = 0.004$) (Table 1 and Figure 2). There was no significant difference in PDW, neither in comparison between MMVD+PH and MMVD groups nor in comparison between MMVD+PH and PH groups. The results of hematologic profiles are shown in Table 1. To clarify whether the changes in MCH, MCHC, and PDW were associated with MMVD, a comparison of MCH, MCHC, and PDW between the different stages of MMVD was performed in dogs that were included in the MMVD group from the first analysis. The dogs in stage B2 had lower MCH compared to normal dogs ($p < 0.001$) and dogs in stage B1 MMVD ($p = 0.006$). The dogs in stage C MMVD had lower MCH compared to normal dogs ($p < 0.001$) and dogs in stage B1 MMVD ($p = 0.009$). MCHC of normal dogs was greater than dogs with stage B1 ($p = 0.004$), B2 ($p < 0.001$), and C ($p < 0.001$) (Table 3 and Figure 3). The dogs with stage C MMVD had lower PDW compared to normal dogs ($p = 0.042$) and dogs with stage B1 MMVD ($p = 0.002$) (Table 3 and Figure 4). Analysis of WBC revealed no significant

TABLE 2 Blood chemistry profiles of dogs in the present study.

| | Normal ($n = 49$) | MMVD ($n = 102$) | MMVD + PH ($n = 78$) | PH ($n = 17$) | $P$-value |
|---|---|---|---|---|---|
| ALT (U/L) | 45.00 (34.00–56.50) | 54.00 (37.00–80.75) | 56.50 (36.00–90.00) | 53.00 (38.00–69.00) | 0.050 |
| ALP (U/L) | 50.00 (24.00–87.00) | 56.50 (38.00–100.00) | 67.00 (45.00–119.75) | 69.00 (37.50–143.00) | 0.047* |
| BUN (mg/dL) | 17.60 (13.95–23.25) | 25.30 (19.18–32.90) [a] | 31.00 (22.93–39.68)[a,c] | 19.50 (10.60–31.00) | <0.001 |
| Creatinine (mg/dL) | 0.80 (0.70–0.90) | 0.80 (0.60–1.00) | 0.85 (0.70–1.10)[c] | 0.60 (0.50–0.90) | 0.017 |
| Total protein (g/dL) | 6.40 (6.00–6.90) | 6.70 (6.40–7.10) | 6.70 (6.03–7.00) | 6.90 (6.25–7.30) | 0.061 |
| Albumin (g/dL) | 3.20 (3.00–3.50) | 2.80 (2.60–3.20)[a,c] | 2.80 (2.50–3.00)[a] | 2.60 (2.42–2.67) [a] | <0.001 |

Values are median (interquartile).
ALP, alkaline phosphatase; ALT, alanine aminotransferase; BUN, blood urea nitrogen.
*No significant difference was found after analysis with Dunn's test.
[a]Indicates significant difference from the normal group.
[b]Indicates significant difference from the MMVD group.
[c]Indicates significant difference from the PH group.

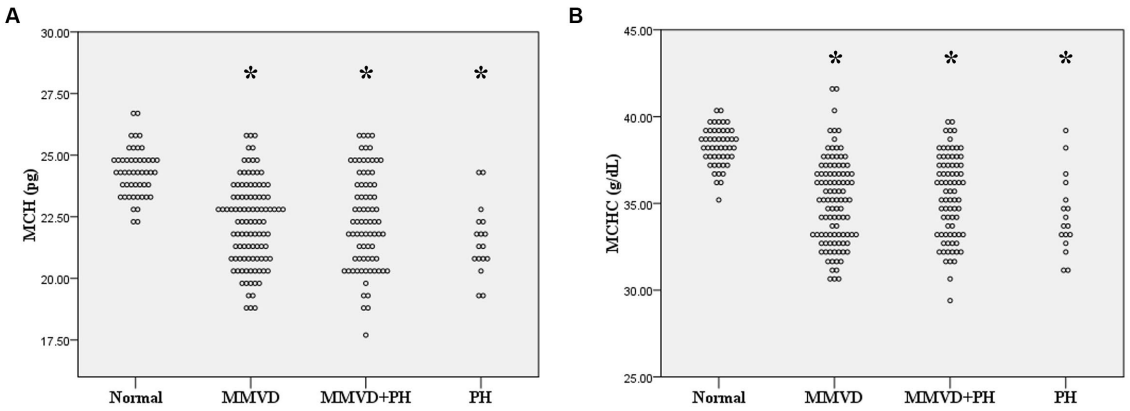


FIGURE 1
Dot plot of **(A)** mean corpuscular hemoglobin (MCH) and **(B)** mean corpuscular hemoglobin concentration (MCHC) of normal dogs ($n = 49$), dogs with MMVD ($n = 102$), MMVD dogs with PH ($n = 78$), and PH dogs without MMVD ($n = 17$). The MCH and MCHC of all disease groups were less than normal dogs ($p < 0.001$). The single asterisk presents a significant difference from the normal group.

difference among the groups, except for lower monocyte count in dogs with stage B2 MMVD compared to the normal group ($p = 0.010$) (Table 3). The results of hematological profiles of all dogs are shown in Tables 1, 3.

The sensitivity and specificity for discriminating between normal dogs and diseased dogs including dogs with MMVD (both with and without PH), as well as dogs with PH from other causes, were 91.80 and 67.50%, respectively, for MCH, and 87.80 and 77.20%, respectively for MCHC. The AUC values of MCH and MCHC were 0.83 and 0.87, indicating a discriminative value in distinguishing between normal dogs and those with MMVD. The optimal cut-off values 23.05 pg. for MCH, and 37.05 g/dL for MCHC (Figure 5). However, PDW values were unable to differentiate between normal dogs and diseased dogs.

Greater blood urea nitrogen (BUN) was found in dogs with MMVD ($p < 0.001$) and MMVD+PH ($p < 0.001$) compared to the normal dogs. Moreover, sub-analysis in MMVD dogs showed that the stage C MMVD dogs had greater BUN compared to normal dogs ($p < 0.001$) and stage B1 MMVD dogs ($p = 0.011$). Creatinine levels of MMVD+PH group were higher than those in PH group ($p = 0.010$). Sub-analysis of MMVD dogs showed that creatinine levels in stage C MMVD dogs were also higher than those in stage B1 MMVD dogs ($p = 0.010$). Comparison of the albumin level to normal dogs revealed a decrease in albumin levels in all disease groups ($p < 0.001$). The blood chemical profiles of all dogs are presented in Tables 2, 4.

Correlation analysis revealed no relationship between RBC and platelet indices, and age, weight, and breed of the dogs in the present study. MCH had a weak negative correlation with RBC count ($r = -0.38$, $p < 0.001$), a moderate positive correlation with MCV ($r = 0.48$, $p < 0.001$), and a strong positive correlation with MCHC ($r = 0.72$, $p < 0.001$). Weak negative correlations were found between MCH and LA/Ao ($r = -0.26$, $p < 0.001$) and LVIDd ($r = -0.29$, $p < 0.001$), as well as weak correlations between MCHC and LA/Ao ($r = -0.24$, $p < 0.001$) and LVIDd ($r = -0.27$, $p < 0.001$). RBC count had a weak negative correlation with peak TR velocity and calculated PAP ($r = -0.279$, $p = 0.006$) (Figure 6). PDW of dogs in the present study had a weak positive correlation with MPV ($r = 0.23$, $p < 0.001$) but had a weak negative correlation with platelet count ($r = -0.32$, $p < 0.001$), LA/Ao ($r = -0.30$, $p < 0.001$), and LVIDd ($r = -0.31$, $p < 0.001$) (Figure 7).

## Discussion

Pulmonary hypertension due to respiratory problems and heartworm disease is classified as precapillary PH, while PH secondary

10.3389/fvets.2023.1234768

TABLE 3 Signalment, hematological profiles and echocardiographic data of dogs with myxomatous mitral valve disease.

| | Normal (*n* = 49) | MMVD B1 (*n* = 20) | MMVD B2 (*n* = 15) | MMVD C (*n* = 67) | *P*-value |
|---|---|---|---|---|---|
| Age (years) | 8.00 (7.00–10.00) | 11.00 (8.25–13.00) [a] | 11.00 (10.00–13.00)[a] | 12.00 (10.00–13.00)[a] | <0.001 |
| Gender (M/F) | 21/28 | 9/11 | 13/2 | 40/27 | |
| Weight (kg) | 5.50 (2.92–6.80) | 4.09 (2.50–5.95) | 3.80 (3.25–4.90) | 4.60 (3.50–5.80) | 0.240 |
| RBC ($\times 10^6$ cells/μL) | 6.57 (6.16–7.44) | 6.95 (6.35–7.55) | 7.15 (6.62–7.50) | 7.19 (6.36–7.66) | 0.164 |
| Hematocrit (%) | 42.80 (38.80–47.00) | 44.75 (39.60–49.60) | 45.00 (43.20–47.60) | 44.90 (39.70–48.20) | 0.223 |
| MCV (fL) | 63.80 (61.80–64.95) | 64.90 (62.33–66.70) | 63.90 (60.30–67.40) | 63.60 (60.90–65.50) | 0.327 |
| MCH (pg) | 24.29 (23.55–24.90) | 23.75 (22.00–24.63) | 21.00 (20.50–22.90)[a,b] | 22.40 (20.90–23.20)[a,b] | <0.001 |
| MCHC (g/dL) | 38.20 (37.50–39.05) | 36.55 (33.53–37.78) [a] | 32.90 (32.00–35.00)[a] | 35.30 (33.30–36.80)[a] | <0.001 |
| RDW (%) | 14.00 (13.05–14.55) | 13.70 (13.08–14.25) | 13.30 (12.80–14.50) | 14.10 (13.20–14.90) | 0.383 |
| Platelet count ($\times 10^3$ cells/μL) | 283.00 (228.50–341.00) | 315.50 (229.00–386.75) | 346.00 (290.00–413.00) | 328.00 (249.00–432.00) | 0.167 |
| MPV (fL) | 10.10 (9.05–11.35) | 11.05 (10.25–11.88) | 10.90 (10.20–11.90) | 10.50 (9.50–11.30) | 0.098 |
| PDW (%) | 15.30 (15.10–15.50) | 15.35 (15.23–15.68) | 15.10 (14.90–15.40) | 15.10 (15.00–15.30) [a,b] | 0.001 |
| WBC ($\times 10^3$ cells/μL) | 8.37 (6.98–10.82) | 8.33 (7.21–10.80) | 8.41 (7.40–9.37) | 8.74 (7.52–11.30) | 0.651 |
| Neutrophil ($\times 10^3$ cells/μL) | 5.87 (4.05–7.31) | 6.14 (4.14–8.02) | 6.08 (5.06–7.71) | 6.21 (4.97–7.66) | 0.595 |
| Eosinophil ($\times 10^3$ cells/μL) | 0.31 (0.20–0.30) | 0.29 (0.22–0.48) | 0.26 (0.21–0.34) | 0.34 (0.22–0.56) | 0.439 |
| Basophil ($\times 10^3$ cells/μL) | 0.02 (0.01–0.03) | 0.01 (0.00–0.03) | 0.00 (0.00–0.01) [a] | 0.01 (0.00–0.02) [a] | 0.005 |
| Lymphocyte ($\times 10^3$ cells/μL) | 1.53 (1.18–1.94) | 1.43 (1.06–1.86) | 1.47 (1.21–2.28) | 1.28 (1.03–1.70) | 0.196 |
| Monocyte ($\times 10^3$ cells/μL) | 0.57 (0.44–0.83) | 0.62 (0.35–0.90) | 0.32 (0.17–0.56) [a] | 0.53 (0.29–0.75) | 0.015 |
| LA (cm/kg) | 0.92 (0.81–1.04) | 1.30 (0.98–1.66) | 1.71 (1.62–2.25) [a] | 2.17 (1.85–2.59) [a,b] | <0.001 |
| Ao (cm/kg) | 0.76 (0.68–0.86) | 0.88 (0.74–1.38) | 1.18 (0.89–1.31) [a] | 1.16 (0.97–1.31) [a] | <0.001 |
| LA/Ao | 1.20 (1.11–1.35) | 1.37 (1.13–1.49) | 1.70 (1.46–2.03) [a] | 1.88 (1.59–2.37) [a,b] | <0.001 |
| IVSd (cm/kg) | 0.47 (0.40–0.52) | 0.41 (0.38–0.50) | 0.44 (0.42–0.48) | 0.43 (0.38–0.49) | 0.152 |
| LVIDd (cm/kg) | 1.22 (1.17–1.37) | 1.30 (1.25–1.45) | 1.80 (1.55–1.94) [a,b] | 1.78 (1.60–1.99) [a,b] | <0.001 |
| LVPWd (cm/kg) | 0.38 (0.33–0.43) | 0.40 (0.36–0.45) | 0.45 (0.35–0.50) | 0.39 (0.36–0.45) | 0.235 |
| IVSs (cm/kg) | 0.61 (0.52–0.67) | 0.60 (0.51–0.67) | 0.70 (0.59–0.76) | 0.64 (0.55–0.73) | 0.027* |
| LVIDs (cm/kg) | 0.74 (0.62–0.80) | 0.79 (0.62–0.90) | 0.91 (0.67–0.98) | 0.90 (0.76–1.06) [a] | <0.001 |
| LVPWs (cm/kg) | 0.64 (0.56–0.71) | 0.62 (0.54–0.69) | 0.66 (0.61–0.76) | 0.69 (0.61–0.76) | 0.025* |
| %FS | 39.86 (34.75–45.68) | 39.80 (31.97–48.43) | 49.17 (45.47–54.48)[a] | 48.85 (43.48–53.51)[a,b] | <0.001 |

Ao, aorta; FS, fractional shortening; IVSd, interventricular septal thickness at end diastole; IVSs, interventricular septal thickness at end systole; LA, left atrium; LA/Ao, the ratio of the left atrial dimension to the aortic annulus dimension; LVIDd, left ventricular internal diameter at end diastole; LVIDs, left ventricular internal diameter at end systole; LVPWd, left ventricular posterior wall thickness at end diastole; LVPWs, left ventricular posterior wall thickness at end systole; MCH, mean corpuscular hemoglobin; MCHC, mean corpuscular hemoglobin concentration; MCV, mean corpuscular volume; MPV, mean platelet volume; PDW, platelet distribution width; RBC, red blood cell; RDW, red cell distribution width; WBC, white blood cell. The *p*-values represent the significant difference among four groups by the Kruskal-Wallis test.

*No significant difference was found after analysis with Dunn's test.

[a]Indicates significant difference from the normal group.

[b]Indicates significant difference from the MMVD B1 group.

to MMVD is postcapillary PH (1). A previous study found increased RDW in dogs with precapillary PH compared to normal dogs but not in dogs with post-capillary PH (30). On the other hand, another study revealed increased RDW in both dogs with precapillary and postcapillary PH compared to normal dogs (31). However, an increase in RDW was not associated with the severity of PH (31, 35). In this study, we found no difference in RDW among normal and dogs with precapillary and postcapillary PH. The reason for RDW alteration remains unclear in both human patients and dogs with PH. Besides, RDW can be altered by other diseases and conditions including immune-mediated diseases, hormonal diseases, lung worms, pulmonary fibrosis, thromboembolism, systemic-to-pulmonary shunts, aging, and unknown causes (30, 31, 36). Therefore, concurrent diseases may also affect RDW. However, we made efforts to exclude dogs with other diseases from the study. Although an increase in RDW values was found in dogs with several diseases and conditions, the values were still within the normal reference interval.

MCV reflects the RBC size, while MCH and MCHC define the weight and concentration of hemoglobin per RBC, respectively, (23). Decreases in MCH and MCHC were found in human patients with pulmonary arterial hypertension compared to the healthy controls, and these changes may be affected by decreases in RBC count, hemoglobin and hematocrit, and an increase in RDW (24). Moreover, decreased MCHC or hypochromasia in anemic dogs may indicate iron deficiency (22). In the present study, MCH and MCHC were reduced in MMVD, MMVD+PH, and PH groups compared to the normal dogs. Even though the AUC values of the ROC curves of these two indices suggest moderate discriminatory power, caution might

be warranted when considering their use as markers for distinguishing between normal dogs, dogs with MMVD (with and without PH), and dogs with PH from other causes. This is due to the fact that the values of MCH and MCHC remained within the normal limits for all groups of dogs, whether they were normal or diseased. Furthermore, MCH was found to be correlated to RBC count and MCV. However, no differences in RBC count, MCV and RDW were observed among the groups. This evidence indicates that MMVD and PH may alter the concentration of hemoglobin in dogs, but these conditions may not affect the size and number of RBCs. A study in humans demonstrated that anemia was commonly observed in patients with advanced stages of PH (37). In current study, weak negative correlations were observed between RBC count and both peak TR velocity and estimated PAP. Furthermore, the RBC count for all groups in the present study fell within the normal reference range, and there were no differences in RBC count among the groups. Collectively, it can be inferred that the severity of PH, as assessed by TR velocity and estimated PAP, may have a weak relationship with RBC numbers, which may not hold clinical significance.

Increased MPV has been detected in human patients with mitral stenosis (38), mitral regurgitation (13), ischemic heart disease (29), and PH (8, 11, 14). On the other hand, decreased MPV was found in children with congenital heart disease and PH compared to those without PH (39). In this study, no change in MPV was detected in dogs with MMVD without PH, MMVD with PH (post-capillary PH) and PH due to other causes (pre-capillary PH). Due to the conflicting findings in humans and dogs, the usefulness of MPV as an indicator for monitoring MMVD and PH in dogs is uncertain.

In the present study, a reduction in PDW was observed in the MMVD+PH groups compared with the normal group. However, there was no difference in PDW between MMVD dogs with and without PH. To clarify whether decreased PDW was related to MMVD, we assessed PDW according to the severity of MMVD. A decrease in PDW was found in dogs with stage C MMVD, along with a negative correlation between PDW and left atrial and ventricular size without correlation with peak TR velocity. Therefore, decreased PDW may be related to the severity of MMVD, but not the occurrence of PH because the change in PDW was not found in dogs with PH secondary to MMVD and other causes. Previous studies showed that PDW was increased in human patients with PH, and positively correlated with left ventricular hypertrophy and dysfunction (14, 28). In another previous study, children with PH due to congenital heart disease were found to have lower PDW than children without PH (39). In general, PDW reflects variation in platelet sizes and platelet activation (40). Therefore, a decrease in PDW may indicate that activated platelets are being consumed or destroyed in blood vessels (39). Based on the result of the present study, it is speculated that the platelet consumption and/or destruction was increased in dogs with MMVD with increased severity. Platelet fragmentation and decreased function can be caused by shear stress from mitral regurgitation (41, 42). However, this event

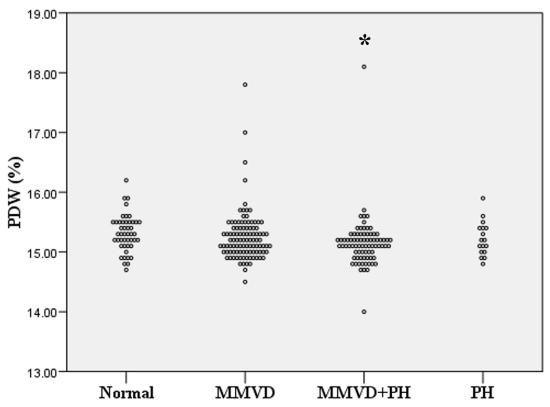


FIGURE 2
Dot plot of platelet distribution width (PDW) of normal dogs ($n = 49$), dogs with MMVD ($n = 102$), MMVD dogs with PH ($n = 78$), and PH dogs without MMVD ($n = 17$). The PDW of normal dogs was greater than those of MMVD dogs with PH ($p = 0.04$). The single asterisk presents a significant difference from the normal group.

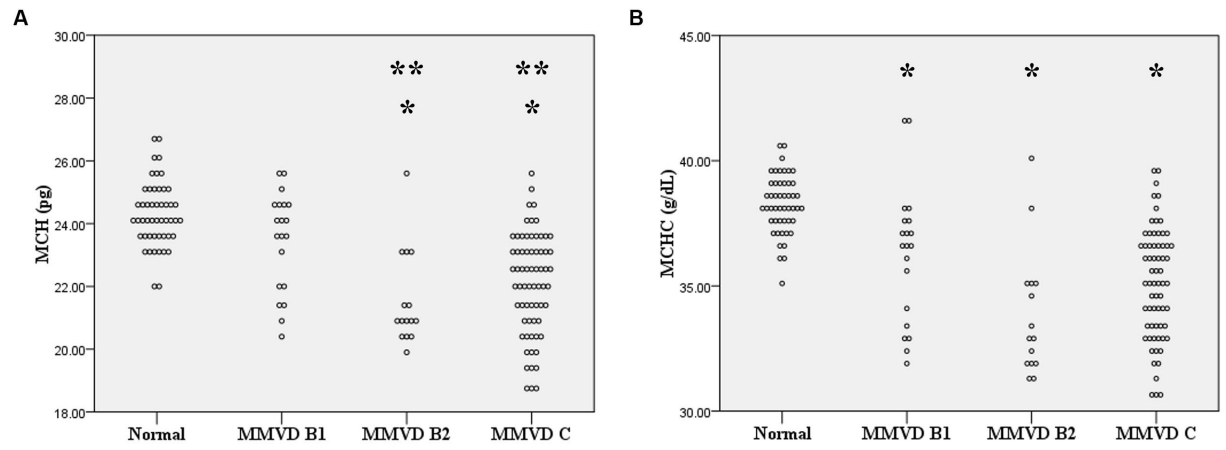


FIGURE 3
Dot plot of mean corpuscular hemoglobin (MCH) and mean corpuscular hemoglobin concentration (MCHC) of normal dogs ($n = 49$), dogs with stage B1 MMVD ($n = 20$), dogs with stage B2 MMVD ($n = 15$), and dogs with stage C MMVD ($n = 67$). **(A)** MCH of dogs with stage B2 and C MMVD groups were lower than those of normal dogs ($p < 0.001$) and dogs with stage B1 MMVD ($p = 0.006$ and $p < 0.001$ respectively). **(B)** MCHC of dogs with stage B1 ($p = 0.004$), B2 ($p < 0.001$) and C MMVD ($p < 0.001$) were lower than that of normal dogs. The single asterisk presents a significant difference from the normal group. The double asterisk presents a significant difference from the MMVD B1 group.

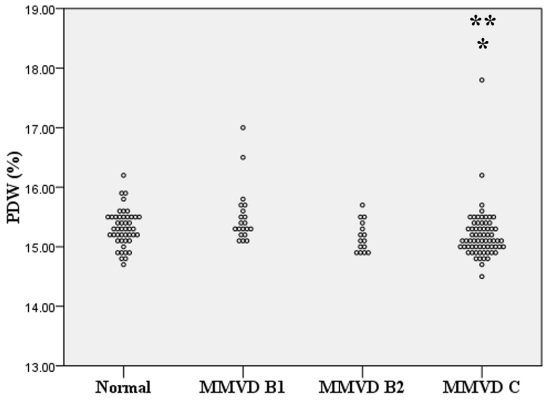


FIGURE 4
Dot plot of platelet distribution width (PDW) of normal dogs ($n$=49), dogs with stage B1 MMVD ($n$=20), dogs with stage B2 MMVD ($n$=15), and dogs with stage C MMVD ($n$=67). The PDW of dogs with stage C MMVD was lower than those of normal dogs ($p$=0.042) and dogs with stage B1 MMVD ($p$=0.02). The single and double asterisk presents a significant difference from the normal group and stage B1 MMVD, respectively.

may not relate to PH in dogs. Further investigation of the role of platelets in canine MMVD and PH is needed to improve the understanding of the association between platelets and MMVD and PH.

This study investigated the changes in RBC and platelet indices in dogs with PH. Because many diseases, including neoplasia and inflammatory diseases in other organs, can affect RBC and platelet indices, data of dogs with these concurrent diseases were excluded in this study (27, 43, 44). A significant age difference was found between the normal group and the other groups. However, there was no correlation between age and RBC and platelet indices suggesting that age may not affect these indices.

Monocytes are the mononuclear cells that play an essential role in the immune response. In addition to their involvement in immunity, monocytes also have a part in inflammation and tissue remodeling, including myocardial tissue (45). A previous study reported that monocytes were increased in dogs with CHF compared to control dogs, which may indicate cardiac remodeling in heart failure (46). Monocyte-to-lymphocyte ratio (MLR) is one of the inflammatory markers indicating the severity of heart diseases such as, human myocarditis (47). A greater MLR was revealed in dogs with CHF due to MMVD (48). However, this study found a decreased monocyte

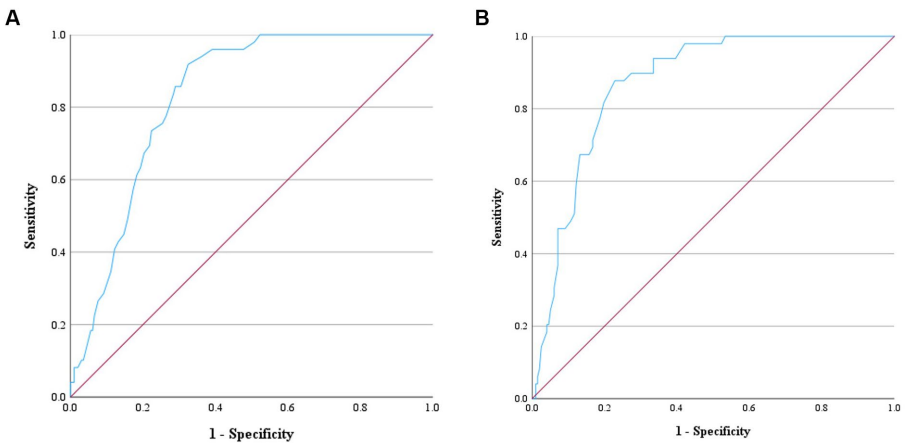


FIGURE 5
Receiver operating characteristic (ROC) curve for ascertaining the prediction of MCH and MCHC to distinguish normal dogs from dogs with MMVD and/or PH. The positive actual state is normal dogs. **(A)** ROC curve of MCH showed the area under the curve (AUC) value of 0.83 and the cut-point value of 23.05 pg. Therefore, dogs with MCH > 23.05 pg. can be predicted as normal dogs with the sensitivity of 91.80% and specificity of 67.50%. **(B)** ROC curve of MCHC showed the AUC value of 0.87 and the cut-point value of 37.05 g/dL. Therefore, dogs with MCHC>37.05 g/dL can be predicted as normal dogs with the sensitivity of 87.80% and specificity of 77.20%.

TABLE 4 **Blood chemistry profiles of dogs with myxomatous mitral valve disease.**

| | Normal ($n$ = 49) | MMVD B1 ($n$ = 20) | MMVD B2 ($n$ = 15) | MMVD C ($n$ = 67) | $P$-value |
|---|---|---|---|---|---|
| ALT (U/L) | 45.00 (34.00–56.50) | 49.00 (30.00–66.00) | 50.00 (30.00–79.00) | 58.00 (38.00–86.00)[a] | 0.013 |
| ALP (U/L) | 50.00 (24.00–87.00) | 55.00 (27.00–84.00) | 51.00 (29.00–100.00) | 58.00 (39.50–107.00) | 0.556 |
| BUN (mg/dL) | 17.60 (13.95–23.25) | 19.00 (13.40–27.60) | 24.00 (19.10–29.30) | 27.35 (22.25–37.60)[a,b] | <0.001 |
| Creatinine (mg/dL) | 0.80 (0.70–0.90) | 0.70 (0.50–0.80) | 0.70 (0.60–0.90) | 0.85 (0.68–1.10)[b] | 0.014 |
| Total protein (g/dL) | 6.40 (6.00–6.90) | 6.60 (6.30–6.80) | 6.40 (6.10–6.80) | 6.70 (6.50–7.20)[a] | 0.005 |
| Albumin (g/dL) | 3.20 (3.00–3.50) | 3.00 (2.70–3.50) | 2.50 (2.40–2.70)[a,b] | 2.80 (2.60–3.20)[a,c] | <0.001 |

Values are median (interquartile).
ALP, alkaline phosphatase; ALT, alanine aminotransferase; BUN, blood urea nitrogen.
[a]Indicates significant difference from the normal group.
[b]Indicates significant difference from the MMVD B1 group.
[c]Indicates significant difference from the MMVD B2 group.

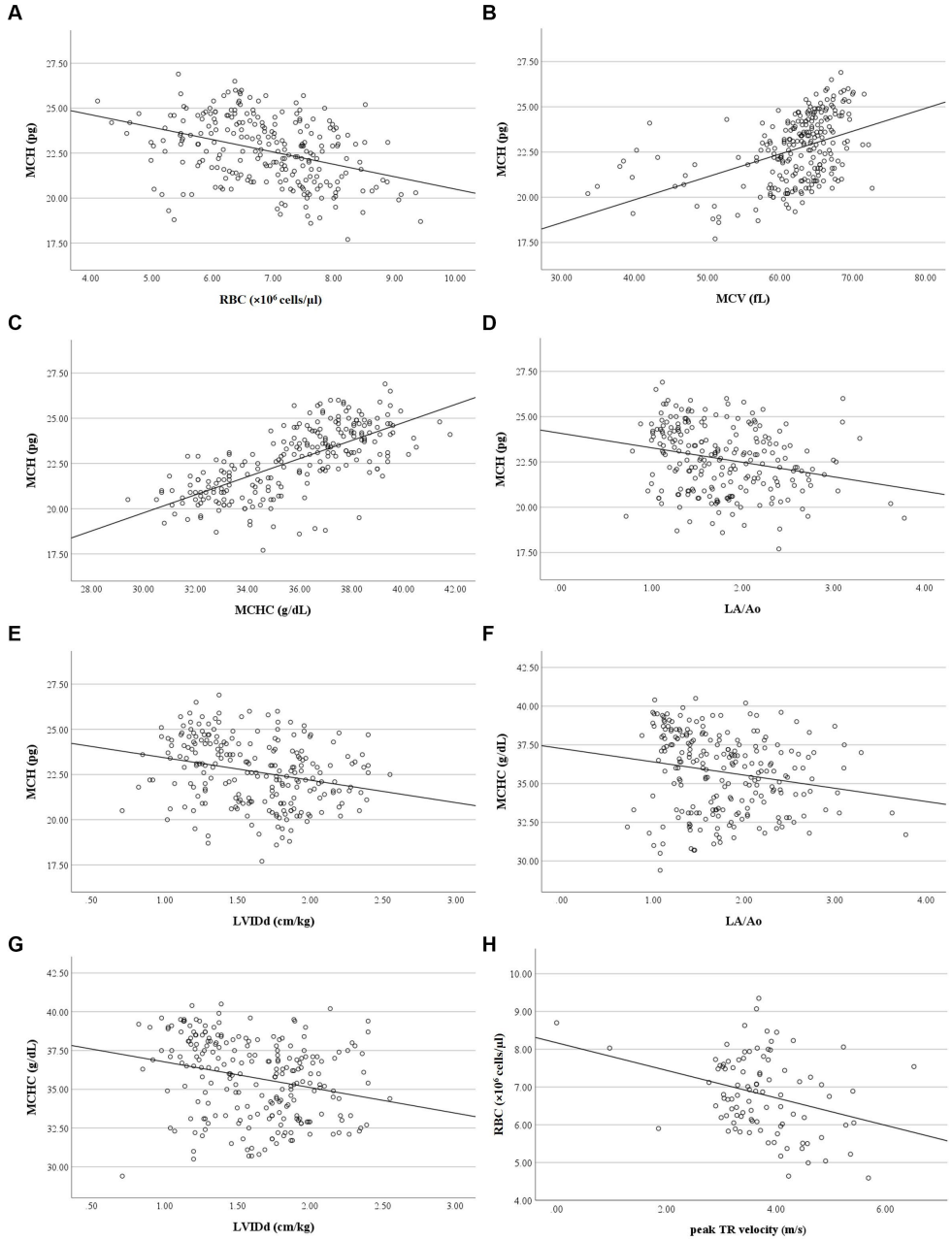


FIGURE 6
Correlation of RBC indices, RBC count, LA/Ao LVIDd and peak TR velocity. **(A)** MCH was negatively correlated with RBC count ($r = -0.377$, $p < 0.001$). **(B)** MCH was positively correlated with MCV ($r = 0.484$, $p < 0.001$). **(C)** MCH was positively correlated with MCHC ($r = 0.717$, $p < 0.001$). **(D)** MCH was negatively correlated with LA/Ao ($r = -0.263$, $p < 0.001$). **(E)** MCH was negatively correlated with LVIDd ($r = -0.291$, $p < 0.001$). **(F)** MCHC was negatively correlated with LA/Ao ($r = -0.237$, $p < 0.001$). **(G)** MCHC was negatively correlated with LVIDd ($r = -0.266$, $p < 0.001$). **(H)** RBC count was negatively correlated with peak TR velocity ($r = -0.279$, $p = 0.006$).

count of dogs with stage B2 MMVD compared to the normal dogs, while no difference of monocyte count between stage C MMVD and normal dogs was found. This finding is not consistent with previous studies. Therefore, the change in monocyte count of dogs with stage B2 MMVD in the present study may have occurred accidentally and does not provide clinical significance.

In the present study, alterations of BUN and albumin levels were found. BUN levels were elevated in dogs with MMVD and MMVD+PH compared to the normal dogs, and sub-analysis in MMVD dogs revealed that BUN levels were increased in stage C MMVD dogs. This finding is in accordance with a previous study in dogs with precapillary and postcapillary PH, where BUN concentration was increased without an elevation of creatinine levels (31). Increased BUN in heart disease can be a complication of CHF (49). Furthermore, the treatment of CHF using the diuretics and angiotensin converting enzyme inhibitors can cause an increase in BUN levels (31, 50). Creatinine levels of dogs enrolled in the present study were increased in MMVD+PH dogs compared to PH dogs, and

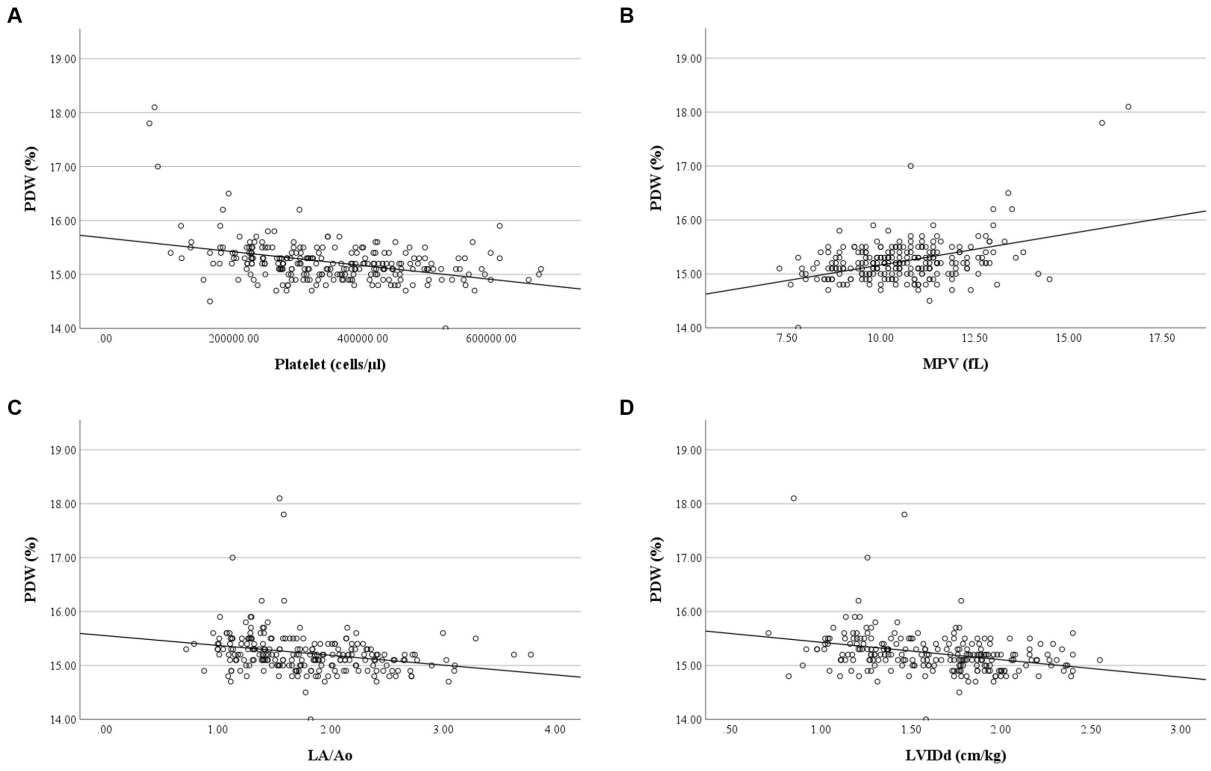


FIGURE 7
Correlation of PDW and platelet count, MPV, LA/Ao and LVIDd. **(A)** PDW was negatively correlated with platelet count ($r = -0.317$, $p < 0.001$). **(B)** PDW was positively correlated with MPV ($r = 0.233$, $p < 0.001$). **(C)** PDW was negatively correlated with LA/Ao ($r = -0.304$, $p < 0.001$). **(D)** PDW was negatively correlated with LVIDd ($r = -0.312$, $p < 0.001$).

stage C MMVD dogs compared to stage B1 MMVD dogs. These findings indicated that elevated creatinine levels were found in dogs with CHF due to MMVD. Azotemia and decreased glomerular filtration rate can be found in dogs with advanced stage of chronic valvular disease and associated with the severity of the disease (51). For this reason, greater BUN and creatinine levels can arise from CHF owing to progressive MMVD.

Decreased albumin levels were found in dogs with MMVD, MMVD+PH and precapillary PH, and sub-analysis of MMVD dogs showed that low albumin levels were related to severity of the disease. Several diseases and abnormalities including chronic heart failure and PH, were associated with low levels of albumin as a result of hemodilution caused by volume overload (52). Consequently, the evidence of decreased BUN and albumin in dogs with CHF and PH may reveal the progression of MMVD and PH.

A limitation of the study is the small sample size, which may affect the statistical significance of the RBC and platelet indices. A larger number of dogs could provide more accurate results, depicting the changes in these indices in dog populations.

In conclusion, the present study found that the decrease in PDW of dogs with MMVD was related to the severity of MMVD but not PH. No changes in platelet indices were not found in dogs with PH from other causes when compared to normal dogs. However, the RBC indices, MCH and MCHC, were associated with MMVD, precapillary and postcapillary PH. Further investigation of the role of RBC and platelets in canine MMVD and PH may improve the understanding of the association between PDW and MMVD and PH.

## Data availability statement

The raw data supporting the conclusions of this article will be made available by the authors, without undue reservation.

## Ethics statement

The requirement of ethical approval was waived by the Chulalongkorn University Animal Care and Use Committee for the studies involving animals because the design of the study was retrospective. The studies were conducted in accordance with the local legislation and institutional requirements.

## Author contributions

NT was responsible for data collection, data analysis, and manuscript writing and revision. EO was responsible for manuscript revision and editing. SS was responsible for data analysis and manuscript revision and editing. All authors contributed to the article and approved the submitted version.

## Funding

This research project was supported by the Secondary Century Fund (C2F), Chulalongkorn University and the research grant form Faculty of Veterinary Science, Chulalongkorn University.

## Acknowledgments

The authors would like to thank Small Animal Teaching Hospital, Faculty of Veterinary Science, Chulalongkorn University and Veterinary Diagnostic Laboratory, Faculty of Veterinary Science, Chulalongkorn University for providing all medical data.

## Conflict of interest

The authors declare that the research was conducted in the absence of any commercial or financial relationships that could be construed as a potential conflict of interest.

## Publisher's note



## References

1. Reinero C, Visser LC, Kellihan HB, Masseau I, Rozanski E, Clercx C, et al. ACVIM consensus statement guidelines for the diagnosis, classification, treatment, and monitoring of pulmonary hypertension in dogs. *J Vet Intern Med*. (2020) 34:549–73. doi: 10.1111/jvim.15725

2. Pyle RL, Abbott J, MacLean H. Pulmonary hypertension and cardiovascular sequelae in 54 dogs. *Intern J Appl Res Vet Med*. (2004) 2:99–109.

3. McCall JW, Genchi C, Kramer LH, Guerrero J, Venco L. Heartworm disease in animals and humans. *Adv Parasitol*. (2008) 66:193–285. doi: 10.1016/S0065-308X(08)00204-2

4. Jaffey J, Wiggen K, Leach S, Masseau I, Girens R, Reinero C. Pulmonary hypertension secondary to respiratory disease and/or hypoxia in dogs: clinical features, diagnostic testing and survival. *Vet J*. (2019) 251:105347. doi: 10.1016/j.tvjl.2019.105347

5. Matos JI, Caro-Vadillo A, Falcón-Cordón Y, García-Rodríguez SN, Costa-Rodríguez N, Carretón E, et al. Echocardiographic assessment of the pulmonary vein to pulmonary artery ratio in canine heartworm disease. *Animals*. (2023) 13:703. doi: 10.3390/ani13040703

6. Al-Najjar Y, Goode KM, Zhang J, Cleland JG, Clark AL. Red cell distribution width: an inexpensive and powerful prognostic marker in heart failure. *Eur J Heart Fail*. (2009) 11:1155–62. doi: 10.1093/eurjhf/hfp147

7. Felker GM, Allen LA, Pocock SJ, Shaw LK, McMurray JJ, Pfeffer MA, et al. Red cell distribution width as a novel prognostic marker in heart failure: data from the CHARM program and the Duke databank. *J Am Coll Cardiol*. (2007) 50:40–7. doi: 10.1016/j.jacc.2007.02.067

8. Güvenc TS, Erer HB, Ilhan S, Zeren G, Ilhan E, Karakus G, et al. Comparison of mean platelet volume values among different causes of pulmonary hypertension. *Cardiol J*. (2012) 19:180–7. doi: 10.5603/CJ.2012.0031

9. Hampole CV, Mehrotra AK, Thenappan T, Gomberg-Maitland M, Shah SJ. Usefulness of red cell distribution width as a prognostic marker in pulmonary hypertension. *Am J Cardiol*. (2009) 104:868–72. doi: 10.1016/j.amjcard.2009.05.016

10. Kaya H, Yıldırımlı MK, Kurt R, Beton O, Yilmaz MB. Mean platelet volume as a predictor of heart failure-related hospitalizations in stable heart failure outpatients with sinus rhythm. *Acta Cardiol Sin*. (2017) 33:292. doi: 10.6515/acs20160930a

11. Mohamed MF, Ali A, Abbas A, Awad MS, Gouda M, Sediq AM. Mean platelet volume as a predictor of pulmonary hypertension in patients with stable COPD. *Int J Chron Obstruct Pulmon Dis*. (2019) 14:1099–108. doi: 10.2147/COPD.S176413

12. Sato Y, Yoshihisa A, Watanabe K, Hotsuki Y, Kimishima Y, Yokokawa T, et al. Association between platelet distribution width and prognosis in patients with heart failure. *PLoS One*. (2020) 15:e0244608. doi: 10.1371/journal.pone.0244608

13. Ulu SM, Özkeçeci G, Akci O, Ahsen A, Altug A, Demir K, et al. Mean platelet volume, in predicting severity of mitral regurgitation and left atrial appendage thrombosis. *Blood Coagul Fibrinolysis*. (2014) 25:119–24. doi: 10.1097/MBC.0b013e328364c453

14. Zheng Y-G, Yang T, Xiong C-M, He J-G, Liu Z-H, Gu Q, et al. Platelet distribution width and mean platelet volume in idiopathic pulmonary arterial hypertension. *Heart Lung Circ*. (2015) 24:566–72. doi: 10.1016/j.hlc.2014.11.025

15. Simel DL, DeLong ER, Feussner JR, Weinberg JB, Crawford J. Erythrocyte anisocytosis: visual inspection of blood films vs automated analysis of red blood cell distribution width. *Arch Intern Med*. (1988) 148:822–4. doi: 10.1001/archinte.1988.00380040062012

16. Evans TC, Jehle D. The red blood cell distribution width. *J Emerg Med*. (1991) 9:71–4. doi: 10.1016/0736-4679(91)90592-4

17. Montagnana M, Danese E. Red cell distribution width and cancer. *Ann Transl Med*. (2016) 4:399. doi: 10.21037/atm.2016.10.50

18. Cakal B, Akoz AG, Ustundag Y, Yalinkilic M, Ulker A, Ankarali H. Red cell distribution width for assessment of activity of inflammatory bowel disease. *Dig Dis Sci*. (2009) 54:842–7. doi: 10.1007/s10620-008-0436-2

19. Förhécz Z, Gombos T, Borgulya G, Pozsonyi Z, Prohászka Z, Jánoskuti L. Red cell distribution width in heart failure: prediction of clinical events and relationship with markers of ineffective erythropoiesis, inflammation, renal function, and nutritional state. *Am Heart J*. (2009) 158:659–66. doi: 10.1016/j.ahj.2009.07.024

20. Dabbah S, Hammerman H, Markiewicz W, Aronson D. Relation between red cell distribution width and clinical outcomes after acute myocardial infarction. *Am J Cardiol*. (2010) 105:312–7. doi: 10.1016/j.amjcard.2009.09.027

21. Guglielmini C, Valentini CM, Contiero B, Valente C, Poser H. Red cell distribution width has a negative prognostic role in dogs with myxomatous mitral valve disease. *Animals*. (2021) 11:778. doi: 10.3390/ani11030778

22. Harvey JW. Chapter 4 - evaluation of erythrocytes In: JW Harvey, editor. *Veterinary hematology*. Saint Louis: W.B. Saunders (2012). 49–121.

23. Walker HK, Hall HD, Hurst JW. *Clinical methods: the history, physical, and laboratory examinations*. 3rd ed. Boston: Butterworths. (1990).

24. Yaylali YT, Kilic-Toprak E, Ozdemir Y, Senol H, Bor-Kucukatay M. Impaired blood rheology in pulmonary arterial hypertension. *Heart Lung Circ*. (2019) 28:1067–73. doi: 10.1016/j.hlc.2018.07.014

25. Bath P, Butterworth R. Platelet size: measurement, physiology and vascular disease. *Blood Coagul Fibrinol*. (1996) 7:157–61. doi: 10.1097/00001721-199603000-00011

26. Flaumenhaft R, Sharda A. Platelet secretion In: AD Michelson, editor. *Platelets*. Cambridge, MA: Elsevier (2019). 349–70.

27. Korniluk A, Koper-Lenkiewicz OM, Kamińska J, Kemona H, Dymicka-Piekarska V. Mean platelet volume (MPV): new perspectives for an old marker in the course and prognosis of inflammatory conditions. *Mediat Inflamm*. (2019) 2019:1–14. doi: 10.1155/2019/9213074

28. Fujita S-I, Takeda Y, Kizawa S, Ito T, Sakane K, Ikemoto T, et al. Platelet volume indices are associated with systolic and diastolic cardiac dysfunction, and left ventricular hypertrophy. *BMC Cardiovasc Disord*. (2015) 15:1–9. doi: 10.1186/s12872-015-0047-8

29. Slavka G, Perkmann T, Haslacher H, Greisenegger S, Marsik C, OF W, et al. Mean platelet volume may represent a predictive parameter for overall vascular mortality and ischemic heart disease. *Arterioscler Thromb Vasc Biol*. (2011) 31:1215–8. doi: 10.1161/ATVBAHA.110.221788

30. Swann JW, Sudunagunta S, Covey HL, English K, Hendricks A, Connolly DJ. Evaluation of red cell distribution width in dogs with pulmonary hypertension. *J Vet Cardiol*. (2014) 16:227–35. doi: 10.1016/j.jvc.2014.08.003

31. Mazzotta E, Guglielmini C, Menciotti G, Contiero B, BaronToaldo M, Berlanda M, et al. Red blood cell distribution width, hematology, and serum biochemistry in dogs with echocardiographically estimated precapillary and postcapillary pulmonary arterial hypertension. *J Vet Intern Med*. (2016) 30:1806–15. doi: 10.1111/jvim.14596

32. Keene BW, Atkins CE, Bonagura JD, Fox PR, Haggstrom J, Fuentes VL, et al. ACVIM consensus guidelines for the diagnosis and treatment of myxomatous mitral valve disease in dogs. *J Vet Intern Med*. (2019) 33:1127–40. doi: 10.1111/jvim.15488

33. Fan J, Upadhye S, Worster A. Understanding receiver operating characteristic (ROC) curves. *Can J Emerg Med*. (2006) 8:19–20. doi: 10.1017/S1481803500013336

34. Youden WJ. Index for rating diagnostic tests. *Cancer*. (1950) 3:32–5. doi: 10.1002/1097-0142(1950)3:1<32::AID-CNCR2820030106>3.0.CO;2-3

35. Kim S-J, Suh S-I, Hyun C. Evaluation of red blood cell profiles in dogs with heartworm disease. *Can J Vet Res*. (2020) 84:265–71.

36. Martinez C, Mooney CT, Shiel RE, Tang PK, Mooney L, O'Neill EJ. Evaluation of red blood cell distribution width in dogs with various illnesses. *Can Vet J*. (2019) 60:964.

37. Krasuski RA, Hart SA, Smith B, Wang A, Harrison JK, Bashore TM. Association of anemia and long-term survival in patients with pulmonary hypertension. *Int J Cardiol*. (2011) 150:291–5. doi: 10.1016/j.ijcard.2010.04.038

38. Varol E, Ozaydin M, Türker Y, Alaca S. Mean platelet volume, an indicator of platelet activation, is increased in patients with mitral stenosis and sinus rhythm. *Scand J Clin Lab Invest*. (2009) 69:708–12. doi: 10.3109/00365510903007000

39. Arslan D, Cimen D, Guvenc O, Kaya F, Sert A, Oran B. Platelet distribution width and mean platelet volume in children with pulmonary arterial hypertension secondary to congenital heart disease with left-to-right shunt: new indices of severity? *Pediatr Cardiol*. (2013) 34:1013–6. doi: 10.1007/s00246-012-0600-5

40. Vagdatli E, Gounari E, Lazaridou E, Katsibourlia E, Tsikopoulou F, Labrianou I. Platelet distribution width: a simple, practical and specific marker of activation of coagulation. *Hippokratia*. (2010) 14:28–32.

41. Brown CH, Leverett LB, Lewis CW, Alfrey CP, Hellums JD. Morphological, biochemical, and functional changes in human platelets subjected to shear stress. *J Lab Clin Med*. (1975) 86:462–71.

42. Tarnow I, Kristensen AT, Texel H, Olsen LH, Pedersen HD. Decreased platelet function in cavalier king Charles spaniels with mitral valve regurgitation. *J Vet Intern Med*. (2003) 17:680–6. doi: 10.1111/j.1939-1676.2003.tb02500.x

43. Kılınçalp S, Ekiz F, Başar Ö, Ayte MR, Çoban Ş, Yılmaz B, et al. Mean platelet volume could be possible biomarker in early diagnosis and monitoring of gastric cancer. *Platelets*. (2014) 25:592–4. doi: 10.3109/09537104.2013.783689

44. Abide ÇY, Vural F, Kılıççı Ç, Ergen EB, Yenidede İ, Eser A, et al. Can we predict severity of intrahepatic cholestasis of pregnancy using inflammatory markers? *Turkish J Obstet Gynecol*. (2017) 14:160–5. doi: 10.4274/tjod.67674

45. Apostolakis S, Lip GY, Shantsila E. Monocytes in heart failure: relationship to a deteriorating immune overreaction or a desperate attempt for tissue repair? *Cardiovasc Res*. (2010) 85:649–60. doi: 10.1093/cvr/cvp327

46. Hamilton-Elliott J, Ambrose E, Christley R, Dukes-McEwan J. White blood cell differentials in dogs with congestive heart failure (CHF) in comparison to those in dogs without cardiac disease. *J Small Anim Pract*. (2018) 59:364–72. doi: 10.1111/jsap.12809

47. Mirna M, Schmutzler L, Topf A, Hoppe UC, Lichtenauer M. Neutrophil-to-lymphocyte ratio and monocyte-to-lymphocyte ratio predict length of hospital stay in myocarditis. *Sci Rep*. (2021) 11:18101. doi: 10.1038/s41598-021-97678-6

48. Ku D, Chae Y, Kim C, Koo Y, Lee D, Yun T, et al. Severity of myxomatous mitral valve disease in dogs may be predicted using neutrophil-to-lymphocyte and monocyte-to-lymphocyte ratio. *Am J Vet Res*. (2023) 84:ajvr.23.01.0012. doi: 10.2460/ajvr.23.01.0012

49. Kazory A. Emergence of blood urea nitrogen as a biomarker of neurohormonal activation in heart failure. *Am J Cardiol*. (2010) 106:694–700. doi: 10.1016/j.amjcard.2010.04.024

50. Peddle GD, Singletary GE, Reynolds CA, Trafny DJ, Machen MC, Oyama MA. Effect of torsemide and furosemide on clinical, laboratory, radiographic and quality of life variables in dogs with heart failure secondary to mitral valve disease. *J Vet Cardiol*. (2012) 14:253–9. doi: 10.1016/j.jvc.2012.01.003

51. Nicolle AP, Chetboul V, Allerheiligen T, Pouchelon JL, Gouni V, Tessier-Vetzel D, et al. Azotemia and glomerular filtration rate in dogs with chronic valvular disease. *J Vet Intern Med*. (2007) 21:943–9. doi: 10.1111/j.1939-1676.2007.tb03047.x

52. Gotsman I, Shauer A, Zwas DR, Tahiroglu I, Lotan C, Keren A. Low serum albumin: a significant predictor of reduced survival in patients with chronic heart failure. *Clin Cardiol*. (2019) 42:365–72. doi: 10.1002/clc.23153

## Glossary

| | |
|---|---|
| Ao | Aorta |
| ALP | Alkaline phosphatase |
| ALT | Alanine aminotransferase |
| BUN | Blood urea nitrogen |
| CHF | Congestive heart failure |
| FS | Fractional shortening |
| IQR | Interquartile range |
| IVSd | Interventricular septal thickness at end diastole |
| IVSs | Interventricular septal thickness at end systole |
| LA | Left atrium |
| LVIDd | Left ventricular internal diameter at end diastole |
| LVIDs | Left ventricular internal diameter at end systole |
| LVPWd | Left ventricular posterior wall thickness at end diastole |
| LVPWs | Left ventricular posterior wall thickness at end systole |
| MCH | Mean corpuscular hemoglobin |
| MCHC | Mean corpuscular hemoglobin concentration |
| MCV | Mean corpuscular volume |
| MMVD | Myxomatous mitral valve disease |
| MPV | Mean platelet volume |
| PAP | Pulmonary arterial pressure |
| PDW | Platelet distribution width |
| PH | Pulmonary hypertension |
| RBC | Red blood cell |
| RDW | Red cell distribution width |
| TR | Tricuspid regurgitation |
| WBC | White blood cell |

frontiers | Frontiers in Veterinary Science

TYPE Original Research
PUBLISHED 21 December 2023
DOI 10.3389/fvets.2023.1327484



OPEN ACCESS

EDITED BY
Muhammad Saqib,
University of Agriculture, Faisalabad, Pakistan

REVIEWED BY
Cristin Coman,
"Cantacuzino", National Institute of Medical-Military Research and Development, Romania
Hakyoung Yoon,
Jeonbuk national University,
Republic of Korea

*CORRESPONDENCE
Asmaa Elhaieg
asmaaelhaieg@gmail.com
Ahmed Farag
ahmedfarag9331@gmail.com
Ryou Tanaka
ryo@vet.ne.jp

RECEIVED 25 October 2023
ACCEPTED 06 December 2023
PUBLISHED 21 December 2023

CITATION
Elhaieg A, Farag A, Elfadadny A, Yokoi A, Hendawy H, Mandour AS and Tanaka R (2023) Effect of experimental periodontitis on cardiac functions: a comprehensive study using echocardiography, hemodynamic analysis, and histopathological evaluation in a rat model.
*Front. Vet. Sci.* 10:1327484.
doi: 10.3389/fvets.2023.1327484



# Effect of experimental periodontitis on cardiac functions: a comprehensive study using echocardiography, hemodynamic analysis, and histopathological evaluation in a rat model

Asmaa Elhaieg[1]*, Ahmed Farag[1,2]*, Ahmed Elfadadny[3], Aimi Yokoi[1], Hanan Hendawy[4], Ahmed S. Mandour[5] and Ryou Tanaka[1]*

[1]Department of Veterinary Surgery, Faculty of Veterinary Medicine, Tokyo University of Agriculture and Technology, Fuchu, Japan, [2]Department of Surgery, Anesthesiology, and Radiology, Faculty of Veterinary Medicine, Zagazig University, Zagazig, Egypt, [3]Department of Animal Internal Medicine, Faculty of Veterinary Medicine, Damanhur University, Damanhour, Egypt, [4]Department of Veterinary Surgery, Faculty of Veterinary Medicine, Suez Canal University, Ismailia, Egypt, [5]Department of Animal Medicine (Internal Medicine), Faculty of Veterinary Medicine, Suez Canal University, Ismailia, Egypt

**Introduction:** Periodontitis is a prevalent and severe dental condition characterized by the gradual degradation of the bone surrounding the teeth. Over the past two decades, numerous epidemiological investigations have suggested a potential link between periodontitis and cardiovascular disease. However, the complex mechanistic relationship between oral health issues and cardiovascular disorders remains unclear.

**Aim:** This study aimed to explore comprehensively the cardiac function through various methods, including conventional echocardiography, intraventricular pressure gradient (IVPG) analysis, speckle tracking echocardiography (STE), and hemodynamics analysis.

**Methods:** Ligature-induced periodontitis was established in a group of rats while the second group served as sham. The successful establishment of the periodontitis model was confirmed through staining and radiographic examination of the affected mandibles.

**Results:** X-ray films and methylene blue staining revealed alveolar bone resorption in the affected first molar in the model rats, confirming the successful induction of periodontitis. The rats with periodontitis displayed a decrease in ejection fraction compared to the sham group, accompanied by a decrease in mid-to-apical IVPG and mid IVPG. Lower values of strain rate were recorded in the apical segment of the septum, the middle segment of the septum, and the basal segment of the lateral free wall in the periodontitis group, which was associated with histopathological examination showing some degree of myocardial tissue damage. Conversely, rats with periodontitis showed an increase in heart rate, end-systolic volume, and arterial elastance when compared to the sham rats. However, they also exhibited a decrease in stroke work, stroke volume, cardiac output, and end-systolic pressure.

**Conclusion:** This study suggests that experimental periodontitis may lead to cardiac dysfunction especially compromised systolic function and myocardial

relaxation, potentially indicating an increased risk of cardiovascular events in clinical periodontitis cases. The comprehensive assessment of cardiac function, hemodynamics, and histopathological evaluation underscores the profound impact of periodontitis on heart functions within this specific experimental model.

KEYWORDS

experimental periodontitis model, alveolar bone, cardiac function, intraventricular pressure gradients, speckle-tracking echocardiography, pressure-volume analysis

## Introduction

Cardiovascular disease (CVD) represents a substantial public health concern in various communities, resulting in approximately 17 million fatalities each year (1). In recent times, there has been growing consensus that chronic inflammatory ailments, which induce a widespread inflammatory state, can elevate the susceptibility to CVD alongside traditional risk factors like diabetes, smoking, elevated cholesterol levels, and a lack of physical activity (2–4).

Periodontal disease is a persistent, infectious, and inflammatory ailment arising from an unbalanced subgingival biofilm. As time progresses, it has the potential to lead to the deterioration of the supportive structures around the teeth, encompassing connective attachment loss and the absorption of alveolar bone (5). The progression of periodontal disease is influenced by a multifaceted etiopathology, marked by complex interactions between microorganisms within dental biofilms and the host's immune-inflammatory response, these microorganisms within dental plaque impact periodontal tissues through both direct and indirect mechanisms, releasing molecules that induce tissue damage and, in turn, initiate the immune-inflammatory response (6).

At the molecular level, cases of active periodontitis exhibit an inflammatory response that can disrupt the overall homeostasis of the individual. This systemic inflammatory reaction may extend to areas beyond the oral cavity (7). Considering the systemic ramifications of periodontal disease, it undeniably wields a substantial influence on overall health, potentially exerting a profound impact on an individual's quality of life (8, 9).

Remarkably, individuals afflicted with severe chronic periodontitis have shown a significantly heightened risk of developing cardiovascular disease, a correlation that persists even after accounting for various traditional risk factors (10). A meta-analysis involving over 200,000 individuals revealed that periodontal disease (PD) increases the risk of CVD by 35%, underscoring its significant impact on public health (11).

A substantial and increasing body of evidence has established an epidemiological association between periodontal inflammation and cardiovascular diseases, including conditions like arterial hypertension, myocardial infarction, stroke, and atherosclerotic vascular disease (12–14). This relationship has been suggested to occur through both indirect and direct pathways. Indirectly, it may involve shared risk factors that contribute to both periodontitis and cardiovascular diseases (15). On the other hand, a direct mechanism has been postulated, where oral bacteria from periodontal infections can enter the bloodstream, triggering a systemic inflammatory response (16).

Despite the growing evidence supporting the link between periodontitis and cardiovascular disease, the precise mechanisms underpinning this relationship are not yet fully comprehended. Further research is needed to better understand the complex interplay between these conditions and identify the specific pathways involved in their association. Given the limited investigation into the role of periodontal disease in causing cardiovascular dysfunctions, the objective of this study was to evaluate the cardiovascular consequences in a rat model of induced periodontitis. To achieve this goal, various approaches were employed, including echocardiographic assessment of cardiac performance, histopathological examination of myocardium, and hemodynamic recordings. By utilizing these methodologies, the current research aimed to gain insights into the potential impact of periodontitis on cardiac functions in the rat model.

## Materials and methods

### Animal housing and experimental design

The study involved 16 male Sprague–Dawley rats, weighing between 300 and 350 grams and aged 12 to 16 weeks. The experimentation took place in specific laboratories at Tokyo University of Agriculture and Technology. All procedures adhered to the guidelines outlined in the Guide for the Care and Use of Laboratory Animals, as issued by the US National Institute of Health (NIH). The protocols were thoroughly reviewed and approved by the Institutional Animal Care and Use Committee of Tokyo University of Agriculture and Technology (Approval No. R05-159).

The rats were housed in conventional cages, with two rats per cage, and utilized Aspen Shavings as bedding. The housing conditions included an air-conditioned room maintained at (24 ± 2°C), operating on a 12 h light/dark cycle with a relative humidity of 58%. Food and water were provided *ad libitum*, and the rat diets were sourced from the commercial company Oriental Yeast Co., Ltd., based in Tokyo, Japan.

The rats were divided into two groups, with eight rats in each group: sham operated group and the group with experimentally induced periodontitis (IP). For periodontitis induction, the rats were anesthetized using a combination of medetomidine hydrochloride (Domitor, Orion Pharma Animal Health, Helsinki, Finland), midazolam (Dormicum, Astellas Pharma Inc., Tokyo, Japan), and butorphanol (Vetorphale, Meiji Seika Pharma Co., Ltd.) at the dose rate of 0.3, 5.0, and 5.0 mg/kg body weight, administered subcutaneously, following the completion of all surgical procedures, atipamezole was administered at a dose rate of 1.0 mg/kg

subcutaneously to promote a smooth and rapid recovery (17, 18) and the mandibular first molar was ligatured with 3-0 sterile silk sutures as illustrated in Figure 1 (3, 19, 20).

.After 5 weeks of periodontitis induction, the animals underwent anesthesia, followed by echocardiographic and hemodynamic examinations. Subsequently, the rats were euthanized using isoflurane overdose via inhalation, and both mandibles and heart tissues were collected for further analysis.

## Conventional echocardiography

After 5 weeks following surgery, cardiac functions were evaluated in 16 animals (sham and IP groups) one day before euthanasia using an ultrasonographic ProSound 7 system equipped with a 12-MHz transducer supported by CMME and simultaneous ECG from Hitachi-Aloka Medical Ltd., Tokyo, Japan. The echocardiography followed the American Society of Echocardiography (ASE) guidelines (21, 22).

To assess the left ventricle (LV), a two-dimensional right parasternal short-axis view was obtained at the level of the papillary muscles using M-mode. All LV structures were manually measured by the same observer following the leading-edge method of the ASE (22). The recorded values represented the average of a minimum of five consecutive cardiac cycles on the M-mode tracings. Using this perspective, the following parameters were derived: left ventricular internal diameter during diastole (LVIDd), left ventricular internal diameter during systole (LVIDs), left ventricular posterior wall diameter during diastole (LVPWd), left ventricular posterior wall diameter during systole (LVPWs), ejection fraction (EF%), and fractional shortening (FS%). Furthermore, trans-mitral inflow indices, encompassing early (E) and late (A) velocities, along with the E/A ratio, were acquired through pulsed-wave (PW) Doppler echocardiography from the left apical four-chamber view. Tissue Doppler imaging (TDI) was also obtained from the same view. PW TDI echocardiography, utilizing a sample volume of 0.5 mm, was employed to capture the movement of the left ventricular (LV) septal and posterior walls. The TDI velocity profile comprised systolic (s′) and diastolic velocities [early (e′) and late (a′)] at the point of attachment of the mitral valve to the septal and lateral walls of the LV, and these velocities were recorded.

The E/e′ ratio was calculated using the following formula: E/e′ = (E/e′ lateral + E/e′ septal)/2.

## Color M-mode echocardiography

The color M-mode echocardiography (CMME) technique was employed to evaluate the intraventricular pressure gradient (IVPG). To ensure accurate tracing of the continuous mitral valve inflow (CMME), the ultrasound machine was set with a sweep speed of 300 mm/s and a color baseline shift of −64, effectively elevating the Nyquist limit. This configuration enhanced the visualization of the blood flow pathway from the left atrium to the left ventricular (LV) apex through the mitral valve in the left apical four-chamber view. Following this, M-mode was activated to capture the inflow, and color M-mode images were saved for subsequent offline analysis using MATLAB (The MathWorks, Natick, MA, United States).

The calculation of IVPG was carried out using the following formula (23, 24): IVPG (mmHg/cm) = IVPD/LV length.

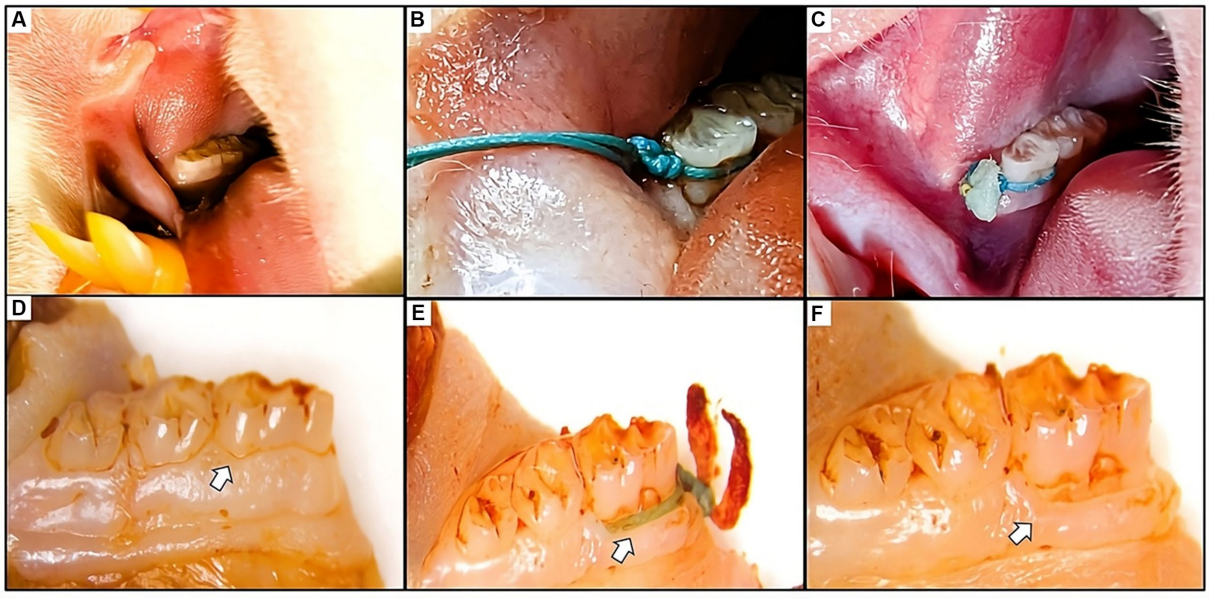


FIGURE 1
**(A)** Visual representation of the healthy gum tissue before the ligature application. **(B)** Figure depicting the placement of the ligature around the first mandibular molar. Ligatures remained in place throughout the study, with regular assessments and repositioning as needed. **(C)** Clinical observation of the gum tissue at the experiment's end revealed the presence of the ligature, accompanied by inflammation, food residue, and necrotic tissue. **(D)** Macroscopic images of the molar displaying normal tissue in the sham group. **(E,F)** Macroscopic views of the molar illustrate ligature placement post-soft tissue removal and the resulting alveolar bone loss caused by the ligature around the affected molar.

The IVPD, commonly characterized as the pressure disparity occurring in the initial phase of diastole between specific segments within the left ventricle (LV), arises when the pressure at the LV apex falls below that at the base (25). The total IVPG was then divided into two segments, based on dividing the LV length into three equal parts. The smaller segment near the mitral valve was termed basal IVPG, while the mid-to-apical segment, covering the other two-thirds near the apex, was considered the other IVPG segment, as shown in Figure 2. For precision and dependability, each data point was measured a minimum of five times at every interval, and the resultant average values were documented and reported for analysis.

## Speckle tracking echocardiography

The study involved acquiring loops of left ventricle (LV) movement from four apical views. To analyze these movements, speckle tracking analysis was conducted using an algorithm incorporated into EchoPAC PC DAS-RSI from Hitachi Aloka Co., Tokyo, Japan.

In the analysis process, Manual tracing of the endocardium was performed for both the end-systole and end-diastole phases. Subsequently, the software algorithm automatically segmented each imaging plane of the left ventricle (LV) into three equally circular sections: basal, midventricular, and apex on both the septal and lateral aspects (Figure 3). The longitudinal strain rate was calculated and obtained in six sections for further examination (26). This comprehensive analysis aimed to assess the LV movement and longitudinal strain in different regions of the heart, allowing for a detailed evaluation of cardiac function.

## Hemodynamic measurements

After evaluation of all echocardiographic parameters, pressure and volume measurements were calibrated using the MPVS-Ultra system (Millar Inc., Houston, TX, United States). Anesthetized rats were placed in a supine position on a heated pad. A midline incision along the anterior neck exposed the trachea. Following this, the right carotid artery was dissected, and a Millar catheter was inserted through the artery and guided into the left ventricle (LV) via the aortic valve. After a stabilization period of 5–10 min, pressure-volume (PV) loop signals were continuously recorded at a sampling rate of 1,000 Hz using the MPVS-Ultra Single Segment Pressure-Volume unit (Millar Inc., Houston, TX, United States) (27). Through dedicated PV loop analysis software (Millar Inc., Houston, TX, United States), numerous LV parameters were computed and derived. These encompassed end-systolic volume, LV end-diastolic volume, end-systolic pressure, end-diastolic pressure, the time constant of left ventricular pressure decay (Tau), stroke work (SW), stroke volume (SV), and cardiac output (CO).

Furthermore, an assessment of the relationship between LV and PV was undertaken via the occlusion of the caudal vena cava. Essential indices such as the slope of the end-systolic pressure-volume

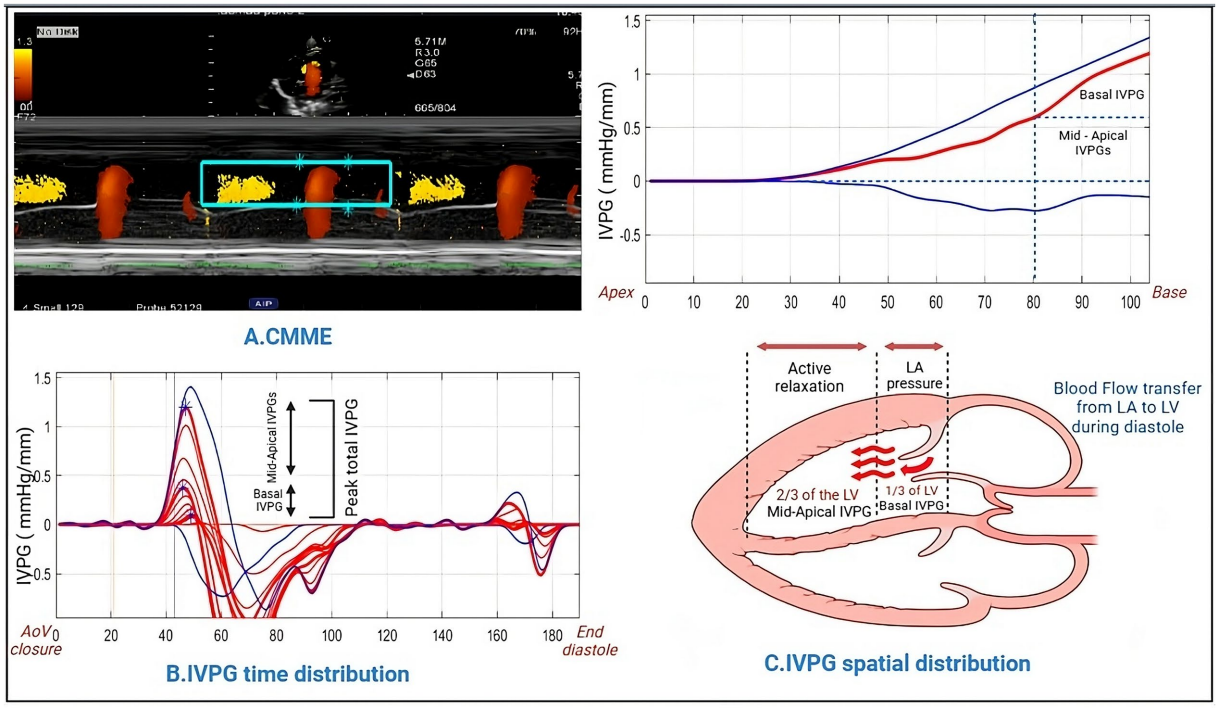


FIGURE 2
Methodology for IVPG analysis using Matlab. Color M-mode echocardiography was captured and sampled **(A)**, followed by the assessment of time distribution **(B)**. Utilizing Matlab, the spatial distribution of intraventricular pressure gradients was computed, yielding basal IVPG and mid-to-apical IVPG values **(C)**.

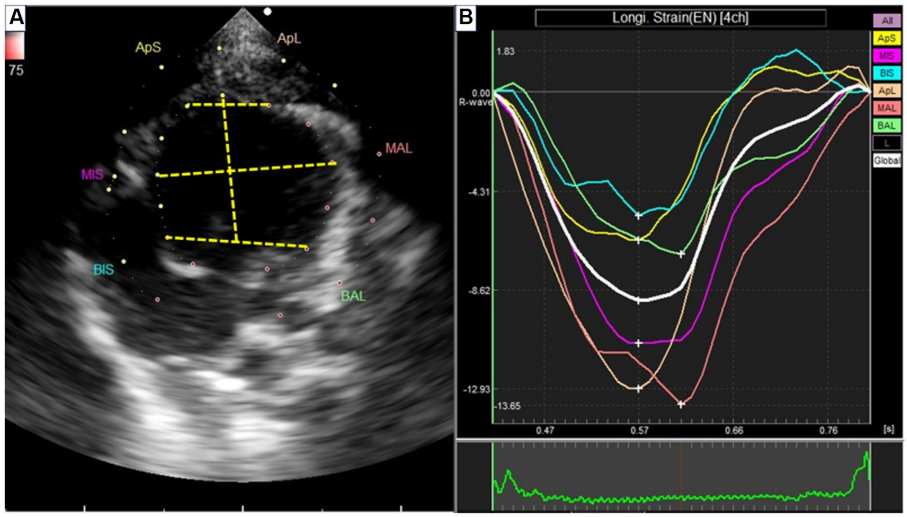


FIGURE 3
Speckle tracking echocardiography from left apical four-chamber view. **(A)** Segmentation of the left ventricle. APS, the apical segment of the septum; MS, the middle segment of the septum; BS, the basal segment of the segment; APL, the apical segment of the lateral free wall; ML, the middle segment of the lateral free wall; BL, the basal segment of the lateral free wall. **(B)** The strain rate of each segment.

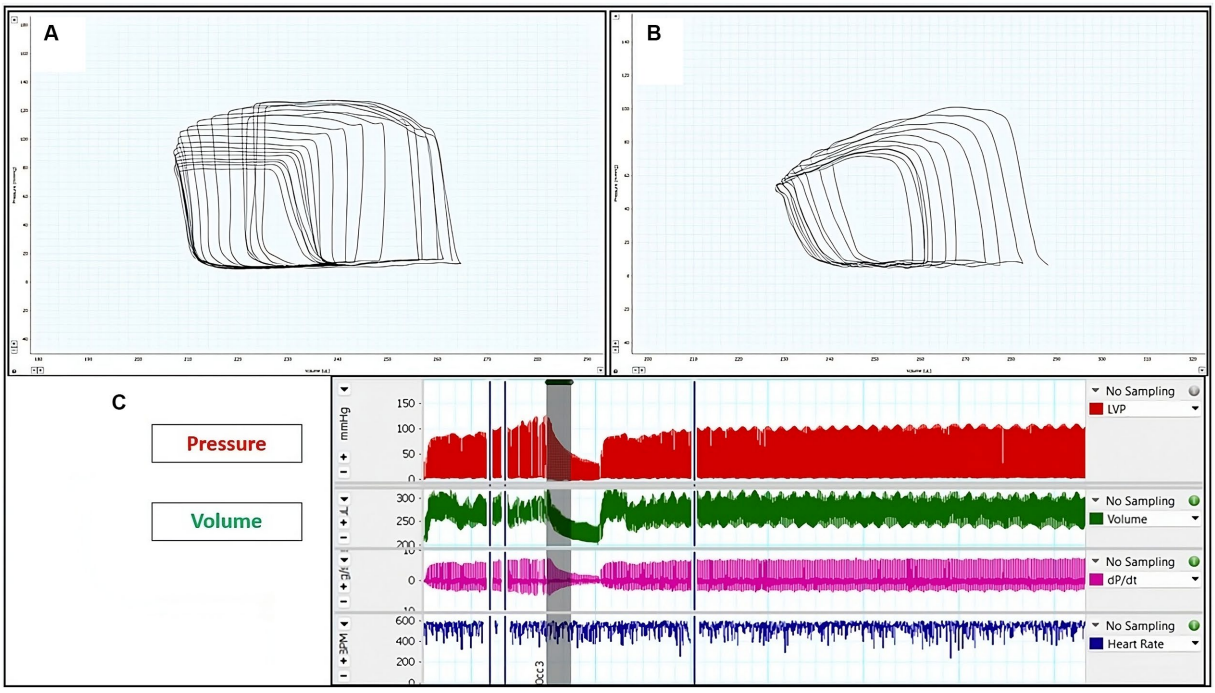


FIGURE 4
Representative left ventricular (LV) pressure-volume (PV) loops: **(A)** LV PV-loop from sham rats. **(B)** LV P-V loop from rats with induced periodontitis, subsequent to caudal vena cava occlusion. The reduction in pressure signal amplitude within the P-V loop signifies reduced contractility. **(C)** Illustration depicting alterations in pressure and volume following preload reduction achieved by caudal vena cava occlusion.

relationship (ESPVR), preload recruitable stroke work (PRSW), and the slope of the end-diastolic PV relationship (EDPVR) were computed to gain insights into the cardiovascular dynamics. Upon the conclusion of each experiment, an intravenous injection of 10 µL of a 15% saline solution was administered to establish a parallel conductance volume. This volume ascertained from the alteration of PV loop relations, was employed to rectify the cardiac mass volume (28, 29). The volume calibration process employed a Millar volume calibration cuvette. All measurements were analyzed using LabChart8 software (ADInstruments, Colorado Springs, CO, United States) (Figure 4).

## Histopathological examination

Following euthanasia through the inhalation method of isoflurane overdose (5%), all animals underwent necropsy. Subsequently, the heart was dissected into smaller fragments and then preserved in a solution of 10% neutral buffered formalin to facilitate fixation. In preparation for analysis, the heart tissue underwent a series of steps: it was sectioned into slices measuring 5 μm using an automated benchtop tissue processor (LEICA TP 1020, Biosystem Tokyo, Japan), followed by deparaffinization and rehydration. The tissue was then subjected to hematoxylin and eosin (H&E) staining, which enabled the assessment of potential inflammatory changes within the cardiac tissue.

To analyze these slides, a light microscope was utilized. To capture these visual insights, image software (CellSens Standard; Olympus, Tokyo, Japan) was employed. Following this, a histopathologist, who remained blind to the experimental groups, assessed 10 sections per group. The analysis encompassed the identification of specific features, including mononuclear cell infiltration, interstitial edema, necrosis, and the arrangement of myocardial cells (whether organized or disorganized and the direction of alignment) (30).

## Evaluation of alveolar bone loss (confirmation of model induction)

### Methylene blue staining

Macroscopic assessment was employed to evaluate the extent of bone resorption on the lingual and buccal surfaces of the first molars. The specimens were retrieved from alcohol, dried, and subsequently immersed in a solution comprising 0.7 g/L of methylene blue (Sigma, MO, United States) for a duration of 5 min. Excess dye was eliminated by rinsing the samples with tap water (31).

Digital photographs of the lingual and buccal sides of stained first molars were taken from a uniform 90-degree perspective utilizing a stereomicroscope (Leica M60) configured at a 20× magnification level. In these visuals, we conducted an assessment of the region lying between the junction of the cementoenamel and the crest of the alveolar bone on both the buccal and lingual surfaces. This measurement accounts for the entirety of the exposed root surfaces stained in a blue hue, except the enamel on the crown, and was subsequently quantified. This measurement was performed by an examiner who was unaware of the experimental groups, utilizing Image Tool 3.0 software. An increase in the exposed root area, compared to sham, non-ligated teeth, signifies the presence of alveolar bone resorption (20, 31, 32).

### Radiographic analysis

Radiographs of the affected hemimandibles were taken to evaluate the alveolar bone loss and validate the successful establishment of the animal model. For each rat within the two experimental groups, radiographic assessments were conducted using an X-ray machine (Collimator Type R-20J, Shimadzu Corporation, Japan). The X-ray tube operated at 30 kW, with a current of 6 mA, for 0.01 s, and the distance from the source to the sensor was set at 50 cm. Upon the conclusion of the experiment, the radiographs were utilized to evaluate the dental alveolar bone level, represented by the amount of alveolar bone present and wrapped around the root (33–35).

## Statistical analysis

All statistical analyses were performed using GraphPad Prism 8.0 software (GraphPad Software, San Diego, California). The Mann–Whitney test was utilized for the analysis, and the results are presented as mean ± SD. Differences were deemed statistically significant when the $p$-value was less than 0.05. Spearman's rank correlation and linear regression analysis were employed to evaluate the relationships between hemodynamic, IVPG, and STE measurements. The coefficient of determination ($R^2$) was calculated based on the sum of the squares of the distances of the data points from the best-fit curve.

# Results

## Conventional echocardiography

The assessment of cardiac function through conventional echocardiography is presented in Table 1. The findings reveal that in rats with ligature-induced periodontitis, there was a statistically significant increase in LVIDs. Conversely, there were significant reductions in EF% and Sm when compared to the sham group. Nevertheless, parameters such as IVSd, LVIDd, LVPWd, IVSs, LVPWs, FS%, early mitral velocity (E), late mitral velocity (A wave), E/A ratio, Em, Em/Am ratios, and E/Em ratio exhibited comparable values in both groups.

## IVPG measurements

The findings from the analysis of IVPG data are outlined in Table 2. Notably, the mid-to-apical IVPG in the IP group (0.577 ± 0.047) exhibited a significant reduction compared to the sham group (0.717 ± 0.108). Similarly, the mid IVPG in the IP group (0.515 ± 0.052) was significantly lower than that observed in the sham group (0.637 ± 0.099). Conversely, no statistically significant differences were detected in Total IVPG, Basal IVPG, and Apical IVPG.

## Speckle tracking echocardiography

Table 3 presents the strain rates obtained through speckle tracking echocardiography. Notably, the IP group exhibited significantly reduced strain rates in specific segments compared to the sham group. Specifically, the apical segment of the septum in the IP group (−3.175 ± 0.696) showed a significant decrease compared to the sham group (−4.663 ± 1.208) with a $p$-value of 0.025. Similarly, the middle segment of the septum in the IP group (−8.411 ± 2.403) displayed a significant reduction compared to the sham group (−13.29 ± 4.009) with a $p$-value of 0.014. Additionally, the basal segment of the lateral free wall in the IP group (−2.811 ± 0.690) exhibited a significantly

TABLE 1 Assessment of cardiac function using conventional echocardiography.

| | Sham group | IP group | *p*-value |
|---|---|---|---|
| IVSd (mm) | 1.713 ± 0.112 | 1.675 ± 0.183 | 0.96 |
| LVIDd (mm) | 8.238 ± 0.702 | 8.675 ± 0.523 | 0.08 |
| LVPWd | 2.163 ± 0.396 | 1.988 ± 0.155 | 0.39 |
| IVSs (mm) | 2.275 ± 0.243 | 2.288 ± 0.28 | 0.97 |
| LVIDs (mm) | 5.288 ± 0.458 | 5.713 ± 0.419* | 0.04 |
| LVPWs (mm) | 2.763 ± 0.199 | 2.475 ± 0.349 | 0.08 |
| EF % | 74.83 ± 2.932 | 71.11 ± 3.647* | 0.04 |
| FS % | 36.03 ± 2.100 | 33.89 ± 2.553 | 0.06 |
| eV | 72.10 ± 5.530 | 70.84 ± 8.835 | >0.99 |
| aV | 32.23 ± 3.991 | 33.10 ± 3.122 | 0.39 |
| E/A | 2.266 ± 0.329 | 2.066 ± 0.199 | 0.22 |
| Sm | 5.150 ± 0.484 | 4.575 ± 0.395* | 0.02 |
| Em | 5.350 ± 0.730 | 5.300 ± 0.282 | 0.62 |
| Am | 4.213 ± 0.502 | 4.14 ± 0.551 | 0.88 |
| Em/Am | 1.273 ± 0.127 | 1.276 ± 0.153 | 0.89 |
| E/Em | 12.09 ± 1.929 | 13.52 ± 2.286 | 0.19 |

Data are presented as the mean ± standard deviation (SD) for each group ($n = 8$).
IVSd and IVSs: interventricular septal thickness in end-diastole and systole, respectively. LVIDd and LVIDs: left ventricular diastolic and systolic internal diameter, respectively. LVPWd and LVPWs: left ventricular diastolic and systolic posterior wall thickness, respectively. EF: ejection fraction. FS: fractional shortening. eV: early diastolic transmitral flow velocity. aV: late diastolic transmitral flow velocity. E/A: ratio of early to late diastolic transmitral flow velocities. Sm: left ventricular wall velocity at systole. Em: left ventricular wall velocity at early diastole. Am: left ventricular wall velocity at late diastole. Em/Am: ratio of early to late diastolic velocity of the left ventricular wall. E/Em: ratio of early diastolic velocity mitral to early diastolic velocity of the LV wall.

TABLE 2 Variability of CMME indices.

| | Sham group | IP group | *p*-value |
|---|---|---|---|
| Total IVPG | 1.714 ± 0.130 | 1.635 ± 0.089 | 0.3282 |
| Basal IVPG | 1.047 ± 0.119 | 1.013 ± 0.103 | 0.8785 |
| Mid to apical IVPG | 0.717 ± 0.108 | 0.577 ± 0.047* | 0.0104 |
| Mid IVPG | 0.637 ± 0.099 | 0.515 ± 0.052* | 0.0047 |
| Apical IVPG | 0.080 ± 0.038 | 0.061 ± 0.037 | 0.2786 |

Data are presented as the mean ± standard deviation (SD) for each group ($n = 8$).
TIVPG, total intraventricular pressure gradient; BIVPG, basal intraventricular pressure gradient; mid-to-apical IVPG, middle-to-apical intraventricular pressure gradient; MIVPG, middle intraventricular pressure gradient; AIVPG, apical intraventricular pressure gradient.

TABLE 3 2D-speckle tracking echocardiography measurements.

| | Sham Group | IP Group | *p*-value |
|---|---|---|---|
| APS | −4.663 ± 1.208 | −3.175 ± 0.696* | 0.025 |
| MS | −13.29 ± 4.009 | −8.411 ± 2.403* | 0.014 |
| BS | −11.73 ± 2.504 | −11.63 ± 2.261 | 0.899 |
| APL | −5.782 ± 2.790 | −4.338 ± 1.055 | 0.368 |
| ML | −7.675 ± 1.388 | −7.583 ± 1.749 | 0.823 |
| BL | −7.959 ± 0.689 | −2.811 ± 0.690* | 0.0002 |

Data are presented as the mean ± standard deviation (SD) for each group ($n = 8$).
APS, strain rate of the apical segment of the septum; MS, strain rate of the middle segment of the septum; BS, strain rate of the basal segment of the septum; APL, strain rate of the apical segment of the lateral free wall; ML, strain rate of the middle segment of the lateral free wall; BL, strain rate of the basal segment of the lateral free wall.

lower strain rate than the sham group (−7.959 ± 0.689) with a *p*-value of 0.0002. Conversely, in the remaining segments, the IP group demonstrated myocardial movement levels comparable to those observed in the sham-operated rats.

## Pressure-volume loop analysis

Table 4 provides a comprehensive overview of the hemodynamic data in the rats. Notably, the IP group demonstrated significant

TABLE 4 Hemodynamic measurements.

| | Sham group | IP group | *p*-value |
|---|---|---|---|
| HR (bpm) | 301.8 ± 6.573 | 322.2 ± 1.413 | <0.001 |
| SW (mmHg*uL) | 3,608 ± 628.6 | 2,302 ± 751.4 | <0.01 |
| CO (uL/min) | 8,490 ± 4,057 | 3,875 ± 148.0 | <0.01 |
| SV (uL) | 49.66 ± 11.11 | 31.56 ± 6.708 | <0.001 |
| ESV (uL) | 241.9 ± 12.18 | 255.6 ± 7.380 | <0.01 |
| EDV (uL) | 280.4 ± 11.81 | 281.2 ± 19.81 | 0.8785 |
| ESP (mmHg) | 119.8 ± 5.928 | 78.53 ± 10.12 | <0.001 |
| EDP (mmHg) | 4.326 ± 0.972 | 5.271 ± 1.726 | 0.2657 |
| Ea (mmHg/uL) | 2.342 ± 0.295 | 2.845 ± 0.479 | 0.02 |
| Tau (ms) | 19.10 ± 2.253 | 21.59 ± 1.856 | 0.047 |
| ESPVR (mmHg/uL) | 1.262 ± 0.279 | 0.880 ± 0.185 | 0.01 |
| EDPVR | 0.032 ± 0.011 | 0.046 ± 0.028 | 0.3282 |
| PRSW | 99.14 ± 6.771 | 72.83 ± 12.21 | <0.001 |

The values are presented as means ± standard deviations (SD).
HR, heart rate; SV, stroke volume; SW, stroke work; CO, cardiac output; ESV, end-systolic volume; EDV, end-diastolic volume; ESP, end-systolic pressure; EDP, end-diastolic pressure; Ea, arterial elastance, Tau, time constant of left ventricular pressure decay; ESPVR, end-systolic pressure-volume relationship; PRSW, preload recruitable stroke work; EDPVR, end-diastolic pressure-volume relationship.

differences in the majority of parameters when compared to the sham group. Specifically, stroke work, stroke volume, cardiac output, and end-systolic pressure in the IP group exhibited a significant decrease compared to their respective values in the sham group. In contrast, heart rate, end-systolic volume, arterial elastance, and the time constant of left ventricular pressure decay (Tau) in the IP group demonstrated a significant increase compared to their values in the sham group. However, no statistically significant changes were observed in end-diastolic volume and end-diastolic pressure between the two experimental groups.

In Figure 4, representative original P-V loops obtained during the reduction of preload (achieved through transient occlusion of the caudal vena cava) are shown for both sham and IP animals. Functional indices were computed through P-V loop analysis at various preloads during this transient occlusion. Furthermore, it was observed that the end-systolic pressure-volume relationship (ESPVR) was steeper in sham rats compared to IP rats. Conversely, the end-diastolic pressure-volume relationship (EDPVR) showed a tendency to increase in IP rats, although this difference did not reach statistical significance. Moreover, the preload recruitable stroke work (PRSW) values were notably lower in IP rats in comparison to the sham rats.

## Histopathological findings

In terms of the histological alterations observed in the hearts of the sham and IP groups, a distinct contrast was evident. The myocardial tissues within the sham group exhibited a normal and unremarkable structure and morphology, as depicted in Figures 5A,B. However, clear histopathological changes were evident in the cardiac tissues of the IP group. These alterations included evident cell degeneration, notable modifications in the shape of cardiac myocytes accompanied by a loss of organized arrangement, and a discernible absence of nucleation. Additionally, there was a noticeable increase in the interstitial tissues, and inflammatory cells were observed around the arterioles, as illustrated in Figures 5C,D. These histological findings substantiate our initial hypothesis. They collectively imply that the observed myocardial tissue damage within the IP group may indeed exert an influence on both the structural integrity and functional aspects of the heart.

## Establishment of the periodontitis model in experimental rats

At the initiation of the experiment, the gingival tissues exhibited a standard appearance characterized by a smooth texture and a light pink hue. The attached gingiva firmly adhered to the underlying structures, while the free gingival margin displayed a distinct outline aligned with the cementoenamel junction (CEJ) of neighboring teeth.

Upon completion of the experiment, notable changes were observed in the clinical state of the gingiva. The macroscopic view showed a cyanotic shift, accompanied by pronounced edema encompassing the observed teeth. Furthermore, the free gingival margin displayed irregularities, including the presence of food debris (Figure 1).

Alveolar bone resorption stands as a defining characteristic of periodontitis triggered by the ligature. The contrast between ligature-induced periodontitis rats and the sham group is illustrated in Figure 6, displaying a comprehensive comparison of morphometric measurements. Notably, substantial bone loss is evident on both surfaces, as indicated by significantly increased areas extending from the cementoenamel junction to the alveolar bone crest in ligature-induced periodontitis rats when contrasted with their counterparts that underwent sham procedures (1.313 ± 0.172 vs. 0.362 ± 0.106 for lingual side) and (1.238 ± 0.140 vs. 0.275 ± 0.103 for buccal side).

X-ray images revealed evident alveolar bone resorption around the affected molars in the rats with experimentally induced periodontitis, as compared to the sham rats. Notably, the alveolar bone of the sham rats displayed a continuous wrapping around the root, confirming that successful induction of periodontitis had been achieved by the fifth week of the modeling process (Figure 7).

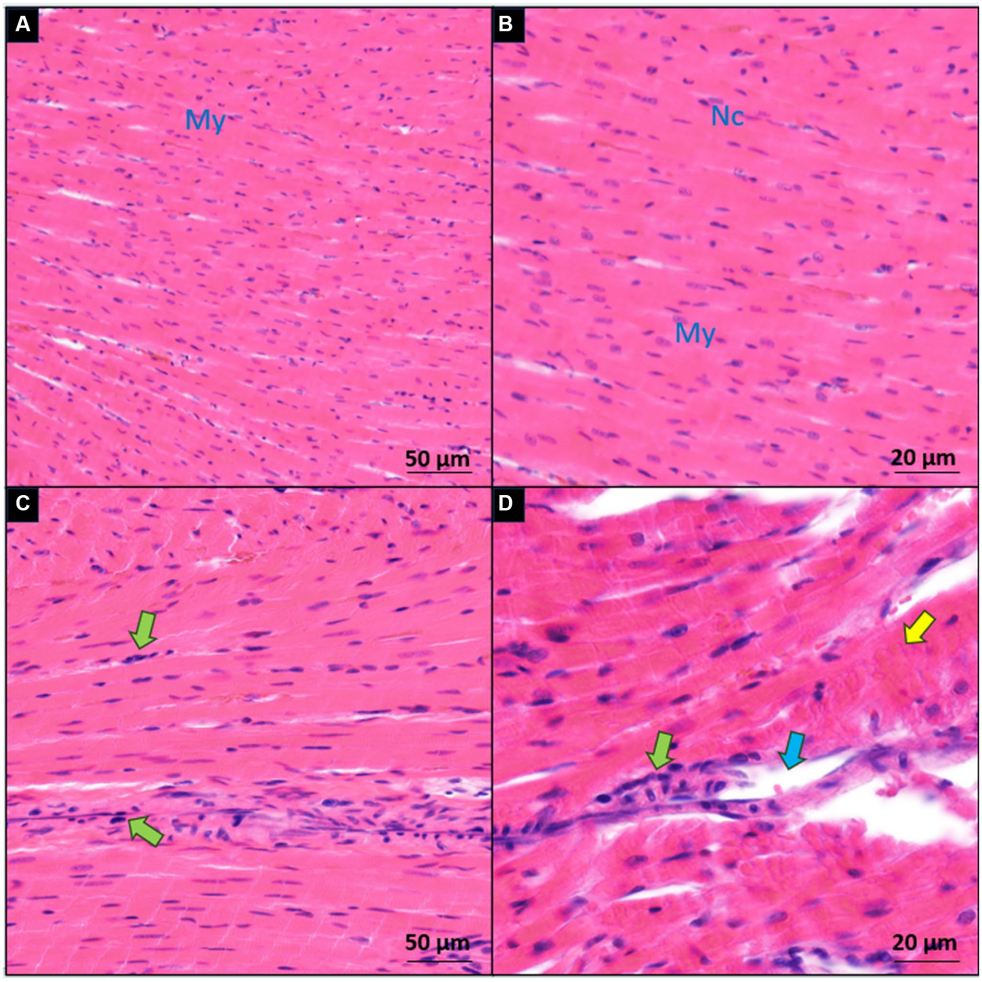


FIGURE 5
Microscopic comparison of myocardial sections between the sham **(A,B)** and induced periodontitis **(C,D)** groups. Inflammatory cells are highlighted with green arrows, degenerated cells with yellow arrows, and interstitial edema with blue arrows. Cardiac myocytes are denoted as My, and their nuclei as Nc. Histological examination of heart tissue in both groups is presented at two magnification levels [10× for **(A,C)** and 20× for **(B,D)**].

## Correlation and regression analysis between P-V measurements and IVPG indices

Table 5 summarizes the correlation and linear regression analysis results between PV-loop measurements and IVPG indices.

Significant correlations were found between HR, SW, CO, and ESP with both the mid-apical IVPG and mid IVPG segments ($p < 0.001$, 0.01, 0.01, and 0.01, respectively, for the mid-apical IVPG segment; and $p < 0.001$, 0.02, 0.03, and 0.016, respectively, for the mid IVPG segment). Additionally, Ea and PRSW showed significant correlations with the mid-apical IVPG segment only ($p = 0.005$ and 0.05, respectively).

Similarly, a statistically significant effect of HR, SW, CO, and ESP was observed on both the mid-apical IVPG and mid IVPG segments ($p = 0.0001$, 0.0118, 0.0105, and 0.0132, respectively, for the mid-apical segment; and $p < 0.0001$, 0.0237, 0.0314, and 0.0164, respectively, for the mid IVPG segment). Moreover, there was a significant effect of EDV and ESP on mid and mid-to-apical IVPG.

## Correlation and regression analysis between P-V measurements and STE parameters

Table 6 summarizes the correlation outcomes between P-V measurements and STE parameters. It also presents the coefficient of determination ($R^2$) derived from linear regression analysis, indicating the extent of its impact on the corresponding parameters.

HR exhibited significant correlations with APS, MIS, and BAL segmental regions ($p = 0.04$, 0.02, and <0.001, respectively). SW, CO, and ESV were also correlated with the BAL segment ($p = 0.002$, 0.01, and 0.041, respectively). Additionally, SV showed significant correlations with APS, MIS, and BAL segmental regions ($p = 0.04$, 0.01, and 0.0006, respectively). Furthermore, Ea correlated with MIS and BAL ($p = 0.03$ and 0.01), while Tau correlated with APS, MIS, and ApL regions ($p = 0.03$, 0.08, and 0.03, respectively). ESPVR exhibited correlations with APS and BAL ($p < 0.01$ for both), and PRSW correlated with MIS and BAL regions ($p = 0.02$ and <0.001).

Moreover, HR, SV, and ESP demonstrated significant effects on APS, MIS, and BAL segmental regions ($p = 0.04$, 0.04, and

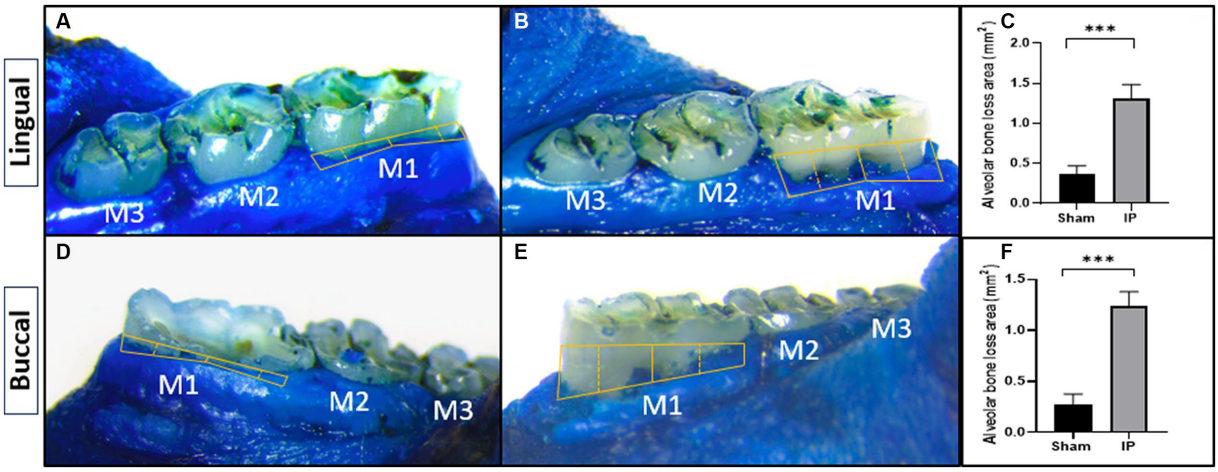


FIGURE 6
Effect of periodontitis on alveolar bone loss (methylene blue staining). The alveolar bone loss area was macroscopically measured on the lingual **(A,B)** and buccal **(C,D)** surfaces in rats with sham **(A,C)** or induced periodontitis **(B,D)**. Bar graphs show the alveolar bone loss area from the lingual **(E)** and buccal **(F)** surfaces. Yellow solid lines depict the alveolar bone loss region. Data are presented as mean ± standard deviation (SD) ***$p < 0.001$. IP, induction of periodontitis through ligation of the left mandibular first molar.

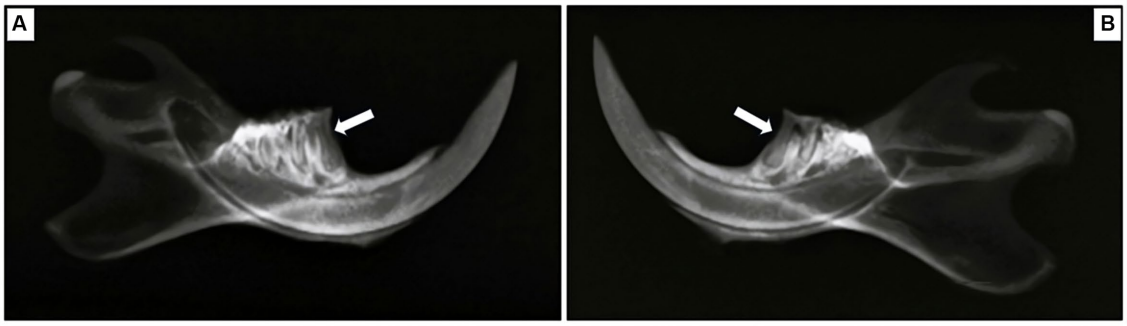


FIGURE 7
Radiographic exploration of mesial root areas in the first mandibular molar for two groups. **(A)** Sham rats, **(B)** rats with induced periodontitis. Sham rats demonstrate the absence of alveolar bone loss, as the alveolar bone is displayed continuously wrapping around the root, in contrast to their counterparts in the model group. Alveolar bone loss is indicated by the white arrow.

0.004, respectively, for APS; 0.02, 0.01, and 0.02, respectively, for MIS; and <0.001 for all for BAL segmental region). Ea had a significant effect on MIS and BAL ($p = 0.03$ and 0.0132), while Tau exhibited a significant effect on APS and APL ($p = 0.03$ for both). ESPVR showed significant effects on APS and BAL ($p < 0.01$), and PRSW also had significant effects on MIS and BAL ($p = 0.02$ and <0.001).

## Discussion

In this study, the bone loss seen in rats subjected to dental ligation indicated that the examined model of periodontitis was straightforward. Through the evaluation of cardiac function (using echocardiography), hemodynamics (via PV loop analysis), and histopathological examination of myocardial tissue structure, the impact of periodontitis on the cardiovascular system was revealed in this experimental periodontitis model.

In this study, we employed an anesthetic protocol involving a combination of MMB and atipamezole. Numerous studies on the use of MMB in mice and rats have been documented (18, 36–38). Beyond these species, the anesthetic efficacy of MMB has been explored in other laboratory animals, including monkeys (39), cotton rats (40), and hamsters (41).

According to Kirihara et al. (42), following the administration of MMB, a reduction in blood pressure was observed until the 20 min mark, after which it stabilized during anesthesia. MMB, acting as an alpha2-adrenergic receptor agonist, is known to decrease blood pressure (43). However, Kirihara et al. (42) noted a significant increase in systolic blood pressure at 10 min post-administration in the MMB group compared to the KX group. This contradictory effect may be attributed to MED's specificity as an alpha2-adrenergic receptor agonist in comparison to XYL (44). The elevated blood pressure at 10 min post-MMB administration suggests MED's interaction with alpha2B receptors, causing a temporary peripheral vessel constriction (45).

TABLE 5 Correlation and regression analysis between P-V measurements and IVPG indices.

| | HR | | SW | | CO | | SV | | ESV | | EDV | | ESP | |
|---|---|---|---|---|---|---|---|---|---|---|---|---|---|---|
| | *r* | $R^2$ | *r* | $R^2$ | *r* | $R^2$ | *r* | $R^2$ | *r* | $R^2$ | *r* | $R^2$ | *r* | $R^2$ |
| Total IVPG | −0.495* | 0.245 | 0.184 | 0.034 | 0.491 | 0.241 | 0.225 | 0.05 | −0.579* | 0.335* | 0.155 | 0.024 | 0.312 | 0.097 |
| Basal IVPG | −0.177 | 0.031 | 0.107 | 0.011 | 0.228 | 0.052 | 0.261 | 0.068 | −0.31 | 0.096 | −0.109 | 0.011 | 0.178 | 0.031 |
| Mid-Apical IVPG | −0.611* | 0.373* | 0.818* | 0.67*** | 0.619* | 0.384* | 0.326 | 0.106 | −0.305 | 0.093 | 0.222 | 0.049 | 0.604* | 0.365* |
| Mid IVPG | −0.538* | 0.289* | 0.85* | 0.723*** | 0.561* | 0.315* | 0.386 | 0.149 | −0.282 | 0.079 | 0.353 | 0.124 | 0.588* | 0.346* |
| Apical IVPG | −0.338 | 0.114 | 0.115 | 0.013 | 0.301 | 0.091 | −0.078 | 0.006 | −0.134 | 0.017 | −0.288 | 0.082 | 0.185 | 0.034 |

| | EDP | | Ea | | Tau | | ESPVR | | EDPVR | | PRSW | |
|---|---|---|---|---|---|---|---|---|---|---|---|---|
| | *r* | $R^2$ | *r* | $R^2$ | *r* | $R^2$ | *r* | $R^2$ | *r* | $R^2$ | *r* | $R^2$ |
| Total IVPG | −0.082 | 0.006 | −0.416 | 0.173 | −0.012 | 0.0001 | 0.154 | 0.023 | −0.133 | 0.017 | 0.266 | 0.07 |
| Basal IVPG | −0.242 | 0.058 | −0.242 | 0.058 | −0.053 | 0.002 | −0.171 | 0.029 | −0.299 | 0.089 | −0.129 | 0.016 |
| Mid-Apical IVPG | 0.0002 | 0.0004 | −0.539* | 0.291* | −0.16 | 0.025 | 0.395 | 0.156 | −0.047 | 0.002 | 0.617* | 0.381* |
| Mid IVPG | −0.058 | 0.003 | −0.483* | 0.233 | −0.074 | 0.005 | 0.233 | 0.054 | 0.11 | 0.012 | 0.661* | 0.437** |
| Apical IVPG | 0.152 | 0.023 | −0.276 | 0.076 | −0.263 | 0.069 | 0.517 | 0.268* | −0.424 | 0.18 | 0.034 | 0.001 |

*, **, *** Respectively represent significance $p < 0.05$, $p < 0.001$, and $p < 0.0001$ and are shown in bold.

TABLE 6 Correlation and regression analysis between P-V measurements and STE parameters.

| | HR | | SW | | CO | | SV | | ESV | | EDV | | ESP | |
|---|---|---|---|---|---|---|---|---|---|---|---|---|---|---|
| | *r* | $R^2$ | *r* | $R^2$ | *r* | $R^2$ | *r* | $R^2$ | *r* | $R^2$ | *r* | $R^2$ | *r* | $R^2$ |
| ApS | 0.501* | 0.251* | −0.255 | 0.065 | −0.379 | 0.143 | −0.499* | 0.249* | 0.32 | 0.102 | 0.07 | 0.004 | −0.66** | 0.443** |
| MIS | 0.573* | 0.328* | −0.384 | 0.147 | −0.231 | 0.053 | −0.577* | 0.333* | 0.409 | 0.167 | −0.034 | 0.001 | −0.542* | 0.294* |
| BIS | 0.078 | 0.006 | −0.143 | 0.02 | −0.056 | 0.003 | −0.058 | 0.003 | −0.073 | 0.005 | −0.299 | 0.089 | 0.011 | 0.0001 |
| ApL | 0.329 | 0.108 | −0.342 | 0.117 | −0.312 | 0.097 | −0.034 | 0.001 | 0.1 | 0.01 | 0.245 | 0.06 | −0.354 | 0.125 |
| MAL | −0.084 | 0.007 | −0.331 | 0.11 | 0.005 | 0.00002 | −0.151 | 0.022 | 0.039 | 0.001 | −0.092 | 0.008 | −0.073 | 0.005 |
| BAL | 0.872*** | 0.761*** | −0.694** | 0.482** | −0.621* | 0.385* | −0.757*** | 0.573*** | 0.513* | 0.263* | −0.101 | 0.01 | −0.908 | 0.824*** |

| | EDP | | Ea | | Tau | | ESPVR | | EDPVR | | PRSW | |
|---|---|---|---|---|---|---|---|---|---|---|---|---|
| | *r* | $R^2$ | *r* | $R^2$ | *r* | $R^2$ | *r* | $R^2$ | *r* | $R^2$ | *r* | $R^2$ |
| ApS | 0.284 | 0.08 | 0.353 | 0.125 | 0.522* | 0.272* | −0.629** | 0.396** | 0.479* | 0.229 | −0.34 | 0.115 |
| MIS | 0.164 | 0.026 | 0.541* | 0.293* | 0.442* | 0.196 | −0.395 | 0.156 | 0.323 | 0.104 | −0.552* | 0.305* |
| BIS | 0.029 | 0.0008 | 0.001 | 0.0001 | −0.201 | 0.04 | 0.106 | 0.011 | −0.279 | 0.078 | −0.393 | 0.154 |
| ApL | −0.101 | 0.01 | 0.238 | 0.057 | 0.519* | 0.269* | −0.346 | 0.119 | 0.222 | 0.049 | −0.119 | 0.014 |
| MAL | −0.298 | 0.088 | 0.038 | 0.001 | 0.057 | 0.003 | 0.31 | 0.096 | −0.454 | 0.207 | −0.187 | 0.035 |
| BAL | 0.402 | 0.161 | 0.604* | 0.365* | 0.47 | 0.221 | −0.639** | 0.408** | 0.346 | 0.12 | −0.856*** | 0.734*** |

*, **, *** Respectively represent significance $p < 0.05$, $p < 0.001$, and $p < 0.0001$ and are shown in bold.

Baumgartner et al. (46) also reported a transient increase in blood pressure with the anesthetic mixture of MED, mid, and fentanyl, attributed to MED's initial peripheral vasoconstrictive properties. Notably, this temporary rise in blood pressure post-MMB administration was documented in dogs (47) but not in monkeys (48) and mice (42).

Kirihara et al. (42) further observed a decrease in heart rate from approximately 240 beats/min to around 170 beats/min for the initial 20 min post-MMB administration, with stability thereafter. The heart rate gradually increased after the surgical anesthesia duration, with no significant differences between MMB and KX groups. In a separate investigation, it was documented that following the administration of the MMB anesthetic mixture, the respiratory rate in the SD strain was lower compared to that observed after saline administration. Conversely, the respiratory rates in the WST and F344 strains did not show any significant difference following the administration of the anesthetic mixture compared to saline. Subsequent to the administration of the anesthetic mixture, the respiratory rates across the three distinct rat strains became nearly identical and remained stable for the duration of the experiment (49).

## Top of form

Alveolar bone loss stands out as a significant characteristic of periodontitis. This deterioration of bone structure results from a complex interplay of immune and inflammatory processes, as our body seeks to combat oral bacterial dysbiosis (50). The outcomes of our study illustrated that the bone loss detected in rats undergoing dental ligation, as evidenced by both methylene blue staining and radiographic analysis, faithfully recreated the periodontitis model. These findings are consistent with earlier research, which affirms the successful establishment of a periodontitis model through the induction of alveolar bone resorption (20, 31, 51).

The conventional echocardiographic analysis showed a significant reduction in ejection fraction and a decrease in fractional shortening, although the fractional shortening did not reach a statistical significance level. This suggests a potential compromise in left ventricular systolic function in rats with ligature-induced periodontitis. This finding is in line with Ribeiro and colleagues' research (20), which demonstrated that experimental periodontitis leads to cardiac dysfunction, elevated cardiac cytokines, and sympathetic overactivity. These results align with epidemiological studies that indicate an elevated risk of cardiovascular events in clinical periodontitis cases. Furthermore, several studies have highlighted the correlation between the severity of periodontitis and cardiac dysfunction in human subjects (52, 53). On the other hand, in our study, most of the conventional echocardiographic parameters were not found to be statistically significant between the two experimental groups. This suggests that conventional echocardiographic examination may not be suitable for detecting subtle changes in systolic and diastolic function, emphasizing the need for the use of other advanced examination methods such as IVPG and STE analysis.

Echocardiography is a prevalent diagnostic tool in cardiovascular research trials and clinical settings (54). Furthermore, there is a growing interest in noninvasive diagnostic tools. Currently, IVPG stands out as a reliable, noninvasive, preload-independent, and highly precise indicator of diastolic function. This is particularly pertinent in the evaluation of cardiac structure and function in cases of myocardial pathology. It is calculated by dividing the intraventricular pressure decay (IVPD) by the left ventricular (LV) length (25). Our study findings underscore a decrease in IVPG (specifically Mid, and Mid-to-apical regions) in rats with ligature-induced periodontitis. Earlier research by Courtois et al. (55) investigating IVPG determinants showcased significant reductions in IVPG during acute coronary occlusion, along with a correlation between diminished IVPG and extensive regional systolic dysfunction. This, combined with their prior research, contributed to their hypothesis concerning the interaction between IVPG and the left ventricle's (LV) elastic recoil. This suggests a mechanism that supports LV filling at lower diastolic pressures. Impairments in regional systolic function could lead to reduced energy release during diastole, subsequently resulting in abnormal or decreased intraventricular flow. In addition, our hemodynamic measurements, especially end-systolic volume (ESV), support this hypothesis. In animals with periodontitis, ESV increased, these findings are in accordance with Steine et al. (56), who compared results from color M-mode echocardiography with invasively acquired pressure gradients. In their study, they observed a decrease in IVPG along with an inverse relationship with end-systolic volume (ESV). However, it remains uncertain from these findings whether isolated changes in systolic function, such as ESV, can manifest independently of alterations in diastolic function, or if these two properties are interconnected through the elastic recoil properties of the LV (57).

Speckle-tracking echocardiography operates by tracing the movement of speckle patterns generated by the interference of ultrasound beams within the myocardium over time (26). This technique captures the degree and velocity of deformation within a particular myocardial area in relation to its initial dimensions. One of the key advantages of speckle-tracking echocardiography lies in its ability to evaluate cardiac function across both long and short-axis viewing planes, enabling the assessment of longitudinal, radial, and circumferential strain for any selected area of interest. This method has proven valuable in detecting ischemic regions, particularly in studies related to myocardial infarction (58, 59). Moreover, it holds promise for advancing our comprehension of regional cardiac dysfunction within chronic disease conditions (60).

While the application of speckle tracking echocardiography as a tool for *in vivo* assessment of myocardial strain in mice was introduced over 15 years ago (61), only a limited number of studies have utilized this technique to examine specific measures of cardiac function in rodents. In our study, the regional analysis of longitudinal strain rate unveiled noteworthy findings, particularly within the apical and middle segments of the septum, as well as the basal segment of the lateral free wall. These regions appear particularly susceptible to diastolic dysfunction caused by periodontitis, suggesting that they could potentially serve as indicators of early systolic impairment in the longitudinal plane.

The examination of pressure-volume loops (PV loops) in hemodynamics has emerged as the widely accepted method for studying intricate, *in vivo* cardiac function. This approach facilitates the concurrent measurement of pressure and volume signals in the beating hearts of intact rodents. On one hand, PV-loop analysis has significantly enhanced our understanding of molecular cardiac physiology by facilitating the identification of crucial functional relationships. On the other hand, it permits the examination of the cardiovascular effects of particular therapeutic interventions or specific signaling pathways through the use of transgenic disease models (62). Regarding hemodynamic measurements, we observed tachycardia in rats with periodontitis, which aligns with the findings of Ribeiro and colleagues (20), lending support to the concept of sympathetic overactivation. It is widely recognized that persistent sympathetic overactivity is linked to the development of organ damage, including cardiac hypertrophy and compromised kidney function (63). Within this context, the outcomes of our present study bolster the notion of an elevated cardiovascular risk associated with gingival infection in the evaluated model especially compromised systolic function and myocardial relaxation.

Both load-dependent parameters (including stroke volume, stroke work, and cardiac output) and load-independent parameters (such as ESPVR and preload recruitable stroke work) derived from pressure-volume (P-V) loops indicated a gradual decline in left ventricular (LV) function in the periodontitis rat models. This decline is evidenced by a reduction in the amplitude of the P-V loops, signifying waning contractility in the affected hearts. The overall deterioration in LV function seems to stem from an initial substantial decline in systolic function (manifested as reduced end-systolic pressure—ESP, SV, CO, and SW). In addition, throughout the cardiac cycle, the heart's work operates within the boundaries delineated by the End-diastolic

pressure-volume relationship (EDPVR) and the ESPVR. Within the normal physiological range of LV systolic and diastolic pressures, ESPVR remains relatively unaffected by preload and afterload variations, making it a dependable marker of LV contractility. Notably, the slope of the ESPVR was significantly reduced in the periodontitis rat models. This trend, in conjunction with other contractility measures (such as PRSW), clearly indicates a subtle deterioration in contractility and subsequent systolic function (64).

Our investigation also encompassed an examination of the impact of induced periodontitis on the left ventricular muscle tissue, with a specific focus on myocyte morphology, histopathological assessments following 5 weeks of induced periodontitis revealed a range of noteworthy observations. These included instances of inflammatory cell infiltration, myocyte degeneration, and a loss of organized arrangement. Furthermore, interstitial changes were also noted. Notably, comparable studies employing similar experimental designs have reported substantial inflammatory cell infiltration in various cardiac tissues. For instance, IP was found to induce significant inflammatory cell infiltration in myocardial tissue (19), the aortic wall (4), and the atrium (65).

The research conducted by Köse et al. (19) provided insights into the early chronic phase effects of periodontitis on heart tissue, revealing degenerative and hypertrophic changes. Furthermore, the authors posited that extended exposure to systemic inflammatory stress might elevate the risk of hypertrophic alterations. Miyajima et al. (4) demonstrated that periodontitis triggers the adherence of monocytes and macrophages to aortic endothelial cells, achieved through an increase in p65 NF-kB-mediated vascular cell adhesion molecule-1 expression. This adhesion mechanism is postulated to also apply to ventricular endothelial cells, potentially influencing muscle tissue. The consequential release of a multitude of cytokines and growth factors by these adhered cells is believed to contribute to the histopathological changes mentioned earlier. In another study, Yu et al. (65) discovered hypertrophy, particularly in left atrial myocytes, during histopathological evaluations conducted 90 days after exposure to experimental periodontitis in dogs. Notably, this hypertrophy was not significantly observed in ventricular myocytes. From this perspective, it is plausible to consider that histopathological changes in heart tissue due to periodontitis entail degenerative changes during the initial phase, which potentially transition to hypertrophic changes during the chronic stage, dependent on the extent of exposure to inflammatory stress.

## Conclusion

The study highlights the potentially significant role of periodontitis in causing cardiovascular dysfunction. Comprehensive cardiac assessments showed subtle changes in cardiac parameters, demonstrating how periodontal inflammation may functionally compromise CVD progression. Advanced cardiac evaluation techniques such as pressure gradient analysis, speckle tracking, and PV loop analysis were employed to emphasize the importance of using cutting-edge methods to understand complex biological relationships. This research marks a crucial step in comprehending the intricate links between periodontal health and cardiovascular well-being, with the potential to advance clinical practices and improve patient outcomes in these interconnected domains.

## Limitations

While our study has yielded valuable insights, it is important to acknowledge certain limitations. We did not elucidate the intricate mechanistic pathways responsible for the observed cardiac changes, potentially overlooking crucial components that contribute to the link between periodontitis and cardiac dysfunction. This omission underscores the need for further investigations into the molecular underpinnings of this relationship. Nevertheless, our research has provided valuable non-invasive data on cardiac function and structure. This data serves as a foundation for future research endeavors aiming to delve deeper into the molecular intricacies of this connection and the relationship between the severity of periodontitis and the degree of impairment in heart function requires further research.

## Data availability statement

The original contributions presented in the study are included in the article/supplementary material, further inquiries can be directed to the corresponding authors.

## Ethics statement

The animal study was approved by the Tokyo University of Agriculture and Technology's Institutional Animal Care and Use Committee (Approval No. R05-159). The study was conducted in accordance with the local legislation and institutional requirements.

## Author contributions

AsE: Data curation, Formal analysis, Methodology, Visualization, Writing – original draft. AF: Data curation, Formal analysis, Methodology, Investigation, Writing – original draft. AhE: Methodology, Visualization, Writing – original draft. AY: Formal analysis, Visualization, Writing – original draft. HH: Formal analysis, Visualization, Writing – original draft. AM: Investigation, Writing – review & editing. RT: Investigation, Methodology, Supervision, Visualization, Writing – review & editing.

## Funding

The author(s) declare that no financial support was received for the research, authorship, and/or publication of this article.

## Conflict of interest

The authors declare that the research was conducted in the absence of any commercial or financial relationships that could be construed as a potential conflict of interest.

## Publisher's note



## References

1. Dahlöf B. Cardiovascular disease risk factors: epidemiology and risk assessment. *Am J Cardiol*. (2010) 105:3A–9A. doi: 10.1016/j.amjcard.2009.10.007

2. Chun YP, Chun KJ, Olguin D, Wang H. Biological foundation for periodontitis as a potential risk factor for atherosclerosis. *J Periodontal Res*. (2005) 40:87–95. doi: 10.1111/j.1600-0765.2004.00771.x

3. Brito LCW, DalBo S, Striechen TM, Farias JM, Olchanheski LR Jr, Mendes RT, et al. Experimental periodontitis promotes transient vascular inflammation and endothelial dysfunction. *Arch Oral Biol*. (2013) 58:1187–98. doi: 10.1016/j.archoralbio.2013.03.009

4. Miyajima S, Naruse K, Kobayashi Y, Nakamura N, Nishikawa T, Adachi K, et al. Periodontitis-activated monocytes/macrophages cause aortic inflammation. *Sci Rep*. (2014) 4:5171. doi: 10.1038/srep05171

5. Ferreira MC, Dias-Pereira AC, Branco-de-Almeida LS, Martins CC, Paiva SM. Impact of periodontal disease on quality of life: a systematic review. *J Periodontal Res*. (2017) 52:651–65. doi: 10.1111/jre.12436

6. Fernandes LA, Martins TM, de Almeida JC, Theodoro LH, Garcia VG. Radiographic assessment of photodynamic therapy as an adjunctive treatment on induced periodontitis in immunosuppressed rats. *J Appl Oral Sci*. (2010) 18:237–43. doi: 10.1590/S1678-77572010000300007

7. Ionel A, Lucaciu O, Tăbăran F, Berce C, Toader S, Hurubeanu L, et al. Histopathological and clinical expression of periodontal disease related to the systemic inflammatory response. *Histol Histopathol*. (2017) 32:379–84. doi: 10.14670/HH-11-803

8. de Souza DM, Ricardo LH, Prado MA, Prado FA, Rocha RF. The effect of alcohol consumption on periodontal bone support in experimental periodontitis in rats. *J Appl Oral Sci*. (2006) 14:443–7. doi: 10.1590/S1678-77572006000600010

9. Meusel DRDZ, Ramacciato JC, Motta RHL, Júnior RBB, Flório FM. Impact of the severity of chronic periodontal disease on quality of life. *J Oral Sci*. (2015) 57:87–94. doi: 10.2334/josnusd.57.87

10. DeStefano F, Anda RF, Kahn HS, Williamson DF, Russell CM. Dental disease and risk of coronary heart disease and mortality. *Br Med J*. (1993) 306:688–91. doi: 10.1136/bmj.306.6879.688

11. Humphrey LL, Fu R, Buckley DI, Freeman M, Helfand M. Periodontal disease and coronary heart disease incidence: a systematic review and meta-analysis. *J Gen Intern Med*. (2008) 23:2079–86. doi: 10.1007/s11606-008-0787-6

12. Munoz Aguilera E, Suvan J, Buti J, Czesnikiewicz-Guzik M, Barbosa Ribeiro A, Orlandi M, et al. Periodontitis is associated with hypertension: a systematic review and meta-analysis. *Cardiovasc Res*. (2020) 116:28–39. doi: 10.1093/cvr/cvz201

13. Górska R, Gregorek H, Kowalski J, Laskus-Perendyk A, Syczewska M, Madaliński K. Relationship between clinical parameters and cytokine profiles in inflamed gingival tissue and serum samples from patients with chronic periodontitis. *J Clin Periodontol*. (2003) 30:1046–52. doi: 10.1046/j.0303-6979.2003.00425.x

14. Chistiakov DA, Orekhov AN, Bobryshev YV. Links between atherosclerotic and periodontal disease. *Exp Mol Pathol*. (2016) 100:220–35. doi: 10.1016/j.yexmp.2016.01.006

15. Hujoel PP, Drangsholt M, Spiekerman C, DeRouen TA. Periodontal disease and coronary heart disease risk. *JAMA*. (2000) 284:1406–10. doi: 10.1001/jama.284.11.1406

16. Loos BG, Craandijk J, Hoek FJ, Dillen PMEW, Van Der Velden U. Elevation of systemic markers related to cardiovascular diseases in the peripheral blood of periodontitis patients. *J Periodontol*. (2000) 71:1528–34. doi: 10.1902/jop.2000.71.10.1528

17. Farag A, Mandour AS, Hendawy H, Elhaieg A, Elfadadny A, Tanaka R. A review on experimental surgical models and anesthetic protocols of heart failure in rats. *Front Vet Sci*. (2023) 10:386. doi: 10.3389/fvets.2023.1103229

18. Farag A, Mandour AS, Hamabe L, Yoshida T, Shimada K, Tanaka R. Novel protocol to establish the myocardial infarction model in rats using a combination of medetomidine-midazolam-butorphanol (MMB) and atipamezole. *Front Vet Sci*. (2022) 9:1880. doi: 10.3389/fvets.2022.1064836

19. Köse O, Arabacı T, Gedikli S, Eminoglu DÖ, Kermen E, Kızıldağ A, et al. Biochemical and histopathologic analysis of the effects of periodontitis on left ventricular heart tissues of rats. *J Periodontal Res*. (2017) 52:176–85. doi: 10.1111/jre.12380

20. Ribeiro AB, Santos-Junior NN, Luiz JPM, de Oliveira M, Kanashiro A, Taira TM, et al. Cardiovascular and autonomic dysfunction in murine ligature-induced periodontitis. *Sci Rep*. (2020) 10:1–9. doi: 10.1038/s41598-020-63953-1

21. Zacchigna S, Paldino A, Falcão-Pires I, Daskalopoulos EP, Dal Ferro M, Vodret S, et al. Towards standardization of echocardiography for the evaluation of left ventricular function in adult rodents: a position paper of the ESC Working Group on Myocardial Function. *Cardiovasc Res*. (2021) 117:43–59. doi: 10.1093/cvr/cvaa110

22. Lang RM, Bierig M, Devereux RB, Flachskampf FA, Foster E, Pellikka PA, et al. Recommendations for chamber quantification: a report from the American Society of Echocardiography's Guidelines and Standards Committee and the Chamber Quantification Writing Group, developed in conjunction with the European Association of Echocardiography, a branch of the European Society of Cardiology. *J Am Soc Echocardiogr*. (2005) 18:1440–63. doi: 10.1016/j.echo.2005.10.005

23. Kitpipatkun P, Matsuura K, Shimada K, Uemura A, Goya S, Yoshida T, et al. Key factors of diastolic dysfunction and abnormal left ventricular relaxation in diabetic rats. *J Med Ultrason*. (2020) 47:347–56. doi: 10.1007/s10396-020-01021-x

24. Farag A, Mandour AS, Kaneda M, Elfadadny A, Elhaieg A, Shimada K, et al. Effect of trehalose on heart functions in rats model after myocardial infarction: assessment of novel intraventricular pressure and heart rate variability. *Front Cardiovasc Med*. (2023) 10:1182628. doi: 10.3389/fcvm.2023.1182628

25. Mandour AS, Farag A, Helal MAY, El-Masry G, Al-Rejaie S, Takahashi K, et al. Non-invasive assessment of the intraventricular pressure using novel color M-mode echocardiography in animal studies: current status and future perspectives in veterinary medicine. *Animals*. (2023) 13:2452. doi: 10.3390/ani13152452

26. Dandel M, Lehmkuhl H, Knosalla C, Suramelashvili N, Hetzer R. Strain and strain rate imaging by echocardiography-basic concepts and clinical applicability. *Curr Cardiol Rev*. (2009) 5:133–48. doi: 10.2174/157340309788166642

27. Oh JE, Jun JH, Hwang HJ, Shin EJ, Oh YJ, Choi YS. Dexmedetomidine restores autophagy and cardiac dysfunction in rats with streptozotocin-induced diabetes mellitus. *Acta Diabetol*. (2019) 56:105–14. doi: 10.1007/s00592-018-1225-9

28. Berry MF, Engler AJ, Woo YJ, Pirolli TJ, Bish LT, Jayasankar V, et al. Mesenchymal stem cell injection after myocardial infarction improves myocardial compliance. *Am J Physiol Circ Physiol*. (2006) 290:H2196–203. doi: 10.1152/ajpheart.01017.2005

29. Kovács A, Oláh A, Lux Á, Mátyás C, Németh BT, Kellermayer D, et al. Strain and strain rate by speckle-tracking echocardiography correlate with pressure-volume loop-derived contractility indices in a rat model of athlete's heart. *Am J Physiol Circ Physiol*. (2015) 308:H743–8. doi: 10.1152/ajpheart.00828.2014

30. Aboubakr M, Farag A, Elfadadny A, Alkafafy M, Soliman A, Elbadawy M. Antioxidant and anti-apoptotic potency of allicin and lycopene against methotrexate-induced cardiac injury in rats. *Environ Sci Pollut Res*. (2023) 30:88724–33. doi: 10.1007/s11356-023-28686-4

31. de Souza JAC, Nogueira AVB, de Souza PPC, Cirelli JA, Garlet GP, Rossa C Jr. Expression of suppressor of cytokine signaling 1 and 3 in ligature-induced periodontitis in rats. *Arch Oral Biol*. (2011) 56:1120–8. doi: 10.1016/j.archoralbio.2011.03.022

32. Wu T, Trevisan M, Genco RJ, Dorn JP, Falkner KL, Sempos CT. Periodontal disease and risk of cerebrovascular disease: the first national health and nutrition examination survey and its follow-up study. *Arch Intern Med*. (2000) 160:2749–55. doi: 10.1001/archinte.160.18.2749

33. Casili G, Ardizzone A, Lanza M, Gugliandolo E, Portelli M, Militi A, et al. Treatment with Luteolin improves lipopolysaccharide-induced periodontal diseases in rats. *Biomedicines*. (2020) 8:442. doi: 10.3390/biomedicines8100442

34. Milojevic Samanovic A, Jakovljevic V, Vasovic M, Mitrovic S, Rankovic M, Mihajlovic K, et al. Cardiac, biochemical and histopathological analysis reveals impaired heart function in hypertensive rats with apical periodontitis. *Int Endod J*. (2021) 54:1581–96. doi: 10.1111/iej.13562

35. Sarıtekin E, Üreyen Kaya B, Aşcı H, Özmen Ö. Anti-inflammatory and antiresorptive functions of melatonin on experimentally induced periapical lesions. *Int Endod J*. (2019) 52:1466–78. doi: 10.1111/iej.13138

36. Ochiai Y, Iwano H, Sakamoto T, Hirabayashi M, Kaneko E, Watanabe T, et al. Blood biochemical changes in mice after administration of a mixture of three anesthetic agents. *J Vet Med Sci*. (2016) 78:951–6. doi: 10.1292/jvms.15-0474

37. Tsubokura Y, Kobayashi T, Oshima Y, Hashizume N, Nakai M, Ajimi S, et al. Effects of pentobarbital, isoflurane, or medetomidine-midazolam-butorphanol anesthesia on bronchoalveolar lavage fluid and blood chemistry in rats. *J Toxicol Sci*. (2016) 41:595–604. doi: 10.2131/jts.41.595

38. Osanai H, Tateno T. Neural response differences in the rat primary auditory cortex under anesthesia with ketamine versus the mixture of medetomidine, midazolam and butorphanol. *Hear Res*. (2016) 339:69–79. doi: 10.1016/j.heares.2016.06.012

39. Ochi T, Nishiura I, Tatsumi M, Hirano Y, Yahagi K, Sakurai Y, et al. Anesthetic effect of a combination of medetomidine-midazolam-butorphanol in cynomolgus

monkeys (*Macaca fascicularis*). *J Vet Med Sci*. (2014) 76:917–21. doi: 10.1292/jvms.13-0589

40. Nakamura T, Ichii O, Irie T, Hosotani M, Dantsuka A, Nakamura S, et al. Usefulness of an anesthetic mixture of medetomidine, midazolam, and butorphanol in cotton rats (*Sigmodon hispidus*). *Jpn J Vet Res*. (2016) 64:273–6. doi: 10.14943/jjvr.64.4.273

41. Nakamura T, Karakida N, Dantsuka A, Ichii O, Elewa YHA, Kon Y, et al. Effects of a mixture of medetomidine, midazolam and butorphanol on anesthesia and blood biochemistry and the antagonizing action of atipamezole in hamsters. *J Vet Med Sci*. (2017) 79:1230–5. doi: 10.1292/jvms.17-0210

42. Kirihara Y, Takechi M, Kurosaki K, Matsuo H, Kajitani N, Saito Y. Effects of an anesthetic mixture of medetomidine, midazolam, and butorphanol and antagonism by atipamezole in rabbits. *Exp Anim*. (2019) 68:443–52. doi: 10.1538/expanim.18-0183

43. Feldman J, Fellmann L, Bousquet P. The central hypotensive effect induced by α2-adrenergic receptor stimulation is dependent on endothelial nitric oxide synthase. *J Hypertens*. (2008) 26:1033–6. doi: 10.1097/HJH.0b013e3282f7cbab

44. Flecknell P. *Laboratory animal anaesthesia*. *Fourth Edition*. Newcastle-upon-Tyne, UK: Academic Press (2015).

45. Nichols AJ, Hieble JP, Ruffolo RR. The pharmacology of peripheral at and α2-andrenoceptors. *J Basic Clin Physiol Pharmacol*. (1988) 7:129–206. doi: 10.1515/JBCPP.1988.7.1-4.129

46. Baumgartner C, Bollerhey M, Ebner J, Schuster T, Henke J, Erhardt W. Effects of medetomidine-midazolam-fentanyl IV bolus injections and its reversal by specific antagonists on cardiovascular function in rabbits. *Can J Vet Res*. (2010) 74:286–98.

47. Itamoto K, Hikasa Y, Sakonjyu I, Itoh H, Kakuta T, Takase K. Anaesthetic and cardiopulmonary effects of balanced anaesthesia with medetomidine-midazolam and butorphanol in dogs. *J Veterinary Med A*. (2000) 47:411–20. doi: 10.1046/j.1439-0442.2000.00302.x

48. Kalema-Zikusoka G, Horne WA, Levine J, Loomis MR. Comparison of the cardiorespiratory effects of medetomidine-butorphanol-ketamine and medetomidine-butorphanol-midazolam in patas monkeys (*Erythrocebus patas*). *J Zoo Wildl Med*. (2003) 34:47–52. doi: 10.1638/1042-7260(2003)34[0047:COTCEO]2.0.CO;2

49. Kirihara Y, Takechi M, Kurosaki K, Kobayashi Y, Saito Y, Takeuchi T. Effects of an anesthetic mixture of medetomidine, midazolam, and butorphanol in rats—strain difference and antagonism by atipamezole. *Exp Anim*. (2016) 65:27–36. doi: 10.1538/expanim.15-0036

50. Hienz SA, Paliwal S, Ivanovski S. Mechanisms of bone resorption in periodontitis. *J Immunol Res*. (2015) 2015:1–10. doi: 10.1155/2015/615486

51. Wang Y, Fan Q, Xu Y, Zeng F, Liu X, Zhao D, et al. Effect of Eucommia water extract on gingivitis and periodontitis in experimental rats. *BMC Oral Health*. (2022) 22:326. doi: 10.1186/s12903-022-02353-5

52. Angeli F, Verdecchia P, Pellegrino C, Pellegrino RG, Pellegrino G, Prosciutti L, et al. Association between periodontal disease and left ventricle mass in essential hypertension. *Hypertension*. (2003) 41:488–92. doi: 10.1161/01.HYP.0000056525.17476.D7

53. Shimazaki Y, Saito T, Kiyohara Y, Kato I, Kubo M, Iida M, et al. Relationship between electrocardiographic abnormalities and periodontal disease: the Hisayama study. *J Periodontol*. (2004) 75:791–7. doi: 10.1902/jop.2004.75.6.791

54. Yoshida T, Uemura A, Tanaka R, Farag A, Mandour AS, Hamabe L, et al. Secondary right atrial thrombosis in three dogs: antithrombotics therapy and echocardiographic follow-up. *Vet Med Sci*. (2023) 9:1973–9. doi: 10.1002/vms3.1210

55. Courtois M, Kovacs SJ, Ludbrook PA. Physiological early diastolic intraventricular pressure gradient is lost during acute myocardial ischemia. *Circulation*. (1990) 81:1688–96. doi: 10.1161/01.CIR.81.5.1688

56. Steine K, Stugaard M, Smiseth OA. Mechanisms of retarded apical filling in acute ischemic left ventricular failure. *Circulation*. (1999) 99:2048–54. doi: 10.1161/01.CIR.99.15.2048

57. Firstenberg MS, Smedira NG, Greenberg NL, Prior DL, McCarthy PM, Garcia MJ, et al. Relationship between early diastolic intraventricular pressure gradients, an index of elastic recoil, and improvements in systolic and diastolic function. *Circulation*. (2001) 104:I-330–5. doi: 10.1161/hc37t1.094834

58. Bauer M, Cheng S, Jain M, Ngoy S, Theodoropoulos C, Trujillo A, et al. Echocardiographic speckle-tracking based strain imaging for rapid cardiovascular phenotyping in mice. *Circ Res*. (2011) 108:908–16. doi: 10.1161/CIRCRESAHA.110.239574

59. Bhan A, Sirker A, Zhang J, Protti A, Catibog N, Driver W, et al. High-frequency speckle tracking echocardiography in the assessment of left ventricular function and remodeling after murine myocardial infarction. *Am J Physiol Circ Physiol*. (2014) 306:H1371–83. doi: 10.1152/ajpheart.00553.2013

60. Daniels LJ, Macindoe C, Koutsifeli P, Annandale M, Raaijmakers AJA, Weeks KL, et al. Myocardial deformation imaging by 2D speckle tracking echocardiography for assessment of diastolic dysfunction in murine cardiopathology. *Sci Rep*. (2023) 13:12344. doi: 10.1038/s41598-023-39499-3

61. Peng Y, Popovic ZB, Sopko N, Drinko J, Zhang Z, Thomas JD, et al. Speckle tracking echocardiography in the assessment of mouse models of cardiac dysfunction. *Am J Physiol Circ Physiol*. (2009) 297:H811–20. doi: 10.1152/ajpheart.00385.2009

62. Miranda-Silva D, Sequeira V, Lourenço AP, Falcão-Pires I. Assessing rodent cardiac function *in vivo* using hemodynamic pressure-volume loops. *Front Physiol*. (2022) 12:751326. doi: 10.3389/fphys.2021.751326

63. Sata Y, Head GA, Denton K, May CN, Schlaich MP. Role of the sympathetic nervous system and its modulation in renal hypertension. *Front Med*. (2018) 5:82. doi: 10.3389/fmed.2018.00082

64. Shioura KM, Geenen DL, Goldspink PH. Assessment of cardiac function with the pressure-volume conductance system following myocardial infarction in mice. *Am J Physiol Circ Physiol*. (2007) 293:H2870–7. doi: 10.1152/ajpheart.00585.2007

65. Yu G, Yu Y, Li YN, Shu R. Effect of periodontitis on susceptibility to atrial fibrillation in an animal model. *J Electrocardiol*. (2010) 43:359–66. doi: 10.1016/j.jelectrocard.2009.12.002

# Frontiers in Veterinary Science

**Transforms how we investigate and improve animal health**

The third most-cited veterinary science journal, bridging animal and human health with a comparative approach to medical challenges. It explores innovative biotechnology and therapy for improved health outcomes.

---

## Discover the latest Research Topics

See more →

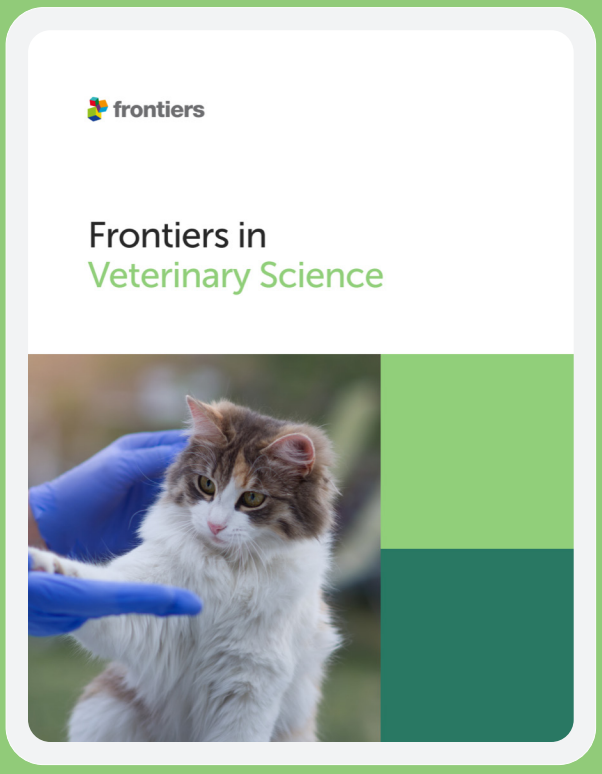


**Frontiers**

Avenue du Tribunal-Fédéral 34
1005 Lausanne, Switzerland
frontiersin.org

**Contact us**

+41 (0)21 510 17 00
frontiersin.org/about/contact